A Microscale Approach to Optimizing the Performance of Microbial Fuel Cells

Thèse

Mehran Abbaszadeh Amirdehi

Doctorat en chimie
Philosophiæ doctor (Ph. D.)

Québec, Canada

A Microscale Approach to Optimizing the Performance of Microbial Fuel Cells

Thèse

Mehran Abbaszadeh Amirdehi

Sous la direction de:

Jesse Greener, directeur de recherche

Amine Miled, co-directeur de recherche

Résumé

Une pile microbienne (MFC) est un type de système bioélectrochimique (BES) dans lequel l'oxydation d'un large éventail de molécules organiques produit un courant électrique utilisable à travers un circuit externe. En tant que tel, ces biofilms respirant les anodes (BRA) ont établi les MFC comme une technologie d'énergie propre de nouvelle génération prometteuse, car ils peuvent produire de l'électricité tout en atteignant simultanément une biorestauration. Les MFC offrent également des solutions durables pour les systèmes d'alimentation distribués et le traitement des eaux usées pouvant être exploités localement à la source de la génération de celles-ci, telles que les maisons et les sites industriels, afin de réduire la dépendance aux installations centralisées. Les MFC ont même fait leurs preuves en tant que sources d'alimentation pour les dispositifs implantés autonomes et la détection à distance. Ce travail vise à améliorer l'efficacité des MFC en se concentrant sur les considérations à l'échelle microscopique. Les progrès techniques dans les électrodes microstructurées et la conception de MFC microfluidique sont démontrés. Ces développements ouvrent des possibilités d'optimisation et de recherche fondamentale sur les MFC et la technologie BES associée. Plus précisément, ces travaux démontrent des améliorations basées sur la structure et les matériaux des électrodes et leur intégration dans des canaux microfluidiques protégés contre les gaz présentant une configuration sans membrane. Le résultat est le MFC microfluidique le plus stable jamais décrit dans la littérature, capable de temps de fonctionnement les plus longs sur la plage de débit la plus large. Nous utilisons cette conception d'appareil robuste pour étudier l'effet du débit afin de surmonter les limitations de la disponibilité des nutriments sur les rendements de puissance, les problèmes de dépassement de puissance, ainsi que d'autres obstacles qui ont un impact plus large sur les MFC dans le secteur des énergies alternatives.

Abstract

A microbial fuel cell (MFC) is a type of bioelectrochemical system (BES) in which oxidation of a broad range of organic molecules produces a usable electric current through an external circuit. As such, such anode respiring biofilms (ARBs) have positioned MFCs as a promising next-generation clean energy technology because they can produce electricity while simultaneously achieving bioremediation. MFCs also offer sustainable solutions for distributed power systems and wastewater treatment that can be operated locally at the source of wastewater generation, such as homes and industrial sites, to reduce reliance on centralized facilities. MFCs have even been demonstrated as power sources for autonomous implanted devices and remote sensing. This work seeks to improve the efficiency of MFCs by focusing on the microscale considerations. Technical advancements in microstructured electrodes and microfluidic MFC design are demonstrated. These developments open up possibilities for optimization and fundamental research into MFCs and related BES technology. Specifically, this work demonstrates improvements based on electrode structure and materials and their integration into gas-protected microfluidic channels featuring a membraneless configuration. The result is the most stable microfluidic MFC yet reported in the literature, capable of the longest operating times over the largest range of flow rates. We use this robust device design in study of the effect of flow to overcome the limitations of nutrient availability on power outputs, the so-called power overshoot problems and other obstacles to achieving wider impact of MFCs in the alternative energy sector.

Table of Contents

List of Figures

List of Tables

List of Equations

List of abbreviations

∇	Laplacian
A	Anode surface area
ADP	Adenosine Diphosphate
AEM	Anion exchange membrane
AFC	Alkaline Fuel Cell
ATP	Adenosine triphosphate
Au	Gold
BES	Bio-electrochemical systems
BOD	Biological Oxygen Demand
BPM	Bipolar membrane
CC	Carbon Cloth
CE	Counter-Electrodes
CEM	Cation Exchange Membrane
CNT	Carbon Nanotube
COC	Cyclic-Olefin Copolymer
COD	Chemical Oxygen Demand
CV	Cyclic Voltammetry
DET	Direct Electron Transfer
e^-	Electron
EABs	Electroactive Biofilms
E-Coli	Escherichia Coli
EIS	Electrochemical Impedance Spectroscopy
EPS	Extracellular Polymeric Substances
ETC	Electron Transport Chain
F	Faraday's Constant

Fe-EDTA	Iron Ethylenediaminetetraacetic Acid
H+	Protons
I	Current
IMDs	Implantable Medical Devices
IPCC	Intergovernmental Panel On Climate Change
ITO	Indum Thin Oxide
L	Persistence Length
Mdcs	Microbial Desalination Cells
MEMS	Micro-Electro-Mechanical System
MES	Microbial Electrosynthesis
MET	Mediated Electron Transfer
MFC	Microbial Fuel Cell
mM	Mili Molar
OCV	Open Circuit Voltage
ORR	Oxygen Reduction Reaction
P	Pressure
PAFC	Phosphoric Acid Fuel Cell
PANI	Polyaniline
PBS	Phosphate Buffer Saline
PC	Polycarbonate
PC	Polycarbonate
PDMS	Polydimethyl Dimethylsiloxane
PEGDA	Poly-Ethylene Glycol Diacrylate
PEM	Polymeric Exchange Membrane
PEMFC	Polymer Electrolyte Membrane Fuel Cells
PET	Polyethylene Terephthalate
PI	Polyimide

P_{max}	Power Density
PMFC	Plant Microbial Fuel Cells
PMMA	Poly-Methyl Methacrylate
PMMA	Polymethyl Methacrylate
PS	Polystyrene
PTFE	Polytetrafluoroethylene
PU	Polyurethane
R	Load Resistance
Re	Reynolds Number
RE	Reference Electrode
RMS	Root Mean Square
RVC	Reticulated Vitreous Carbon
SEM	Scanning Electron Microscopy
SOFC	Solid Oxide Fuel Cells
SS	Stainless Steel
Tg	Transition Temperature
TPE	Thermoset Polyester
u	Velocity
UF	Ultrafiltration
WE	Working Electrode
μ	Viscosity

Acknowledgments

During my entire PhD study period, I received so much help and support from numerous brilliant people. Firstly, I would like to express my deep and sincere appreciation to my supervisor, Professor Jesse Greener. Without his great help, I could not start and finish my studies. I am really grateful for his knowledge, support and creative thinking about all my projects and in my whole study period. I would also like to thank my co-director, Professor Amine Miled, for his support to get me here during my PhD study. I thank all the members of the chemistry as well as the biochemistry, electrical and computer engineering department.

My sincere gratitude belongs to my amazing colleagues and friends: Mohammad, Pouyan, François, Nastaran, Adnane, Hamza, Sepideh, Gong, Jia, Dirk, Tanver, Erica, Farnaz, Mazeyar, Brandon, Dima, Eya, Mona, Ali, Sara, Hossein and Milad for their help in this project and for their friendship and support that will make my PhD period a beautiful memory.

Finally, I would like to sincerely acknowledge my family for their support and unconditional kindness and love. They have been the most supportive and helpful people in everything I have decided to accomplish during my life. They have given me the best love and support than anyone could ask for. Thank you.

Foreword

The following section lists the published work for each chapter including the contribution of each author.

Chapter 3: Mehran Abbaszadeh Amirdehi; Sokunthearath Saem; Mirpouyan Zarabadi; Jose Moran-Mirabal; Jesse Greener., Microstructured Anodes by Surface Wrinkling for Studies of Direct Electron Transfer Biofilms in Microbial Fuel Cells. ***Advanced Materials Interfaces,*** 2018***,*** *5* (13), 1800290.

Author contributions: M.A.A., J.G. and J.M.M. formed the concepts of the project and experiments. M.A.A. prepared MFC setup, made microbiological and bacterial preparations, conducted all MFC experiments. S.S. Fabricated and evaluated of anode electrodes. The manuscript writing and editing was mostly done by J.G, M.A.A. Some part of manuscript which is related to anode electrodes was writing and editing by S.S and J.M.M. The manuscript was edited by M.P.Z.

Chapter 4: Mehran Abbaszadeh Amirdehi, Nastaran Khodaparastasgarabad; Hamza Landari; MirPouyan Zarabadi; Amine Miled; Jesse Greener, A membraneless microfluidic microbial fuel cell for stable, long-term operation under a wide range of flow rates. ***ChemElectroChem (2020).***

Author contributions: M.A.A. and J.G. formed the concepts of the project and experiments. M.A.A. fabricated membraneless device, made microbiological and bacterial preparations, and conducted all experiments and analysis. The manuscript writing and editing was done by M.A.A and J.G.

Introduction

Although fossil fuels are the most common energy sources, it is clear that the planet cannot withstand their continued use. Therefore, development of new viable alternative energies is urgently needed. Microbial fuel cell (MFC) technology represents one of the newest alternative energy approaches, whereby electricity is generated from bacteria that can catalyze the conversion of organic molecules into usable energy. Thus, in addition to representing new clean energy sources, MFCs are also promising for wastewater treatment. In their simplest form, the MFC consists of two electrodes, an electron donor (metabolic nutrient) and an electron acceptor, microorganisms that catalyze the reactions, an electrolyte that allows movement of the compounds within the system, and a circuit that transfers electrons between the two electrodes. Usually, MFC contain two chambers that are connected through a cation exchange membrane (CEM). Two major areas of focus that have produced excellent progress in MFC development are microbiological aspects and electrode design. For example, bacterial species, genetic mutations, and their combinations[1,2] have been shown an impact of optimal ways to transfer electrons from the microorganisms to the anode and a number of possible electron transfer processes that enable production of electricity in MFCs.[3] Electrode materials[4] and their structures have also become a major focus of study.[5] Important electrode properties such as excellent electrical conductivity, electron transfer kinetics, surface area, biocompatibility, corrosion resistance and chemical stability can directly affect key performance parameters such as microbial adhesion, electron transfer and fuel oxidation.[6] Generally, structured anodes are designed to increase the total surface area, but little effort has been made to isolate and rigorously study the role of surface topography. This is likely because it is difficult to vary feature geometries in a controlled manner and without introducing competing effects such as changes in total surface area, exposed materials or surface chemistry.

The effect of the hydrodynamic environment has been demonstrated as important in controlling mass transport of nutrients.[7] This aspect has not been deeply investigated due to difficulty in gaining the necessary control in macro-MFCs.[8,9] Microfluidics is the science and technology of devices and processes that deal with small amount of fluids via the use of

micro-scale channels (at least one critical dimension less than 1000 μm). Certain studies of hydrodynamic effects using microchannels have shown beneficial effects, such as higher power with increased flow, but until now, microfluidic MFCs have been plagued by certain device-level instabilities. Designing a device that overcomes these problems can combine the capabilities of flow control with other unique advantages, such as the ability to eliminate CEMs using a membraneless format based on laminar co-flowing streams, high surface-area-to-volume ratios and reduced diffusion barriers. Together, these qualities can reduce ohmic losses, improve fuel consumption efficiency and enhance power densities.

With these factors in mind, this PhD thesis addresses (i) gold structured anodes for MFCs, (ii) the need for a robust microfluidic platform, and (iii) the use of a stable microfluidic MFC to study how flow can improve power outputs and conversion efficiencies.

Chapter 1: Literature review and background

1.1. Energy landscape and need for MFC technology

Research by the Intergovernmental Panel on Climate Change (IPCC) shows that the world's population is growing, e.g., from approximately 6 billion in 2001 to 9.4 billion people by 2050, and thus the world energy consumption rate is expected to grow due to population and economic growth.[2,10] In this decade, the most important portion of the world's energy was obtained from fossil fuels for industrialization and economic growth of countries. For example, in the United States, 83 percent of energy consumption in 2012 (3.3 TW) was based on natural coal, gas and petroleum sources (fossil fuels). This high percentage of consumption is expected to remain almost unchanged until at least 2030 (Figure 1.1).

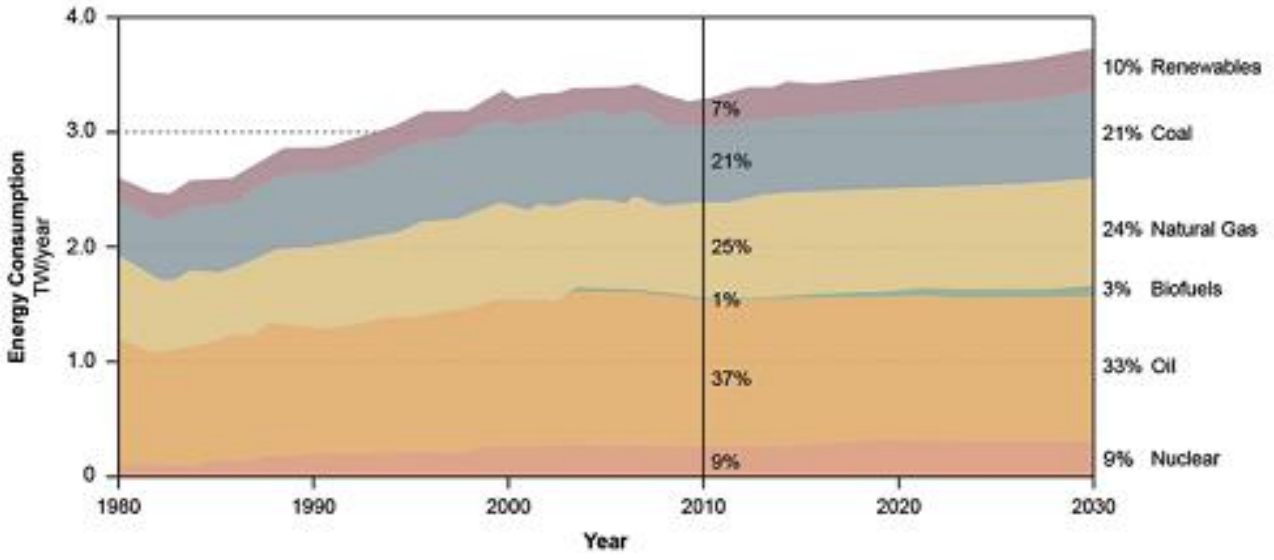

Figure 1.1: Historical, current, and predicted energy consumption in the United States in TW/year. Percentages shown indicate total energy consumption in the United States between 2010 and 2030. [11]

Fossil fuels, which include oil, methane gas, coal, tars and oil shales, are the most commonly used energy source worldwide. These fuels are non-renewable energy sources that are predicted to last for only another century. However, because energy is extracted by combustion, which produces greenhouse gases, climate scientists predict that the resulting climate change could be significant and to increase over time. Other problems with fossil

fuels include environmental pollution at the extraction and processing sites. Nuclear fission, in which atoms are split apart and release energy, is categorized as renewable. However, nuclear fission alone is not the answer to energy demands because the uranium world supply is sufficient only for 100 TW-h of electricity for the next decade. [12]

To address the need for new approaches to energy production, renewable energies are targeted for rapid development. Renewable energy is derived from natural sources and replenished at a rate equal to or faster than the rate at which they are consumed.[13] Many forms of renewable energy exist, and widely popular sources of renewable energy include biomass, solar, wind, tidal and marine, and geothermal power.[14] Increasingly, harvesting of energy from industrial and municipal waste streams is a topic of investigation as well. Next, we review a subset of alternative energy approaches.

Biomass is derived from living organisms, plants and animals. Popular variants include wood, crop residues, lipids from algae, and animal waste. Biomass can be burned directly to produce heat and energy. Generally, it can combust to produce heat energy. Although burning of biomass does produce CO_2, it is considered carbon neutral because its natural growth occurs by fixation of carbon from the atmosphere. However, other problems include competition with alternative land uses such as agriculture, which limits its potential usage. it is estimated that it could supply approximately 7-15% of the global energy requirements.

The solar energy that reaches the Earth's surface includes visible (45%), ultraviolet (1% at shorter wavelengths) and infrared radiation (54% is converted to heat). When sunlight hits an object, it can be reflected (same wavelength) or absorbed (short wavelength energy is changed to long wavelength energy (heat)). This form of energy power from the core of the sun can be used in two forms, namely, electric or thermal energy. This source of energy is a clean, inexpensive, renewable power source that is rapidly becoming economical with two forms of solar collectors (panels) and solar photovoltaic devices that generate a flow of electricity by allowing photons of light to free electrons from their atoms.

Wind energy, or electricity from wind energy, has become the cheapest and fastest growing energy source in the world (and in Canada). Wind energy provides 4% of electricity generation in Canada. Geothermal energy uses heat energy from deep inside the earth to

generate steam and make electricity. The core of the earth is as hot as the surface of sun. This thermal energy is obtained by drilling deep and bringing extremely hot water from underground to the surface using a geothermal heat pump system. The hot water is used as a hydrothermal resource, which is subsequently pumped into turbines to generate electricity. Currently, 0.4 percent of the net electricity generation in the United States comes from geothermal energy.

In this thesis, we focus on the emerging technology known as microbial fuel cells (MFCs). MFCs are a class of bio-electrochemical systems (BES) that can convert potential chemical energy into electrical energy via catalytic oxidation of nutrients or substrates by electroactive biofilms (EABs). Another successful application of MFC was found as one of the popular wastewater treatment technology to provide clean water and produce a green energy. [15]

1.2. History of MFCs

Microbial fuel cell (MFC) technologies represent one of the newest alternative green energy approaches, whereby electricity is generated from waste biomass using electroactive bacteria. The observation that microorganisms can generate electrical current was first reported in 1910 by Michael Cresse Potter at the University of Durham (UK), and at that time, the recorded voltage generated was 0.5 V. Using a glass container and two platinum electrodes, Potter demonstrated that electricity can be generated from a mixed bacteria sample containing *Escherichia coli* (e-coli) and *Saccharomyces Cerevisiae* yeast. Wider use of biological fuel cells began in the 1990s.[16]

MFCs with enhanced power outputs have been developed only within the past 20 years. The slow development of MFC research is likely due to the unclear mechanism of fuel oxidation and electron transfer between microorganisms and the electrode. In the 1980s, certain researchers [17,18] found that the addition of electron-transfer mediators could greatly enhance power output of MFCs.[19]

Recently, investigation of biological fuel cells has accelerated due to economic and environmental pressures related to fossil fuels. [20] In the most recent decade, researchers' interest in the design and performance of MFCs has increased, resulting in power output improvement from less than 0.1 mW/m^2 to over 3 W/m^2, and selected studies are summarized

in table 1.1. [21, 22] They focused on improvements of power generation, development of cost-effective anode and cathode electrode materials and new designs for setups that can be applied in commercial and larger-scale applications.

Table 1.1: List of commonly used MFCs and power density results from experiments with different microorganisms and anode and cathode materials, as described in previous research reports.

Microorganism	Substrate	MFC type	Anode electrode	Cathode electrode	Current or power density	References
Geobacter SPP (Firmicutes)	Glucose	Two-chamber	Carbon paper	Carbon paper	40.3 ± 3.9 mW/m^2	[23]
Escherichia coli	Sewage sludge	Single chambered	Composite electrode (Graphite/PTFE)	Composite electrode (Graphite/PTFE)	76 mW/m^2	[24]
Activated sludge	Wastewater	Cylinder type membrane-less MFC	Graphite felt	Graphite felt (aeration)	1.3 mW/m^2, 6.9 mA/m^2	[25]
G. sulfurreducens	Acetate	Two - chambered MFC w/ PEM	Graphite	Graphite (aeration)	65 mA/m^2	[26]
Mixed bacterial culture	Glucose	Two - chambered (flat type)	Graphite	Graphite (aeration)	3600 mW/m^2	[27]
Anaerobic sludge	Organic wastewater	Two-chambered (flat type)	Graphite felt	Graphite felt	40 mA/m^2	[28]
Wastewater	Wastewater glucose	Single-chambered	Carbon paper	Carbon/Pt (expose to air)	146 mW/m^2 494 mW/m^2	[29]
Mixed culture	Sewage sludge	Single-chambered	Carbon cloth	Carbon cloth	3359 mW/m^2	[30]
Bacteria from another MFC	Glucose wastewater	Tubular, single-chambered	Graphite granules	Woven graphite mat (with ferricyanide)	49 W/m^3 8 W/m^3	[31]
S. oneidensis MR-1	Wastewater	Dual chamber	PANI	Carbon cloth	867 mw/m^2	[32]
P. aeruginosa	Glucose	Dual chamber	Graphene	Carbon cloth	52.5 mW/m^2	[33]
Mixed culture	Anaerobic sludge	Dual chamber	Carbon brush	Carbon cloth	3.3 w/m^3	[34]
Shewanella affinis (KMM3586)	Cyctenin	Two-chamber	Carbon paper	Carbon paper	36 mW/ m^2	[35]
Domestic wastewater	Domestic wastewater	Single-chambered	Carbon cloth	Pt/Carbon/PTFE (Diffusion layer)	766 mW/m^2	[36]
Domestic wastewater	Mixed culture	Single-chambered	Graphite plates	Graphite plates	283 mW/m^2	[37]

1.3. Bacterial biofilms

Bacteria are microorganisms that were among the first life forms to appear on Earth. They appear 3 billion years ago in first oceans. At beginning, there were only anaerobic kind of bacteria because at primordial the atmosphere was free of oxygen. The arrival of new resource (oxygen) lead to a change in the way organisms respired as well. Bacteria can exist in two general forms known as planktonic (swimming) and sessile (surface adhered). According to the official definition from IUPAC, biofilms are surface-attached aggregates of microorganisms that are frequently embedded within a self-produced matrix of extracellular polymeric substances (EPS) consisting of polysaccharides, DNA, and proteins. [38, 39]

Generally, it is accepted that biofilms are formed in five stages: (1) planktonic bacteria attach themselves reversibly to the surface, (2) irreversible adhesion or attachment, (3) microcolony formation, (4) maturation of the biofilm and formation of EPS, and (5) detachment and dispersion of the cells for further downstream colonization. [40] These five steps are shown in Figure 1.2. Although recent work from our group challenges this simplistic idea by demonstrating that proliferation of planktonic bacteria occurs at all stages. [41] Biofilm-forming bacteria have advantages such as enhanced resistance to antimicrobial agents and other harsh chemical and physical environmental conditions.

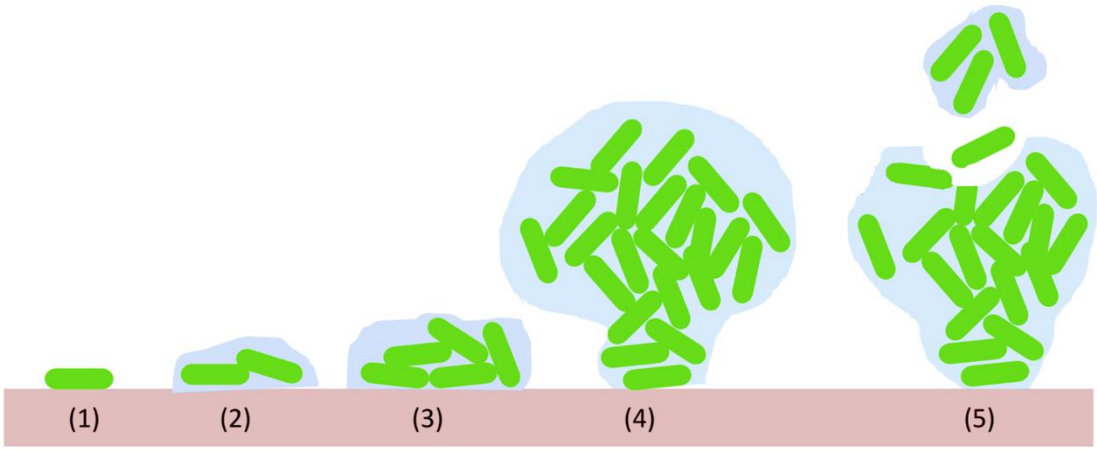

Figure 1.2: Biofilm life cycle formation and spreading in five states: (1) planktonic bacteria attach themselves reversibly to the surface, (2) irreversible adhesion or attachment, (3) microcolony formation, (4) maturation of the biofilm and formation of EPS, and (5) detachment and dispersion of the cells for further downstream colonization.

1.3.1. Electroactive bacteria and biofilms

Electrochemically active biofilms or electroactive bacteria (EABs) have great impacts in natural ecosystems, such as metal oxidation/reduction and the associated effects on mineral dissolution and the carbon cycle. [42] The majority of these bacteria in the nature are living in anaerobic conditions. Terrestrial and aquatic habitats are both exploited for EABs in the natural state.[43]

An electroactive microorganism can transfer electrons to an extracellular acceptor, which is a conductive material. [44] These terminal electron accepters can be chemical (O_2, NO_3-, Fe(III), Mn(III)) or physical (electrodes) in nature. In microbial respiration, electrons released during oxidation of substrate molecules are passed down the electron transport chain (ETC), a process that occurs within the bacterial cell membrane, to a final electron acceptor. The process which is described as Krebs cycle can catalyzes redox reactions by respiration enzymes (e.g., malate dehydrogenase and succinyl-CoA synthetase). In this cycle, energy is generated and adenosine triphosphate (ATP) is formed from adenosine diphosphate (ADP). The important enzymes in this cycle are NAD^+-dependent and FAD-dependent enzymes. [45] Several microbes have been reported that have the ability to oxidize organic substrates and transfer their electrons to an anode electrode via catabolic reaction, and these microbes include the *Geobacter* species (*Geobacter sulfurreducens, Geobacter metallireducens*), Shewanella species (*Shewanella oneidensis MR-1, Shewanella putrefacians IR-1, Shewanella oneidensis DSP10*), *Pseudomonas* species (*Pseudomonas aeruginosa KRP1*), *Rhodopseudomonas palustris DX-1,* [46] *Saccharomyces cerevisiae* ,[47,48] and *Escherichia coli* [49] These microbes are often referred to as exoelectrogen or anode-respiring bacteria. [50]

In general, two main mechanisms (Figure 1.3) exist for extracellular electron transfer between microorganisms and electron acceptors such as an anode in an MFC. (i) The first mechanism is direct electron transfer (DET) in which EABs can transfer electrons via direct physical-electrical contact between the bacterial cell membrane and a solid electron acceptor. This type of electron transfer is due to the presence of redox-active proteins such as c-type cytochromes on the outer cell surface as well as metal-like pili that can extend as far as 3-5 nm and are as long as tens of micrometers. (ii) The second mechanism is mediated electron transfer (MET) in which electron transport occurs via soluble redox mediator molecules (e.g.,

methylene blue, phenazine and pyocyanin), which can shuttle electrons away from the bacteria. [51] These mechanisms are discussed in more detail below.

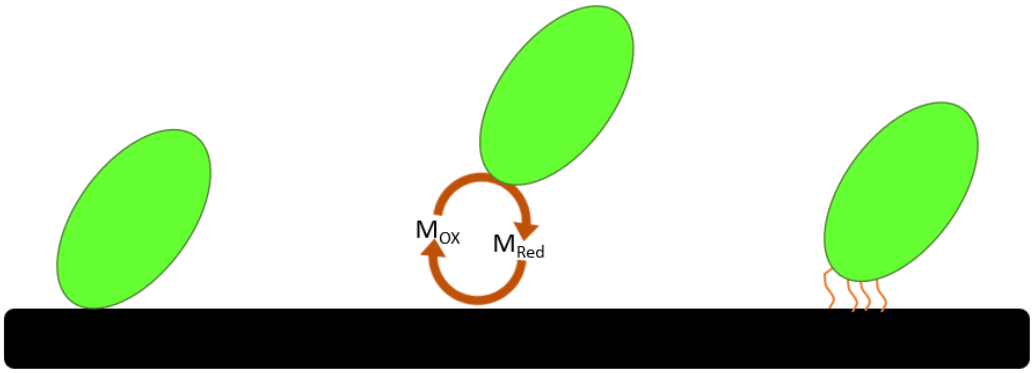

Figure 1.3. Schematic of extracellular electron transfer mechanisms from an electroactive biofilm to an electrode. (a) DET via outer membrane c-type cytochromes, (b) MET from anode or anode-associated organisms via redox shuttles , (c) long-range DET via conductive pili.

1.3.2. Direct electron transfer

Mediator-less MFCs do not require a mediator but use electrochemically active bacteria to directly transfer electrons to the electrode. Among the electrochemically active bacteria, Shewanella sp. or *G. sulfurreducens* strains are widely used [52] and have pili on their external membrane that are able to transfer electrons directly to the anode via to conductive protein groups such as cytochrome c. The presence of long pili enables DET in many bacteria even if they are not located directly on the anode surface. *G. sulfurreducens,* another Fe(III)-reducing bacterium,[53,54] is a widely researched microorganism for MFC applications [55] and was first introduced by D. R. Bond and D. R. Lovely. [26] These bacteria can naturally oxidize substrate molecules and are gram-negative organisms that undergo strictly anaerobic respiration with use of an electrode as an electron acceptor.

G. sulfurreducens also have a greater ability to transfer electrons to the electrode surface in the MFC. As shown in Figure 1.4, *G. sulfurreducens* species can use DET from microbial

biofilms to the electrodes via conductive pili. These pilis, also known as bacterial nanowires, are flexible structures made of protein (known as pillin) that help the bacteria to stick to surfaces or to distinguish different materials in its surroundings. Pili are structures contains aromatic amino acids and pi-pi orbitals overlapping at pili facilitate and it leads to metal like conductivity. In MFC, *G. sulfurreducens* act as the catalyst and acetate serves as the fuel, but the organic nanowires act as a connector to the electrode, thus eliminating the need for an electron mediator. This property of *G. sulfurreducens* has made it possible to design novel anaerobic MFCs and electrodes that can efficiently convert organic matter to electricity.

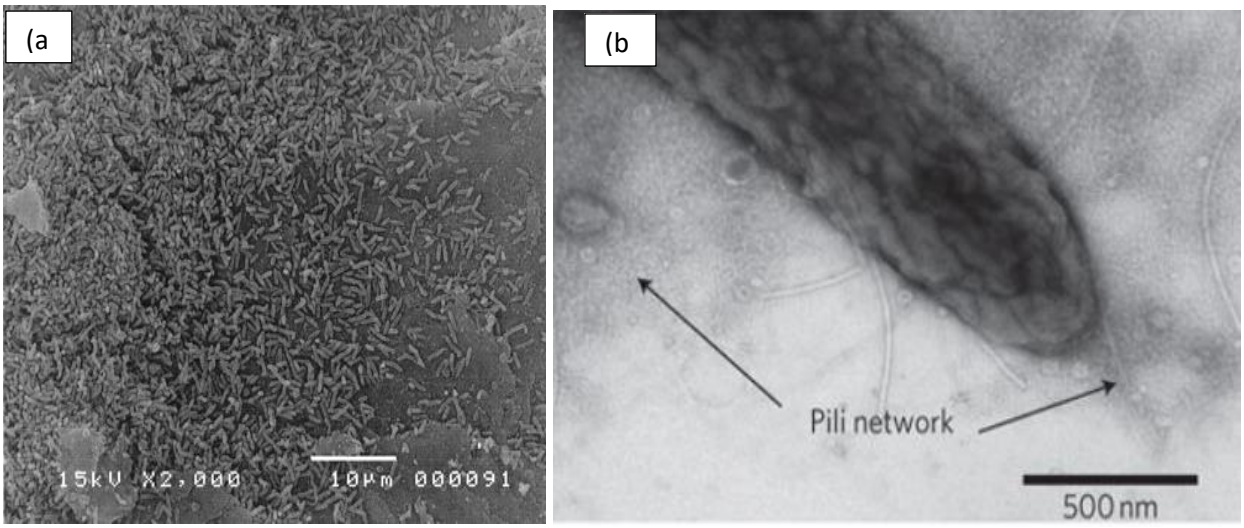

Figure 1.4. (a) SEM image of a graphite electrode surface following growth of *G. sulfurreducens* with acetate as an electron donor (2 mM). (b) Visible pilis. [56,26]

1.3.3. Mediated electron transfer

Certain bacteria are able to transfer electrons generated during oxidation via dissolved mediators such as thionines, phenazines, flavins, humic acid, etc. [57] These mediators are secreted from bacteria in low concentrations and transport electrons to the acceptors. *Pseudomonas* is a well-known bacterium that has been used in this type of MFC due to secretion of phenazine mediators under special nutrient conditions. Microorganisms that do not require a mediator to transfer electrons to an electrode are currently of interest to many researchers. In 1999, Kim et al. reported the first bacterial strain with electrochemical

activity, the Fe(III)-reducing bacterium *Shewanella putrefaciens*. To date, this bacterium has been widely used in mediator-less MFCs. However, the potential toxicity and instability of the artificial redox mediators of these mediator-containing MFCs create major impediments to practical application. In the late 1990s and early 2000s, the discovery of electrochemically active bacterial strains that can transfer electrons directly to electrodes[58,59] made it possible to construct mediator-less MFCs, which further enhanced the power output of MFCs.[26]

1.3.4. Mixed communities

In the MFC, the generated power is a direct function of microbial colonization, which must be studied. The presence of at least one electrogene bacteria is required for MFCs to generate electricity. However, a mixture of electrogene bacteria can also contribute to current production, and it is known that MFCs with mixed cultured communities have much higher performance in terms of power outputs, in most cases, compared with those that use pure cultures.[27, 60, 2] However, MFCs with single electrogene bacteria (pure culture) are useful for studying the electron transfer mechanism at the microbiological level. A subset of pure-culture and mixed-culture MFCs are listed in table 1.1 with their corresponding power outputs.

In a portion of the reported research, the development of a wastewater MFC containing mixed cultures was investigated to produce electricity generation.[29,61] In addition to various studies of wastewater MFCs, other organic wastes such as manure sludge waste, [62] heat-treated soil[63] and anaerobic activated sludge can also supply the mixed microbial consortium used in most MFC studies.

1.4. Typical fuel cell

1.4.1. Chemical Fuel cells

A fuel cell is a device that produces electrons (electricity), protons, heat and water by conversion of chemical energy (in an electrochemical process). Usually fuel cells are consists of two electrodes, known as the cathode and anode. Hydrogen is the main feed source in chemical fuel cells, but they also need oxygen (from the air), which enters to the fuel cell and oxidation and reduction reactions takes place at the anode and cathode electrodes. Because

no combustion of fuel occurs, the distinct advantage of fuel cells is generation of clean energy and elimination of the pollution caused by burning fossil fuels. Much of the hydrogen and oxygen in fuel cells is finally combined and converted into a harmless byproduct, i.e., water molecules. Therefore, the only byproduct is water.

Generally, in all fuel cells, hydrogen atoms reach the anode, where a chemical reaction separates them from their electrons and the hydrogens are ionized and have a positive charge. The negative electrodes in the anode section cause a current in the wires.

Several types of fuel cells are available, and each one operates slightly differently and has its own unique chemistry, the table 1.2 is shown some of important fuel cells mechanism briefly. Researchers have continued to improve fuel cell technologies by examining different catalysts and electrolytes with the goal of improving performance and reducing costs. New fuel cell technologies, such as MFCs (explained later), are also under development in the laboratory, and a number of these fuel cell types are commercially available today.

Table 1.2: Physicochemical comparison of different fuel cells types.

Fuel cell	**Electrolyte**	**Operating temperature**	**Reactions**
PEMFC	Polymer membrane	50-100 (Nafion)	Anode: $2H_2 \rightarrow 4H^+ + 4e^-$ Cathode: $O_2 + 4H^+ + 4e^- \rightarrow 2\ H_2O$ Overall: $2H_2 + O_2 \rightarrow 2\ H_2O$
DMFCs	Polymer membrane	90-120	Anode: $CH_3OH + H_2O \rightarrow CO_2 + 6H^+ + 6e^-$ Cathode: $3/2\ O_2 + 6\ H^+ + 6e^- \rightarrow 3\ H_2O$ Overall: $CH_3OH + 3/2\ O_2 \rightarrow CO2 + 2\ H_2O$
Solid Oxide Fuel Cells (SOFC)	Solid ceramic	500-1100	Anode: $2\ H_2 + 2\ O^{2-} \rightarrow 2\ H_2O + 4\ e^-$ Cathode: $O_2 + 4\ e^- \rightarrow 2\ O^{2-}$ Overall: $2\ H_2 + O_2 \rightarrow 2\ H_2O$
Phosphoric Acid Fuel Cel (PAFC)	Liquid phosphoric acid ceramic	150-200	Anode: $2\ H_2 \rightarrow 4\ H^+ + 4\ e^-$ Cathode: $O_2 + 4\ H^+ + 4\ e^- \rightarrow 2\ H_2O$ Overall: $2\ H_2 + O_2 \rightarrow 2\ H_2O$
Alkaline Fuel Cell (AFC)	Potassium hydroxide solution	< 80	Anode: $2\ H_2 + 4\ OH^- \rightarrow 4\ H_2O + 4\ e^-$ Cathode: $O_2 + 2\ H_2O + 4\ e^- \rightarrow 4\ OH^-$ Overall: $2\ H_2 + O_2 \rightarrow 2\ H_2O$

1.4.2. Proton Exchange Membrane (PEM) fuel cells

This type of fuel cell was first used by NASA in the 1960s. In PEM cells, solid polymers act as the electrolyte, and a porous carbon material containing a platinum acts as the electrode. PEM fuel cells can operate at low temperature with high efficiency. The only fuel in PEMs is hydrogen, together with oxygen from the air for operation, and the byproduct material is water. Because of the solid and flexible electrolytes used in this PEMFC, it does not leak or crack.

PEM operation occurs at a sufficiently low temperature and over short time period, making it suitable for application in homes and cars. However, the fuels must be purified before introduction, and a platinum catalyst is used as a cathode and anode, thus increasing costs.

Several types of fuel cells exist, and each one operates slightly differently and has unique chemistry. Here we talked about some of important fuel cells briefly in table 1.2. Researchers have continued to advance fuel cell technologies by examining different catalysts and electrolytes to improve performance and reduce costs. New fuel cell technologies, such as MFCs (that will be explained later), are also under development in the laboratory. A number of these fuel cell types are commercially available today.

1.5. Biological fuel cell and MFC concepts

The biological fuel cell operates in a manner similar to that of chemical fuel cells. In these systems, bacteria generate electrical power by oxidizing the organic matter present in wastewater.

As a biological fuel cell, an MFC is a bioelectrochemical device in which bacteria catalyze redox reactions and convert the energy stored within the substrates to usable electricity. The fundamental physical components of a typical dual-chamber MFCs include anode and cathode chambers separated by a cation exchange membrane, which is permeable to protons produced at the anode while separating other chemical species (primarily oxygen and other oxidants). The basic principles of a dual-chamber MFC system are illustrated in Figure 1.5. Two electrodes, i.e., the anode and cathode, are placed in the anode and cathode chambers, respectively. Bacterial degradation of organic matter at the anode chamber leads to the

generation of protons, electrons and CO_2. The protons produced in the anode chamber diffuse through the CEM to create a potential difference between the anode and cathode. This potential difference causes electrons produced by the bacteria to flow from the anode to the cathode through an electrical load, such as a resistor, at the external circuit. The anode-produced electrons and protons recombine in the cathode side, reducing oxygen (as a terminal electron acceptor) to form water and generating electricity. The entire process is shown in a conventional dual-chamber configuration MFC in Figure 1.5.

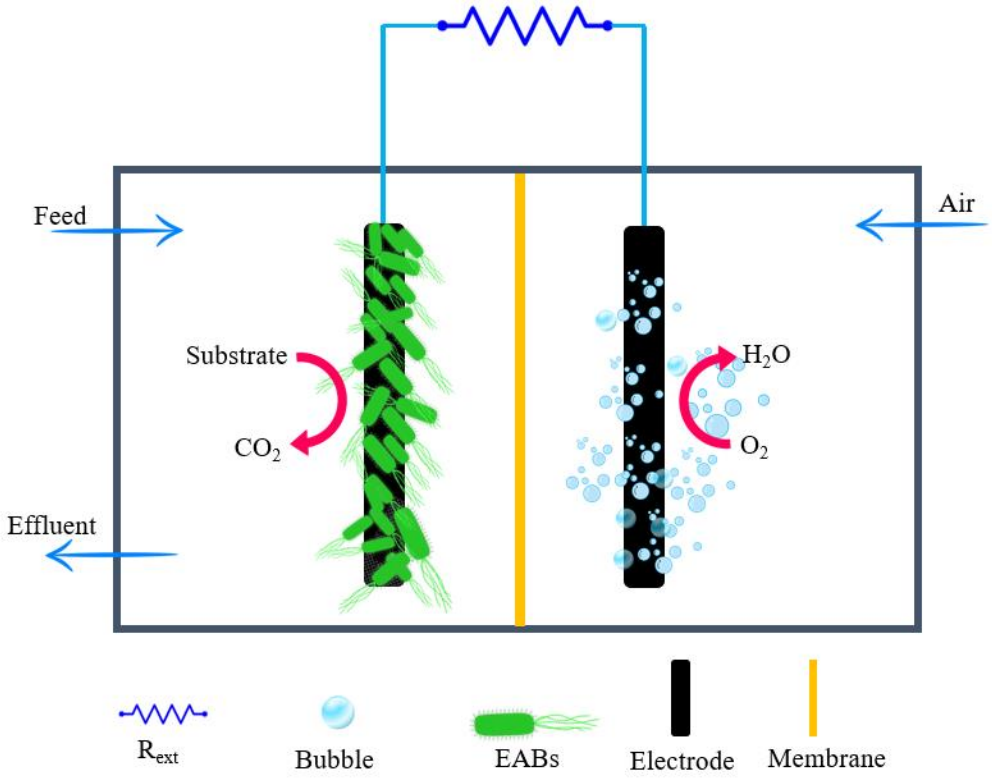

Figure 1.5: Schematic of a typical MFC. Microorganisms catalyze anodic reactions and release electrons and protons from organic matter (such as acetate and glucose) to generate energy. The electrons are transferred to an anode by passing through an external load.

Chemical reactions in fuel cells or MFCs can be analyzed by the half-cell reactions that occur at the anode and cathode sections. Table 1.3 shows the simplified stoichiometric reactions in the anode for a typical acetate-fed MFC via reduction of an acetate ion (CH_3COO^-) to bicarbonate (HCO_3^-), with ferricyanite (Fe^{3+}) as the terminal electron acceptor at the cathode. The equations in Table 1 show that eight electrons are generated for every acetate molecule

consumed. [64] After oxygen, the next most commonly used electron acceptor in MFC is hexacyanoferrate, $Fe(CN)_6^{3-}$, and its advantages include a standard potential of 0.361 V, high solubility in water, no requirement for modified electrodes or precious metals such as Pt, environmental friendliness, and rapid reduction kinetics. [65]

Table 1.3: Half-cell reactions of MFC using acetate as the substrate.

Anode/Cathode	Reactions	E_{anode} or $E_{cathode}^{**}$(V vs NHE*)
Acetate oxidation reaction:	$CH_3COO^- + 4H_2O \rightarrow 2HCO_3^- + 9H^+ + 8e^-$	-0.296
Glucose oxidation reaction:	$C_6H_{12}O_6 + H_2O \rightarrow C_6H_{12}O_7 + 2H^+ + 2e^-$	-0.43
Ferricyanide reduction reaction:	$Fe(CN)_6^{3-} + e^- \rightarrow Fe(CN)_6^{4-}$	0.361
Water reduction reaction:	$O_2 + 4H^+ + 4e^- \rightarrow 2H_2O$	0.805
Manganese dioxide reduction reaction:	$MnO_2 + 4H^+ + 2e^- \rightarrow Mn^{2+} + 2H_2O$	0.85

*NHE = Normal hydrogen electrode
**Negative and positive potentials occur at the anode and cathode, respectively.

To evaluate the reaction in terms of the overall cell electromotive force, E is defined as the potential difference in equation 1:

$$E = E^0 - RT \ln (\Pi)/nf \quad (1)$$

where n is the number of electrons transferred, E^0 is the standard cell potential and f is Faraday's constant (f = 96,485 C/mol) at standard conditions Π=1, which is the ratio of the activities of products to those of the reactant. By considering Equation (1) for oxidation of acetate at the anode surface, we have:

$$E_{anode} = E^0 - RT \ln ([CH_3COO^-]/ [HCO_3^-]^2 [H^+]^9)/nf \quad (2)$$

which gives E_{anode}= -0.296V [2]. For the cathode, we have:

$$E_{cathode} = E^0 - RT \ln ([Fe (CN)_6^{3-}]/[Fe(CN)_6^{2-}])/nf \quad (3)$$

where $E_{cathode}$ = 0.361V [2] from Table 1.3. The overall cell potential (E_{cell}) that can be produced with any fuel cell is the difference between these two anode and cathode values:

$$E_{cell} = E_{cathode} - E_{anode} \quad (4)$$

Therefore, the total E_{cell} = 0.657 V (for conditions of 298 K, 1 bar, pH = 7). This value represents the theoretical maximum cell potential with the acetate substrate. The positive value of total E_{cell} for acetate MFC means that the total cell reactions are thermodynamically favorable. However, the cathode potential with oxygen is much lower in practice than that with ferricyanide. In the oxygen reduction reaction to water, the reaction kinetics are the most important parameter because this reaction requires four electrons and hydrogen, which might not always be achieved, and most importantly, it needs a type of catalyst on the surface of the electrode.

1.6. Power generation characterization of MFCs

The first parameter measured at any electrical source is the voltage. The voltage in batteries and fuel cells is usually increased by linking them in series.

The cell voltage produced by the MFC is typically in the range of 0.3-0.8 V, and Ohm's law states its relation to load resistance (R_{ext}) and current (I):

$$E_{cell}=I\cdot R_{ext} \tag{5}$$

The open circuit voltage (OCV) is the maximum voltage produced by an MFC when the load resistance is infinite. The power generation of an MFC is calculated from voltage and current across a loading resistance. The current is calculated from the voltage across the load resistance, as shown in equation 6. The most useful parameter for MFC is the maximum power that an MFC can produce and can be predicted with equation 7. [66]

$$I=E_{cell}/R_{ext} \tag{6}$$

$$P=I\cdot E_{cell} \quad \text{or} \quad P=E_{cell}^2/R_{ext} \tag{7}$$

Because the surface areas used in the power calculations are not the same, power output is generally reported after normalization by the anode surface area:

$$P=I\cdot E_{cell}/A_{anode} \tag{8}$$

The polarization curve is used to represent the I-V characteristics of the MFC. By varying different sets of external resistances (R_{ext}), a new voltage can be obtained for each applied resistance and hence a new current. Therefore, the calculated voltage is plotted against the

current (as shown in Figure 1.6) to obtain a polarization curve. The polarization curve shows how well the MFC maintains a voltage as a function of current production. [67,42] There are three regions of a fuel cell polarization curve: activation losses, concentration losses and ohmic losses. Activation losses are caused by kinetics of the electrode reactions. Ohmic resistance losses are associated with the ionic resistance of the electrolyte and charge flow. Concentration losses are related to decrease in reactant at the surface of the electrodes.

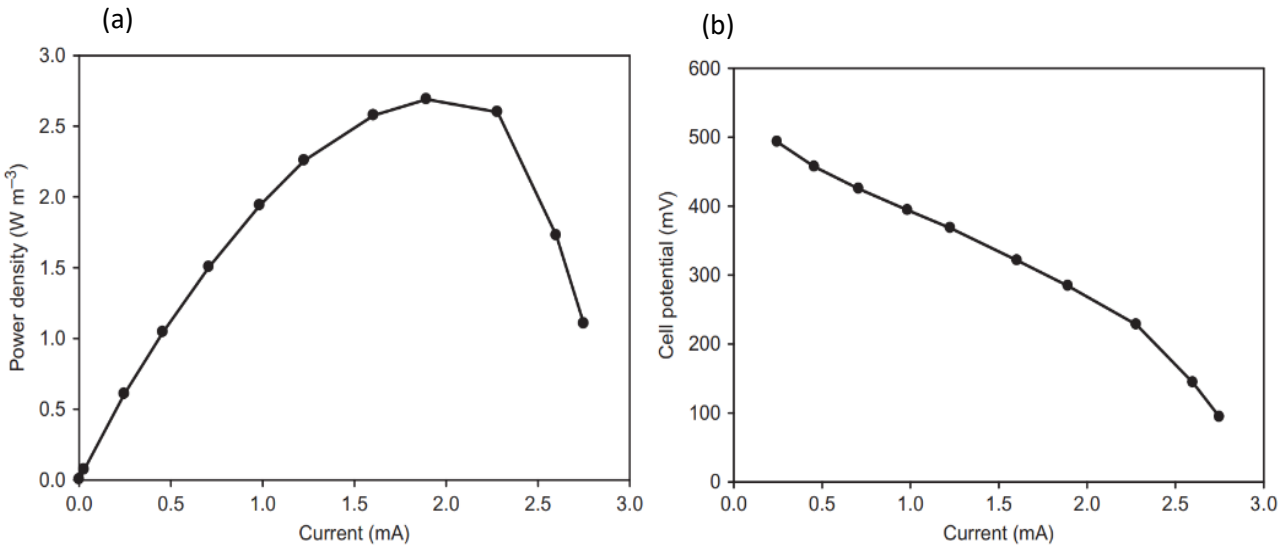

Figure 1.6: A power (a) and polarization (b) curves for an air-cathode MFC.[68]

1.7. Optimization of MFC configuration

Similar to other types of fuel cells, the MFC is composed of components such as an anode, cathode, separator and external circuits. Depending on the MFC application, different configurations have been developed, i.e., single chamber or double chamber. For both of these configurations, the basic principles remain the same.

1.7.1. Single-chamber MFC

When using oxygen as an oxidant in the cathode component of MFCs, it is not necessary to place the cathode in a separate chamber. In single-chamber MFCs (Figure 1.7), an air cathode is commonly used with the anode at the opposite side (the cathode electrode is exposed to air). Liu et al. built a single-chamber MFC with an air cathode for the first time.[61,69] In this

configuration of MFC, an ion exchange membrane is used to keep reducing oxygen diffusion into anodic area.

Generally, an ion exchange membrane is required in both dual-chamber and single-chamber MFCs to separate the anode and the cathode and to balance the charge.[29] (A cloth-electrode assembly is also used in this type of MFC instead of a membrane[70]). Single-chamber MFCs usually exhibit much better power performance than aqueous-cathode MFCs using dissolved oxygen because of the higher mass transfer rate and concentration of oxygen in air compared with bubbled oxygen in water.[71] Other oxidants, such as ferricyanide and permanganate [72] in dual-chamber MFCs, can greatly improve the MFC performance compared with the use of air.[73] However, the power generated from this type of MFC is not sustainable because the oxidants are consumed in the cathodic reaction and need to be replenished.[74,75]

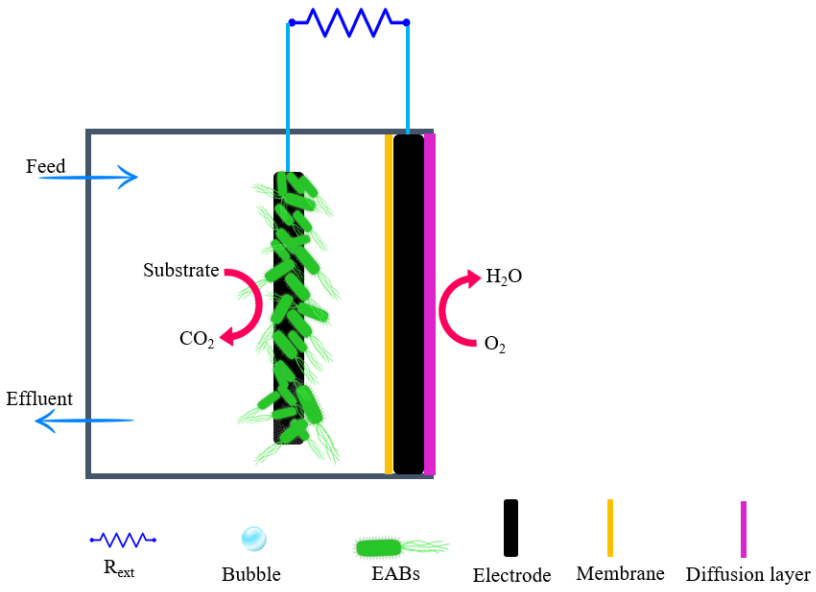

Figure 1.7: An air cathode single-chamber MFCs.

1.7.2. Salt bridge MFC

The reactor configuration of the MFC significantly affects its performance. The most widely used type of MFC in lab investigations is the "H"-type dual-chamber MFC (Figure 1.5). In this type of MFC, the bacteria in the anode chamber are separated from the cathode chamber

by a polymeric membrane. However, certain models of dual-chamber MFCs do not need to use an ion exchange membrane, and a salt bridge (Figure 1.8), which consists of a tube filled with agar and salt capped with porous caps, connects the two chambers. This model is an inexpensive way to replace a membrane and connect the two chambers of MFCs, but the power output of a salt-bridge MFC is quite low, as shown by the high internal resistance measured using electrochemical impedance spectroscopy (EIS). [76] Dual-chamber or "H"-shape MFCs are acceptable for fundamental laboratory research, such as development of new electrode materials and investigation of microbial cell behaviour.

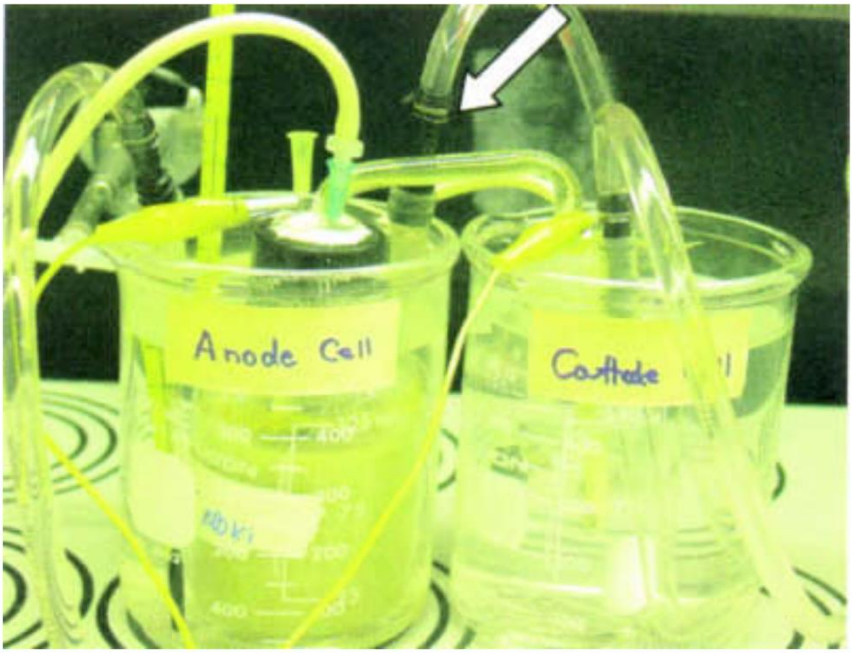

Figure 1.8. Variations on two-chamber reactors. A salt bridge-type MFC used by Min et al. (2005a) between the chambers (arrow), but the system had high internal resistance resulting in low power densities.[77]

1.7.3. Sediment MFC

In recent years, researchers have primarily focused on a form of MFC that can generate electricity for small remote sensors, requires low maintenance and can also perform wastewater treatment at low cost. The sediment MFC harvests energy from marine sediment. [78, 79, 80] This MFC can be easily fabricated and installed by inserting a graphite-plate anode in marine sediment connected at a depth of 5-10 cm to degrade organic matter for collection of

electrons and a graphite-plate cathode placed in overlying seawater. It is better for the cathode to be positioned immediately below the air-water interface, where reduction of the terminal electron acceptor (mostly O2) occurs by combining electrons and protons. The anode and cathode are connected across an external load.[81,82] Sediment permits the flow of protons from the anode to the cathode side and acts as a proton-permeable natural medium. An applicable SMFC is shown in Figure 1.9.

Figure 1.9. A real benthic microbial fuel cell. [83,84]

1.7.4. Stack designs

MFC voltages remain limited. One single MFC can produce low voltage, but by stacking several MFCs together in series, it is possible to increase the voltage. A practical application configuration of MFCs is the stacked MFC (Figure 1.10). Because voltage generation of an MFC is completely related to the surface area of electrodes, stacks of them are considered to

be the most appropriate configuration and are essential to increasing the voltages and currents produced by MFCs together with higher wastewater treatment efficiencies. [85,86]

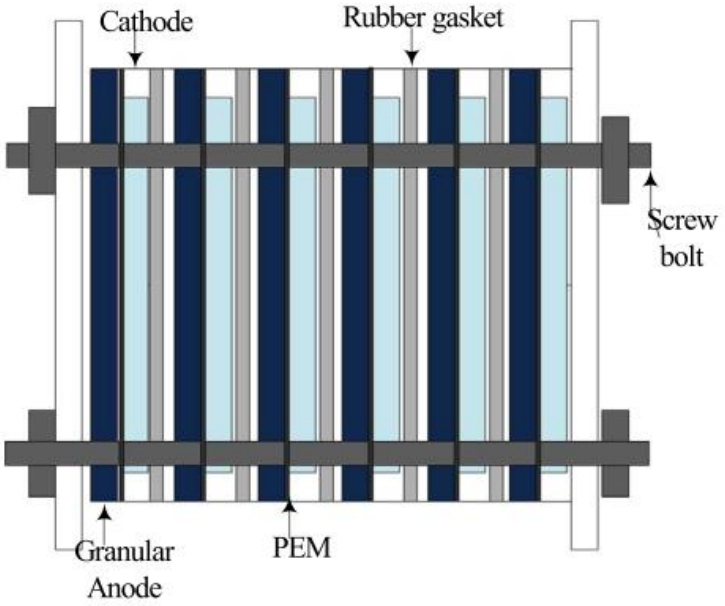

Figure 1.10. Stacked MFCs integrated by six separate MFC units. Connection in stacked MFCs can be classified into two groups: series or parallel. [87]

1.8. MFC components

The main three components of the MFC are the anode, cathode, and if present, the membrane. The MFC configuration, the nature of the separator or membrane, and the electrocatalysis of the anode and cathode are differing and important parameters that might affect the overall MFC performance, and all are discussed in the following sections.

1.8.1. Anode materials and developments

The main challenge in constructing an MFC is to identify materials and architectures that improve the maximum power output of system, but another challenge is reduction of cost and creation of useful architectures. One important component of the MFC is the anode, which allows the electroactive bacteria to form electroactive biofilm. Therefore, materials used in the anode component should have attributes such as high conductivity, non-

corrosivity, high specific surface area, high porosity, and good biocompatibility. These materials must supply a large surface area for adhesion, stability and electron transport across electrode and electroactive microbes. [88, 89] Figure 1.11 shows the usual conventional carbon-based material used in MFCs.

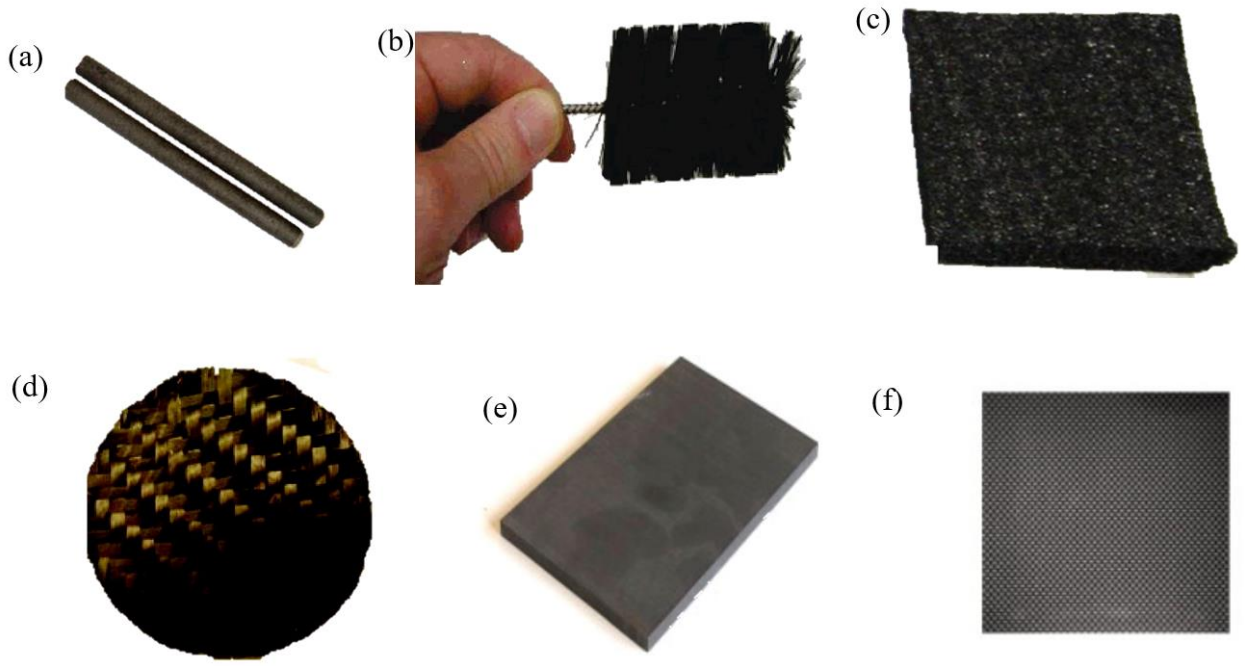

Figure 1.11. Photographs of some carbonaceous materials used for MFC anodes: graphite rod (a), [90] graphite brush (b), [21] carbon felt (c), [91] carbon mesh (d), [92] graphite plate (e) [93] and carbon cloth (f).[93]

Carbon-based materials are commonly selected for the MFCs anode and can fulfill almost all of the abovementioned requirements. Therefore, these materials are widely investigated as anodes in MFC technology. Certain carbon materials, including graphite rods, [61] graphite plates, [27] graphite foam, [94] woven graphite, graphite felt, [95] graphite granules, [26] reticulated vitreous carbon (RVC),[31] carbon paper,[29] carbon cloth,[96] and graphite fiber brushes,[21] have been frequently studied as anode electrodes for MFCs. Non-carbon-based materials or metal electrodes are more conductive than carbonaceous electrodes and have also been explored for MFC anodes. However, these materials are not widely applicable as carbonaceous electrodes because the smooth surfaces of metals do not facilitate the adhesion of bacteria

(relatively low surface area of metal electrodes). [93] These materials included various metals such as platinum,[97] gold,[98, 99] titanium, [95] stainless steel (SS), [100] and copper [101].

Solid carbon materials such as graphite plates or sheets are the most common materials for plain electrodes used in bulk MFCs because they are relatively inexpensive, easy to handle, and have a defined surface area.[61,89]

An early study by Logan et al. reported an air-cathode MFC (maximum generated power density of 26 $mW \cdot m^{-2}$), as shown in Figure 1.12(a), that used a graphite rod as the anode electrode, and up to 80% of the COD in the industrial wastewater used as fuel [61] was removed. In another study, Lovley [94] and co-workers investigated the effect of different electrode materials such as graphite rod, graphite felt, and graphite foam on the output power. Based on the results obtained, increasing the surface area of the electrodes might substantially increase the power production (Figure 1.12(b)). Further improvement was achieved using a graphite brush as the anode, which produced one of the highest specific surface areas of carbon materials for anodes (maximum power density of 2400 mW m^{-2}). [21]

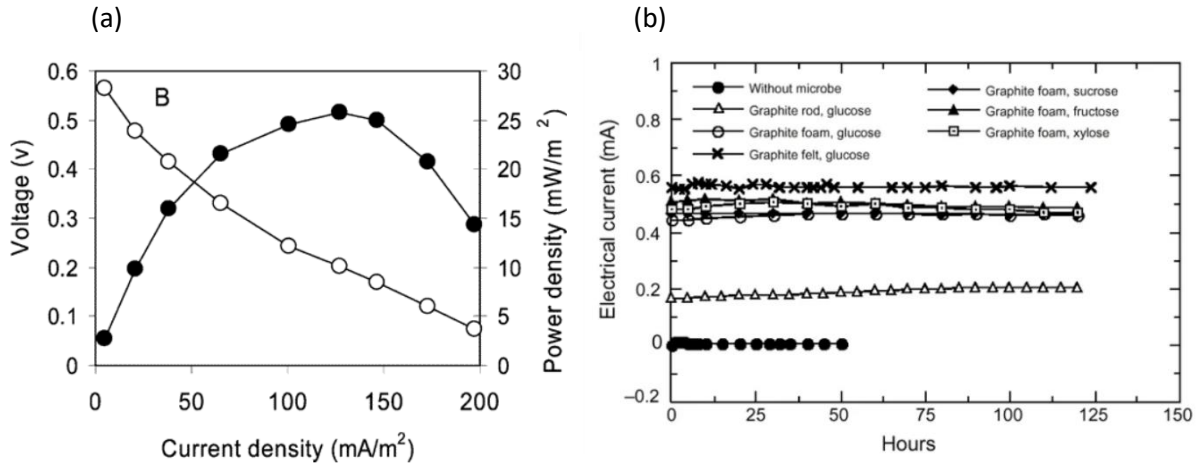

Figure 1.12. Power generation of a graphite rod as a function of circuit load (16-5000 Ω). b) Effect of different graphite electrode materials on electricity generation. Total accessible geometric surface area of the electrodes: graphite rod, 6.5×10^{-3} m^2; graphite foam, 6.1×10^{-3} m^2; graphite felt, 20.0×10^{-3} m^2.

Structured anodes are an important method for improving the power output of MFCs by changing the surface properties of the electrode. Modified anodes can be built using carbon

nanotubes (CNTs)[102, 103] or graphenes, [104] and their composites can facilitate extracellular electron transfer and enhance biofilm formation. As shown in Figure 1.13, CNTs coated with carbon textile create an open 3D space with a macroporous structure. This CNT-textile anode structure improves microorganism colonization and helps the substrate to deeply penetrate inside the entire electrode. As a result, the maximum current density and maximum power density are 157% and 68% higher, respectively.[105]

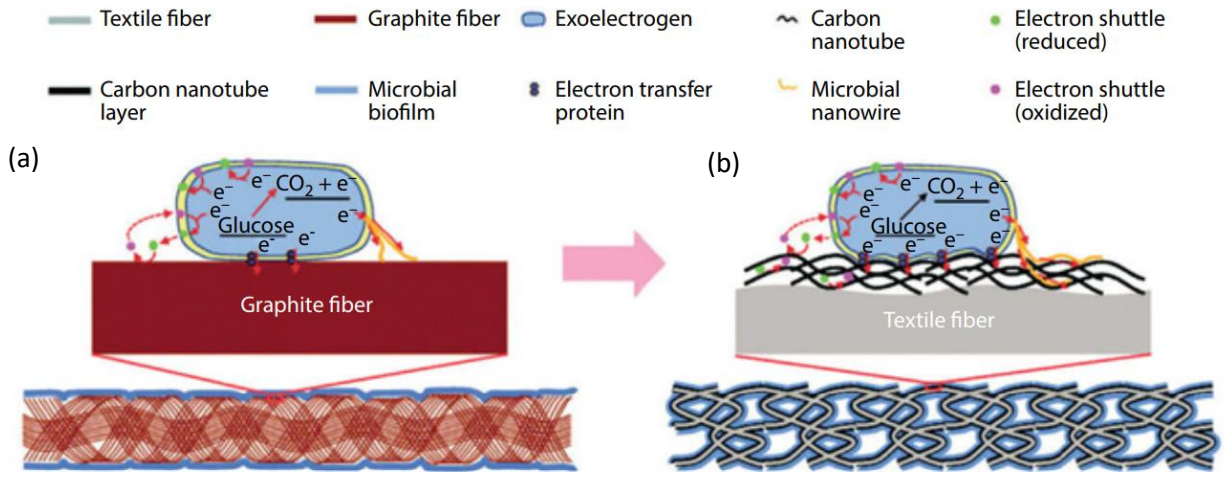

Figure 1.13: Illustration of carbon-cloth anode (a) compared with CNT-textile anode (b) and their electron-transfer mechanism. [105]

1.8.2. Cathode

On the cathode side, the same materials that were previously discussed as anode materials can also be used as cathode materials in MFCs. The electrons produced in the anode chamber are transferred to the cathode and consumed by the cathodic reactions to create a closed electrical circuit, and thus electrical energy can be harvested. [106] Related studies have used carbon paper,[107] carbon cloth,[108] graphite, carbon fiber brushes [109] and carbon felt [110] for this purpose.

1.8.2.1. Oxygen reduction reaction

At the cathode, oxygen, with its high reduction potential (1.229 V vs. NHE) and natural abundance, is the most widely used electron acceptor for practical MFC applications.

The ORR pathway in aqueous solutions is based on following equation in which one O_2 molecule requires four electrons ($4e^-$) and four protons to produce water:

$$O_2 + 4\,H^+ + 4e^- \rightarrow 2H_2O \; (E'^0 = 1.229\ V) \qquad (9)$$

Generally, the ORR has slow kinetics (which is the main limitation of the power output) at the electrode, and thus a catalyst is needed at the MFC cathode to enable a practical ORR. Platinum and Pt-based materials (highly active catalysts) are the most frequently applied catalysts for ORR due to their high surface area and low overpotential for ORR. [111] Oxygen reduction on the Pt surface occurs by a direct four-electron transfer process,[112] which is a complete and non-destructive process for ORR. However, the high cost of Pt creates certain problems for application of Pt in a cathode in practical MFCs. Therefore, it is necessary to coat Pt on a carbon-based material. Certain nanomaterials such as CNTs have been used to improve the performance of Pt cathodes. Ghasemi et al.[113] reduced the Pt loading by depositing it over CNTs, showing that the ORR catalytic activity was improved for the CNT-Pt composite. Furthermore, the ORR was not considerably affected by decreasing the Pt loading by 20-fold.[114]

1.8.2.2. Other cathodes and catholytes

Catalysts are not necessary when oxygen is not used as a final electron accepter, and carbon materials are sufficient as an electrode. Several different aqueous catholytes have been investigated as electron acceptors (oxidants) in MFCs. These catholytes include potassium ferricyanide ($Fe(CN)_6^{3-} + e^- \rightarrow Fe(CN)_6^{4-}$) and potassium permanganate ($MnO_4^- + 8H^+ + 5e \rightarrow Mn^{2+} + 4H_2O$), which were demonstrated to improve the MFC output compared with ORR.[73] Wei et al.[65] reported higher power and voltage output with use of $Fe(CN)_6^{3-}$ as a catholyte (426 mV, 181.48 $mW.m^{-3}$) rather than a dissolved oxygen catholyte (150 mV, 22.5 $mW.m^{-3}$). Although ferricyanide has low cost and is a good electron acceptor, it is not a sustainable material and must be chemically regenerated or replaced after consumption in the

cathodic reaction. [75] Aelterman et al. demonstrated that it is also possible to replace potassium ferricyanide with an iron ethylenediaminetetraacetic acid (Fe-EDTA) catholyte. [115]

1.8.2.3. Biocathode

The ORR of the cathode is one of the most critical challenges in MFC technology. For platinum, the higher cost, short-lived nature, non-environmentally friendly property and complexity with respect to loading ratio without loss of catalytic performance has forced several researchers to develop biocathodes in which microorganisms can also be used as catalysts in the cathode. The basic idea of a biocathode is similar to that of the anode in MFCs, with the difference that in the anode area, bacteria donate electrons to the electrode via mediators or nanowires, but in the biocathode, transfer of electrons is reversible, and bacteria can accept the electrons. [68,116,117,42] Recently, development of oxygen-reducing biocathodes has been explored because the microorganisms are a low-cost and potentially renewable catalyst for ORR. [118]

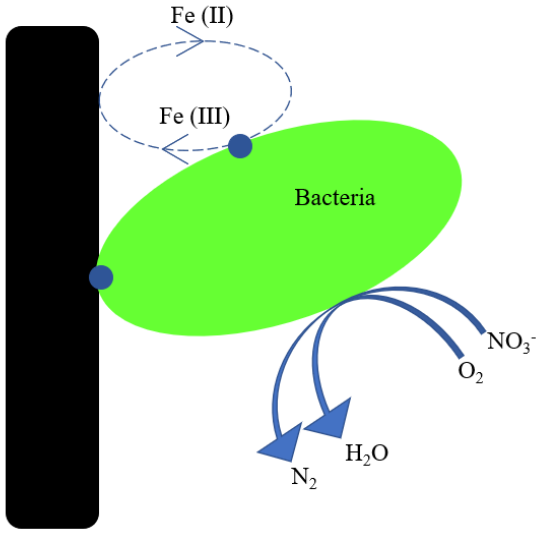

Figure 1.14. MFC biocathode in which oxygen and nitrate is reduced using direct electron transfer or using a mediator. Iron acts as a mediator to transfer electrons to oxygen. [90]

Generally, MFC biocathodes are categorized into two types, aerobic and anaerobic biocathodes: (i) In aerobic biocathodes, oxygen acts as a terminal electron acceptor, and

electrotrophic microorganisms carry out the oxidation of transition metals such as iron(II) and manganese (II) for electron delivery to the terminal electron acceptor, oxygen in this case.[119] (ii) In anaerobic biocathodes, where oxygen is not present, compounds such as manganese, sulfate, nitrate, iron and carbon dioxide are used as electron acceptors [120,121,116] (the cathodic potentials of these components are comparable to that of O_2).[90] Figure 1.14 summarizes a mediated biocathode in which nitrate and oxygen compounds are catalyzed by biofilm. In mediator-less biocathodes, bacteria capture electrons directly from the cathode electrode surface and catalyze the reduction of oxidants.

1.8.2.3. Metal recovery with biocathode

Biocathodes can also be useful in metal removal and recovery while also producing electricity in the MFC. For a biocathode MFC, the performance of Cr(VI) reduction was investigated by Xafenias et al. with the use of *Shewanella oneidensis MR-1* (MR-1) as a catalyst in the presence of lactate.[122] A maximum current density of 32.5 $mA.m^{-2}$ was produced after a 10 mg L-1 Cr(VI) addition in the cathode. Tandukar et al.[123] also reported a biocathode MFC for Cr(VI) reduction. The cathode chamber was inoculated with anaerobic mixed cultures enriched in the presence of Cr(VI). A maximum current and power density of 123.4 mA/m^2 and 55.5 mW/m^2, respectively, were achieved, with a maximum specific Cr(VI) reduction rate of 0.46 mg Cr(VI)/g VSS·h at an initial Cr(VI) concentration of 63 mg Cr(VI)/L.

1.8.3. Types of separators/membranes

The separator represents an important component within the MFC and is a key function that physically separates the anode and cathode (to avoid direct electrical contact, i.e., short circuit, between anodes and cathodes) and exchanges and passes ions (either H+ or OH−)[29,124] for charge balancing and reduction of oxygen diffusivity or other substances. Different types of membranes have been explored for application in MFCs, including the salt bridge, cation exchange membrane (CEM), anion exchange membrane (AEM),[125] bipolar membrane (BPM),[126] ultrafiltration (UF)[125] membrane and nanoporous polymer filters. The most commonly used membrane is CEM (such as Nafion 117) in which protons (H^+) are transported via the Grotthuss mechanism (proton jumping) in the fully hydrated condition.

In this mechanism, the proton can hop from one water molecule to another within the hydrogen bond network.

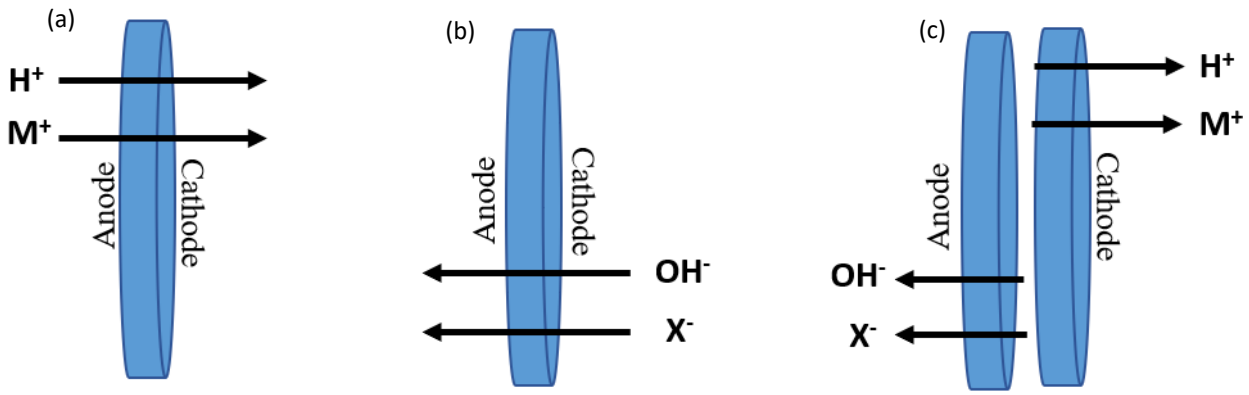

Figure 1.15: Schematic diagram of ion transport across: (a) the cation exchange membrane (CEM), (b) anion exchange membrane (AEM), and (c) bipolar membranes (BPM).

A bipolar membrane consists of a cation and anion membrane which sandwiched with a catalytic intermediate layer (junction layer) to accelerate the splitting of water into protons and hydroxide ions, which results in the transport of anions (OH^-) to the anode and cations (H') to the cathode to balance the total charge (Figure 1.15).[42]

It is also possible to eliminate this expensive and complicated membrane system, which can cause fouling problems. One example of a membrane-less system is the sediment MFC[127] or the membrane-less air cathode MFC system.[29,70]

1.9. Application of MFC

In the beginning, MFCs were considered as a wastewater treatment technology in the early 1990s,[128] but recently, this technology has revealed several energies, environmental, economic, and operational benefits.[129] MFCs have also been shown to be useful as an alternative source of energy. Of course, with further improvements in design, cost and performance, it might be possible to scale up MFCs to compete with other renewable energy technologies and apply them as an important applicable source of energy.[88] However, it is only within the last decade that MFCs have changed from μL to a few litres, which has improved their performance as a larger source of energy,[130] and these advantages have attracted much research attention focused on their improvements.

In addition to cleaning of wastewater and energy recovery, MFCs are expected to find more numerous applications in the future with increasing power generation.[129] The following list shows that MFCs have also been used in a variety of applications:

Wastewater treatment

Renewable energy

Electricity

Bioremediation[131]

Removal and recovery of heavy metals

Constructed wasteland management for powering underwater monitoring devices (sediment or marine MFC)

Water desalination with microbial desalination cells (MDCs)[132]

Biophotovoltaics with plant microbial fuel cells (PMFC)[133]

Biosensors

Biochemical production via microbial electrosynthesis using microbial electrosynthesis (MES)

Implantable medical devices (IMDs)[134]

BOD sensing[135]

Hydrogen production[136]

Organic removal in MFCs[22]

1.10. Microfluidics

Microfluidics, which originated in the 1980s, is described as the science and technology that deals with small volumes of fluids or gases (less than microlitres to nanolitres) for manipulation of fluid flow using micro-scale channels.[137] Microfluidics is one of the key sciences and technologies for miniaturization.[138] Many physical, biological and chemical (surface chemistry, chemical synthesis) studies have benefited from microfluidic technology because it supplies a basis for reliable, fast, in-situ detection and sensitive measurement with a considerably small number of reagents and portable and low-cost commercial devices. The

basic idea behind using microfluidics is implementation of an entire lab in a single micro-sized device that can deliver all requirements. These devices are also known as lab-on-a-chip devices. Microfluidic devices are defined as having at least one critical dimension that is between 10 and 100 µm. Due to the small size of the channels, the surface-area-to-volume ratio plays a highly important role in microfluidics.

The initial microfluidic devices were primarily prepared in silicon and glass, as introduced several years ago.[139] However, these materials are expensive and require high-cost fabrication methods. Recently, other types of materials such as polydimethyl dimethylsiloxane (PDMS), polycarbonate (PC) and polymethyl methacrylate (PMMA) have been successfully used in fabrication processes to generate microfluidic devices and are excellent alternatives to the silicon and glass used in early work. The advantages of these materials are faster design times, lower cost, and the ability to seamlessly integrate nanoscale features.

The following sections outline the principle of laminar flow in microchannels, materials for microfluid devices, and the associated microfabrication processes.

1.10.1. Principle of laminar flow in a microchannel

Most microfluidic devices are governed by laminar flow due to their critical and small dimensions. As the dimension of a channel becomes increasingly smaller, at this level, the physics or behavior of fluids under study change significantly as several phenomena take place. Therefore, some of the forces applied at the macro-scale might not be dominant in micro-scale devices, such as the appearance of capillary force in a small flow system. What follows is a short mathematical and semi-empirical description of changes in certain physical behaviors of fluids in a microfluidic system.

In an MFC with water-based solutions, the flow is incompressible. Generally, incompressible flows are governed by equation 10, which is known as the Navier-Stokes equation.

$$\frac{\partial u}{\partial t} + u \times \nabla u = -\frac{\nabla p}{\rho} + \mu \nabla^2 u \quad (10)$$

ρ is the density, u is the velocity, μ is the viscosity, p is the pressure, ∇ is the del operator and ∇^2 denotes the Laplacian operator.

The Navier-Stokes equation contains two important terms that determine the difference between microfluidic flows and large-scale flows. The term $u.\nabla u$ corresponds to the inertia of fluid, and the term $\mu\nabla^2 u$ represents the viscosity in fluids. The flow of a fluid through a microfluidic channel can also be characterized by the Reynolds number.

$$Re = \frac{VL}{\mu} \quad (11)$$

The Reynolds number in equation 2 gives an estimation of the ratio of inertial forces to viscous forces. In this equation, V is the mean velocity of the object relative to the fluid, L is the length that the fluid travels, and μ is the kinematic viscosity. At very low Reynolds numbers (in microfluidic systems), inertia is damped by the viscous effect, and the term corresponding to inertia can be neglected in the above Navier-Stokes equation, which leads to a linear equation that is easier to solve and results in a unique solution. [140,141]

By far, the most important parameter in a microfluidic channel is the Reynolds number Re. This number is given by the ratio of inertial forces over viscous forces, as described in the above equations. Reynolds numbers less than (<2000) qualify regimes of laminar flow, and Reynold numbers higher than (> 3000) indicate turbulent flow (as shown in Figure 1.16).

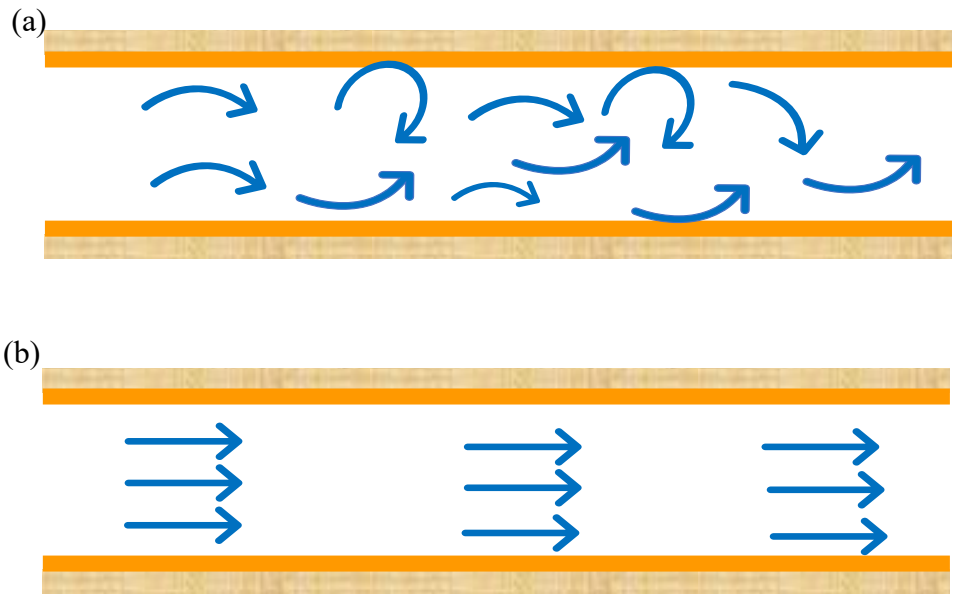

Figure 1.16 Representation of a turbulent flow with mixing across layers (a) and laminar flow with fluid flow in parallel layers (b).

1.10.2. Materials for microfluid devices

This technology offers the advantages of stable laminar flow, precise control of liquid flow rates and the ability to control chemical concentrations by modulating the flow rate ratios between the inlet channels. Thus, enhancement of the interaction between the material of the microchannel wall and the solution environment is required, and depending on the desired application, the microchannel design must meet all requirements. Therefore, the materials used in microfluidic chips should be selected precisely, e.g., a device that is optically transparent or very tough or non-diffusive to air is needed. In this section, we review a subset of the main materials and their properties for use in fabrication of microfluidic devices. [142]

1.10.2.1. Silicon microfluidic chip

Silicon is the second most abundant element in the crust of earth, after oxygen. The physical properties of silicon devices is similar to glass, and it was the first material used in microfabrication, although it was quickly replaced by glass and other polymer materials. [143] Silicon was selected because of excellent properties such as high resistivity to organic solvents, compatibility with metal deposition and high thermoresistivity. However, certain

drawbacks of silicon make it an unattractive material for microfluidic chips, namely, hardness, high cost, low transparency ….[144,145,146]

1.10.2.2. Glass microfluidic chip

After the initial use of silicon, glass was the second most popular material applied in fabrication of microfluidic devices. The most advantageous property of silicon is its excellent resistance to most chemical environments, high temperatures and pressures, insulating ability, impermeability to gas, transparency, and low fluorescence emission. Glass is also typically hydrophilic, and these properties make it suitable for use in biological or optical applications as a microfluidic device. However, glass is fragile, hard, and costly and time consuming for fabrication of microfluidic devices with custom geometries, and these factors limit its application compared with polymer/plastic materials. [144, 147]

Various methods, including wet/dry chemical etching,[148] plasma etching,[149] powder machining, [150] laser micromachining,[151] and ultrasonic drilling,[152] have been used to manufacture microstructure glass.

1.10.2.3. Polymer microfluidic chip

Polymers enable lower-cost and easier microfabrication methods (compared with those of silicon and glass) and are particularly used in commercial biological detection applications. Polymers have gained greater attention for microfluidic device microfabrication due to ease of replicability, flexibility, transparency (thus enabling optical measurements), low-toxicity, ease of access, biocompatibility and desirable thermal and electrical properties.[142] Polymers are the most commonly used material in fabrication (currently accounting for approximately 50% of sales in the world market). The two main types of polymeric materials are elastomers and thermoplastics, which are the most used materials in microfluidic systems. Elastomer polymers consist of cross-linked chains that react to external forces. When external forces are applied, an elastomeric polymer stretches or compresses and subsequently returns to its original shape.[142] One of the newest and most widely used elastomeric polymer materials in microfabrication is polydimethylsiloxane (PDMS), which is described below.

1.10.2.3.1. PDMS

PDMS is the most frequently used material in microfluidic applications (e.g., analytical chemistry, biology, biomedical devices and medicine), particularly in academic research or for developmental purposes. This material has been extensively used in microfluidic devices due to its low cost, biocompatibility, simple fabrication procedure, good optical transparency, ease of casting and curing, and mechanical flexibility. [153] PDMS consists of repeating Si-O with two CH3 in the polymeric chain and can change into its elastomeric form via a process known as cross-linking. The ratio of PDMS and its cross-linker is 10:1 by weight, but by varying this ratio, we can create different mechanical and chemical properties. PDMS is highly sensitive to changes in pressures and can be suitable for valves and pump fabrication and production of 3D multilayered devices.[143,154] Drawbacks of PDMS include gas permeability and a hydrophobic nature, which can limit certain applications. For example, a hydrophobic analyte can be absorbed by PDMS due to hydrophobic-hydrophobic interactions. However, plasma exposure can aid in hydrophilizing the exposed PDMS surfaces. In future, use of PDMS is expected to continue as one of the popular materials for microfluidic devices in both academic and industrial use. The fabrication process widely applied with PDMS as a microdevice material is soft lithography.[155]

Others type of materials have also been used in microfluidic devices and are categorized as shown: Inorganic materials (like Silicon, Glass, Ceramic), Metals (like Stainless, Copper), Polymers Elastomers (like PDMS, Thermoset polyester (TPE)), Thermoplastic polymers (like Polystyrene (PS), Polycarbonate (PC), Polyethylene terephthalate (PET), Poly-methyl methacrylate (PMMA), Poly-ethylene glycol diacrylate (PEGDA), Teflon:Perfluorinated compounds (PFEP/ PFA/PFPE), Polyurethane (PU), Polyimide (PI), Paper microfluidic chip, Hydrogels, Composite materials (Cyclic-olefin copolymer (COC)), Paper/polymer hybrid).

1.10.3. Microfabrication techniques

Many microfabrication techniques have been developed (in any application) that depend on the type of the microfluidic device substrate, cost, speed, feature size, and profile, and these techniques are characterized into two types: replication and photolithography. In the replication method, a master mold is made by either photolithographic or machining techniques and is used to replicate the pattern onto another softer material through direct

physical contact. However, in photolithographic microfabrication, light is used to define patterns on a photosensitive material. The following sections briefly describe template-based method microfabrication technology. We use this method in our project because the moulding approaches are rapid and accurate (for PDMS as microfluidic material). The fabrication of microfluidic templates for either PDMS casting or embossing of thermoplastics [156] is based on photolithography, as discussed in the following section.

1.10.3.1. Photolithography

Photolithography (the most widely used form of lithography) is a technique used to rapidly and easily fabricate a wide range of elastomeric devices such as PDMS. This technique uses light to pattern the substrates [157] and generally involves a set of basic processing steps: design of the pattern and construction of the masks, photoresist deposition, exposure of the photoresist to UV light, development of the exposed surface, and final casting over the features, as illustrated in Figure 1.17.

In step (1), the desired microchannel structure is designed using CAD software and printed as a photomask. Two types of positive and negative photoresists are used. In positive photoresists, the area exposed to the light is soluble and is removed by a developer solution, but in negative photoresists (typically SU-8), the area exposed to the UV light remains on top of the substrate, and the unexposed portions are removed by immersion in the SU-8 developer liquid. Figure 1.17(a) and (b) shows different patterns generated from the use of positive and negative photoresists. In step (2), the remaining portion is used as a mold (microchannel geometry is defined on the mold fabricated from photoresists). In step (3), a mixture of PDMS and its cross-linker at an appropriate volumetric ratio is cast onto the mold. Cross-linking and polymerization are achieved through proper heating (65-90°C for 2-4 h), after which the formed PDMS elastomer is peeled from the mold to obtain the desired microstructure (in step 4). The process of cross-linking and polymerization is accelerated by heat treatment.[158]

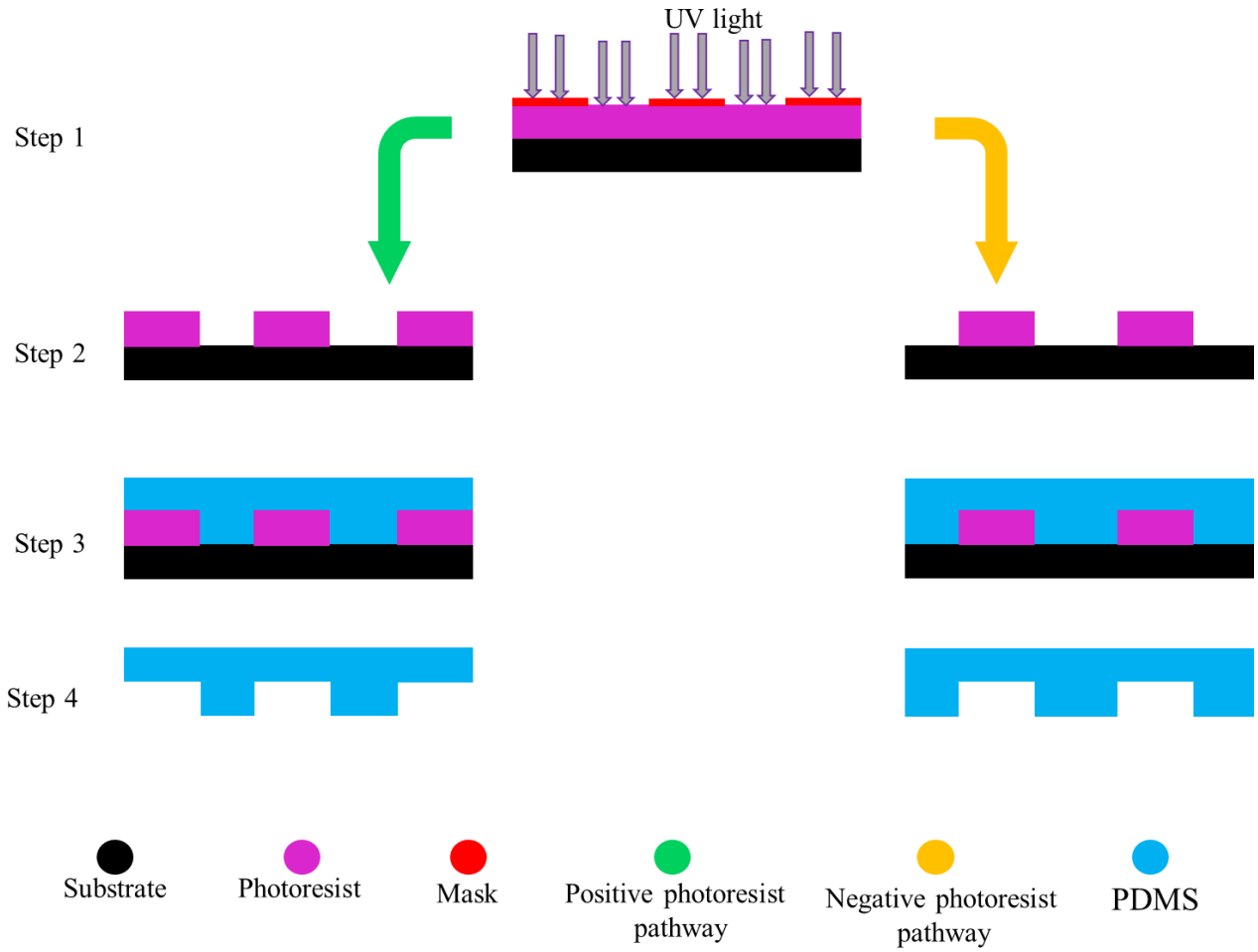

Figure. 1.17. Schematic of photolithography fabrication process: A schematic of positive and negative photoresist patterning. In positive photoresists, the area exposed to the light is removed, but in negative photoresists (b), the unexposed portions are removed by the developer liquid.

1.10.3.2. Hot embossing

Hot embossing is a method that uses high pressure and elevated temperature to transfer the mold features into the polymer. This approach addresses a wide range of applications, including microfluidics (micromixers, microreactors), due to low cost, flexibility in the fabrication method, and very clean and precise features. As shown in Figure 1.18, in this method, a polymer is heated to just higher than its glass transition temperature (Tg), and the microstructures with features are transferred from the mold to the polymer by stamping the mold into the polymer (pressing the film with high force.). This method is limited to

thermoplastic polymers, including polycarbonate,[159] polyimide,[160] cyclic olefin copolymer (COC),[161] and PMMA,[162] and is similar to the moulding injection method in that complete melting is not required in this method, which reduces consumption of energy and thermal residuals.[163,164,165] The quality of the surfaces, temperature uniformity, and chemical compatibility of the master molds are parameters that can aid in improving the success of hot embossing. An accuracy of a few (tens of) nanometers has been achieved using this method.[166,158]

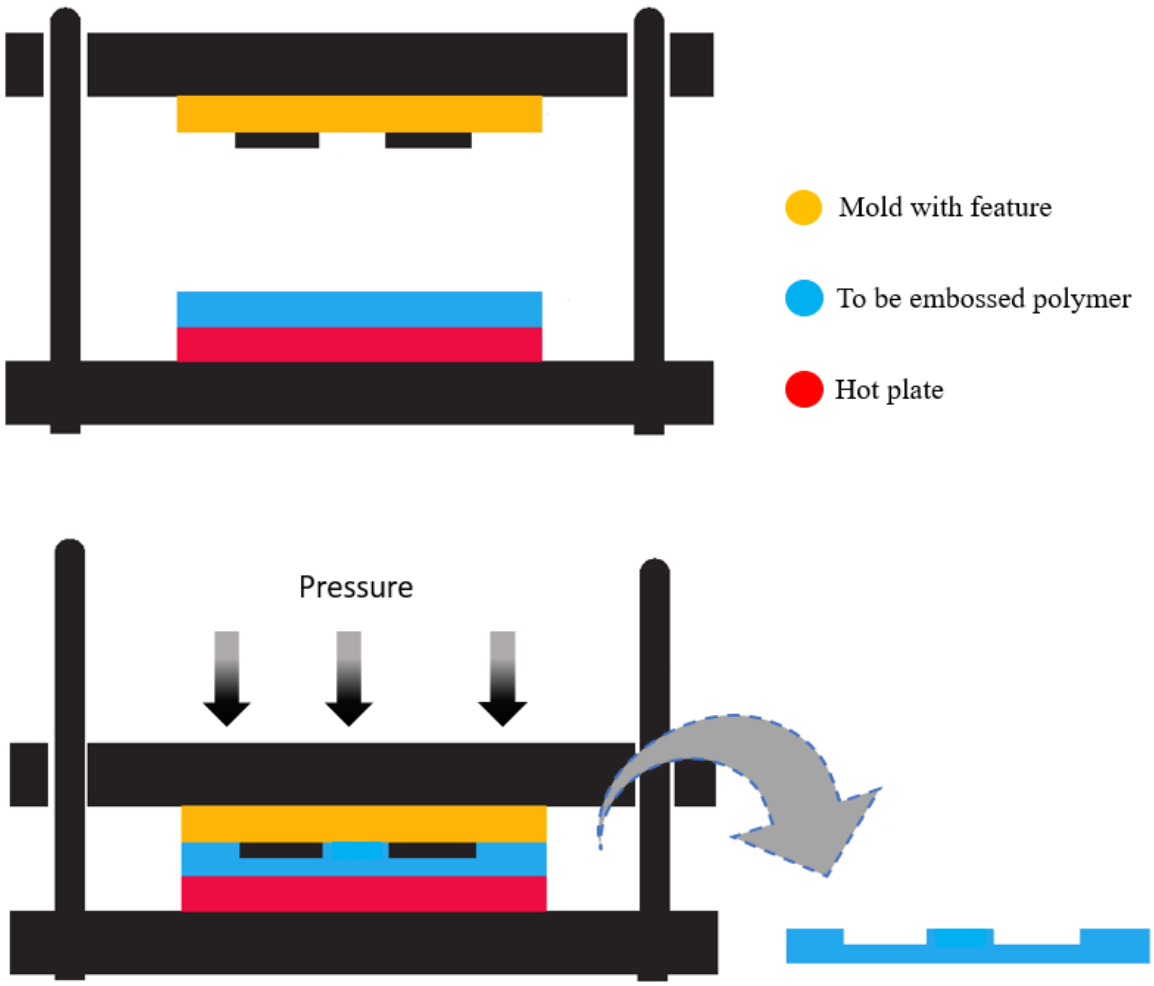

Figure 1.18: Process flow for the hot embossing fabrication method of polymers.

1.11. Microfluidics and MFC

A demand currently exists in the portable electronics industry for compact energy devices that allow consumers to run power applications remotely for long periods of time. Batteries cannot meet this demand due to their poor energy densities per mass and volume. As discussed in previous sections, MFCs can offer alternative and environmentally friendly energy sources.[167, 168] Although MFCs with micro-scale (microfluidic MFC) size can supply sufficient energy to power miniature electronic components, such as implantable pacemakers[169] and wireless networks[170] and biosensors[171] that enable rapid screening of microorganisms[172] and monitoring of toxicity and environmental factors,[173] to increase the power output, microfluidic MFCs can also be stacked and used in larger power applications.[174]

Use of a microfluidic system in MFC technology can aid in revealing a better understanding of the fundamentals of microorganisms and also offers real-time recognition, high throughput capacity, a unique/large surface area-to-volume ratio, rapid response time and the ability to control nutrient delivery.

Recently, selected fabrication methods have been successfully applied for micro-MFCs in which the microchannels (or MFC chambers) were assembled based on photolithography[175] (due to precise and inexpensive processes). Moreover, the materials used in this method are often inert and suitable for biological application in MFC research. Fabrication of micro-sized MFCs was mostly designed in the form of two-chamber MFCs, which are generally scaled-down macro-size MFCs with conventional two-chamber constructions and proton exchange via a membrane. Other common methods (after photolithography) for fabrication of microfluidic MFCs are etching, polymer molding, and metal deposition. [176] [177]

Qian and Morse[178] proposed a 1.5 µL micro-MFC constructed by stacking a silicon wafer with gold and a SU-8 microfluidic anode chamber with a membrane and a PDMS cathode chamber. The dual-chamber micro-MFC device was sandwiched between two acrylic plates, as shown in Figure 1.19(a). A maximum current and power density of 1300 A/m^3 and 15 W/m^3 were achieved by *Shewanella oneidensis* strain MR-1 as the microorganism on a gold anode electrode.

Choi et al.[179] proposed a micro-electro-mechanical system (MEMS)-based MFC with a cation exchange membrane (CEM) sandwiched between two glass slides as a microdevice. Two 4.5-µL chambers were defined for the cathode and anode side with a 20-µm-thick PDMS film acting as a spacer, as shown in Figure 1.19(b). This MEMS MFC used gold as an electrode material and generated a maximum current and power density of (33 $\mu A.cm^{-2}$) and (4.7 $\mu W.cm^{-2}$), respectively.

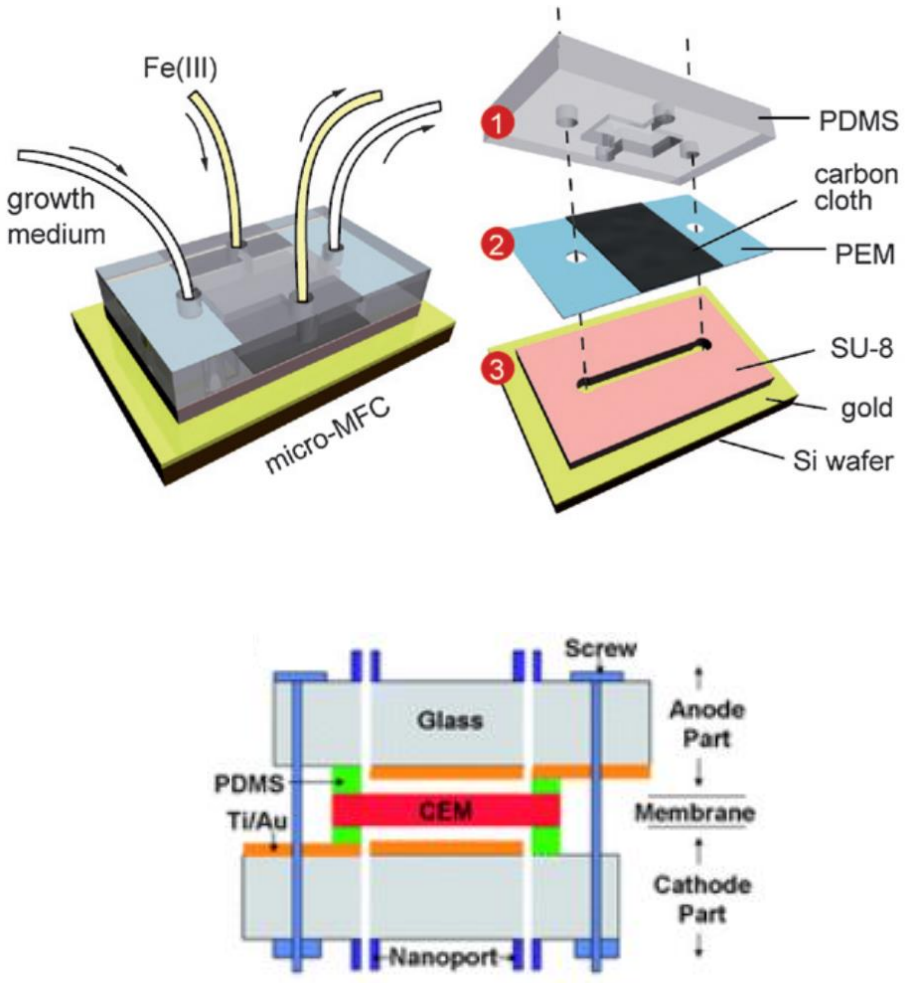

Figure 1.19: Schematic presentation of a two-chamber microfluidic MFC design and the key components.[178, 179]

1.11.2. Membraneless MFCs

One alternative to dual-chamber micro-MFCs is co-laminar microfluidic MFCs in which the reactants are stored externally and delivered to a local reaction zone, away from the reaction zone. In addition, diffusion-only mass transfer in the microchannel enables co-flow of the fluid streams in a side-by-side manner, without significant mixing. A conceptual view of co-laminar flow MFCs is illustrated in Figure 1.20 together with its basic working principle.

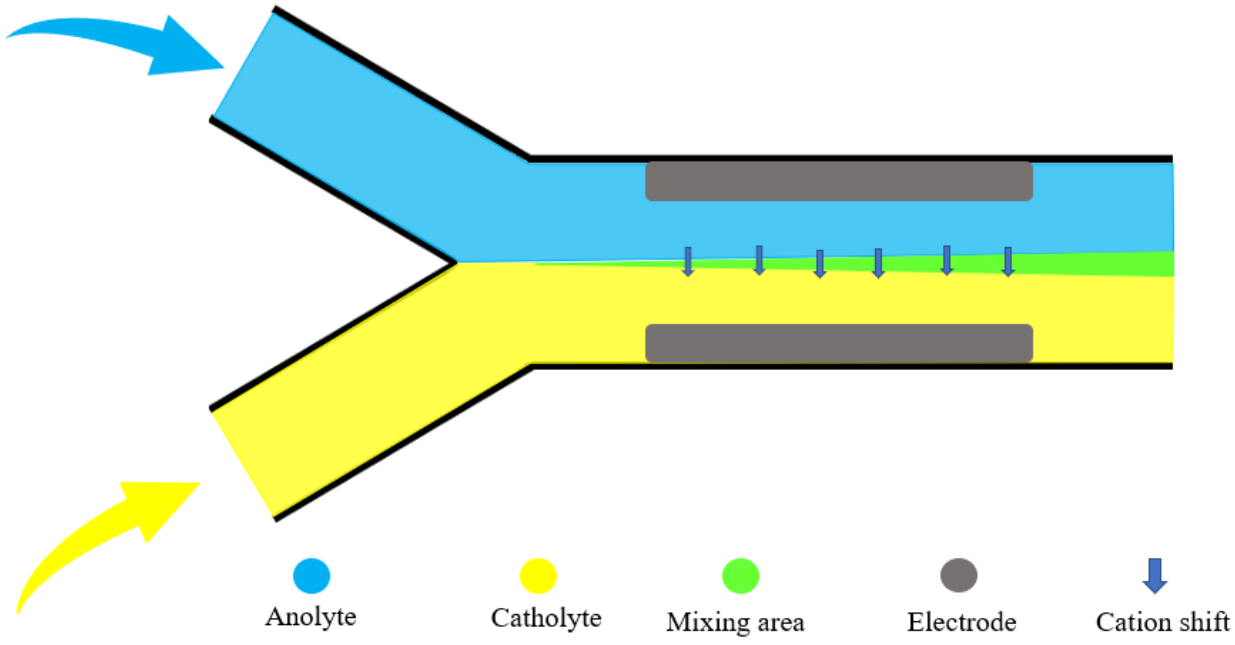

Figure 1.20: A sample schematic point of view of a typical microfluidic membrane-less MFC.

Traditional micro-MFCs (two chamber) must use a PEM or CEM as a separator. One of the most interesting opportunities offered by a microfluidic MFC is elimination of the PEM between the anode and cathode chambers.[180] In a membraneless MFC, when two streams are flowing in parallel in the laminar regime, the streams remain separated, thus eliminating the need for a membrane.[181] This elimination not only reduces the cost and complexity of an MFC but also increases the power output (due to a decrease in internal resistance).[71] The membraneless MFC has a higher proton transfer rate and higher power (264-494 W/m^2), as reported previously. [29,182]

Generally, bacteria are more easily aggregated on the electrode surface under the continuous flow condition compared with batch mode MFCs. Therefore, in the cases of membrane and membraneless designs, microfluidic MFCs are expected to require a short inoculation process.[183]

The first (as claimed by the authors) practical microfluidic MFC based on laminar flow separation of the anolyte and catholyte was proposed in 2013.[184] This laminar flow membraneless microfluidic MFC (Figure 1.21) consisted of a 0.3 μL chamber capacity fabricated by PDMS (via the lithography technique) with two inlets and one outlet plus two gold microelectrodes for anode and cathode components. In this study, maximum current densities of 18.40 mA m^{-2} and 25.42 mA m^{-2} was produced by two types of microorganism, *G. sulfurreducens and Shewanella oneidensis*.

Another membraneless microfluidic MFC was proposed by Wang and Su (2013).[185] The device was fabricated using PDMS with sputtered gold electrodes for both the anode and cathode areas. Those researchers used laminar flow to separate the anode and cathode, for which a maximum open circuit voltage of 246 mV was achieved for active microflora.

Li et al. recently proposed a Y-shaped microfluidic membrane-less fuel cell system in which the anolyte and catholyte flowed in a side-by-side manner through a microfluidic channel. The laminar flow in the microchannel was visualized at varied flow rates, and the distribution of the biofilm along the flow direction of the microchannel was monitored due to the compatibility of microfluidic channels with microscopy. The authors observed a significant increase in the electric current during growth of the biofilm by manipulating the fuel concentrations at different flow rates. A reduction in the internal resistance of the MFC and the ability to manipulate the flow rates enabled higher electric current. [184]

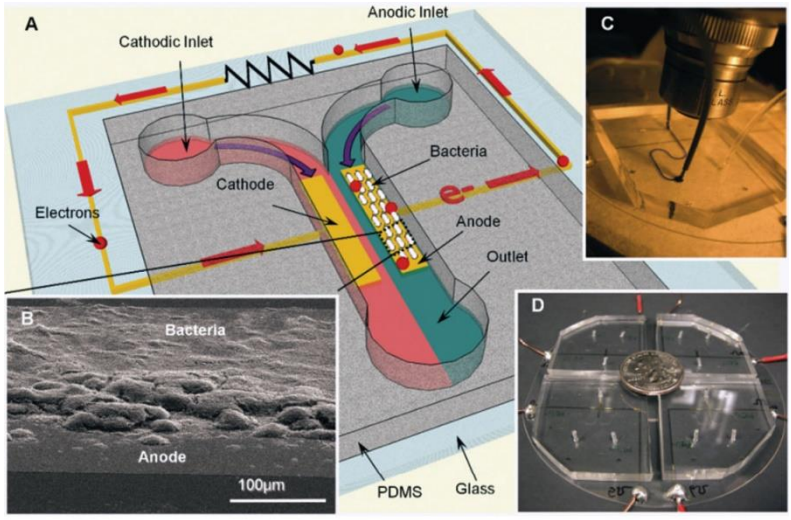

Figure 1.21: (a) Illustration of a microfluidic MFC without membrane. (b) SEM from the surface of the anode. (c) Injection of a dye into the microchannel to confirm the ability to create laminar flow conditions. (d) Multiple devices in one unit.[184]

Only a very small number of research groups have been working on microfluidic MFCs, but interest has increased in recent years. Table 1.4 summarizes certain reported characteristics and performances of microfluidic MFCs. As shown in this table, it is difficult to determine the critical design parameters and materials specifications for microscale MFCs and to establish a general platform for microfabrication of microscale MFCs due to the variable chemical/physical factors among these studies.

Table 1.4: Overview of the performances of microscale MFCs (both co-laminar MFC and conventional two-chamber micro-MFCs).

MF-MFC	µMFC material	Anode material	Cathode material	Bacteria	P_{max} (mW/m2)	Membrane	Ref
Membrane-less	PMMA	Graphite	graphite	Mixed culture	2500	-	[186]
Membrane-less	PDMS	Au	Au	Geobacter/ Shewanella	-	-	[184]
Membrane-less	PMMA	Au	Au	*Geobacter*	-	-	[187]
Membrane-less	PMMA	Graphite	Graphite	Mixed bacteria	1810	-	[188]
Membrane-less	PMMA	Graphite	Graphite	Mixed bacteria	618	-	[189]
Membrane-less	PDMS	Au	Au	*Geobacter-enriched culture*	348 (718)	-	[190]
Membrane-less	PMMA	CP	CP	*Pseudomonas*	-	-	[191]
Dual chamber	Glass/ PDMS	Au	Au	*Geobacter*-enriched mixed culture	950	Nafion 117	[174]
Dual chamber	Polymer	Au	Au	*Geobacter*	120	Nafion 117	[192]
Dual chamber	PDMS	Si coated with CNT	Au	*Geobacter*	36	Nafion 117	[193]
Dual chamber	Glass slides	Au	Au	*Geobacter*-enriched mixed culture	840	Nafion 117	[194]
Dual chamber	Glass slides	Au	Au	*Geobacter*-enriched mixed culture	330		[195]
Dual chamber	PDMS	Au	Au	*Geobacter*-enriched mixed culture	47	Nafion 117	179
Dual chamber	PDMS	Au	Pt/C cloth	*Shewanella*	1.15	Nafion 117	[196]

1.12. Bibliography

[1] Summers, Z. M.; Fogarty, H. E.; Leang, C.; Franks, A. E.; Malvankar, N. S.; Lovley, D. R., Direct exchange of electrons within aggregates of an evolved syntrophic coculture of anaerobic bacteria. *Science* **2010,** *330* (6009), 1413-1415.

[2] Logan, B. E., Exoelectrogenic bacteria that power microbial fuel cells. *Nature Reviews Microbiology* **2009,** *7* (5), 375.

[3] Liu, Y.; Kim, H.; Franklin, R.; Bond, D. R., Gold line array electrodes increase substrate affinity and current density of electricity-producing G. sulfurreducens biofilms. *Energy & Environmental Science* **2010,** *3* (11), 1782-1788.

[4] Zhou, M.; Chi, M.; Luo, J.; He, H.; Jin, T., An overview of electrode materials in microbial fuel cells. *Journal of Power Sources* **2011,** *196* (10), 4427-4435.

[5] Sonawane, J. M.; Yadav, A.; Ghosh, P. C.; Adeloju, S. B., Recent advances in the development and utilization of modern anode materials for high performance microbial fuel cells. *Biosensors and bioelectronics* **2017,** *90*, 558-576.

[6] Brun, N.; Flexer, V., *Functional Electrodes for Enzymatic and Microbial Electrochemical Systems*. World Scientific Publishing UK Limited: 2017.

[7] Ieropoulos, I.; Winfield, J.; Greenman, J., Effects of flow-rate, inoculum and time on the internal resistance of microbial fuel cells. *Bioresource technology* **2010,** *101* (10), 3520-3525.

[8] Ahn, Y.; Logan, B. E., A multi-electrode continuous flow microbial fuel cell with separator electrode assembly design. *Applied microbiology and biotechnology* **2012,** *93* (5), 2241-2248.

[9] Tartakovsky, B.; Manuel, M.-F.; Neburchilov, V.; Wang, H.; Guiot, S., Biocatalyzed hydrogen production in a continuous flow microbial fuel cell with a gas phase cathode. *Journal of Power Sources* **2008,** *182* (1), 291-297.

[10] Logan, B. E., *Environmental transport processes*. John Wiley & Sons: 2012.

[11] Outlook, A. E., Early Release Overview. *US Energy Information Administration* **2014**.

[12] Lewis, N. S.; Nocera, D. G., Powering the planet: Chemical challenges in solar energy utilization. *Proceedings of the National Academy of Sciences* **2006,** *103* (43), 15729-15735.

[13] https://www.nrcan.gc.ca/renewable-energy-facts/20069

[14] Demirbas, A., Potential applications of renewable energy sources, biomass combustion problems in boiler power systems and combustion related environmental issues. *Progress in energy and combustion science* **2005,** *31* (2), 171-192.

[15] Pant, D.; Singh, A.; Van Bogaert, G.; Olsen, S. I.; Nigam, P. S.; Diels, L.; Vanbroekhoven, K., Bioelectrochemical systems (BES) for sustainable energy production and product recovery from organic wastes and industrial wastewaters. *Rsc Advances* **2012**, 2 (4), 1248-1263.

[16] Piccolino, M., Luigi Galvani and animal electricity: two centuries after the foundation of electrophysiology. *Trends in neurosciences* **1997,** *20* (10), 443-448.

[17] Bennetto, H. P.; Stirling, J. L.; Tanaka, K.; Vega, C. A., Anodic reactions in microbial fuel cells. *Biotechnology and bioengineering* **1983,** *25* (2), 559-568.

[18] Tanaka, K.; Vega, C. A.; Tamamushi, R., Thionine and ferric chelate compounds as coupled mediators in microbial fuel cells. *Journal of electroanalytical chemistry and interfacial electrochemistry* **1983,** *156*, 289-297.

[19] Vega, C. A.; Fernández, I., Mediating effect of ferric chelate compounds in microbial fuel cells with Lactobacillus plantarum, Streptococcus lactis, and Erwinia dissolvens. *Bioelectrochemistry and Bioenergetics* **1987,** *17* (2), 217-222.

[20] Shukla, A.; Suresh, P.; Berchmans, S.; Rajendran, A., Biological fuel cells and their applications. *Curr. Sci* **2004,** *87* (4), 455-468.

[21] Logan, B.; Cheng, S.; Watson, V.; Estadt, G., Graphite fiber brush anodes for increased power production in air-cathode microbial fuel cells. *Environmental science & technology* **2007,** *41* (9), 3341-3346.

[22] Pant, D.; Van Bogaert, G.; Diels, L.; Vanbroekhoven, K., A review of the substrates used in microbial fuel cells (MFCs) for sustainable energy production. *Bioresource technology* **2010,** *101* (6), 1533-1543.

[23] Jung, S.; Regan, J. M., Comparison of anode bacterial communities and performance in microbial fuel cells with different electron donors. *Applied microbiology and biotechnology* **2007,** *77* (2), 393-402.

[24] Zhang, T.; Zeng, Y.; Chen, S.; Ai, X.; Yang, H., Improved performances of E. coli-catalyzed microbial fuel cells with composite graphite/PTFE anodes. *Electrochemistry Communications* **2007,** *9* (3), 349-353.

[25] Rabaey, K.; Van de Sompel, K.; Maignien, L.; Boon, N.; Aelterman, P.; Clauwaert, P.; De Schamphelaire, L.; Pham, H. T.; Vermeulen, J.; Verhaege, M., Microbial fuel cells for sulfide removal. *Environmental science & technology* **2006,** *40* (17), 5218-5224.

[26] Bond, D. R.; Lovley, D. R., Electricity production by Geobacter sulfurreducens attached to electrodes. *Appl. Environ. Microbiol.* **2003,** *69* (3), 1548-1555.

[27] Rabaey, K.; Lissens, G.; Siciliano, S. D.; Verstraete, W., A microbial fuel cell capable of converting glucose to electricity at high rate and efficiency. *Biotechnology letters* **2003,** *25* (18), 1531-1535.

[28] Kim, B. H.; Park, H.; Kim, H.; Kim, G.; Chang, I.; Lee, J.; Phung, N., Enrichment of microbial community generating electricity using a fuel-cell-type electrochemical cell. *Applied microbiology and biotechnology* **2004,** *63* (6), 672-681.

[29] Liu, H.; Logan, B. E., Electricity generation using an air-cathode single chamber microbial fuel cell in the presence and absence of a proton exchange membrane. *Environmental science & technology* **2004,** *38* (14), 4040-4046.

[30] Awan, Z.; Nahm, K. S.; Xavier, J. S., Nanotubular MnO2/graphene oxide composites for the application of open air-breathing cathode microbial fuel cells. *Biosensors and Bioelectronics* **2014,** *53*, 528-534.

[31] He, Z.; Minteer, S. D.; Angenent, L. T., Electricity generation from artificial wastewater using an microbial fuel cell. *Environmental science & technology* **2005,** *39* (14), 5262-5267.

[32] Yong, Y.-C.; Dong, X.-C.; Chan-Park, M. B.; Song, H.; Chen, P., Macroporous and monolithic anode based on polyaniline hybridized three-dimensional graphene for high-performance microbial fuel cells. *ACS nano* **2012,** *6* (3), 2394-2400.

[33] Liu, J.; Qiao, Y.; Guo, C. X.; Lim, S.; Song, H.; Li, C. M., Graphene/carbon cloth anode for high-performance mediatorless MFC. *Bioresource technology* **2012,** *114*, 275-280.

[34] Xiao, L.; Damien, J.; Luo, J.; Jang, H. D.; Huang, J.; He, Z., Crumpled graphene particles for microbial fuel cell electrodes. *Journal of Power Sources* **2012,** *208*, 187-192.

[35] Kim, J. R.; Jung, S. H.; Regan, J. M.; Logan, B. E., Electricity generation and microbial community analysis of alcohol powered microbial fuel cells. *Bioresource technology* **2007,** *98* (13), 2568-2577.

[36] Cheng, S.; Liu, H.; Logan, B. E., Increased performance of single-chamber microbial fuel cells using an improved structure. *Electrochemistry Communications* **2006,** *8* (3), 489-494.

[37] Rahimnejad, M.; Ghoreyshi, A. A.; Najafpour, G.; Jafary, T., Power generation from organic substrate in batch and continuous flow microbial fuel cell operations. *Applied Energy* **2011,** *88* (11), 3999-4004.

[38] Fierer, N.; Nemergut, D.; Knight, R.; Craine, J. M., Changes through time: integrating microorganisms into study of succession. *Research in microbiology* **2010,** *161* (8), 635-642.

[39] Hunt, S. M.; Werner, E. M.; Huang, B.; Hamilton, M. A.; Stewart, P. S., Hypothesis for the role of nutrient starvation in biofilm detachment. *Appl. Environ. Microbiol.* **2004,** *70* (12), 7418-7425.

[40] Harper, D.; Parracho, H.; Walker, J.; Sharp, R.; Hughes, G.; Werthén, M.; Lehman, S.; Morales, S., Bacteriophages and biofilms. *Antibiotics* **2014,** *3* (3), 270-284.

[41] Bester, E.; Wolfaardt, G.; Aznaveh, N.; Greener, J., Biofilms' role in planktonic cell proliferation. *International journal of molecular sciences* **2013,** *14* (11), 21965-21982.

[42] Logan, B. E., *Microbial fuel cells*. John Wiley & Sons: 2008.

[43] Hirose, A.; Kasai, T.; Aoki, M.; Umemura, T.; Watanabe, K.; Kouzuma, A., Electrochemically active bacteria sense electrode potentials for regulating catabolic pathways. *Nature communications* **2018,** *9* (1), 1083.

[44] Hernandez, M.; Newman, D., Extracellular electron transfer. *Cellular and Molecular Life Sciences CMLS* **2001,** *58* (11), 1562-1571.

[45] Vert, M.; Doi, Y.; Hellwich, K.-H.; Hess, M.; Hodge, P.; Kubisa, P.; Rinaudo, M.; Schué, F., Terminology for biorelated polymers and applications (IUPAC Recommendations 2012). *Pure and Applied Chemistry* **2012,** *84* (2), 377-410.

[46] Xing, D.; Zuo, Y.; Cheng, S.; Regan, J. M.; Logan, B. E., Electricity generation by Rhodopseudomonas palustris DX-1. *Environ. Sci.* **2008,** *42* (11), 4146-4151.

[47] Potter, M. C., Electrical effects accompanying the decomposition of organic compounds. *Proceedings of the Royal Society of London. Series B, Containing Papers of a Biological Character* **1911,** *84* (571), 260-276.

[48] Chiao, M., A microfabricated PDMS microbial fuel cell. *Journal of Microelectromechanical systems* **2008,** *17* (6), 1329-1341.

[49] Wendisch, V. F.; Bott, M.; Eikmanns, B. J., Metabolic engineering of Escherichia coli and Corynebacterium glutamicum for biotechnological production of organic acids and amino acids. *Current opinion in microbiology* **2006,** *9* (3), 268-274.

[50] Brand, O.; Fedder, G. K.; Hierold, C.; Korvink, J. G.; Tabata, O., *Micro-and nanomanipulation tools*. John Wiley & Sons: 2015.

[51] Arends, J. B.; Verstraete, W., 100 years of microbial electricity production: three concepts for the future. *Microbial biotechnology* **2012,** *5* (3), 333-346.

[52] Gregory, K. B.; Bond, D. R.; Lovley, D. R., Graphite electrodes as electron donors for anaerobic respiration. *Environmental microbiology* **2004,** *6* (6), 596-604.

[53] Mehta, T.; Coppi, M. V.; Childers, S. E.; Lovley, D. R., Outer membrane c-type cytochromes required for Fe (III) and Mn (IV) oxide reduction in Geobacter sulfurreducens. *Appl. Environ. Microbiol.* **2005,** *71* (12), 8634-8641.

[54] Leang, C.; Coppi, M. Lovley, D., OmcB, a c-type polyheme cytochrome, involved in Fe (III) reduction Geobacter sulfurreducens. *Journal of Bacteriology* **2003,** *185* (7), 2096-2103.

[55] Afkar, E.; Reguera, G.; Schiffer, M.; Lovley, D. R., A novel Geobacteraceae-specific outer membrane protein J (OmpJ) is essential for electron transport to Fe (III) and Mn (IV) oxides in Geobacter sulfurreducens. *BMC microbiology* **2005,** *5* (1), 41.

[56] a) Malvankar, N. S.; Vargas, M.; Nevin, K. P.; Franks, A. E.; Leang, C.; Kim, B.-C.; Inoue, K.; Mester, T.; Covalla, S. F.; Johnson, J. P., Tunable metallic-like conductivity in microbial nanowire networks. *Nature nanotechnology* **2011,** *6* (9), 573. b) Vargas, Madeline, et al. "Aromatic amino acids required for pili conductivity and long-range extracellular electron transport in Geobacter sulfurreducens." *MBio* **2013**, 4(2).

[57] Industry, S. o. C., *Journal of chemical technology and biotechnology*. Published for the Society of Chemical Industry by Blackwell Scientific: 2003; Vol. 78.

[58] Kim, B. H.; Ikeda, T.; Park, H. S.; Kim, H. J.; Hyun, M. S.; Kano, K.; Takagi, K.; Tatsumi, H., Electrochemical activity of an Fe (III)-reducing bacterium, Shewanella putrefaciens IR-1, in the presence of alternative electron acceptors. *Biotechnology Techniques* **1999,** *13* (7), 475-478.

[59] Park, H. S.; Kim, B. H.; Kim, H. S.; Kim, H. J.; Kim, G. T.; Kim, M.; Chang, I. S.; Park, Y. K.; Chang, H. I., A novel electrochemically active and Fe (III)-reducing bacterium

phylogenetically related to Clostridium butyricum isolated from a microbial fuel cell. *Anaerobe* **2001,** *7* (6), 297-306.

[60] Cao, Y.; Mu, H.; Liu, W.; Zhang, R.; Guo, J.; Xian, M.; Liu, H., Electricigens in the anode of microbial fuel cells: pure cultures versus mixed communities. *Microbial cell factories* **2019,** *18* (1), 39.

[61] Liu, H.; Ramnarayanan, R.; Logan, B. E., Production of electricity during wastewater treatment using a single chamber microbial fuel cell. *Environmental science & technology* **2004,** *38* (7), 2281-2285.

[62] Scott, K.; Murano, C., A study of a microbial fuel cell battery using manure sludge waste. *Journal of Chemical Technology & Biotechnology: International Research in Process, Environmental & Clean Technology* **2007,** *82* (9), 809-817.

[63] Niessen, J.; Harnisch, F.; Rosenbaum, M.; Schröder, U.; Scholz, F., Heat treated soil as convenient and versatile source of bacterial communities for microbial electricity generation. *Electrochemistry Communications* **2006,** *8* (5), 869-873.

[64] Waaij, V., The ecology of the human intestine and its consequences for overgrowth by pathogens such as Clostridium difficile. *Annual review of microbiology* **1989,** *43* (1), 69-87.

[65] Wei, L.; Han, H.; Shen, J., Effects of cathodic electron acceptors and potassium ferricyanide concentrations on the performance of microbial fuel cell. *International Journal of Hydrogen Energy* **2012,** *37* (17), 12980-12986.

[66] Fan, Y.; Sharbrough, E.; Liu, H., Quantification of the internal resistance distribution of microbial fuel cells. *Environmental science & technology* **2008,** *42* (21), 8101-8107.

[67] Logan, B. E.; Zikmund, E.; Yang, W.; Rossi, R.; Kim, -Y.; Saikaly, P. E.; Zhang, F., Impact of ohmic resistance on measured electrode potentials and maximum power production in microbial fuel cells. *Environmental science & technology* **2018,** *52* (15), 8977-8985.

[68] Scott, K.; Yu, E. H., *Microbial electrochemical and fuel cells: fundamentals and applications*. Woodhead Publishing: 2015.

[69] Liu, H.; Cheng, S.; Logan, B. E., Production of electricity from acetate or butyrate using a single-chamber microbial fuel cell. *Environ. Sci.* **2005,** *39* (2), 658-662.

[70] Fan, Y.; Hu, H.; Liu, H., Enhanced Coulombic efficiency and power density of air-cathode microbial fuel cells with an improved cell configuration. *Journal of Power Sources* **2007,** *171* (2), 348-354.

[71] Fan, Y.; Hu, H.; Liu, H., Sustainable power generation in microbial fuel cells using bicarbonate buffer and proton transfer mechanisms. *Environmental science & technology* **2007,** *41* (23), 8154-8158.

[72] You, S.; Zhao, Q.; Zhang, J.; Jiang, J.; Zhao, S., A microbial fuel cell using permanganate as the cathodic electron acceptor. *Journal of power sources* **2006,** *162* (2), 1409-1415.

[73] Oh, S.; Min, B.; Logan, B. E., Cathode performance as a factor in electricity generation in microbial fuel cells. *Environmental science & technology* **2004,** *38* (18), 4900-4904.

[74] Jang, J. K.; Chang, I. S.; Kim, B. H., Improvement of cathode reaction of a mediatorless microbial fuel cell. *Journal of Microbiology and Biotechnology* **2004,** *14* (2), 324-329.

[75] Borole, A. P.; Hamilton, C. Y.; Aaron, D. S.; Tsouris, C., Investigating microbial fuel cell bioanode performance under different cathode conditions. *Biotechnology progress* **2009,** *25* (6), 1630-1636.

[76] Min, B.; Cheng, S.; Logan, B. E., Electricity generation using membrane and salt bridge microbial fuel cells. *Water research* **2005,** *39* (9), 1675-1686.

[77] Logan, B. E.; Hamelers, B.; Rozendal, R.; Schröder, U.; Keller, J.; Freguia, S.; Aelterman, P.; Verstraete, W.; Rabaey, K., Microbial fuel cells: methodology and technology. *Environmental science & technology* **2006,** *40* (17), 5181-5192.

[78] Tender, L. M.; Reimers, C. E.; Stecher III, H. A.; Holmes, D. E.; Bond, D. R.; Lowy, D. A.; Pilobello, K.; Fertig, S. J.; Lovley, D. R., Harnessing microbially generated power on the seafloor. *Nature biotechnology* **2002,** *20* (8), 821.

[79] Najafgholi, Z.; Rahimnejad, M., Improvement of sediment microbial fuel cell performance by application of sun light and biocathode. *Korean Journal of Chemical Engineering* **2016,** *33* (1), 154-158.

[80] Song, N.; Jiang, H.-L., Effects of initial sediment properties on start-up times for sediment microbial fuel cells. *International Journal of Hydrogen Energy* **2018,** *43* (21), 10082-10093.

[81] Tang, L.; Li, X.; Zhao, Y.; Fu, F.; Ren, Y.; Wang, X., Effect of stirring rates in anodic area of sediment microbial fuel cell on its power generation. *Energy Sources, Part A: Recovery, Utilization, and Environmental Effects* **2017,** *39* (1), 23-28.

[82] Kabutey, F. T.; Antwi, P.; Ding, J.; Zhao, Q.-l.; Quashie, F. K., Enhanced bioremediation of heavy metals and bioelectricity generation in a macrophyte-integrated cathode sediment microbial fuel cell (mSMFC). *Environmental Science and Pollution Research* **2019,** *26* (26), 26829-26843.

[83] Tender, L. M.; Gray, S. A.; Groveman, E.; Lowy, D. A.; Kauffman, P.; Melhado, J.; Tyce, R. C.; Flynn, D.; Petrecca, R.; Dobarro, J., The first demonstration of a microbial fuel cell as a viable power supply: powering a meteorological buoy. *Journal of Power Sources* **2008,** *179* (2), 571-575.

[84] NRL. Continuous Sustainable Power Supply: Benthic Microbial Fuel Cell. Retrieved 16 Desember 2014 from: http://www.nrl.navy.mil (2013).

[85] Aelterman, P.; Rabaey, K.; Pham, H. T.; Boon, N.; Verstraete, W., Continuous electricity generation at high voltages and currents using stacked microbial fuel cells. *Environmental science & technology* **2006,** *40* (10), 3388-3394.

[86] Pasupuleti, S. B.; Srikanth, S.; Mohan, S. V.; Pant, D., Continuous mode operation of microbial fuel cell (MFC) stack with dual gas diffusion cathode design for the treatment of

dark fermentation effluent. *international journal of hydrogen energy* **2015,** *40* (36), 12424-12435.

[87] He, L.; Du, P.; Chen, Y.; Lu, H.; Cheng, X.; Chang, B.; Wang, Z., Advances in microbial fuel cells for wastewater treatment. *Renewable and Sustainable Energy Reviews* **2017,** *71*, 388-403.

[88] Das, D., *Microbial Fuel Cell*. Springer: 2018.

[89] Lu, M., *Materials for low-temperature fuel cells*. John Wiley & Sons: 2014.

[90] Mustakeem, M., Electrode materials for microbial fuel cells: nanomaterial approach. **2015**.

[91] Logan, B. E.; Zikmund, E.; Yang, W.; Rossi, R.; Kim, K.-Y.; Saikaly, P. E.; Zhang, F., Impact of ohmic resistance on measured electrode potentials and maximum power production in microbial fuel cells. *Environmental science & technology* **2018,** *52* (15), 8977-8985.

[92] Wang, X.; Cheng, S.; Feng, Y.; Merrill, M. D.; Saito, T.; Logan, B. E., Use of carbon mesh anodes and the effect of different pretreatment methods on power production in microbial fuel cells. *Environmental science & technology* **2009,** *43* (17), 6870-6874.

[93] Wei, J.; Liang, P.; Huang, X., Recent progress in electrodes for microbial fuel cells. *Bioresource technology* **2011,** *102* (20), 9335-9344.

[94] Chaudhuri, S. K.; Lovley, D. R., Electricity generation by direct oxidation of glucose in mediatorless microbial fuel cells. *Nature biotechnology* **2003,** *21* (10), 1229.

[95] ter Heijne, A.; Hamelers, H. V.; Saakes, M.; Buisman, C. J., Performance of non-porous graphite and titanium-based anodes in microbial fuel cells. *Electrochimica Acta* **2008,** *53* (18), 5697-5703.

[96] Zhao, F.; Rahunen, N.; Varcoe, J. R.; Chandra, A.; Avignone-Rossa, C.; Thumser, A. E.; Slade, R. C., Activated carbon cloth as anode for sulfate removal in a microbial fuel cell. *Environmental science & technology* **2008,** *42* (13), 4971-4976.

[97] Schröder, U.; Nießen, J.; Scholz, F., A generation of microbial fuel cells with current outputs boosted by more than one order of magnitude. *Angewandte Chemie International Edition* **2003,** *42* (25), 2880-2883.

[98] Richter, H.; McCarthy, K.; Nevin, K. P.; Johnson, J. P.; Rotello, V. M.; Lovley, D. R., Electricity generation by Geobacter sulfurreducens attached to gold electrodes. *Langmuir* **2008,** *24* (8), 4376-4379.

[99] Abbaszadeh Amirdehi, M.; Saem, S.; Zarabadi, M. P.; Moran-Mirabal, J. M.; Greener, J., Microstructured Anodes by Surface Wrinkling for Studies of Direct Electron Transfer Biofilms in Microbial Fuel Cells. *Advanced Materials Interfaces* **2018,** *5* (13), 1800290.

[100] Dumas, C.; Mollica, A.; Féron, D.; Basséguy, R.; Etcheverry, L.; Bergel, A., Marine microbial fuel cell: use of stainless steel electrodes as anode and cathode materials. *Electrochimica acta* **2007,** *53* (2), 468-473.

[101] Kargi, F.; Eker, S., Electricity generation with simultaneous wastewater treatment by a microbial fuel cell (MFC) with Cu and Cu–Au electrodes. *Journal of Chemical Technology & Biotechnology: International Research in Process, Environmental & Clean Technology* **2007,** *82* (7), 658-662.

[102] Nguyen, T.-H.; Yu, Y.-Y.; Wang, X.; Wang, J.-Y.; Song, H., A 3D mesoporous polysulfone–carbon nanotube anode for enhanced bioelectricity output in microbial fuel cells. *Chemical Communications* **2013,** *49* (91), 10754-10756.

[103] Qiao, Y.; Li, C. M.; Bao, S.-J.; Bao, Q.-L., Carbon nanotube/polyaniline composite as anode material for microbial fuel cells. *Journal of Power Sources* **2007,** *170* (1), 79-84.

[104] Yu, F.; Wang, C.; Ma, J., Applications of graphene-modified electrodes in microbial fuel cells. Materials 2016, 9 (10), 807.

[105] Xie, X.; Hu, L.; Pasta, M.; Wells, G. F.; Kong, D.; Criddle, C. S.; Cui, Y., Three-dimensional carbon nanotube− textile anode for high-performance microbial fuel cells. *Nano letters* **2010,** *11* (1), 291-296.

[106] Yu, Y.-Y.; Guo, C. X.; Yong, Y.-C.; Li, C. M.; Song, H., Nitrogen doped carbon nanoparticles enhanced extracellular electron transfer for high-performance microbial fuel cells anode. *Chemosphere* **2015,** *140,* 26-33.

[107] Zhao, C. e.; Wang, W. J.; Sun, D.; Wang, X.; Zhang, J. R.; Zhu, J. J., Nanostructured graphene/TiO2 hybrids as high-performance anodes for microbial fuel cells. *Chemistry–A European Journal* **2014,** *20* (23), 7091-7097.

[108] Wang, H.; Wang, G.; Ling, Y.; Qian, F.; Song, Y.; Lu, X.; Chen, S.; Tong, Y.; Li, Y., High power density microbial fuel cell with flexible 3D graphene–nickel foam as anode. *Nanoscale* **2013,** *5* (21), 10283-10290.

[109] Zou, L.; Qiao, Y.; Wu, X.-S.; Ma, C.-X.; Li, X.; Li, C. M., Synergistic effect of titanium dioxide nanocrystal/reduced graphene oxide hybrid on enhancement of microbial electrocatalysis. *Journal of Power Sources* **2015,** *276*, 208-214.

[110] Lv, Z.; Chen, Y.; Wei, H.; Li, F.; Hu, Y.; Wei, C.; Feng, C., One-step electrosynthesis of polypyrrole/graphene oxide composites for microbial fuel cell application. *Electrochimica Acta* **2013,** *111*, 366-373.

[111] Watanabe, K., Recent developments in microbial fuel cell technologies for sustainable bioenergy. *Journal of bioscience and bioengineering* **2008,** *106* (6), 528-536.

[112] Ghasemi, M.; Shahgaldi, S.; Ismail, M.; Kim, B. H.; Yaakob, Z.; Daud, W. R. W., Activated carbon nanofibers as an alternative cathode catalyst to platinum in a two-chamber microbial fuel cell. *International Journal of Hydrogen Energy* **2011,** *36* (21), 13746-13752.

[113] Ghasemi, M.; Shahgaldi, S.; Ismail, M.; Kim, B. H.; Yaakob, Z.; Daud, W. R. W., Activated carbon nanofibers as an alternative cathode catalyst to platinum in a two-chamber microbial fuel cell. *International Journal of Hydrogen Energy* **2011,** *36* (21), 13746-13752.

[114] Cheng, S.; Liu, H.; Logan, B. E., Increased power generation in a continuous flow MFC with advective flow through the porous anode and reduced electrode spacing. *Environmental science & technology* **2006,** *40* (7), 2426-2432.

[115] Aelterman, P.; Versichele; Genettello, E.; Verbeken, K.; Verstraete, W., Microbial fuel cells operated with iron-chelated air cathodes. *Electrochimica acta* **2009,** *54* (24), 5754-5760.

[116] Lefebvre, O.; Al-Mamun, A.; Ng, , A microbial fuel cell equipped with a biocathode for organic removal and denitrification. *Water Science and Technology* **2008,** *58* (4), 881-885.

[117] Ezziat, L.; Elabed, A.; Ibnsouda, S.; El Abed, S., Challenges of microbial fuel cell architecture on heavy metal recovery and removal from wastewater. *Frontiers in Energy Research* **2019,** *7* (1), 1-13.

[118] Clauwaert, P.; Van der Ha, D.; Boon, N.; Verbeken, K.; Verhaege, M.; Rabaey, K.; Verstraete, W., Open air biocathode enables effective electricity generation with microbial fuel cells. *Environmental science & technology* **2007,** *41* (21), 7564-7569.

[119] Park, D. H.; Zeikus, J.G, Improved fuel cell and electrode designs for producing electricity from microbial degradation. *Biotechnology and bioengineering* **2003,** *81* (3), 348-355.

[120] Nguyen, V. K.; Hong, S.; Park, Jo, K.; Lee, T., Autotrophic denitrification performance and bacterial community at biocathodes of bioelectrochemical systems with either abiotic or biotic anodes. *Journal of bioscience and bioengineering* **2015,** *119* (2), 180-187.

[121] Lefebvre, O.; Al-Mamun, A.; Ng, H., A microbial fuel cell equipped with a biocathode for organic removal and denitrification. *Water Science and Technology* **2008,** *58* (4), 881-885.

[122] Xafenias, N.; Zhang, Y.; Banks, C. J., Enhanced performance of hexavalent chromium reducing cathodes in the presence of Shewanella oneidensis MR-1 and lactate. *Environmental science & technology* **2013,** *47* (9), 4512-4520.

[123] Tandukar, M.; Huber, S. J.; Onodera, T.; Pavlostathis, S. G., Biological chromium (VI) reduction in the cathode of a microbial fuel cell. *Environmental science & technology* **2009,** *43* (21), 8159-8165.

[124] Cheng, S.; Logan, B. E., Increasing power generation for scaling up single-chamber air cathode microbial fuel cells. *Bioresource technology* **2011,** *102* (6), 4468-4473.

[125] Kim, J. R.; Cheng, S.; Oh, S.-E.; Logan, B. E., Power generation using different cation, anion, and ultrafiltration membranes in microbial fuel cells. *Environmental science & technology* **2007,** *41* (3), 1004-1009.

[126] Ter Heijne, A.; Hamelers, H. V.; De Wilde, V.; Rozendal, R. A.; Buisman, C. J., A bipolar membrane combined with ferric iron reduction as an efficient cathode system in microbial fuel cells. *Environmental science & technology* **2006,** *40* (17), 5200-5205.

[127] Nastro, R. A.; Gambino, E.; Toscanesi, M.; Arienzo, M.; Ferrara, L.; Trifuoggi, M., Microbial Fuel Cells (MFCs) remediation activity of marine sediments sampled at a dismissed industrial site: What opportunities? *Journal of Cleaner Production* **2019,** *235*, 1559-1566.

[128] Habermann, W.; Pommer, E., Biological fuel cells with sulphide storage capacity. *Applied microbiology and biotechnology* **1991,** *35* (1), 128-133.

[129] Li, W.-W.; Yu, H.-Q.; He, Z., Towards sustainable wastewater treatment by using microbial fuel cells-centered technologies. *Energy & Environmental Science* **2014,** *7* (3), 911-924.

[130] Logan, B. E., Scaling up microbial fuel cells and other bioelectrochemical systems. *Applied microbiology and biotechnology* **2010,** *85* (6), 1665-1671.

[131] Chandrasekhar, K.; Mohan, S. V., Bio-electrochemical remediation of real field petroleum sludge as an electron donor with simultaneous power generation facilitates biotransformation of PAH: effect of substrate concentration. *Bioresource technology* **2012,** *110*, 517-525.

[132] Kim, Y.; Logan, B. E., Microbial desalination cells for energy production and desalination. *Desalination* **2013,** *308*, 122-130.

[133] Strik, D. P.; Timmers, R. A.; Helder, M.; Steinbusch, K. J.; Hamelers, H. V.; Buisman, C. J., Microbial solar cells: applying photosynthetic and electrochemically active organisms. *Trends in biotechnology* **2011,** *29* (1), 41-49.

[134] Mardanpour, M. M.; Yaghmaei, S., Characterization of a microfluidic microbial fuel cell as a power generator based on a nickel electrode. *Biosensors and Bioelectronics* **2016,** *79*, 327-333.

[135] Lovley, D. R., Bug juice: harvesting electricity with microorganisms. *Nature Reviews Microbiology* **2006,** *4* (7), 497.

[136] Liu, H.; Grot, S.; Logan, B. E., Electrochemically assisted microbial production of hydrogen from acetate. *Environmental science & technology* **2005,** *39* (11), 4317-4320.

[137] Lee, S.-J. J.; Sundararajan, N., *Microfabrication for microfluidics*. Artech house: 2010.

[138] Bruus, H., *Theoretical microfluidics*. Oxford university press Oxford: 2008; Vol. 18.

[139] Whitesides, G. M., The origins and the future of microfluidics. *Nature* **2006,** *442* (7101), 368.

[140] Ismagilov, R. F.; Stroock, A. D.; Kenis, P. J.; Whitesides, G.; Stone, H. A., Experimental and theoretical scaling laws for transverse diffusive broadening in two-phase laminar flows in microchannels. *Applied Physics Letters* **2000,** *76* (17), 2376-2378.

[141] Kamholz, A. E.; Weigl, B. H.; Finlayson, B. A.; Yager, P., Quantitative analysis of molecular interaction in a microfluidic channel: the T-sensor. *Analytical chemistry* **1999,** *71* (23), 5340-5347.

[142] a) Ren, K.; Zhou, J.; Wu, H., Materials for microfluidic chip fabrication. Accounts of chemical research 2013, 46 (11), 2396-2406. b) J. Greener, "Microfluidics for chemical synthesis and biological functional materials: from device fabrication to applications", in Functional Materials For Energy, Sustainable Development and Biomedical Sciences, DeGruyter, ISBN 978-3-11-030782-5, 2014.

[143] Nge, P. N.; Rogers, C. I.; Woolley, A. T., Advances in microfluidic materials, functions, integration, and applications. *Chemical reviews* **2013**, 113 (4), 2550-2583.

[144] Iliescu, C.; Taylor, H.; Avram, M.; Miao, J.; Franssila, S., A practical guide for the fabrication of microfluidic devices using glass and silicon. *Biomicrofluidics* **2012,** *6* (1), 016505.

[145] Hermansson, K.; Lindberg, U.; Hok, B.; Palmskog, G. In *Wetting properties of silicon surfaces*, TRANSDUCERS'91: 1991 International Conference on Solid-State Sensors and Actuators. Digest of Technical Papers, IEEE: 1991; pp 193-196.

[146] Jang, A.; Zou, Z.; Lee, K. K.; Ahn, C. H.; Bishop, P. L., State-of-the-art lab chip sensors for environmental water monitoring. *Measurement Science and Technology* **2011,** *22* (3), 032001.

[147] Hof, L.; Guo, X.; Seo, M.; Wüthrich, R.; Greener, J., Glass imprint templates by spark assisted chemical engraving for microfabrication by hot embossing. *Micromachines* **2017,** *8* (1), 29.

[148] Zhang, J.; Tan, K.; Hong, G.; Yang, L.; Gong, H., Polymerization optimization of SU-8 photoresist and its applications in microfluidic systems and MEMS. *Journal of Micromechanics and Microengineering* **2001,** *11* (1), 20.

[149] Li, X.; Abe, T.; Esashi, M., Deep reactive ion etching of Pyrex glass using SF6 plasma. *Sensors and actuators A: Physical* **2001,** *87* (3), 139-145.

[150] Schlautmann, S.; Wensink, H.; Schasfoort, R.; Elwenspoek, M.; van den Berg, A., Powder-blasting technology as an alternative tool for microfabrication of capillary electrophoresis chips with integrated conductivity sensors. *Journal of micromechanics and microengineering* **2001,** *11* (4), 386.

[151] Ke, K.; Hasselbrink, E. F.; Hunt, A. J., Rapidly prototyped three-dimensional nanofluidic channel networks in glass substrates. *Analytical Chemistry* **2005,** *77* (16), 5083-5088.

[152] Egashira, K.; Mizutani, K.; Nagao, T., Ultrasonic vibration drilling of microholes in glass. *CIRP Annals* **2002,** *51* (1), 339-342.

[153] Wu, W.-I.; Sask, K. N.; Brash, J. L.; Selvaganapathy, P. R., Polyurethane-based microfluidic devices for blood contacting applications. *Lab on a Chip* **2012,** *12* (5), 960-970.

[154] Soares, R.; Novo, P.; Azevedo, A.; Fernandes, P.; Aires-Barros, M.; Chu, V.; Conde, J., On-chip sample preparation and analyte quantification using a microfluidic aqueous two-phase extraction coupled with an immunoassay. *Lab on a Chip* **2014,** *14* (21), 4284-4294.

[155] McDonald, J. C.; Whitesides, G. M., Poly (dimethylsiloxane) as a material for fabricating microfluidic devices. *Accounts of chemical research* **2002,** *35* (7), 491-499.

[156] Greener, J.; Li, W.; Ren, J.; Voicu, D.; Pakharenko, V.; Tang, T.; Kumacheva, E., Rapid, cost-efficient fabrication of microfluidic reactors in thermoplastic polymers by combining photolithography and hot embossing. *Lab on a Chip* **2010,** *10* (4), 522-524.

[157] Martinez-Duarte, R.; Madou, M., SU-8 photolithography and its impact on microfluidics. *Microfluidics and Nanofluidics Handbook* **2011**, 231-268.

[158] Li, X. J.; Zhou, Y., *Microfluidic devices for biomedical applications*. Elsevier: 2013.

[159] a) Klintberg, L.; Svedberg, M.; Nikolajeff, F.; Thornell, G., Fabrication of a paraffin actuator using hot embossing of polycarbonate. *Sensors and Actuators A: Physical* **2003,** *103* (3), 307-316. b) Method for producing a stamp for hot embossing J Greener, W Li, E Kumacheva - US Patent App. 13/147,863, 2012. c) Greener, J., Li, W., Ren, J., Voicu, D., Pakharenko, V., Tang, T., Kumacheva, E. Rapid, cost-efficient fabrication of microfluidic reactors in thermoplastic polymers by combining photolithography and hot embossing. *Lab on a Chip* **2010**, *10*(4), 522-524.

[160] Youn, S.-W.; Noguchi, T.; Takahashi, M.; Maeda, R., Dynamic mechanical thermal analysis, forming and mold fabrication studies for hot-embossing of a polyimide microfluidic platform. *Journal of Micromechanics and Microengineering* **2008,** *18* (4), 045025.

[161] Jeon, J. S.; Chung, S.; Kamm, R. D.; Charest, J. L., Hot embossing for fabrication of a microfluidic 3D cell culture platform. *Biomedical microdevices* **2011,** *13* (2), 325-333.

[162] Becker, H.; Heim, U., Hot embossing as a method for the fabrication of polymer high aspect ratio structures. *Sensors and Actuators A: Physical* **2000,** *83* (1-3), 130-135.

[163] Cameron, N. S.; Roberge, H.; Veres, T.; Jakeway, S. C.; Crabtree, H. J., High fidelity, high yield production of microfluidic devices by hot embossing lithography: rheology and stiction. *Lab on a Chip* **2006,** *6* (7), 936-941.

[164] Leech, P. W., Hot Embossing Of Microchannels in Cyclic Olefin Copolymers. *MRS Online Proceedings Library Archive* **2009,** *1191*.

[165] a) Debono, M., Voicu, D., Pousti, M., Safdar, M., Young, R., Kumacheva, E., & Greener, J. One-step fabrication of microchannels with integrated three-dimensional features by hot intrusion embossing. *Sensors* **2016,** *16*(12), 2023. b) Hof, L. A., Guo, X., Seo, M., Wüthrich, R., & Greener, J. Glass imprint templates by spark assisted chemical engraving for microfabrication by hot embossing. *Micromachines* **2017,** *8*(1), 29.

[166] Kolew, A.; Münch, D.; Sikora, K.; Worgull, M., Hot embossing of micro and sub-micro structured inserts for polymer replication. *Microsystem technologies* **2011,** *17* (4), 609-618.

[167] Logan, B. E.; Rabaey, K., Conversion of wastes into bioelectricity and chemicals by using microbial electrochemical technologies. *Science* **2012,** *337* (6095), 686-690.

[168] Wang, H.; Park, J.-D.; Ren, Z., Active energy harvesting from microbial fuel cells at the maximum power point without using resistors. *Environmental science & technology* **2012,** *46* (9), 5247-5252.

[169] Ren, H.;Lee, H-S.; Chae, J., Miniaturizing microbial fuel cells for potential portable power sources: promises and challenges. *Microfluidics and Nanofluidics* **2012,** *13* (3), 353-381.

[170] Shantaram,.; Beyenal,H.; Veluchamy, R. A.; Lewandowski, Z., Wireless sensors powered by microbial fuel cells. *Environmental science & technology* **2005,** *39* (13), 5037-5042.

[171] Li, L.; Nikiforidis, G.; Leung, M. K.; Daoud, W. A., Vanadium microfluidic fuel cell with novel multi-layer flow-through porous electrodes: Model, simulations and experiments. *Applied energy* **2016,** *177*, 729-739.

[172] Mukherjee, S.; Su, S.; Panmanee, W.; Irvin, R. T.; Hassett, D. J.; Choi, S., A microliter-scale microbial fuel cell array for bacterial electrogenic screening. *Sensors and Actuators A: Physical* **2013,** *201*, 532-537.

[173] Qian, F.; He, Z.; Thelen, M. P.; Li, Y., A microfluidic microbial fuel cell fabricated by soft lithography. *Bioresource Technology* **2011,** *102* (10), 5836-5840.

[174] Choi, S.; Chae, J., Optimal biofilm formation and power generation in a micro-sized microbial fuel cell (MFC). *Sensors and Actuators A: Physical* **2013,** *195*, 206-212.

[175] Chen, Y.-P.; Zhao, Y.; Qiu, K.-Q.; Chu, J.; Lu, R.; Sun, M.; Liu, X.-W.; Sheng, G.-P.; Yu, H.-Q.; Chen, J., An innovative miniature microbial fuel cell fabricated using photolithography. *Biosensors and Bioelectronics* **2011,** *26* (6), 2841-2846.

[176] Kim, P.; Kwon, K. W.; Park, M. C.; Lee, S. H.; Kim, S. M.; Suh, K. Y., Soft lithography for microfluidics: a review. **2008**.

[177] Ziaie, B.; Baldi, A.; Lei, M.; Gu, Y.; Siegel, R. A., Hard and soft micromachining for BioMEMS: review of techniques and examples of applications in microfluidics and drug delivery. *Advanced drug delivery reviews* **2004,** *56* (2), 145-172.

[178] Qian, F.; Baum, M.; Gu, Q.; Morse, D. E., A 1.5 μL microbial fuel cell for on-chip bioelectricity generation. *Lab on a Chip* **2009,** *9* (21), 3076-3081.

[179] Choi, S.; Lee, H.-S.; Yang, Y.; Parameswaran, P.; Torres, C. I.; Rittmann, B. E.; Chae, J., A μL-scale micromachined microbial fuel cell having high power density. *Lab on a Chip* **2011,** *11* (6), 1110-1117.

[180] Leang, C.; Qian, X.; Mester, T.; Lovley, D. R., Alignment of the c-type cytochrome OmcS along pili of Geobacter sulfurreducens. *Appl. Environ. Microbiol.* **2010,** *76* (12), 4080-4084.

[181] Kjeang, E.; Djilali, N.; Sinton, D., Microfluidic fuel cells: A review. *Journal of Power Sources* **2009,** *186* (2), 353-369.

[182] Yang, S.; Jia, B.; Liu, H., Effects of the Pt loading side and cathode-biofilm on the performance of a membrane-less and single-chamber microbial fuel cell. *Bioresource Technology* **2009,** *100* (3), 1197-1202.

[183] Yang, Y.; Ye, D.; Li, J.; Zhu, X.; Liao, Q.; Zhang, B., Microfluidic microbial fuel cells: from membrane to membrane free. *Journal of Power Sources* **2016,** *324*, 113-125.

[184] Li, Z.; Zhang, Y.; LeDuc, P. R.; Gregory, K. B., Microbial electricity generation via microfluidic flow control. *Biotechnology and bioengineering* **2011,** *108* (9), 2061-2069.

[185] Wang, H.-Y.; Su, J.-Y., Membraneless microfluidic microbial fuel cell for rapid detection of electrochemical activity of microorganism. *Bioresource technology* **2013,** *145*, 271-274.

[186] Yang, Y.; Ye, D.; Li, J.; Zhu, X.; Liao, Q.; Zhang, B., Biofilm distribution and performance of microfluidic microbial fuel cells with different microchannel geometries. *International Journal of Hydrogen Energy* **2015,** *40* (35), 11983-11988.

[187] Fraiwan, A.; Call, D. F.; Choi, S., Bacterial growth and respiration in laminar flow microbial fuel cells. *Journal of Renewable and Sustainable Energy* **2014,** *6* (2), 023125.

[188] Yang, Y.; Ye, D.; Liao, Q.; Zhang, P.; Zhu, X.; Li, J.; Fu, Q., Enhanced biofilm distribution and cell performance of microfluidic microbial fuel cells with multiple anolyte inlets. *Biosensors and Bioelectronics* **2016,** *79*, 406-410.

[189] Ye, D.; Yang, Y.; Li, J.; Zhu, X.; Liao, Q.; Deng, B.; Chen, R., Performance of a microfluidic microbial fuel cell based on graphite electrodes. *international journal of hydrogen energy* **2013,** *38* (35), 15710-15715.

[190] Yoon, J. Y.; Ahn, Y.; Schröder, U., Parylene C-coated PDMS-based microfluidic microbial fuel cells with low oxygen permeability. *Journal of Power Sources* **2018,** *398*, 209-214.

[191] Yang, W.; Lee, K. K.; Choi, S., A laminar-flow based microbial fuel cell array. *Sensors and Actuators B: Chemical* **2017,** *243*, 292-297.

[192] Parra, E.; Lin, L. In *Microbial fuel cell based on electrode-exoelectrogenic bacteria interface,* 2009 IEEE 22nd International Conference on Micro Electro Mechanical Systems, IEEE: 2009; pp 31-34.

[193] Inoue, S.; Parra, E. A.; Higa, A.; Jiang, Y.; Wang, P.; Buie, C. R.; Coates, J. D.; Lin, L., Structural optimization of contact electrodes in microbial fuel cells for current density enhancements. *Sensors and Actuators A: Physical* **2012,** *177*, 30-36.

[194] Ren, H.; Torres, C. I.; Parameswaran, P.; Rittmann, B. E.; Chae, J., Improved current and power density with a micro-scale microbial fuel cell due to a small characteristic length. *Biosensors and Bioelectronics* **2014,** *61*, 587-592.

[195] Choi, S.; Chae, J., An array of microliter-sized microbial fuel cells generating 100 μW of power. *Sensors and Actuators A: Physical* **2012,** *177*, 10-15.

[196] Hou, H.; Li, L.; Cho, Y.; De Figueiredo, P.; Han, A., Microfabricated microbial fuel cell arrays reveal electrochemically active microbes. *PLOS one* **2009,** *4* (8), e6570.

Chapter 2: Experiments and methodology

2.1. Experimental set up: two-chamber MFCs

Custom MFCs are built under bulk conditions. This type of MFC is easy to use and is well suited to basic research. We propose a conventional dual chamber (Figure 2.1) device for development of a general scientific understanding of bulk MFCs and testing of *G. sulfurreducens* biofilms exposed to different anode materials. This architecture consists of two bottles (150 mL capacity, ADAMS & CHITTENDEN SCIENTIFIC GLASS, NY) connected through a 19.6 cm^2 CEM (CMI-7000S, Membrane International Inc., NJ, USA). The anode chamber in Figure 2.1(a) is filled with growth medium and *G. sulfurreducens* in anaerobic conditions. The cathode chamber (right) is filled with phosphate buffered ferricyanide solution (yellow) as the electron acceptor. Each compartment has one port with a 8 mm diameter used as a feedthrough for electrical connections. The cathode is built using a standard graphite plate electrode (GraphiteStore, USA) with a size of 25 × 25 × 3 mm. A microcontroller board (Arduino Mega 2560) is used to measure the time-dependent current outputs of up to 12 individual MFCs at the same time (Figure 2.1b). We use standard 25 cm^2 (surface area) graphite plates as the electrode (GraphiteStore.com) for both the anode and cathode, which is preferable due to their chemical stability and conductivity.

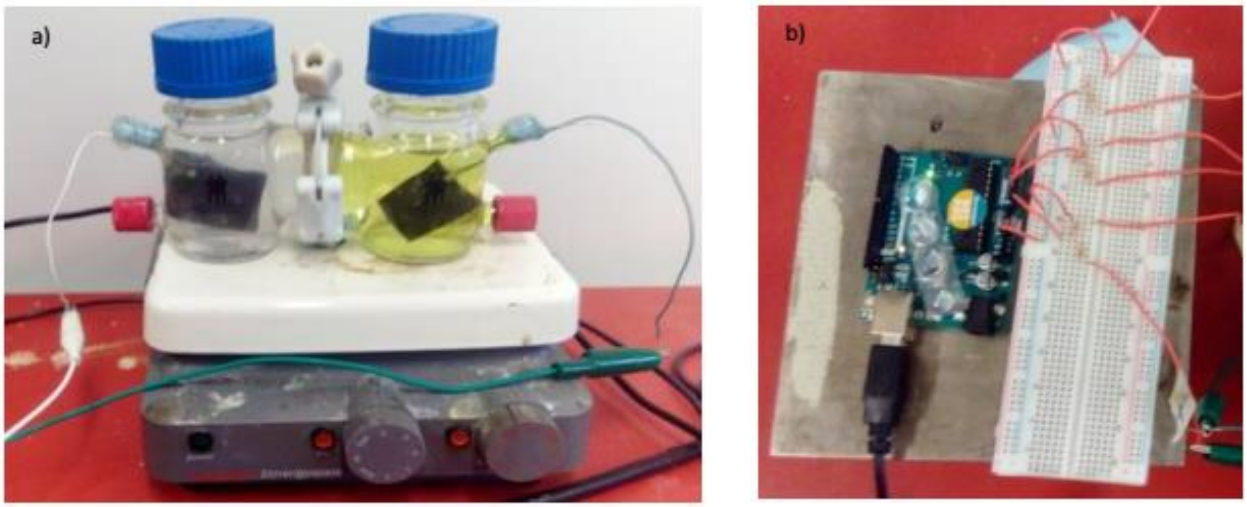

Figure 2.1: Picture of a two-chamber MFC used in this work. The anode chamber (a) is filled with growth medium and *G. sulfurreducens*. The cathode chamber is filled with phosphate buffered ferricyanide solution (30 mM). b) A microcontroller board (Arduino) monitors the voltage through time.

2.1.1. Anode and cathode feed preparation

The MFC anode chamber was inoculated from 10 mM concentrations of redox mediators mixed in freshly harvested bacteria solution. *G. sulfurreducens* (wild type, strain PCA, ATCC 51573), aliquots were stored in a −80 °C biological freezer (Thermo Scientific Revco EXF, Burlington, ON, Canada). All preparatory steps were conducted in an oxygen-free environment in a glovebox (10% H_2, 10% CO_2, and 80% N_2). *G. sulfurreducens* was subcultured in nutrient medium supplemented with 40 × 10^{-3} M sodium fumarate ($Na_2C_4H_2O_4$) as a soluble electron acceptor to support bacterial growth in solution. The medium contained the following (per liter of distilled water): sodium acetate carbon source (CH_3COONa, 10 × 10^{-3} M), NaH_2PHO_4 (3.8 × 10^{-3} M), $NaHCO_3$ (30 × 10^{-3} M), KCl (1.3 × 10^{-3} M), NH4Cl (28 × 10^{-3} M) (all from Sigma-Aldrich, Oakville, ON, Canada), a trace mineral supplement (ATCC® MD-TMS™, 10 mL L^{-1}), and a vitamin supplement (ATCC® MD-VS™, 10 mL L^{-1}). The medium was sterilized before use by autoclaving at 110 °C at 20 psi for 20 min. Sodium fumarate was added through a sterilized filter in the glovebox. All media for the MFC were sterilized prior to use by autoclaving at 110°C and 20 psi for 20 min. *G. sulfurreducens* (PCA, wild type) was grown in freshwater medium with 10 mM acetate as the electron donor and 30 mM fumarate as the electron acceptor under strict anaerobic conditions (glove box at 30ºC). The final solution was used in the anolyte chamber with gentle stirring in an oxygen-free environment. The cathode compartment was filled with 150 mL of phosphate buffer (PBS) containing 30 mM ferricyanide (as an electron accepter) at pH=7.4 (PBS).

2.1.2. Measurements and data acquisition

To evaluate MFC output, power density plots are obtained. Constant resistance measurements of the MFC voltage are acquired using a microcontroller board (Arduino) connected to a personal computer that can be simultaneously connected to up to twelve individual MFCs. The Arduino program code for automatic measurement of 12 inputs can be found at the end of this chapter. The CEM was pretreated by successive exposure to deionized (DI) water with 5 wt% NaCl (Caledon Lab Ltd., ON, Canada) for 12-18 h, followed

by thorough washing with DI water. The MFC anode was inoculated using the sub-culture with a 10 mM solution of acetate as a nutrient with a catholyte (30 mM ferricyanide solution in pH 7.0sodium phosphate buffer). During the inoculation, the MFC anode and cathode remained connected through an external resistor via a breadboard. Measurements of voltage are acquired every 10 minutes such that the current and power were calculated. To determine the maximum power density, R_{ext} is varied automatically in the range of 100 Ω to 100 kΩ using a potientiostat (Princeton Applied Research, VersaSTAT 4_Model 400). The maximum power density is achieved when the external and internal resistances are matched. All reactors were operated in a temperature-controlled laboratory (23 ± 0.5°C).

2.2. Fabrication of the microfluidic device

2.2.1. Microfabrication technique

In our group, we usually use microfabrication techniques (hot embossing and photolithography) to construct our microfluidic devices. In this process, we first design a mask and subsequently create a mould out of the mask. The MF device is fabricated from the mould. In this particular project, photolithography is used as a method to fabricate the microfluidic MFC device.

2.2.2. Mask fabrication

We use AutoCAD software to create the desired design of photomasks for production of the microchannel. This design is printed on an acetate sheet, as shown in Figure 2.2.

Figure 2.2. Printed photomask on a transparent acetate sheet.

2.2.3. Mould fabrication

Photolithography is the process of transferring a pattern from a mask onto a photosensitive resist using light. The photolithography method used in our group uses SU-8 (SU8 3000, Microchem, USA), a negative photoresist, with 1 mm thick glass slides (Fisher Scientific, USA). Fabrication of moulds is typically performed in a cleanroom using these negative photoresists. With exposure of an area to light, this type of photoresist undergoes a transition from insoluble to soluble, and a developer solution is used to remove the exposed areas.

The design is printed with high resolution and can be applied in fabrication with the use of a negative photoresist. The channel design is transparent on the print such that UV light can pass through the mask and cross-link with the photoresist (as shown in figure 2.3).

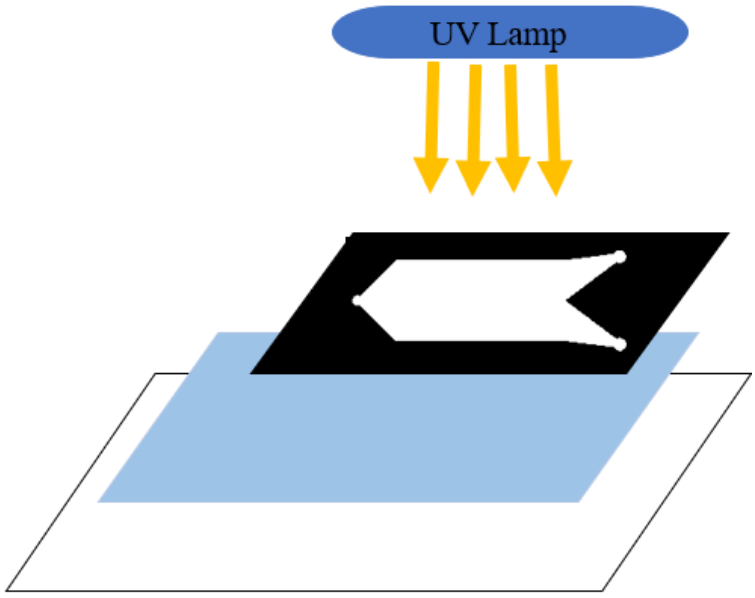

Figure 2.3. Photoresist exposed to UV light under a photomask.

To create the mould, one or two pieces of photoresist (depending on the need for thicker features) are cut and placed on a glass slide and subsequently moved through a laminator in a dark room. Typically, it is passed through the laminator (Figure 2.4a) more than two times to obtain good adhesion to the glass and eliminate all bubbles. Eventually, the photomask (which was previously designed and printed with AutoCAD software) was placed on top of the negative photoresist and positioned under a UV lamp (Figure 2.4b). The light that passes

through the transparent area of the mask causes a cross-linking process to occur over the photoresist, which darkens the color of the photoresist. After washing with photoresist developer solution for approximately 10-15 minutes, which removes all extra uncross-linked segment, the glass substrate and its attached photoresist is ready for use in PDMS molding.

Figure 2.4. (a) Photoresist laminator (film SY 300, Fortex, Royaume-Uni). (b) UV light (AY-315, Fortex, United Kingdom).

Polydimethylsiloxane $CH_3[Si(CH3)_2O]_n Si(CH_3)_3$, also known as PDMS, is a silicon-based polymer widely used in photolithography. The microfluidic MFC device was fabricated by casting of PDMS against its cross-linker (184 Silicone Elastomer Kit, SYLGARD, Midland, USA) at a ratio of 10 to 1 for this work. This mixture was placed in a vacuum pump for approximately 10 minutes to allow escape of gas or bubbles.

Two electrodes with dimensions 10 x 20 mm were cut from a 3 mm thick commercial graphite sheet (GraphiteStore.com Inc., USA). For both the anode and cathode, these graphite plates were placed in contact with the top side of the mould channel feature. Double-sided tape was used to ensure good contact between the graphite and the channel feature. The graphite electrodes were positioned on the opposite sides of the channel. Each electrode was stabilized by placing a small piece of PDMS between the electrode and unpatterned mould surface. Finally, uncross-linked PDMS polymer, in the form of a viscous liquid with its cross-linker (mixed at a ratio of 10 to 1), is poured onto the photoresist mould and graphite electrode in a Petri dish and cured via a cross-linking process in a 70^{o}C oven for 4 hours. After

removing the PDMS and glass slide from the oven, the PDMS is picked up from the Petri dish using a blade. The inlet and outlet ports are punched by a needle. The whole of process is explained in chapter four with details.

In this project, similar to other conventional microfluidic studies, we use a plasma device (Figure 2.5) to adhere the piece of PDMS (containing two electrodes) and the glass slides and to activate their surfaces to create an irreversible bond for completion of the device. The punched PDMS layer and a pre-cleaned glass slide (75×55×1 mm thick) are placed in the plasma cleaner. The PDMS and glass slide are held at this condition for 90 seconds and are subsequently attached irreversibly. During oxidization of PDMS in plasma, the surface of the hydrophobic PDMS relief becomes hydrophilic for strong adhesion.

Figure 2.5. Air plasma instrument.

Liquids were injected by two syringe pumps (NE-1600, New Era, USA) from a 50 mL gastight glass syringe and into the channels via 1.6 mm outer diameter perfluoroalkoxy (PFA) connective tubing (U-1148, IDEX, WA, USA) and syringe tubing connector assemblies (P-200x, P-658, IDEX, WA, USA).

2.4. Programing code for microcontroller:

```
int analogPin1 = 0; // potentiometer wiper (middle terminal) connected to analog pin 3
int analogPin2 = 1;
int analogPin3 = 2;
int analogPin4 = 3;
int analogPin5 = 4;
int analogPin6 = 5;
int analogPin7 = 6;
int analogPin8 = 7;
int analogPin9 = 8;
int analogPin10 = 9;
int analogPin11 = 10;
int analogPin12 = 11;
int val = 0;           // variable to store the value read
unsigned int timer = 0;
float vout = 0.0;

void setup()

{
// analogReference(INTERNAL);
analogReference(DEFAULT);
 pinMode(analogPin1, INPUT);
 pinMode(analogPin2, INPUT);
 pinMode(analogPin3, INPUT);
 pinMode(analogPin4, INPUT);
 pinMode(analogPin5, INPUT);
 pinMode(analogPin6, INPUT);
 pinMode(analogPin7, INPUT);
 pinMode(analogPin8, INPUT);
 pinMode(analogPin9, INPUT);
 pinMode(analogPin10, INPUT);
 pinMode(analogPin11, INPUT);
 pinMode(analogPin12, INPUT);
 Serial.begin(9600);          //  setup serial

}
void loop()
{
  Serial.print("Timer : ");
  Serial.print(timer);

  val = analogRead(analogPin1);
  //vout = (val*1.1)/1023.0;   // read the input pin
  vout = val* (5.0 / 1023.0);
Serial.print("; MFC1 ");
  Serial.print(vout);

  val = analogRead(analogPin2);
  //vout = (val*1.1)/1023.0;   // read the input pin
  vout = val* (5.0 / 1023.0);
Serial.print("; MFC2 ");
  Serial.print(vout);
```

```
  val = analogRead(analogPin3);
  //vout = (val*1.1)/1023.0;   // read the input pin
  vout = val* (5.0 / 1023.0);
Serial.print("; MFC3 ");
  Serial.print(vout);

  val = analogRead(analogPin4);
  //vout = (val*1.1)/1023.0;   // read the input pin
  vout = val* (5.0 / 1023.0);
Serial.print("; MFC4 ");
  Serial.print(vout);

  val = analogRead(analogPin5);
  //vout = (val*1.1)/1023.0;   // read the input pin
  vout = val* (5.0 / 1023.0);
Serial.print("; MFC5 ");
  Serial.print(vout);

  val = analogRead(analogPin6);
  //vout = (val*1.1)/1023.0;   // read the input pin
  vout = val* (5.0 / 1023.0);
Serial.print("; MFC6 ");
  Serial.print(vout);

  val = analogRead(analogPin7);
  //vout = (val*1.1)/1023.0;   // read the input pin
  vout = val* (5.0 / 1023.0);
Serial.print("; MFC7 ");
  Serial.print(vout);

  val = analogRead(analogPin8);
  //vout = (val*1.1)/1023.0;   // read the input pin
  vout = val* (5.0 / 1023.0);
Serial.print("; MFC8 ");
  Serial.print(vout);

  val = analogRead(analogPin9);
  //vout = (val*1.1)/1023.0;   // read the input pin
  vout = val* (5.0 / 1023.0);
Serial.print("; MFC9 ");
  Serial.print(vout);

    val = analogRead(analogPin10);
  //vout = (val*1.1)/1023.0;   // read the input pin
  vout = val* (5.0 / 1023.0);
Serial.print("; MFC10 ");
  Serial.print(vout);

    val = analogRead(analogPin11);
  //vout = (val*1.1)/1023.0;   // read the input pin
  vout = val* (5.0 / 1023.0);
Serial.print("; MFC11 ");
  Serial.print(vout);

    val = analogRead(analogPin12);
  //vout = (val*1.1)/1023.0;   // read the input pin
```

```
  vout = val* (5.0 / 1023.0);
Serial.print("; MFC12 ");
  Serial.println(vout);


  // debug value
    timer = timer + (1);

  delay(300000);

}
```

Chapter 3: Microstructured Anodes by Surface Wrinkling for Studies of Direct Electron Transfer Biofilms in Microbial Fuel Cells

Mehran Abbaszadeh Amirdehi[1], Sokunthearath Saem[2], Mir Pouyan Zarabadi[1], Jose M. Moran-Mirabal[2] and Jesse Greener[1,3]

[1] Département de ChimieUniversité LavalQuébec, QC G1V 0A6, Canada

[2] Department of Chemistry and Chemical BiologyMcMaster University1280 Main Street West, Hamilton, ON L8S 4M1, Canada

[3] CHU de Québec Centre de recherche CentreUniversité Laval10 rue de l'Espinay, Québec, QC G1L 3L5, Canada

Published in *Advanced Materials Interfaces.* 2018 Jul; 5(13):1800290.

3.1. Résumé

Un procédé de production de surfaces d'or froissées hiérarchiques est utilisé pour modifier en permanence les dimensions caractéristiques de la microstructure d'une bioanode dans une pile microbienne, tout en conservant la surface totale électroactive et la chimie des matériaux. En utilisant cette approche, l'effet de la topographie de l'anode sur les générations de puissance du transfert direct d'électrons à partir de biofilms de *Geobacter sulfurnucens* peut être isolé et étudié sans les effets concurrents associés à la fabrication additive. Bien que leurs surfaces électroactives soient identiques pour toutes les anodes structurées, les anodes hautes et bien espacées donnent de meilleurs résultats. En revanche, les anodes avec les structures les plus courtes et les plus compactes ne fonctionnent pas mieux que les surfaces planes ayant le même empreinte et une surface électroactive inférieure. Il est postulé que le grand espacement entre les plis offre un meilleur contact électrique entre le biofilm et l'électrode via une densité bactérienne améliorée à la surface de l'électrode. Une attention particulière aux dimensions structurelles plutôt qu'à la surface électroactive totale est proposée comme une direction importante pour l'optimisation future des bioanodes dans les piles à combustible microbiennes contenant des biofilms électroactifs à transfert direct d'électrons.

3.2. Abstract

A method for producing hierarchical wrinkled gold surfaces is used to continuously change characteristic microstructure dimensions of a bioanode in a microbial fuel cell, while conserving the total electroactive surface area and material chemistry. Using this approach, the effect of anode topography on power outputs from direct electron transfer from *G. sulfurreducens* biofilms can be isolated and studied without the competing effects associated with additive manufacturing. Despite having the same electroactive surface area for all structured anodes, tall and well-spaced features perform best. Anodes with the shortest, most closely packed structures, on the other hand, do not perform any better than planar surfaces with the same footprint and lower electroactive surface area. It is postulated that large interfold spacing provides better electrical contact between the biofilm and the electrode via improved bacterial packing density at the electrode surface. Rigorous attention to structural dimensions rather than total electroactive surface area is proposed as an important direction for future bioanode optimization in microbial fuel cells containing direct electron transfer electroactive biofilms.

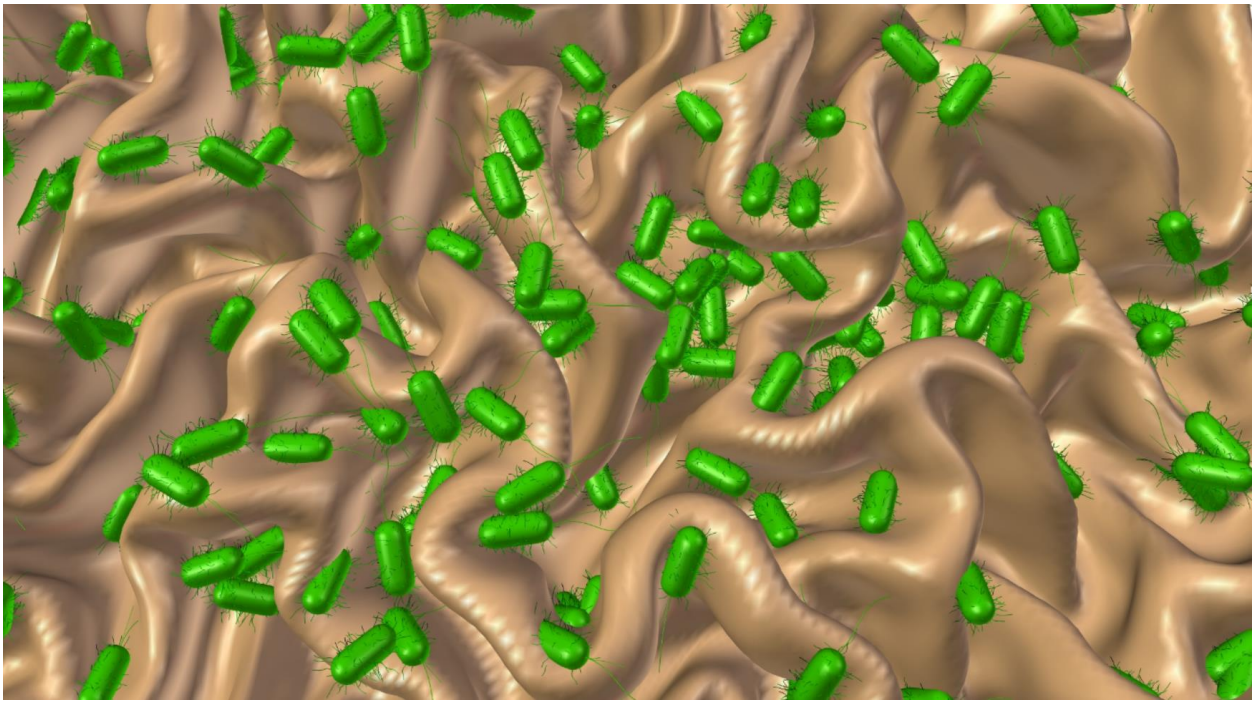

Graphical Abstract: Wrinkled gold electrodes are used to test the effect of anode topography on power outputs from *G. sulfurreducens* biofilms without the competing effects associated with structuring from additive manufacturing. Despite having the same electroactive surface area for all structured anodes, tall and well-spaced features perform best. Anodes with the shortest, most closely packed structures, do not perform better than planar surfaces.

3.3. Introduction

A microbial fuel cell (MFC) is a bioelectrochemical device in which the oxidation of organic molecules produces a usable electric current. MFCs are promising as next generation clean energy technologies because they can produce electricity while achieving bioremediation.[1,2,3,4,5] In addition, they show potential as autonomous power sources for remote environmental sensing applications[6] and even for implanted devices.[7] The electroactive biofilms (EABs), which catalyze the oxidation reaction, are composed of microorganisms that can transfer electrons to extracellular acceptors.[8] In a MFC, EABs are cultured directly on the anode so that electron transfer to an external circuit is efficient. Common bacteria used as EABs include *Geobacter sulfurreducens*,[9] *Shewanellaputrefaciens*,[10] *Desulfovibriodesulfuricans*,[11] and *Rhodopseudo monas palustris*.[12] Biofilms from these bacteria benefit from the ability to directly transfer electrons through a bioconductive network of bacterial appendages and embedded electroactive proteins, via physical contact with the anode.[13,14,15] To enhance MFC performance, high-surface-area anodes have been introduced based on nanoconductive textiles,[16] graphene sponges,[17] and brushes.[18] In other approaches, additive fabrication methods been used to decorate existing anode surfaces with conductive polymers[19] and nanoparticles of different materials, sizes, and shapes.[20, 21, 22, 23] Generally, structured anodes are designed to increase the total surface area, but little effort has been made to isolate and rigorously study the role of surface topography. This is likely because it is difficult to vary feature geometries in a controlled manner, without introducing competing effects such as changes in total surface area, exposed materials or surface chemistry.

Gold is an excellent anode material because it is highly conductive, biocompatible, and electrochemically stable over a wide potential window.[**14**, 24,25,26,27] Recently, a benchtop process has been developed for the controlled buckling of thin gold films on top of shape-memory polymer sheets, with demonstrated applications in point-of-care diagnostic systems.[28, 29, 30, 31] As opposed to other approaches, this method produces chemically homogeneous surface structures (wrinkles) with continuous control over average peak-to-valley heights and distances between folds, based on the initial gold film thickness. The method also conserves the total surface area, making it ideal for investigating the effect of

anode topography on MFC performance, without introducing side-effects. In this work, we have used these surfaces as anodes for *G. sulfurreducens* biofilms in an H-type dual chamber MFC setup. Variations in wrinkle morphologies were achieved using Au layers with thicknesses between 50 and 400 nm, the largest range reported to date. Despite all wrinkled surfaces having the same enhancements to total exposed surface per geometrical area compared to control planar anodes, power density strongly depended on wrinkled surface morphology. Tall, widely spaced structures generated nearly twice the power output compared to planar anodes. However, no performance improvements were observed for wrinkled surfaces with small closely spaced structures. These results were likely due to improved bacterial packing efficiencies at the gold surface for widely spaced, or "open," wrinkle morphologies. We propose that these findings can guide the optimization of MFCs and other bioelectrochemical systems using direct electron transfer EABs by focusing on their physical access to the anode surface, in addition to increased electroactive surface area relative to the electrode geometrical footprint.

3.4. Results and Discussion

3.4.1 Fabrication and evaluation of anode surface

The structured anodes were fabricated using a benchtop method, in which gold electrodes were patterned through a self-adhesive stencil followed by shrinking of the prestressed polystyrene substrate (Figure 3.1). Prestressed polystyrene disks and the stencils were patterned using xurography. The stencils were adhered to the prestressed polystyrene (PS) substrate and used to define the electrode shapes during the gold film sputtering. Individual square masks were used to selectively shield some of the sensing pads during the successive gold deposition cycles. This allowed us to produce sensing pads with final thicknesses of 50, 100, 200, and 400 nm (Figure 3.1, shades of orange) on a single chip. Then, the stencil was peeled from the substrate, revealing 4 sets of 4 patterned electrodes with the targeted film thicknesses. The substrates were subsequently heated at 165 °C, which caused the polystyrene substrate to shrink and introduced the compressive stress that resulted in wrinkling of the gold film. The different electrode film thicknesses were used to tune the wrinkled electrode topography from the nanometer to the micrometer range. Using these simple and inexpensive methods, devices were fabricated containing sets of sensing electrode

pads with identical surface (≈0.8 cm^2, corresponding to the flat gold film) and geometrical area (≈0.13 cm^2 after shrinking), but different surface topographies that could be assayed in a single parallel experiment.

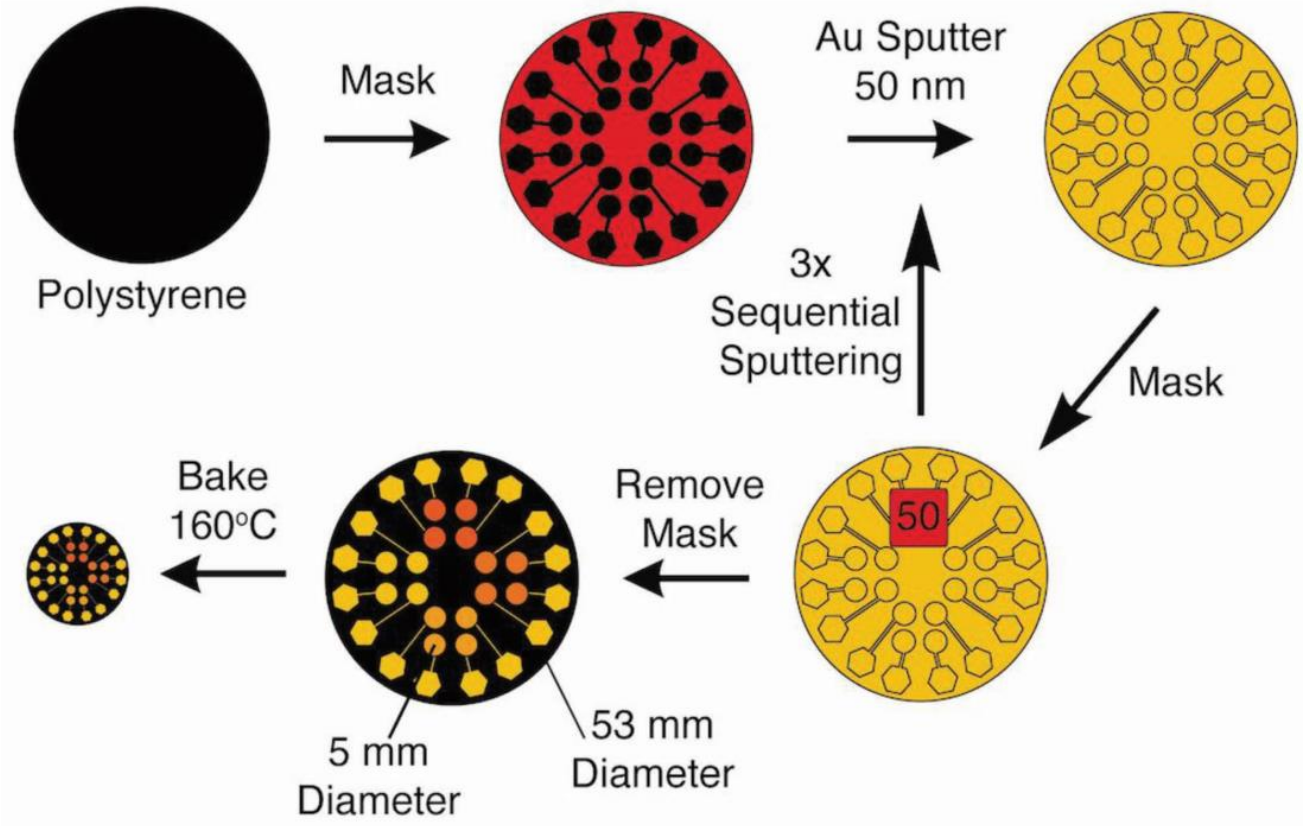

Figure 3.1: Schematic of fabrication process for generating 2 mm diameter wrinkled electrodes. Prestressed polystyrene disks (black) were cut from commercially available sheets. An adhesive vinyl stencil mask (red) was designed, patterned, and adhered to the polystyrene substrates. The sensing electrode pads were masked during the sequential sputtering of gold films, which resulted in sensing electrodes with thicknesses of 50, 100, 200, and 400 nm (shades of orange). The adhesive vinyl mask was removed and the substrates were shrunk at 165 °C. The final area of the substrate was 16% of the original area, and the final diameter of each sensing electrode pad was 2.0 mm (60% reduction in x and y dimensions).

The surface topography of the shrunken Au films was quantified by optical profilometry (for surface roughness) and scanning electron microscopy (SEM) (for wrinkle spacing). First, it was noted that the polystyrene before and after shrinking (Figure 3.2 A) and the unshrunken gold films (Figure 3.2. B) showed smooth surfaces. By contrast, wrinkles formed upon shrinking polystyrene substrates with Au films. Wrinkle dimensions of interest included the root mean square (RMS) roughness (calculated as the root mean square of the peak and valley amplitudes, *A*, of the structured surfaces), and wrinkle spacing (approximated by the persistence length *L*), and their relation to Au film thickness (*t*). The relevant dimensions are shown schematically (Figure **2**C), and by SEM imaging of a cross-section of a wrinkled surface after focused ion beam milling (FIB) milling (Figure 3.2. D). Qualitative analysis of the electron micrographs showed a progression of wrinkle spacing from sub-micrometer for 50 nm thick Au films, to tens of micrometers for 400 nm thick films (Figure 3.2. E–H), with a concomitant increase in wrinkle amplitude. Our observations are consistent with reported trends, [31] and demonstrate that the structured surfaces are a direct result of the compressive stress generated by the polystyrene during shrinking, where the elastic modulus mismatch between the substrate and the gold film causes the latter to buckle and wrinkle.

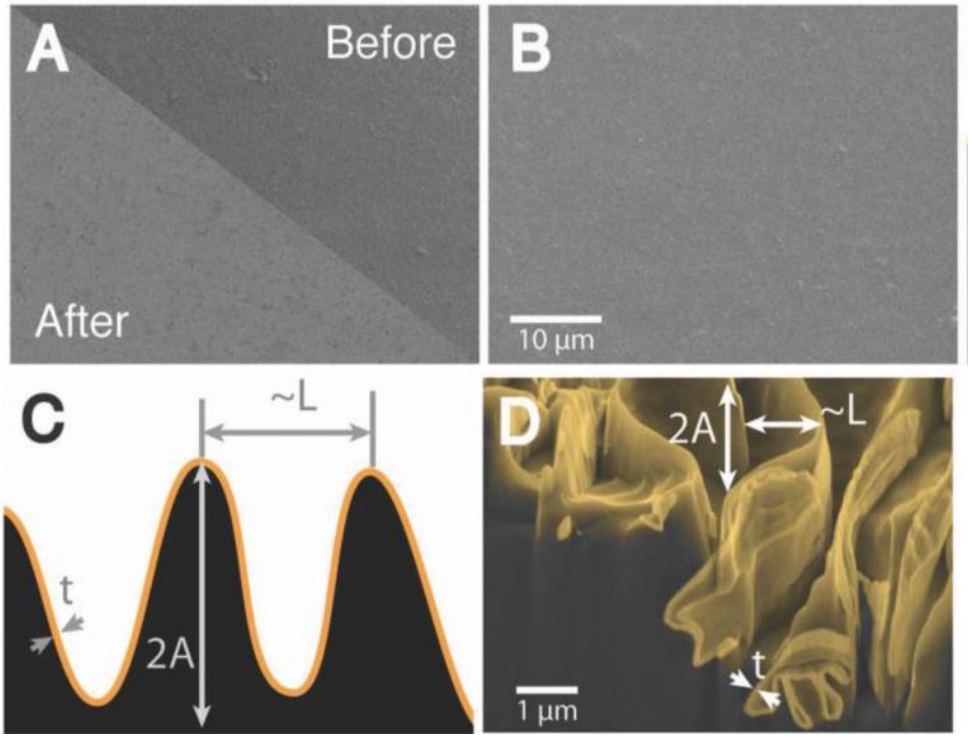

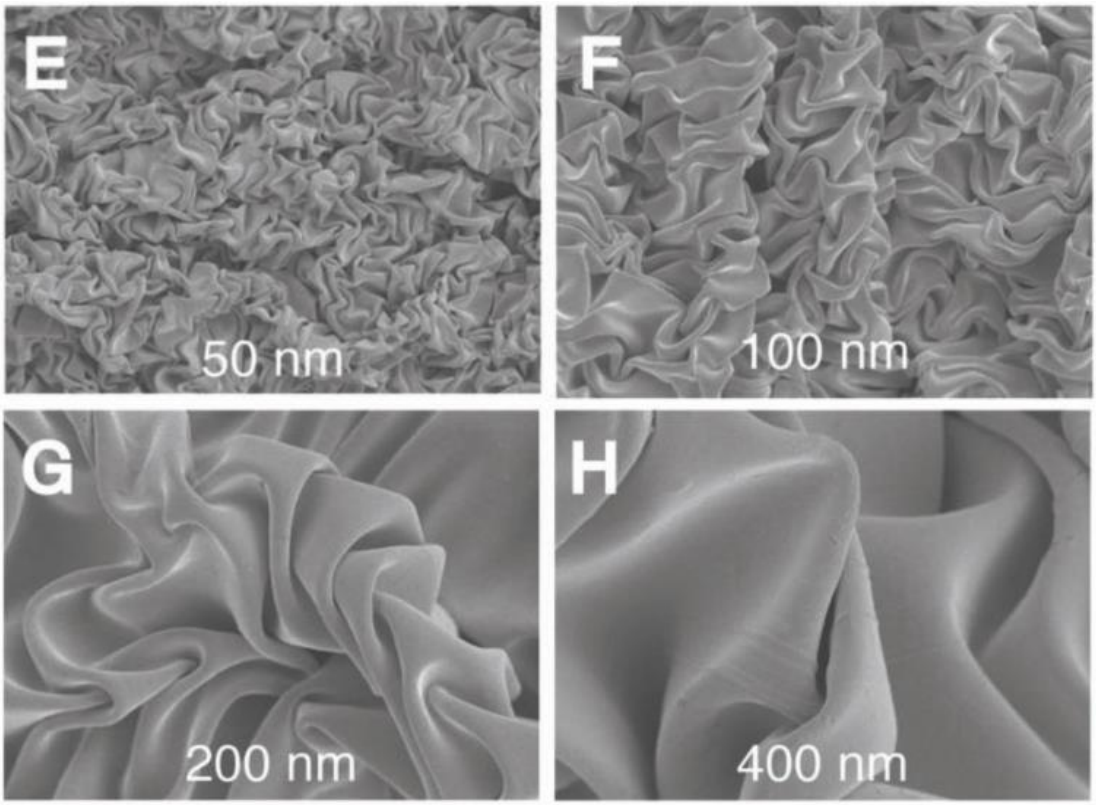

Figure 3.2: Characterization of structured Au electrodes through electron microscopy. SEM images of A) polystyrene before and after shrinking, B) flat Au sputtered on polystyrene. C) Cross-section schematic of the electrode surface after structuring, showing the PS substrate (black) coated by a gold film (yellow) with thickness *t*. The wrinkles are characterized by an amplitude *A* and a periodicity that is approximated by the persistence length *L*. D) SEM image of the cross-section of a 50 nm thick structured film, after focused ion beam milling. Representative amplitude, periodicity and thickness of the wrinkled film are highlighted in the image. The image has been false colored to aid in the identification of the gold film (yellow) and the polymer substrate (gray). Top-down SEM images for wrinkled Au electrode surfaces for film thicknesses of E) 50, F) 100, G) 200, and H) 400 nm. Images (A), (B), and (E)–(H) are all presented at the same scale.

Topographical maps obtained using optical profilometry allowed us to quantify the RMS roughness as a representative measurement of the surface topography. Figure 3.3 A compares the measured RMS roughness for films before (cyan) and after (red) shrinking for the different thicknesses tested. While the RMS roughness for all gold film thicknesses tested was similar (≈15 nm) before shrinking, after shrinking the amplitude and roughness of the films increased with increasing film thickness. In addition, from a 2D fast Fourier transform analysis of the SEM surfaces, the persistence length ($\sim L$) was calculated.[32] Figure 3.3 B shows that the persistence length varied linearly with initial Au film thickness. The RMS roughness and persistence length are relevant parameters for the growth of EABs since the

topographical features can directly impact the bacteria's ability to access the anode surface, especially in the valleys formed between wrinkles, which could affect the efficiency with which charge transferred to the electrode.

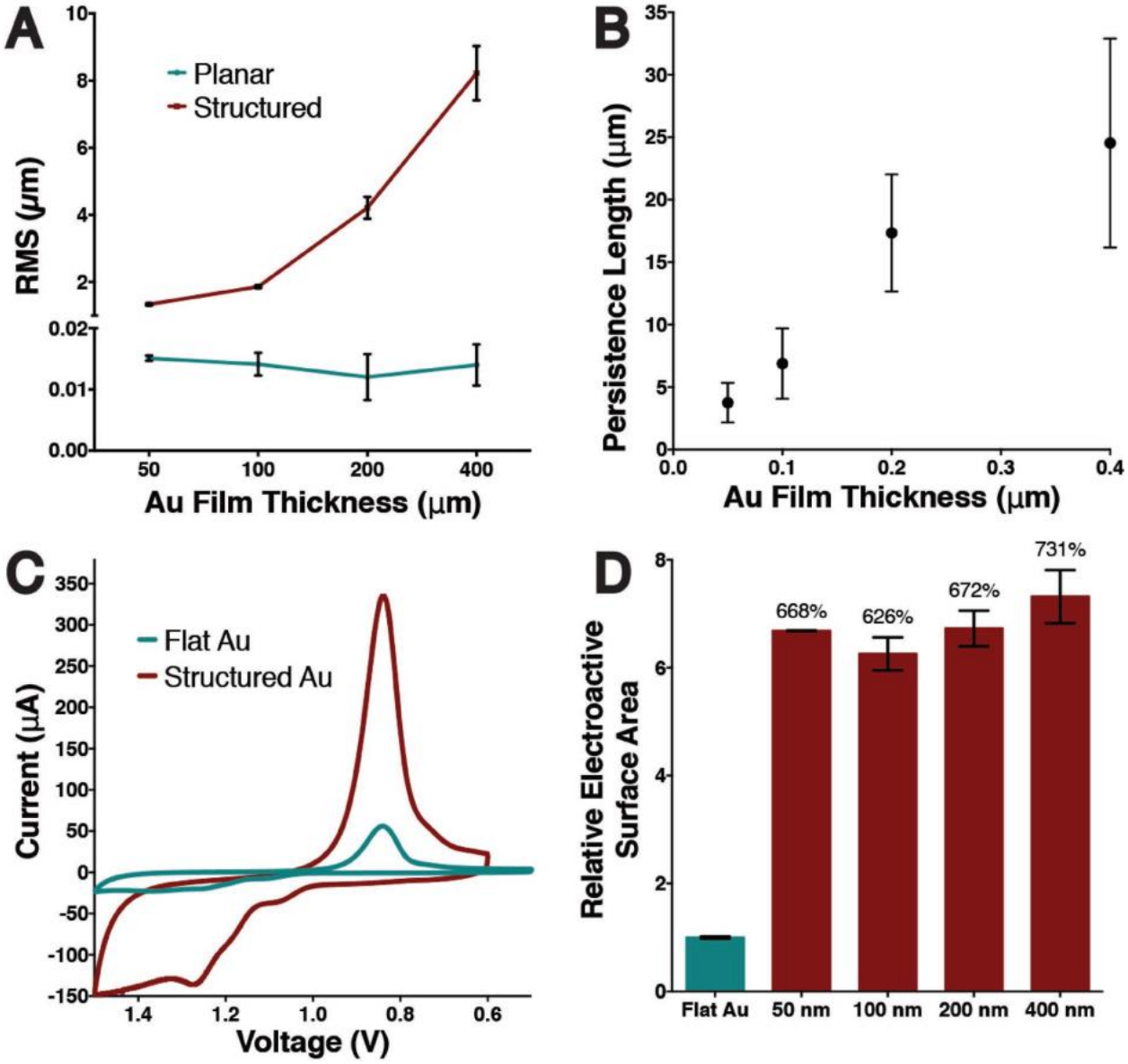

Figure 3.3: Topographical and electrochemical characterization of the structured electrodes. A) RMS surface roughness measurements obtained by optical profilometry for Au films of different thicknesses before (cyan) and after (red) wrinkling. B) Persistence length for the wrinkled surfaces as a function of gold film thickness. C) Typical cyclic voltammogram obtained in a 100 × 10^{-3} m H_2SO_4 redox solution using a gold working electrode with a 2 mm diameter footprint before (cyan) and after (red) wrinkling, show the enhanced charge transfer due to the increased surface area. D) The relative electroactive surface area (normalized to that of a flat electrode with a 2 mm diameter footprint) for planar (cyan) and wrinkled (red) electrodes. All error bars represent the standard deviation of measurements made on *n*'> 3 replicate electrodes.

Finally, the electroactive surface area of the structured electrodes was assessed through cyclic voltammetry. Figure 3.3 C shows a side-by-side comparison of the voltammograms produced by flat and structured electrodes with a 2 mm diameter footprint. As anticipated, the structured electrode presented a higher charge transfer profile than the flat electrode. Integration of the area under the cathodic peak of the voltammogram yielded the total charge transferred during the voltage sweep, which could be used to calculate the electroactive surface area (cf. Experimental Section). A comparison of the electroactive surface area (Figure 3.3. D) showed that, within measurement error, all the structured electrodes, regardless of topographical feature dimensions, exhibited a similar increase to electroactive surface area (>600%) compared to a flat electrode with a similar geometrical footprint. Thus, by using this benchtop fabrication method, we could tune the anode surface topography without changing overall footprint or introducing changes to the electroactive surface area or material homogeneity. In this way, efficiencies in the total current collected from an EAB could be studied as a function of topography without incurring common side-effects of other additive fabrication techniques that could obscure these effects.

3.4.2. Measurements in microbial fuel cells

Next, we examined the performance of wrinkled gold electrodes as anodes for MFC applications using the setup shown in Figure 3.4. A. We conducted parallel experiments using five separate glass MFCs, which were all inoculated simultaneously with *G. sulfurreducens* bacteria from the same preculture. Each parallel experiment was repeated three times. In four of the MFCs, the anode consisted of a 2 × 2 wrinkled anode array based on an initial Au layer thicknesses: 50, 100, 200, and 400 nm. The last MFC contained the planar Au anode array as a control. In all cases, a graphite cathode measuring 25 × 25 × 3 mm was immersed in a phosphate buffer saline (PBS) solution containing potassium ferricyanide (30×10^{-3} m).

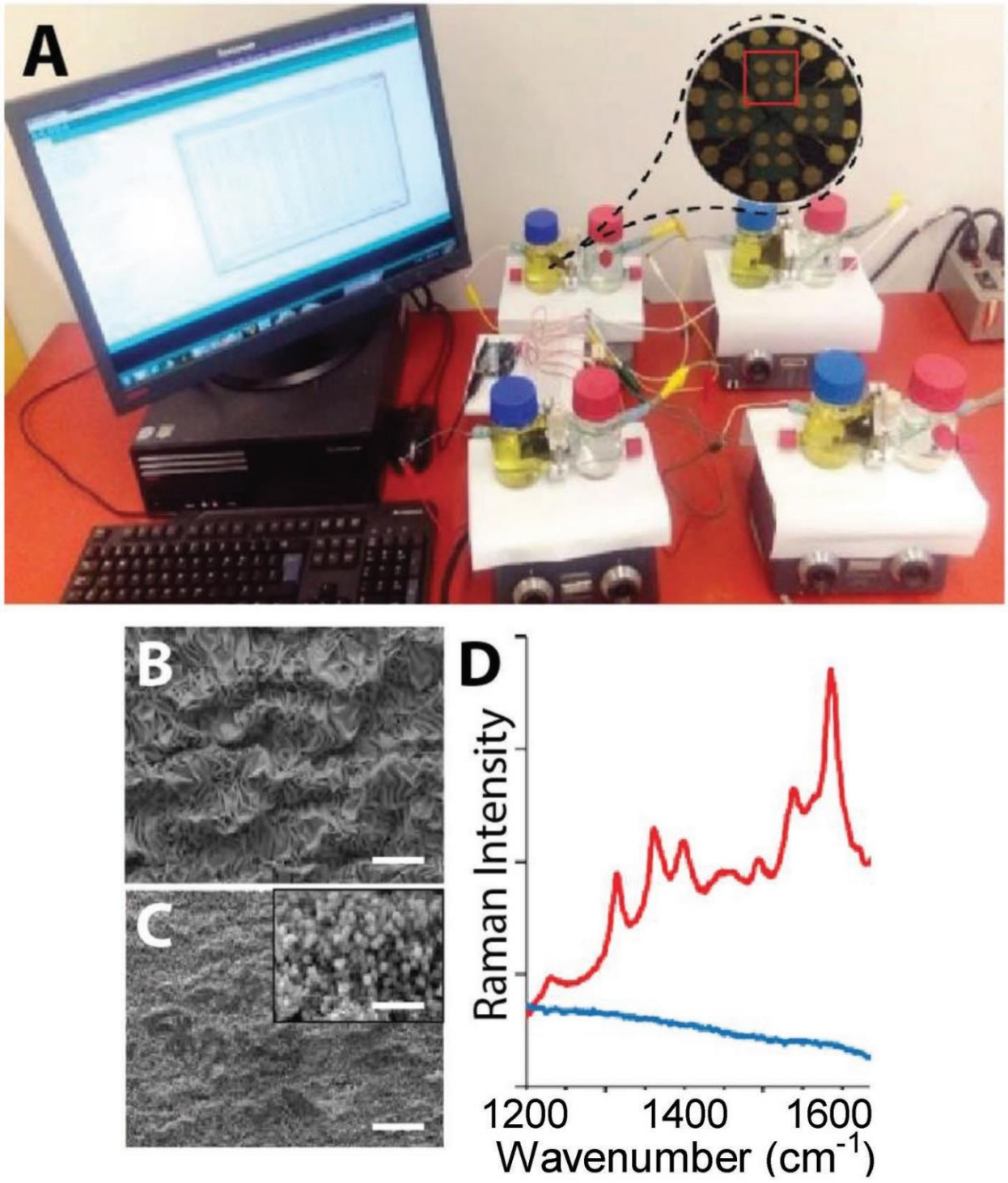

Figure 3.4: A) A picture of 4 two-chamber microbial fuel cells with catholyte (yellow) and anolyte (colourless) reservoirs on stir plates. The fifth control MFC is not shown. Inset shows an active 2 × 2 anode array (highlighted). Not shown in the inset are the protected connections made to each active anode array. All MFCs were connected to a breadboard across R_{ext}. A microcontroller measured V across R_{ext} and stored data on a computer. SEM images of B) a clean wrinkled anode before cathode connection through R_{ext} and C) a biofilm

covered anode after cathode connection through R_{ext}. The inset shows magnified region in (ii) showing individual bacteria and EPS. Scale bars are 100 μm (i and ii) and 15 μm (inset). D) Spectra from resonance Raman spectroscopy of wrinkled anodes formed from Au layers of 400 nm thickness, before (blue) and after experiment was complete (red).

First, we confirmed EAB growth on wrinkled and planar Au anodes by SEM and resonance Raman spectroscopy. Results presented in Figure 3.4 were obtained from 400 nm thick wrinkled gold anodes, but similar results were observed for all thicknesses. Wrinkled and planar Au surfaces were immersed in the anolyte, but not electrically connected to the external circuit. After careful analysis of the SEM images similar to Figure 3.4. B, we observed no evidence of bacterial attachment or biofilm production. This was because electrically isolated wrinkled Au surfaces could not serve as electron sinks, thereby preventing electrode respiration of the EAB. After use as electrically connected anodes, SEM images similar to Figure 3.4. C revealed that dense biofilm layers blanketed the anodes, hiding the wrinkled surface, and demonstrating good biocompatibility and biofilm growth. We also verified the growth of *G. sulfurreducens* biofilms via resonance Raman spectroscopy which produced cytochrome fingerprints at 1316, 1367, 1589, and 1640 cm^{-1} (Figure 3. 4. D).[33] In comparison, a broad featureless background was observed before Au surfaces were connected as MFC anodes through an external resistor even if they had been previously immersed in the anolyte.

To compare the effect of anode topography on MFC start-up, we monitored voltage outputs in time during the initial growth phase. Starting immediately after inoculation, the voltages were measured across R_{ext} at 10 min intervals for all MFCs and current was calculated via directly from Ohm's law. For all MFCs, voltage (and current) increased rapidly during the first 35 h. Figure 3.5 shows average growth curves from three replicate MFC start cycles for control and all wrinkled anode arrays used here. Lower lag time, slightly higher average currents and voltages (V_{ave}) were observed for wrinkled anodes compared to the control surfaces. However, based on their standard deviations (V_{STD}), they were not statistically different. Therefore, we concluded that the degree of anode wrinkling did not have a significant effect on the rate of bacterial colonization and initial growth. After 35 h, MFC voltage outputs began to plateau for all experiments in the range of 0.3–0.6 V. Based on the

calculated coefficient of variance (CV) for voltage (CV = V_{STD}/V_{Ave}) for all like anodes, MFC outputs with like anodes also began to stabilize as the biofilm entered maturity.

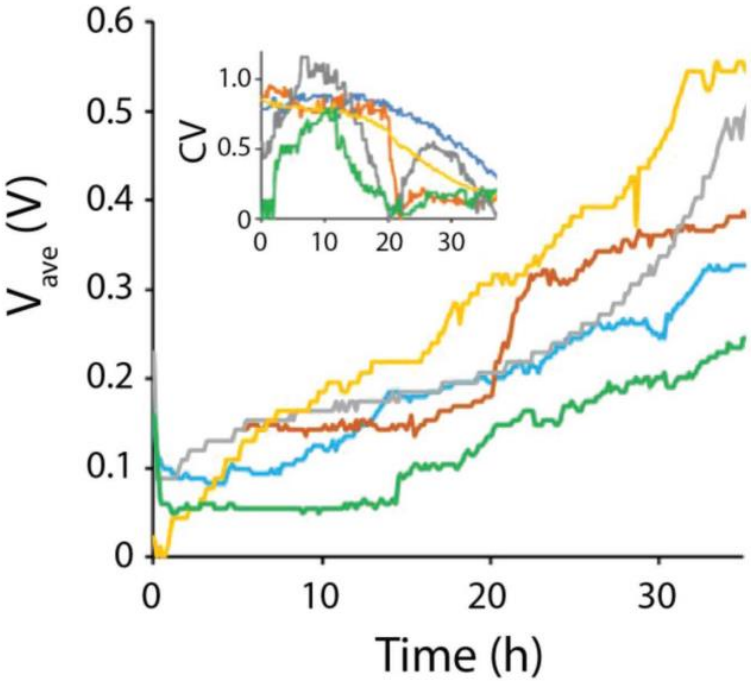

Figure 3.5: The average voltage and current versus time during start up for anodes used in this study. All measurements were conducted across a 100 kΩ external resistor. Current and voltage resolution were 100 nA and 10 mV, respectively. Inset shows the coefficient of variance (CV) based on average voltage (V_{ave}) and their standard deviations (V_{STD}). In all cases color coding follows: 50 nm (blue), 100 nm (orange), 200 nm (gray), 400 nm (yellow), and planar (control) anodes (green).

Power density curves were acquired from polarization measurements after ≈3 d, when MFCs had reached stable operating conditions. Stability was determined by CV < 0.2 in V_{ave}. Following other published approaches to observe the impact of electrode structuration on MFC power outputs, we obtained power density measurements during operation.[21, 34,35,36] As an example, three data sets showing power density and polarization curves are given in Figure 3.6. A for MFCs containing wrinkled anodes made from 400 and 50 nm Au layers and from planar control anodes (with resulting RMS roughness and persistence lengths given in Figure 3.3). It can be seen that both P_{max} and the maximum current density were largest for wrinkled anodes made from 400 nm Au layers (>400 mW m^{-2} and 1 A m^{-2}, respectively).

On the other hand, these values were both smaller and statistically equal for the control and the 50 nm wrinkled anodes.

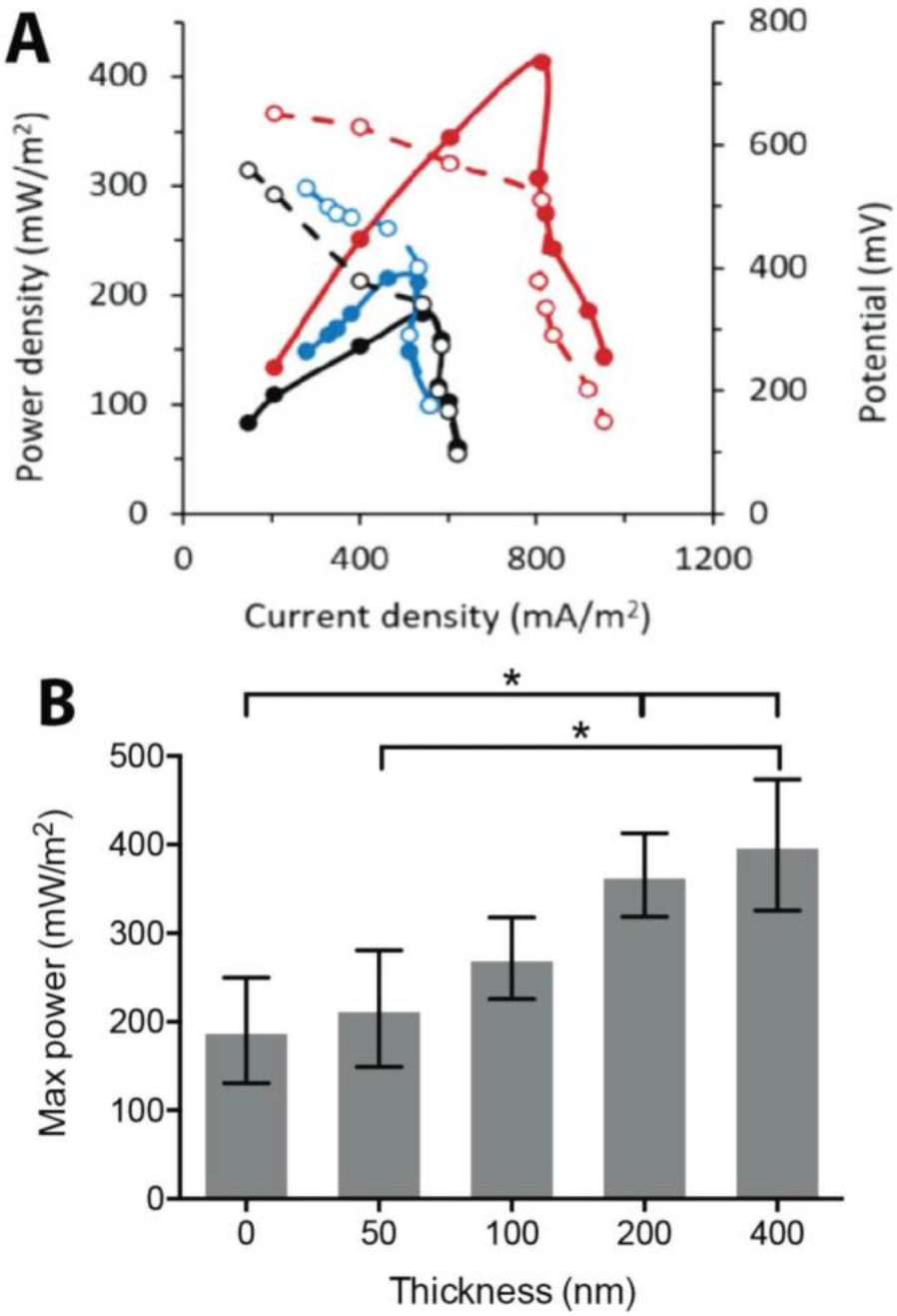

Figure 3.6: A) Example of individual polarization (dashed) and power density (solid) curves acquired from separate samples grown on control (black), 200 (blue), and 400 (red) nm wrinkled electrodes. B) Average of maximum power density as read from at least three separate power density curves for each electrode type. All power density curves were obtained from separate samples after 60 h of growth. The voltage *V*, the current *I*, and the power $P = VI$ are obtained by varying the resistance *R*.

Figure 3.6. B shows the average P_{max} from three independent measurements for each anode type. It was seen that P_{max} increased for wrinkled anodes made from thicker Au layers. The wrinkled surfaces formed from 400 nm thick Au films had values of P_{max} more than twice as large compared to unstructured gold anodes. A pairwise one-way ANOVA comparison showed statistical differences (95% confidence) between unstructured from 200 and 400 nm thick Au films. A significant difference of P_{max} between wrinkled anodes made from 400 and 50 nm thick Au films was also observed. This was somewhat surprising since the total electroactive surface area was the same for both wrinkled anodes. Moreover, there were no significant differences in P_{max} between the wrinkled anodes made from 50 nm thick Au films and the flat controls. Clearly, the enhanced anode electroactive surface area, which was ≈6 times larger than control for all wrinkled surfaces, did not benefit power outputs to the same degree.

In evaluating the origin of microstructure-based enhancements to P_{max}, we assumed that the thickness of the Au layers were not specifically responsible. Therefore, the key to exploiting enhanced electroactive surface area for microstructured anodes for direct electron transfer EABs should be related to their morphology. Since the Au layer thickness had a deterministic effect on both the RMS roughness (feature height) and persistence length (interstitial distance between features), as seen in Figure 3.3. A, D, the changes in performance were assumed to be related to these parameters. Figure 3.7 shows nearly to scale renderings vis-à-vis bacteria size and the wrinkle dimensions. As the persistence length was reduced for thinner Au layers, randomly oriented bacteria could jam between the folds. This resulted in inaccessible domains within the valley portions, thereby reducing direct bacterial access to portions of the anode surface. A dashed line highlights the biointerface boundary where bacteria at the lowest biofilm layer could directly touch some portion of the anode surface. It shows the development of a progressive mismatch between the biointerface and the anode surface as persistence length was decreased. For wrinkled surfaces formed from 50 nm thick Au films, the biointerface became nearly flat, which would explain the similar P_{max} compared to the control anodes. On the other hand, biointerfaces nearly conformed to the entirety of the wrinkled surface area for those anodes formed from 200 and 400 nm thick Au films. In practical terms, a larger biointerface area means more bacteria in contact with the anode. Considering bacteria as parallel resistors, this can be understood to decrease charge transfer

resistance.[37383940] In this context, it can be seen that maximizing microfeature density as a route to increasing electroactive surface area, may actually reduce MFC performance due to reductions in interfeature spacing.

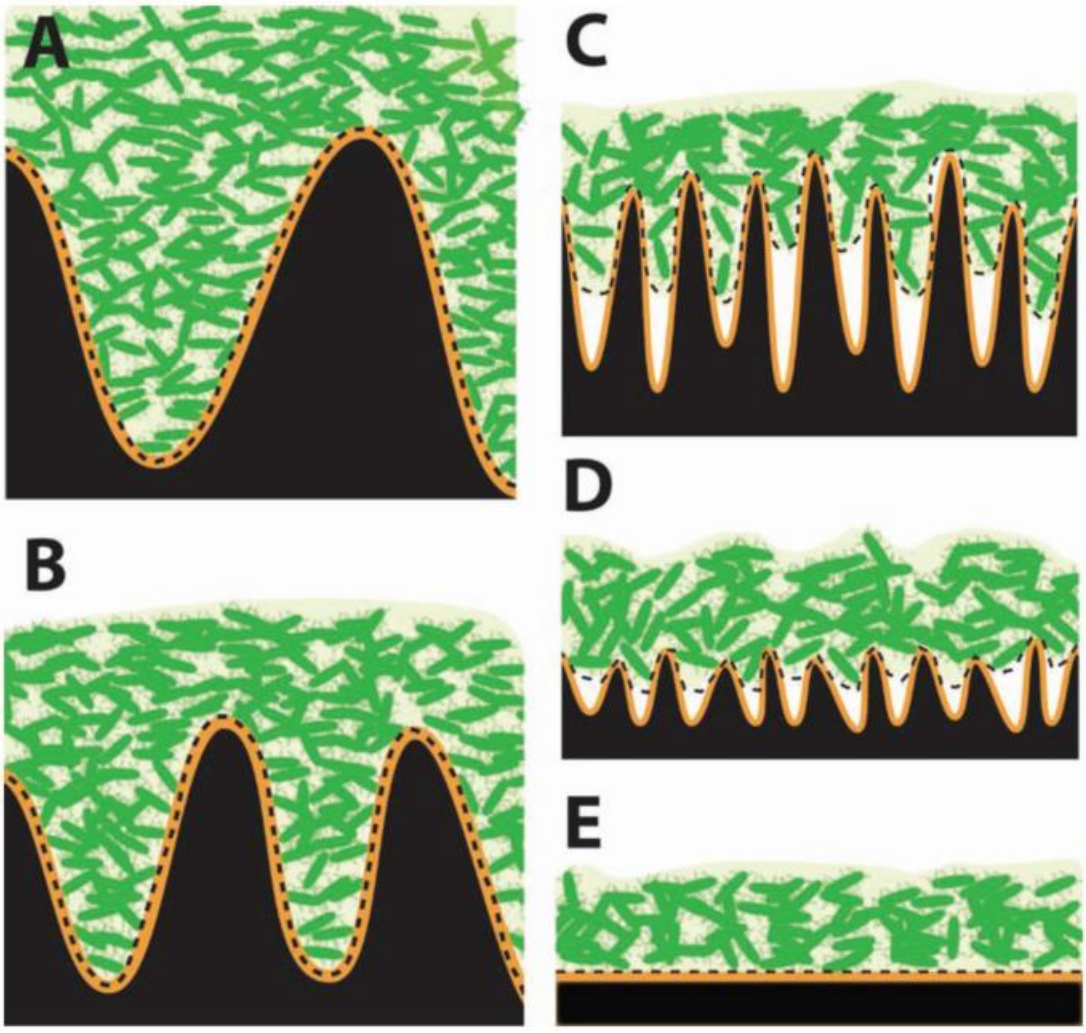

Figure 3.7: Conceptual model of the *G. sulfurreducens* biofilm (green) at a wrinkled anode surfaces (gold) used in this study. The anode surfaces were generated by Au films of A) 400, B) 200, C) 100, D) 50 nm thickness, and E) unshrunken films. Upper bacterial layers are not shown.

To our knowledge, this is the first literature example of wrinkled Au surfaces fabricated from films with thicknesses >200 nm. However, future experiments may be designed to further extend the thickness of the initial Au layers. This could result in differential effects in terms of persistence length and height because, increases to the former should not result in further improvements to bacterial surface density after complete surface coverage is achieved. Thus,

changes to performance beyond this point could be to be correlated to height only. In addition, follow up work can investigate the long-term behavior of the wrinkled bioanodes in terms of their voltage and power generation.[41 42]

3.5. Conclusions

Wrinkled gold films were used for the first time as structured anodes for microbial fuel cells. The approach of structuring gold films by the thermal shrinking of a prestressed polymer support substrate produced structures with tunable wrinkle height and spacing in range of the <1–8 µm, and 4–25 µm, respectively. Because the exposed surface area and material homogeneity were maintained between the samples, the effect of surface topography on MFC power could be investigated without interference from competing effects introduced by additive anode fabrication techniques. It was determined that the anodes with tall, well-spaced features performed best. It is proposed that large interfold spacing resulted in better bacterial packing efficiencies at the biointerface, resulting in enhanced current collection efficiencies. This work opens the way for future experiments that focus on the effect of anode structure dimensionality, rather than on total electroactive surface area. The approach can be beneficial for applications involving any direct electron transfer systems, including, but not limited to microbial fuel cells.

3.6. Experimental section

Structured anode fabrication: PS sheets (Graphix Shrink Film, Graphix, Maple Heights, OH, USA) were cleaned in successive baths of isopropyl alcohol, ethanol, and water, and cut into 53 mm diameter disks using a computer-driven blade cutter (Robo Pro CE5000-40-CRP, Graphtec America Inc., Irvine, CA, USA). Self-adhesive vinyl sheets (FDC-4300, FDC graphic films, South Bend, IN, USA) were patterned using the blade cutter into stencils describing the shape of the electrodes and adhered to the polystyrene substrates. Gold was then deposited from a 99.999% purity gold target (LTS Chemical Inc., Chestnut Ridge, NY, USA) using a Torr Compact Research Coater CRC-600 manual planar magnetron sputtering system (New Windsor, NY, USA) onto the masked polystyrene surface. Successive sputtering depositions were performed, with certain electrodes being masked with adhesive

vinyl to produce sensing pads consisting of gold films of 50, 100, 200, and 400 nm thickness. After removing the vinyl masks, the polystyrene films containing the patterned gold electrodes were shrunk at 165 °C in a temperature controlled vacuum oven (Isotemp, Fisher Scientific, Ottawa, ON, Canada), on aluminum weighing dishes lined with parchment paper. The final diameter of the individual electrodes after shrinking was ≈2 mm.

MFC construction and operation: Dual-chamber glass MFCs with 150 mL capacity were used in this study (MFC 100.25.2, Adams & Chittenden Scientific Glass, NY, USA). Each chamber was joined by a 31 mm diameter glass bridge using a clamp. A cation exchange membrane (CEM) (CMI-7000S, Membrane International Inc., NJ, USA) was immobilized between the two glass bridges. The CEM was pretreated by successive exposure to deionized (DI) water with 5 wt% NaCl (Caledon Lab Ltd., ON, Canada) for 12–18 h, followed by thorough washing with DI water. Each compartment had two feedthrough ports, one with a large (22 mm) diameter, for inserting the electrode, and a second with a small (8 mm) diameter used as a feedthrough for electrical connections. The cathode was made from standard graphite plate electrode (GraphiteStore, Northbrook, IL, USA) with a size of 25 × 25 × 3 mm. Cathode electrodes were polished and reused in the same MFCs for all experiments. Electrical connections to both electrodes were protected with epoxy. Electrodes were placed at a distance 5 mm from each side of the CEM to minimize variations in internal resistance for all MFCs. Ports were sealed with supplied gas-tight cap, except for the wire feedthrough port which was sealed with epoxy.

Bacterial Culture and Nutrients: G. sulfurreducens (wild type, strain PCA, ATCC 51573), aliquots were stored in a −80 °C biological freezer (Thermo Scientific Revco EXF, Burlington, ON, Canada). All preparatory steps were conducted in an oxygen-free environment in a glovebox (10% H_2, 10% CO_2, and 80% N_2). *G. sulfurreducens* was subcultured in nutrient medium supplemented with 40×10^{-3} m sodium fumarate ($Na_2C_4H_2O_4$) as a soluble electron acceptor to support bacterial growth in solution. The nutrient medium consisted of sodium acetate carbon source (CH_3COONa, 10×10^{-3} m), NaH_2PHO_4 (3.8×10^{-3} m), $NaHCO_3$ (30×10^{-3} m), KCl (1.3×10^{-3} m), NH4Cl (28×10^{-3} m) (all from Sigma-Aldrich, Oakville, ON, Canada), a trace mineral supplement (ATCC MD-TMS, 10 mL L^{-1}), and a vitamin supplement (ATCC MD-VS, 10 mL L^{-1}). The medium was

sterilized before use by autoclaving at 110 °C at 20 psi for 20 min. Sodium fumarate was added through a sterilized filter in the glovebox.

MFC preparation: inoculation and start-up: The MFC anode chamber was inoculated with 125 mL of liquid, consisting of 4 mL of *G. sulfurreducens* subculture and the rest being nutrient medium. No fumarate was added to the anolyte solution in order to support growth at the anode only. The catholyte and anolyte solutions, and their ionic strength, were matched to those previously reported.[9] Briefly, the cathode compartment was filled with 125 mL of a PBS (10×10^{-3} m, pH = 7.4); containing 30×10^{-3} m ferricyanide (as an electron acceptor). All operations were conducted inside an anaerobic glovebox. Next, the MFC liquid ports were sealed and the anode and cathode were connected through a resistor, R_{ext}'= 100 kΩ. This was chosen based on measurements of average internal resistances from previous experiments using the same setup and from literature reports with MFCs featuring small gold anodes.[43] All reactors were operated at 24 ± 0.5 °C with gentle stirring in an oxygen-free environment.

Characterization: optical profilometry: Optical profilometry measurements were made using a Zygo NewView 5000 white light interferometer (Zygo Corporation, Middlefield, CT, USA). Data were obtained for the gold films on PS substrates, before and after shrinking. Five different areas on each substrate were imaged onto a charge coupled device camera using a 50× objective with 2× additional optical zoom, resulting in fields of view of 70 × 50 μm, and a pixel size of 112 nm. The topographical maps obtained through optical profilometry were used to calculate the RMS roughness of each of the surveyed areas, from which an average RMS roughness was calculated. For all images, a fast Fourier transform (FFT) bandpass filter was applied to remove noise with cut-off frequencies of 183.35 and 558.79 mm^{-1}. Image analysis was conducted by MetroPro software (Zygo Corporation).

Scanning electron microscopy: SEM images of the gold electrodes were acquired with a JSM-7000S system (JEOL USA Inc., Peabody, MA, USA) operating with an accelerating voltage of 2.5 kV, working distance of 6 mm, and low probe current of 30 μA. The SEM images of gold electrodes were obtained before introduction to MFC anode compartment as well as after exposure to anode compartment for both electrically connected and unconnected gold surfaces. For SEM imaging of wrinkled gold surfaces after exposure to anode chamber,

the anodes were exposed to a fixation solution overnight (2.5% glutaraldehyde in PBS buffer). The anode was then transferred to a solution with 1% osmium tetroxide for 1.5 h and rinsed in phosphate buffer. Samples were then dehydrated in 50%, 75%, 95%, and 100% aqueous ethanol solutions for 15 min each, followed by room temperature drying overnight. Before taking images, a thin gold layer was sputtered onto the biofilms and electrodes (Nanotech Ltd., SEMPREP 2 Sputter Coater, Sandy, UK).

Focused ion beam milling: FIB milling was used to obtain a cross-sectional view of the structured surfaces. A Helios NanoLab 600i DualBeam microscope (FEI, Hillsboro, OR, USA) combining an electronic column (SEM) and an ionic column (FIB) was used to etch the sample using Ga ions. Initial large-scale milling was done at 30 kV/21 nA, to create an opening in the bulk of the material, and a fine-scale finishing milling was done at 30 kV/2.5 nA, to clean the cross-section for imaging with SEM.

Persistence length calculation: The persistence length, defined as the distance over which a wrinkle maintained its original orientation, is a good approximation of the distance between wrinkle features. Persistence lengths corresponding to the different film thicknesses were calculated from the 2D FFT power spectra of the corresponding SEM images as previously described.[32] Briefly, SEM images were cropped into 900 × 900 pixel images and analyzed individually. Each image was adjusted for its brightness and contrast, after which the Canny threshold method in MATLAB was used to determine the edges of the wrinkled structures, which were rendered as a binary image. A MATLAB program was used to run a 2D FFT of the binary image, from which the power spectrum and probability versus length scale (μm) plots were generated. The probability values were normalized to the maximum probability, averaged for all SEM images, and analyzed for each data point. A probability versus log (length scale) plot was used to identify the values corresponding to the highest probability, which were used to determine the persistence length of the structured films.

Cyclic voltammetry: Cyclic voltammetry was performed using an electrochemical workstation (CHI 660D, CH Instruments, Austin, TX, USA) and a standard three-electrode set-up. The electrochemical cell included a Ag/AgCl reference electrode, a Pt auxiliary electrode, and sputtered gold films on polystyrene as working electrodes. To ensure that the planar geometric surface area of the working electrode was consistent between samples

before and after shrinking, an adhesive vinyl mask was placed over the gold electrode with a 2 mm diameter circle cutout to expose the active surface of the electrode. To determine the total electroactive surface area of the samples, 10 voltammograms were acquired in a 100 × 10^{-3} m H_2SO_4 solution at a scan rate of 0.1 V s^{-1} and a voltage sweep range of 0.5–1.5 V. The cathodic peaks from the resulting voltammograms were integrated using OriginPro software to determine the total charge transferred. The electroactive surface area was then calculated by dividing the total charge by the surface charge density of a monolayer of gold (386 μC cm^{-2}).

Electroactive biofilm analyses and calculations: Parallel electrical measurements of the voltage drop across an external resistor (R_{ext}) were conducted for all five MFCs using a microcontroller board (Arduino UNO, Digikey Electronics, Thief River Falls, MN). Measurements were acquired at intervals of 10 min and the time-varying current was calculated using Ohm's law $I' = V/R_{ext}$, where V was the time-varying voltage drop across R_{ext}. Polarization curves were obtained with a commercial potentiostat (VersaSTAT 4, Princeton Applied Research, Oak Ridge, TN) with automatic changes to R_{ext} in the range of 25 to 250 kΩ after a settling time of 10 min. The power (P) of the MFCs was calculated using $P' = V^2/R_{ext}$ and power density curves were generated showing P versus I for different values of R_{ext}.

Resonance Raman Spectroscopy: Analysis by resonance Raman spectroscopy was used to verify the existence of c-type cytochromes within *G. sulfurreducens* biofilms on gold after the experiments. Preparation included removal from the MFC anode chamber, washing with acetate-free medium and exposure to filtered air from a laminar flow hood for drying. Raman spectra were recorded (LABRAM 800HR, Horiba JobinYvon, Villeneuve d'Ascq, France) with a 100×/0.75NA long working distance objective in backscattering mode with excitation provided by an argon-ion laser at 514 nm. At this wavelength, resonant excitation of the cytochrome Q-band (oriented in plane of the porphyrin ring) could be acquired.[44] The acquisition time was 30 s for all samples.

3.8. Bibliography

[1] Liu, H.; Ramnarayanan, R.; Logan, B. E., Production of electricity during wastewater treatment using a single chamber microbial fuel cell. *Environmental science & technology* **2004,** *38* (7), 2281-2285.

[2] Logan, B. E., Microbial fuel cells, a John Wiley & Sons. *Inc., New Jersey* **2007**.

[3] Yang, X.-Y.; Tian, G.; Jiang, N.; Su, B.-L., Immobilization technology: a sustainable solution for biofuel cell design. *Energy & Environmental Science* **2012,** *5* (2), 5540-5563.

[4] Logan, B., Microbial fuels for the future. *Nature* **2008,** *454* (7207), 943.

[5] Lovley, D. R., Bug juice: harvesting electricity with microorganisms. *Nature Reviews Microbiology* **2006,** *4* (7), 497.

[6] Zhang, X., *International trade regulation in China: law and policy*. Bloomsbury Publishing: 2006.

[7] Mardanpour, M. M.; Yaghmaei, S., Characterization of a microfluidic microbial fuel cell as a power generator based on a nickel electrode. *Biosensors and Bioelectronics* **2016,** *79*, 327-333.

[8] Hernandez, M.; Newman, D., Extracellular electron transfer. *Cellular and Molecular Life Sciences CMLS* **2001,** *58* (11), 1562-1571.

[9] Nevin, K. P.; Richter, H.; Covalla, S.; Johnson, J.; Woodard, T.; Orloff, A.; Jia, H.; Zhang, M.; Lovley, D., Power output and columbic efficiencies from biofilms of Geobacter sulfurreducens comparable to mixed community microbial fuel cells. *Environmental microbiology* **2008,** *10* (10), 2505-2514.

[10] Kim, H. J.; Park, H. S.; Hyun, M. S.; Chang, I. S.; Kim, M.; Kim, B. H., A mediator-less microbial fuel cell using a metal reducing bacterium, Shewanella putrefaciens. *Enzyme and Microbial technology* **2002,** *30* (2), 145-152.

[11] Kang, C. S.; Eaktasang, N.; Kwon, D.-Y.; Kim, H. S., Enhanced current production by Desulfovibrio desulfuricans biofilm in a mediator-less microbial fuel cell. *Bioresource technology* **2014,** *165*, 27-30.

[12] Inglesby, A. E.; Beatty, D. A.; Fisher, A. C., Rhodopseudomonas palustris purple bacteria fed Arthrospira maxima cyanobacteria: demonstration of application in microbial fuel cells. *Rsc Advances* **2012,** *2* (11), 4829-4838.

[13] Lovley, D. R., Live wires: direct extracellular electron exchange for bioenergy and the bioremediation of energy-related contamination. *Energy & Environmental Science* **2011,** *4* (12), 4896-4906.

[14] Richter, H.; McCarthy, K.; Nevin, K. P.; Johnson, J. P.; Rotello, V. M.; Lovley, D. R., Electricity generation by Geobacter sulfurreducens attached to gold electrodes. *Langmuir* **2008,** *24* (8), 4376-4379.

[15] Malvankar, N. S.; Tuominen, M. T.; Lovley, D. R., Lack of cytochrome involvement in long-range electron transport through conductive biofilms and nanowires of Geobacter sulfurreducens. *Energy & Environmental Science* **2012,** *5* (9), 8651-8659.

[16] Xie, X.; Hu, L.; Pasta, M.; Wells, G. F.; Kong, D.; Criddle, C. S.; Cui, Y., Three-dimensional carbon nanotube− textile anode for high-performance microbial fuel cells. *Nano letters* **2010,** *11* (1), 291-296.

[17] Xie, X.; Yu, G.; Liu, N.; Bao, Z.; Criddle, C. S.; Cui, Y., Graphene–sponges as high-performance low-cost anodes for microbial fuel cells. *Energy & Environmental Science* **2012,** *5* (5), 6862-6866.

[18] Logan, B.; Cheng, S.; Watson, V.; Estadt, G., Graphite fiber brush anodes for increased power production in air-cathode microbial fuel cells. *Environmental science & technology* **2007,** *41* (9), 3341-3346.

[19] Qiao, Y.; Bao, S.-J.; Li, C. M.; Cui, X.-Q.; Lu, Z.-S.; Guo, J., Nanostructured polyaniline/titanium dioxide composite anode for microbial fuel cells. *Acs Nano* **2007,** *2* (1), 113-119.

[20] Fan, Y.; Xu, S.; Schaller, R.; Jiao, J.; Chaplen, F.; Liu, H., Nanoparticle decorated anodes for enhanced current generation in microbial electrochemical cells. *Biosensors and Bioelectronics* **2011,** *26* (5), 1908-1912.

[21] Mink, J. E.; Rojas, J. P.; Logan, B. E.; Hussain, M. M., Vertically grown multiwalled carbon nanotube anode and nickel silicide integrated high performance microsized (1.25 μL) microbial fuel cell. *Nano Letters* **2012,** *12* (2), 791-795.

[22] Inoue, S.; Parra, E. A.; Higa, A.; Jiang, Y.; Wang, P.; Buie, C. R.; Coates, J. D.; Lin, L., Structural optimization of contact electrodes in microbial fuel cells for current density enhancements. *Sensors and Actuators A: Physical* **2012,** *177*, 30-36.

[23] Tang, X.; Zhang, G.; Zhao, Y., Electrochemical characterization of silver nanorod electrodes prepared by oblique angle deposition. *Nanotechnology* **2006,** *17* (17), 4439.

[24] Kane, A. L.; Bond, D. R.; Gralnick, J. A., Electrochemical analysis of Shewanella oneidensis engineered to bind gold electrodes. *ACS synthetic biology* **2012,** *2* (2), 93-101.

[25] Choi, S.; Lee, H.-S.; Yang, Y.; Parameswaran, P.; Torres, C. I.; Rittmann, B. E.; Chae, J., A μL-scale micromachined microbial fuel cell having high power density. *Lab on a Chip* **2011,** *11* (6), 1110-1117.

[26] Lin, C.-C.; Wei, C.-H.; Chen, C.-I.; Shieh, C.-J.; Liu, Y.-C., Characteristics of the photosynthesis microbial fuel cell with a Spirulina platensis biofilm. *Bioresource technology* **2013,** *135*, 640-643.

[27] Sun, M.; Zhang, F.; Tong, Z.-H.; Sheng, G.-P.; Chen, Y.-Z.; Zhao, Y.; Chen, Y.-P.; Zhou, S.-Y.; Liu, G.; Tian, Y.-C., A gold-sputtered carbon paper as an anode for improved electricity generation from a microbial fuel cell inoculated with Shewanella oneidensis MR-1. *Biosensors and Bioelectronics* **2010,** *26* (2), 338-343.

[28] Saem, S.; Zhu, Y.; Luu, H.; Moran-Mirabal, J., Bench-top fabrication of an all-PDMS microfluidic electrochemical cell sensor integrating micro/nanostructured electrodes. *Sensors* **2017,** *17* (4), 732.

[29] Sonney, S.; Shek, N.; Moran-Mirabal, J. M., Rapid bench-top fabrication of poly (dimethylsiloxane)/polystyrene microfluidic devices incorporating high-surface-area sensing electrodes. *Biomicrofluidics* **2015,** *9* (2), 026501.

[30] Zhu, Y.; Moran-Mirabal, J., Highly bendable and stretchable electrodes based on micro/nanostructured gold films for flexible sensors and electronics. *Advanced Electronic Materials* **2016,** *2* (3), 1500345.

[31] Gabardo, C. M.; Zhu, Y.; Soleymani, L.; Moran-Mirabal, J. M., Bench-Top Fabrication of Hierarchically Structured High-Surface-Area Electrodes. *Advanced Functional Materials* **2013,** *23* (24), 3030-3039.

[32] Gill, U.; Sutherland, T.; Himbert, S.; Zhu, Y.; Rheinstädter, M. C.; Cranston, E. D.; Moran-Mirabal, J. M., Beyond buckling: humidity-independent measurement of the mechanical properties of green nanobiocomposite films. *Nanoscale* **2017,** *9* (23), 7781-7790.

[33] Lebedev, N.; Strycharz-Glaven, S. M.; Tender, L. M., High resolution AFM and single-cell resonance Raman spectroscopy of Geobacter sulfurreducens biofilms early in growth. *Frontiers in Energy Research* **2014,** *2*, 34.

[34] Ren, H.; Pyo, S.; Lee, J.-I.; Park, T.-J.; Gittleson, F. S.; Leung, F. C.; Kim, J.; Taylor, A. D.; Lee, H.-S.; Chae, J., A high power density miniaturized microbial fuel cell having carbon nanotube anodes. *Journal of Power Sources* **2015,** *273*, 823-830.

[35] Wang, H.; Wang, G.; Ling, Y.; Qian, F.; Song, Y.; Lu, X.; Chen, S.; Tong, Y.; Li, Y., High power density microbial fuel cell with flexible 3D graphene–nickel foam as anode. *Nanoscale* **2013,** *5* (21), 10283-10290.

[36] Choi, G.; Hassett, D. J.; Choi, S., A paper-based microbial fuel cell array for rapid and high-throughput screening of electricity-producing bacteria. *Analyst* **2015,** *140* (12), 4277-4283.

[37] Zarabadi, M. P.; Paquet-Mercier, F. o.; Charette, S. J.; Greener, J., Hydrodynamic Effects on Biofilms at the Biointerface Using a Microfluidic Electrochemical Cell: Case Study of Pseudomonas sp. *Langmuir* **2017,** *33* (8), 2041-2049.

[38] Ben-Yoav, H.; Freeman, A.; Sternheim, M.; Shacham-Diamand, Y., An electrochemical impedance model for integrated bacterial biofilms. *Electrochimica Acta* **2011,** *56* (23), 7780-7786.

[39] Ramasamy, R. P.; Ren, Z.; Mench, M. M.; Regan, J. M., Impact of initial biofilm growth on the anode impedance of microbial fuel cells. *Biotechnology and bioengineering* **2008,** *101* (1), 101-108.

[40] Ren, Z.; Ramasamy, R. P.; Cloud-Owen, S. R.; Yan, H.; Mench, M. M.; Regan, J. M., Time-course correlation of biofilm properties and electrochemical performance in single-chamber microbial fuel cells. *Bioresource technology* **2011,** *102* (1), 416-421.

[41] Yu, F.; Wang, C.; Ma, J., Capacitance-enhanced 3D graphene anode for microbial fuel cell with long-time electricity generation stability. *Electrochimica Acta* **2018,** *259*, 1059-1067.

[42] Shen, J.; Wang, C.; Liu, Y.; Hu, C.; Xin, Y.; Ding, N.; Su, S., Effect of ultrasonic pretreatment of the dairy manure on the electricity generation of microbial fuel cell. *Biochemical engineering journal* **2018,** *129*, 44-49.

[43] Qian, F.; Baum, M.; Gu, Q.; Morse, D. E., A 1.5 μL microbial fuel cell for on-chip bioelectricity generation. *Lab on a Chip* **2009,** *9* (21), 3076-3081.

[44] Lebedev, N.; Strycharz-Glaven, S. M.; Tender, L. M., Spatially resolved confocal resonant Raman microscopic analysis of anode-grown Geobacter sulfurreducens biofilms. *ChemPhysChem* **2014,** *15* (2), 320-327.

Chapter 4: A High-Performance Membraneless Microfluidic Microbial Fuel Cell for Stable, Long-Term Benchtop Operation Under Strong Flow

Mehran Abbaszadeh Amirdehi,[a] Nastaran Khodaparastasgarabad,[a] Hamza Landari,[b] MirPouyan Zarabadi,[a] Amine Miled,[b] Jesse Greener[a,c] *

[a] Département de ChimieUniversité LavalQuébec, QC G1V 0A6, Canada

[b] Département de Génie électrique, Université Laval, Québec, Canada

[c] CHU de Québec Centre de recherche CentreUniversité Laval10 rue de l'Espinay, Québec, QC G1L 3L5, Canada

Published in *ChemElectroChem* (2020).

4.1. Résumé

Un contrôle rigoureux des conditions expérimentales dans les canaux microfluidiques offre une opportunité unique d'étudier et d'optimiser les piles à combustible microbiennes sans membrane (MFC), en particulier en ce qui concerne le rôle de l'écoulement. Cependant, l'amélioration des performances et la transférabilité des résultats à la communauté MFC plus large nécessitent des améliorations de la stabilité de l'appareil dans toutes les conditions opérationnelles appliquées. Pour relever ces défis, nous présentons un MFC sans membrane facile à fabriquer qui combine i) la protection O_2 via une barrière de diffusion de gaz, ii) des électrodes en graphite intégrées et iii) un placement optimisé des électrodes pour éviter la contamination croisée sous tous les débits appliqués. L'attention portée à toutes ces caractéristiques de conception dans la même plate-forme a abouti à l'exploitation d'un MFC avec un biofilm anaérobie de culture pure Geobacter sulfurreducens pendant six mois, soit six fois plus longtemps que précédemment rapporté, sans l'utilisation d'un capteur d'oxygène. En raison de la stabilité plus élevée du dispositif sous des débits élevés, les densités de puissance étaient quatre fois plus élevées que celles rapportées précédemment pour les MFC microfluidiques avec le même biofilm.

4.2. Abstract

Strong control over experimental conditions in microfluidic channels provides a unique opportunity to study and optimize membraneless microbial fuel cells (MFCs), particularly with respect to the role of flow. However, improved performance and transferability of results to the wider MFC community require improvements to device stability under all applied operational conditions. To address these challenges, we present an easy-to-fabricate membraneless MFC that combines i) O_2 protection via a gas diffusion barrier, ii) integrated graphite electrodes, and iii) optimized electrode placement to avoid cross-contamination under all applied flow rates. Attention to all of these design features in the same platform resulted in the operation of a MFC with a pure-culture anaerobic *Geobacter sulfurreducens* biofilm for half a year, that is, six times longer than previously reported, without the use of an oxygen scavenger. As a result of higher device stability under high flow rates, power densities were four times higher than reported previously for microfluidic MFCs with the same biofilm.

4.3. Introduction

Microfluidics has emerged as an essential technology in microbiological research, primarily due to its ability to provide rigorous control over experimental conditions.[1-4] A potential area for expanded contribution lies in bio-electrochemical systems (BES), an expanding subdomain of synthetic biology, in which biocatalytic redox steps in certain microbial metabolic cycles perform useful electrochemical functions.[5, 6] Electroactive biofilms (EABs) from anaerobic *Geobacter sulfurreducens* are among the most studied because of their special ability to directly transport electrons to an anode via a conductive extracellular network consisting of cytochrome c proteins and conductive pili.[7] Compared with mixed cultures, the relative simplicity of pure culture EABs from *G. sulfurreducens* makes it easier to gain mechanistic insights. For example, using three-electrode microfluidic BES devices with pure *G. sulfurreducens* electrode-adhered EABs, we recently studied the role of liquid flow on electrobiocatalysis kinetics,[8] EAB pH management,[9] and bacterial metabolic state under highly nutrient-limited conditions.[10] Additionally, accurate simulations of laminar flow streams in microchannels could be achieved with straight-forward models.[11, 12] The most highly developed microfluidic BES are microbial fuel cells (MFCs), which are devices with anode-adhered EABs that convert chemical potential energy from organic waste molecules into electrical energy via biocatalytic oxidation.[13, 14] Among other advantages, microfluidic MFCs can provide a deeper understanding of certain fundamental processes, e. g., how flow conditions can improve power and current densities.[15, 16] However, the adaption of microfluidic MFC platforms is lagging compared with that of macro-systems because the former suffers from lower power outputs, reduced longevity and increased device complexity. Other challenges include flow-induced enhancements to power that fall short of achieving their maximal effect due to instabilities at high flow rates. It is generally believed that shear erosion of the anode-adhered EABs is to blame for this, but competing effects complicate investigations into this effect. For example, the degradation of gold cathodes by the common oxidizing agent ferricyanide can result in continuous changes to the internal resistance, with high flow reported to exacerbate the problem.[15] The use of highly inert carbon-based electrodes should alleviate this problem while conferring other advantages, such as improved charge transfer kinetics and improved relevance to macro-MFC studies.

However, integration of carbon electrodes into microchannels is challenging, so the use of gold electrodes remains a hurdle. Among the most widely acknowledged challenges for microfluidic MFCs is the potential for O_2 contamination via diffusion through polydimethylsiloxane (PDMS). Despite innovative attempts to address the problem[17-19] it is still standard in microfluidic MFC studies to add O_2 scavenging molecules and to use mixed EABs that are more tolerant to O_2, but at the expense of complications arising from additional experimental parameters. To achieve reductions in device complexity and cost, a membraneless approach to isolating anolyte and catholyte solutions in laminar-flow chemical fuel cells [20] has been implemented for microfluidic MFCs by some authors.[21, 22] However, its adaption to microfluidic MFCs is not completely straightforward because the EAB causes deviations to flow patterns, thus enhancing the potential for anolyte/catholyte cross-contamination in the opposite compartment.

A general indicator of the remaining challenges for microfluidic MFC developers is the short operating times, usually less than two weeks, which is a fraction of the time reported for macro-MFCs. Moreover, short operating times are problems in their own right, as they may not provide an accurate representation of the phenomena under study while biofilm changes are still underway.[23] Addressing these challenges can improve fundamental studies and can also lead to more efficient microscale applications, such as sensors [24, 25] and power supplies for ultra-small electronics or implantable medical devices.[22]

To enable flow studies that are independent of technical complications, we present an easy-to-fabricate membraneless microfluidic MFC with graphite electrodes and a protective barrier against O_2 intrusion. Guided by simulations, we optimized the electrode positioning to account for flow deflection around the accumulated biomass at the anode and thus avoid anolyte/catholyte cross-contamination. The result is a robust microfluidic MFC capable of the longest reported operation to date. The system delivers the highest power density outputs recorded to date for any microfluidic MFC with a pure *G. sulfurreducens* EAB.

4.4. Device Design and Validation

4.4.1. Fabrication of an Oxygen-Protected Microfluidic MFC with Embedded Graphite Electrodes

Various configurations of membraneless laminar flow fuel cells, including but not limited to MFCs, can be found elsewhere.[20,21,26] Generally, it is practical to fabricate devices with electrodes in a side-by-side configuration using traditional microfabrication techniques because the electrodes are located only on one wall. Gold electrodes are usually preferred in microfluidic MFCs due to their compatibility with standard microfabrication techniques,[4, 27] particularly as bottom side electrodes in a side-by-side configuration. However, apart from its cost, gold performs sub-optimally as a bioelectrode due to limitations in charge transfer kinetics and in bacterial colonization. Structured electrodes have been implemented to address certain of these drawbacks.[17, 21, 23, 28] However, the instability of gold in the presence of ferricyanide-containing catholyte solutions is often not considered, even though the problem is reported to be worsened at elevated flow rates, thereby limiting one of the main advantages of microfluidic MFCs.[15] The use of gold electrodes also adds a barrier for transferability to the wider BES community because the vast majority of macro-MFC studies use carbon-based electrodes. The integration of graphite or other carbon-based electrodes is expected to be beneficial because of their excellent charge transfer kinetics,[29, 30] favorability to bacterial colonization due to their naturally rough surfaces, and because their inertness should facilitate stable long-term performance.[21, 31]

The fabrication process for a strictly anaerobic microfluidic MFC with two side-by-side top-wall graphite electrodes is illustrated in Figure 4. 1a. A photolithographic mould was created (Figure 4. 1a(i)). Two electrodes with dimensions of 10×20 mm were cut from a 3 mm-thick graphite plate. Integration of the electrodes into the PDMS microchannel was adapted from a previously developed fabrication protocol for straight-forward integration of top-wall electrodes.[32] In brief, graphite plates for the anode and cathode were placed on top of the mould channel feature using double-sided tape to ensure good contact. The tape completely surrounded the entire electrode to prevent the previously observed de-activation after immersion in liquid PDMS. The overhanging portion of each electrode was stabilized with a small piece of PDMS (Figure 4. 1a(ii)). A liquid PDMS solution was cured against the

assembly, thereby immobilizing the electrodes within the device (Figure 4. 1a(iii)). Subsequently, the PDMS device with embedded graphite electrodes was carefully separated from the mould, and the intervening double-sided tape was removed from the portion of the electrode exposed to the channel (Figure 4. 1a (iv)). This method of electrode integration resulted in an exposed electrode surface that was flush with the PDMS wall, thus preventing flow disturbances as liquid flowed across it. Three holes were created for two inlets and one outlet, and the assembly was sonicated in water to remove debris. A 1 M HCl solution was applied to the electrodes using sterile cotton swabs, followed by rinsing of the entire open channel with 70 % ethanol and by sterile deionized water. The channel was sealed with a microscope slide (75×55×1 mm) via standard air plasma activation (Figure 4.1 a(v)). Finally, a protective barrier was added against all exposed PDMS at the top and side surfaces to block gas exchange with the device exterior. This was accomplished using a second glass slide that was plasma-bonded to the top side of the device and the addition of a thin layer of epoxy (LOCTITE®, Ohio, US) along the device edges (Figure 4.1 a(vi)). Access to the fluid connects was achieved by drilling 1/16″ holes through the upper glass layer (Figure 4.1 b) with a diamond drill bit. Protection of the inlet and outlet tubing from O_2 intrusion was achieved with a gas-barrier coating, as described previously.[9] The final device was fully transparent, protected against small molecule diffusion and capable of generating co-flow of miscible liquids (Figure 1.1c).

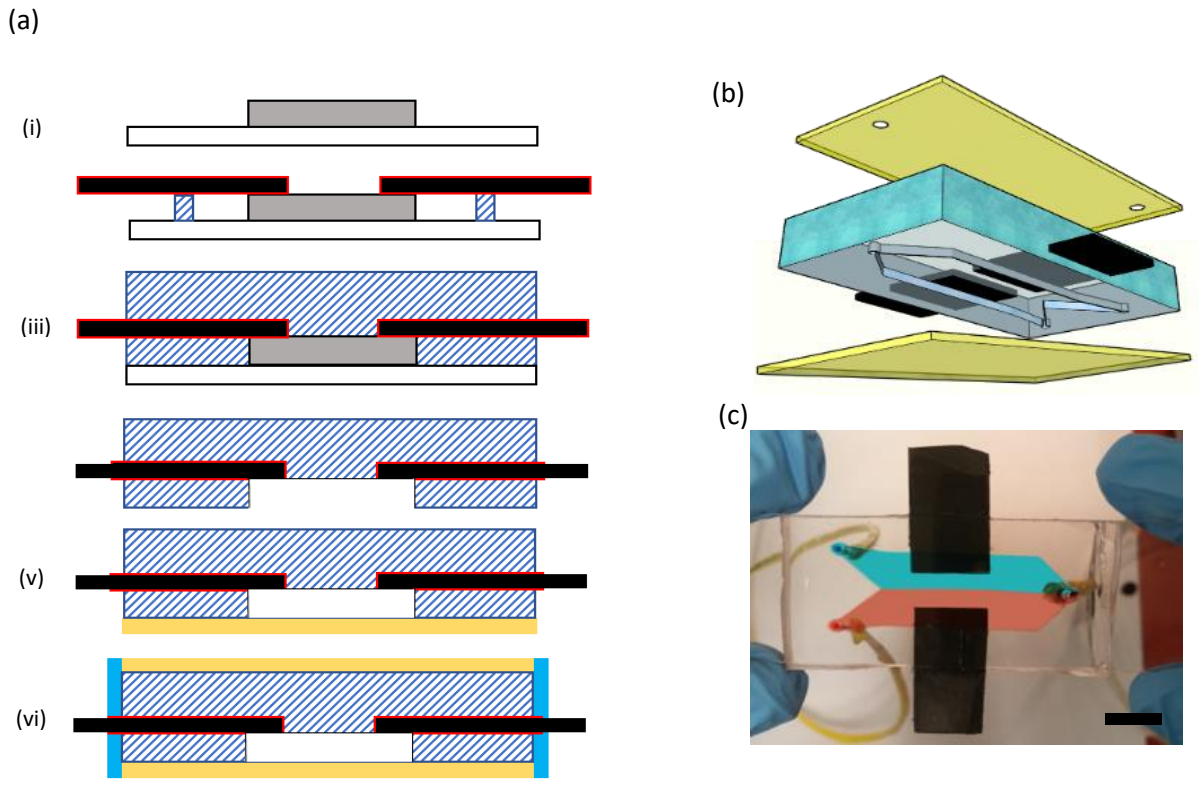

Figure 4.1. a) Device fabrication steps. i) Cross-sectional view of the mould with a raised feature that defines the microchannel. The dimensions of the main channel were 160 μm (height), 12 mm (width), and 3 cm (length). ii) Two 1 cm wide graphite electrodes (black) with a protective external barrier (red) placed on top of the mould channel feature (grey) with small PDMS spacers (blue cross-hatch) for stabilization. iii) Liquid PDMS (blue cross-hatch) poured over the mould/electrode assembly and cured. iv) Microfluidic device with embedded electrodes after removal from the mould and removal of the graphite protective barrier in the channel and external to the device. v) Channel-side (only) sealed with a glass slide (yellow), referred to as the "unprotected" device. vi) Microfluidic device featuring top and bottom glass sealing and side sealing with epoxy (blue), referred to as the "gas-protected" device. b) Microfluidic device with drilled inlets and outlet in the top glass sealing layer. Glass and epoxy are shown in yellow and blue. (c) Photo image of the assembled experimental design with blue- and red-colored liquids to visualize the laminar flows in the device (Q_{blue}=Q_{red}=20 mL · h^{-1}). Scale bar is 1 cm.

4.4.2. Protection Against Small Molecule Diffusion

Despite the preference for PDMS in most microfluidic MFCs, its use presents a hurdle for anaerobic EABs because of its high permeability to O_2 and other small gas-phase molecules such as water,[28, 33] which even impacts devices with minimal exposed PDMS, such as for spacers.[34] Apart from negatively impacting performance, intruding O_2 is expected to become diluted to different concentrations in studies where the flow rate is varied, resulting in

complications in the interpretation of results.[19] We first tested the sealing of the microfluidic MFC against small molecule exchange with the ambient conditions outside of the device by monitoring the water evaporation.

Avoidance of water evaporation is important in its own right due to potential side effects, such as increased solute concentrations or precipitation. Two devices were prepared, an unprotected device as shown in Figure 1.1 a(v) and a gas-protected device as shown in Figure 4.1 a(vi). After filling both devices with pure degassed water, the flow was stopped, and the inlets/outlet were sealed shut. Time-lapse imaging was conducted on each device to observe the appearance of gas bubbles in the channel due to H_2O exchange with the ambient air outside of the devices. Figure 4.2 a shows the results from experiments in each device. Bubbles appeared within the unprotected device and continuously grew until 24 hours had elapsed, at which time all water had disappeared from view. Based on the nearly linear slope, it was estimated that 0.16 mm^3 of liquid water was lost to diffusion through 1 mm^2 of PDMS per day. The effect was slower but still present for thicker devices due to more intervening PDMS. In the second experiment, UV-Vis spectrophotometry was used to accurately observe small changes to the absorbance spectra of the common O_2 indicator resazurin after passing through the MFC.[35] In anaerobic aqueous solutions, the initially colorless dye changes color after it is oxidized to one of two oxidation states at intermediate or near-saturated O_2 conditions (see Supporting Information, Section S1, Figure 4. S1) with absorption bands at 573 nm and 605 nm for intermediate and high O_2 concentrations, respectively. Figure 4.2 b shows the UV-Vis spectra after passing an anaerobic aqueous resazurin solution (0.15 $mg\,L^{-1}$) through the unprotected and gas-protected membraneless MFCs and finally into a sealed glass syringe at the device outlet. After transit through the unprotected MFC, the emerging solution was pink in color, demonstrating that it had been exposed to O_2 within the device, but did not change color or intensity during the accumulation in the syringe, thus confirming that no further O_2 exposure occurred off-chip. The absorbance intensity was observed to have in inverse relationship to total flow rate (Q_T) in the range of 1 to 140 $mL \cdot h^{-1}$, suggesting that the O_2 concentration becomes diluted with increasing Q_T. In contrast, Figure 4.2b confirms that after transit of the indicator solution through the gas-protected

device, the accumulated liquid at the outlet remained anaerobic, independent of Q_T. Thus, operation at a range of flow rates is possible without affecting on-chip O_2 levels.

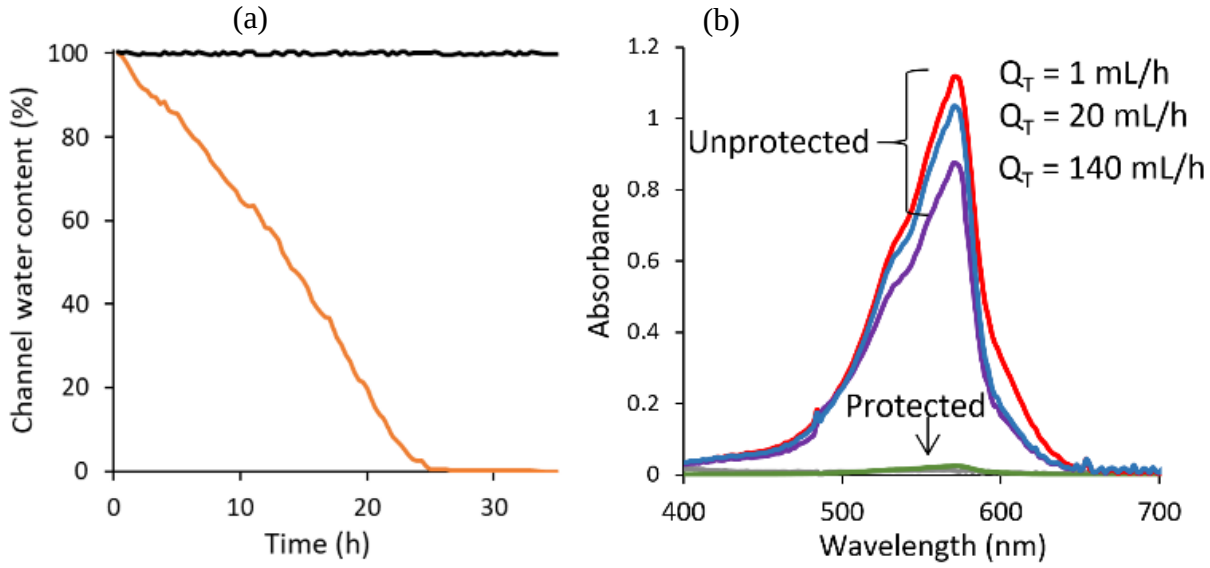

Figure 4.2. a) Water content in the microchannel vs. time. Data obtained from a field of view that was approximately 20 % of the total channel volume in a gas-protected device (black) and unprotected device (orange). b) UV/Vis spectra of aqueous resazurin solutions collected from the outlet of an unprotected MFC at the indicated total flow rates of Q_T=140 (red), 20 (blue) and 1 mL · h^{-1} (purple) and of a gas-protected MFC device at Q_T=140 (grey) and 1 mL · h^{-1} (green).

4.4.3. Optimization of Electrode Positioning using Flow Simulations

An often-overlooked problem in membraneless MFCs is the possibility of contamination via solution crossover to the opposite electrode compartment due to the presence of an anode-adhered EAB. This can reduce performance due to thermodynamic-based reductions in cell potential and because of ferricyanide toxicity to the EAB. In some work, cross-over contamination has been acknowledged and simulations have shown the result of a diffusive process[17] in an equivalent manner to laminar flow chemical fuel cells. However, this problem has not been strictly evaluated based on the flow deflection around the anode-adhered EAB, which is expected to be significantly more impactful than pure diffusion. This problem is more severe for the popular side-by-side electrode configuration used in this study, due to shorter inter-electrode distances than in opposing wall electrodes. In the Supporting

Information, we present simulation results demonstrating several related hydrodynamic phenomena in side-by-side MFCs. These results show that significant displacement of the co-flow interface away from the centre of the channel are a result of the presence of an electrode-adhered biofilm (Supporting Information, Section S2, Figure 4. S2). Visualization of the deflection of the simulated fluid streamlines around the anode-adhered EAB confirms flow deflection as the primary driver of this effect, but secondary flow profiles are also observed, which that can have additional impacts such as mixing at the co-flow interface. Therefore, we begin with a series of simulations to predict the effect of flow on the acetate concentration profiles in the channel, with the goal of minimizing cross-contamination.

Figure 4.3 a shows a schematic of the channel used in these simulations. A low aspect ratio of $1:75$ ($H:W=0.16$ mm : 12 mm) was selected to increase the surface-area-to-volume ratio,**21** effectively increasing the contact between the electrodes and the relatively thin fluidic layer above them. The wide channel also allows a large electrode insertion distance (E_x) while maintaining sufficient space between the electrodes to accommodate flow deflection around the anode-adhered EAB. The conventional approach is to place electrodes close together to reduce solution resistance,[21] but we hypothesize this can result in electrode contamination from solution crossover in membraneless devices. Thus, we first simulated crossover contamination as the inter-electrode distance was varied (Figure 4.3 a) while equal flow rates of anolyte (Q_A) and catholyte (Q_C) were applied to each inlet ($Q_A=Q_C=10$ mL $\cdot$ h^{-1}), with total flow rate $Q_T=Q_A+Q_C=20$ mL $\cdot$ h^{-1}. To accommodate the widest range of conditions from MFC inoculation to maturity, we analyzed the crossover acetate concentration for an EAB thickness (h_B) of 10, 30 and 80 μm. Based on our experience and other literature reports, this is a reasonable range, with 80 μm representing a good estimation for mature *G. sulfurreducens* EABs in microchannels. As observed in Figure 4.3b, electrode separation distances of 4 mm and lower resulted in acetate concentration at the cathode that were more than 10 % of the inlet concentration (10 mM) for $h_B=80$ μm. For the separation distance of 5 mm, the anolyte concentration at the cathode fell to 0.1 mM, or approximately 1 % of the inlet concentration, whereas at 6 mm separation, the concentration decreased to 0.01 mM or approximately 0.1 % of the inlet concentration. Because one of the main objectives of this paper was to study flow effects in the absence of device-level instabilities such as crossover

contamination, not to generate the highest power possible, we chose a wide electrode separation distance of 6 mm. Supporting information, Figure 4. S3, shows that simulated flow displacement of the anolyte/catholyte co-flow system and the mixing region at its interface are both increased with h_B. It is also noted that total flow rate does not play a significant role in flow deflection (Figure 4. S4). The reader is referred to Supporting Information for a full discussion on these points.

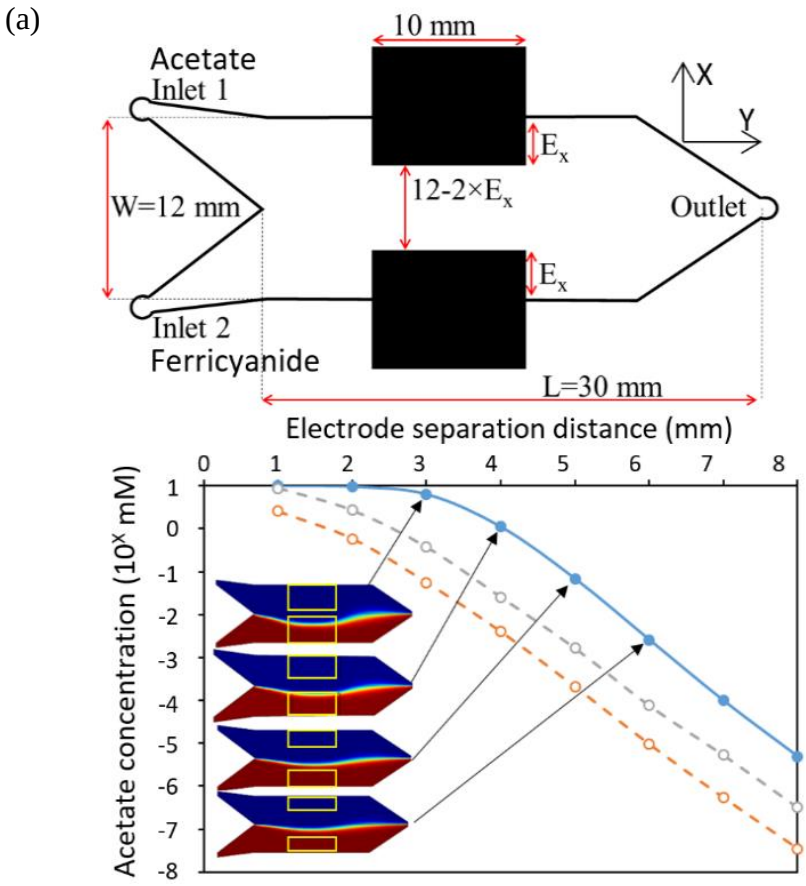

Figure 4.3. a) Device architecture for flow simulations of the microfluidic MFC with electrode penetration into the channel of E_x. Electrode widths and channel dimensions width (W) and length (L) are also shown. Channel height H=160 μm is not shown. The anolyte (10 mM acetate) and catholyte (30 mM ferricyanide) are supplied at equal flow rates through inlets 1 and 2, respectively, at a total flow rate Q_T=20 mL · h^{-1}. b) Plot showing the acetate concentration at the cathode edge as electrode separation is varied from 1 to 8 mm for anode-adhered EABs with heights h_B=80 (blue), 30 (grey) and 10 μm (orange). Inset images show acetate concentration profiles for selected electrode separation distances. Color bar indicates acetate concentrations.

While most experiments use anolyte and catholyte flow rates (Q_A and Q_C) that are equal (Q_A/Q_C=1), simulations are also presented in the Supporting Information for unbalanced flow

conditions ($Q_A/Q_C \neq 1$) which can occur due to user error or maybe implemented intentionally to reposition the co-flow interface within the channel (Figure 4. S5). Finally, supporting simulation of shear stress applied to the anode-adhered EAB were also conducted because this is otherwise difficult to calculate due to the complex flow patterns around the partially occluded channel at the anode position. It is observed that average shear stress against the EAB increased linearly with flow rate and with h_B (Figure 4. S6).

4.5 Results

4.5.1. Growth of Pure-Culture *G. sulfurreducens* EABs

We tested the effectiveness of the gas-protected MFC in supporting growth of anode-adhered *G. sulfurreducens* EAB compared with the unprotected device. A pure culture was used as a more rigorous test of the anoxic environment compared with mixed-culture MFCs, which are more tolerant to oxygenated conditions because obligatory and facultative aerobes can produce local anaerobic conditions by consuming O_2. The inoculation procedure for both devices was identical and was conducted simultaneously using the same bacteria sub-culture as inoculant. After 2 hours of injecting inoculant at $Q_A=Q_C=0.5\ mL \cdot h^{-1}$, a background potential of 10 mV was recorded across the 25 kΩ external resistor. A 48-hour pre-growth phase followed during which the inoculant was replaced with a growth solution flowing through the channel at the same values of Q_A and Q_C. Voltage measurements commenced after the pre-growth phase with both MFCs producing approximately 200 mV. Figure 4.4a shows the potential after pre-growth (t=0) immediately after the environmental enclosure was opened, exposing both gas-protected and unprotected devices to ambient (oxygenated) conditions. Exposure of the unprotected device to oxygenated conditions caused the growth in potential to stop, followed by a rapid decrease at 30 h down to 100 mV. This event was followed by a slow decline down to background levels (not shown). Interestingly, the potential in the gas-protected device continued to increase, reaching approximately 500 mV after 2 days and eventually reaching a steady output near 565 mV (see Supporting Information, Section S3, Figure 4.S7 for continuous measurements of potential until the end of the experiment). Figure 4.4b shows the power density curves obtained at 40 and 80 h for the gas-protected and unprotected devices. We note that the calculated power densities in Figure 4a matched the maximum power density obtained from curves in Figure 4.4b at the

corresponding time. An additional power density curve is shown after 6 months, immediately before the device was sacrificed for SEM (Supporting Information, Section S4, Figure 4. S8). Therefore, the gas-protected design enabled long-term benchtop operation in ambient conditions without the need for O_2 scavengers.

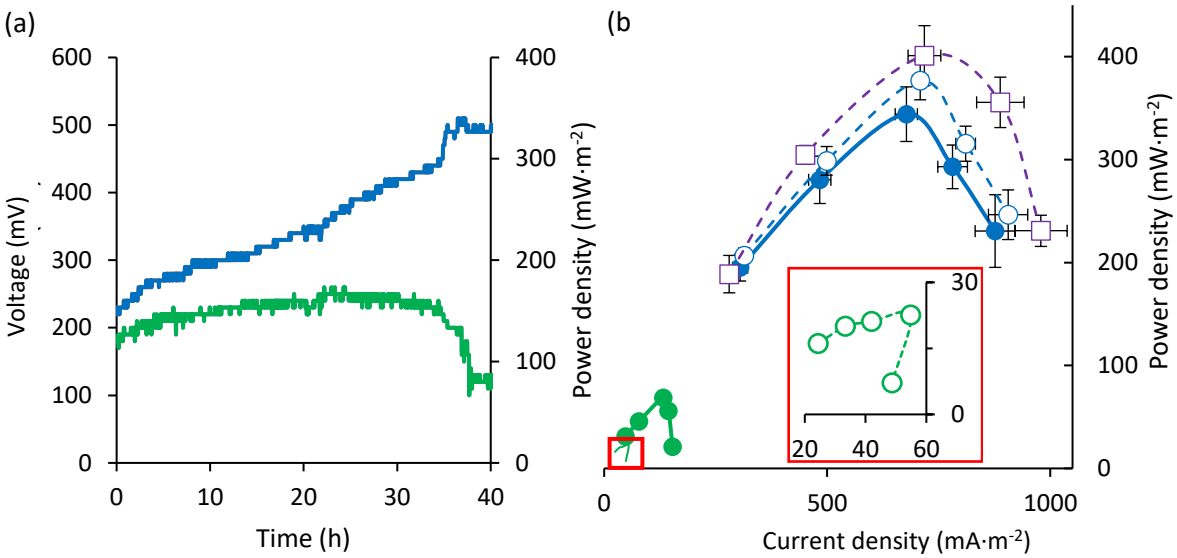

Figure 4.4. a) Voltage comparison across the external resistor (25 kΩ) of gas-protected (blue) and unprotected (green) MFCs. Time of 0 h corresponds to the time at which the environmental enclosure was opened after 48 h pre-growth under a 10 mM acetate growth solution. The second vertical axis shows the calculated power density. b) Power density curves for both devices at t=40 h (solid) and t=80 h (dashed) after opening the anaerobic enclosure for the gas-protected (blue) and unprotected (green) MFCs using external resistances R_{ext}=10, 16, 25, 40, and 70 kΩ. A third power density is shown for the gas-protected device at t=6 months (dashed purple). Error bars in (b) are calculated from 3 separate measurements but are smaller than the data markers for the unprotected device. The inset (red box) shows a zoom view of the highlighted curve for the unprotected device after 80 h. In all cases, the flow rate was Q_T=1 mL · h^{-1}.

4.5.2. Flow Effects on MFC Performance

We present the results for the effect of flow on the performance of the gas-protected membraneless MFC with optimized electrode spacing. After growth under R_{ext}=25 kΩ for approximately 25 days, the MFC reached stable operating conditions. For statistical purposes, power density and polarization curves were acquired weekly during months 2 to 6 while flow was supplied in the range of Q_T=1 to 40 mL · h^{-1}. Figures 4.5 a and 4.5b show that the maximum power density increased from 376 mW · m^{-2} to 430 mW · m^{-2} (14 %), and the

maximum current density increased (at R_{ext}=10 kΩ) from 905 mA · m^{-2} to 1100 mA · m^{-2} (22 %).

We note that the maximum power density was always observed when the external resistance was set to R_{ext}=25 kΩ. Therefore, flow did not significantly affect the internal resistance in the flow rate range of 1 to 40 mL · h^{-1}. Higher flow rates were not attainable while acquiring power density and polarization curves because the length of time required for the measurement surpassed the discharge time of the syringes used. To extend the range of applicable flow rates, voltage was measured across a single external resister of R_{ext}=25 kΩ and converted to power density using Eqn. 3, as discussed in the experimental section. Figure 4.5c shows the changes to the potential and calculated power density as the total flow rate was changed between a baseline value (1 mL · h^{-1}) and an elevated value (between Q_T=2 and 140 mL · h^{-1}) with a duty cycle of approximately 15 min. Figure 4.5d shows that both methods produced a similar response to flow rate from 1 to 40 mL · h^{-1} within the experimental error, as indicated by the error bars. The constant resistor method produced changes in power density from 368 mW · m^{-2} at Q_T=1 mL · h^{-1} to 456 mW · m^{-2} at Q_T=140 mL · h^{-1} with no further increases for flow rates as high as 200 mL · h^{-1} (data not shown). This is equivalent to an increase of 24 % over baseline flow rates (Q_T=1 mL · h^{-1}) (Figure 4.5d inset). An important corollary is that the benefits of enhanced flow attain their maximum effect on power density before the onset of sheer-induced erosion, contrary to many reports in the literature.

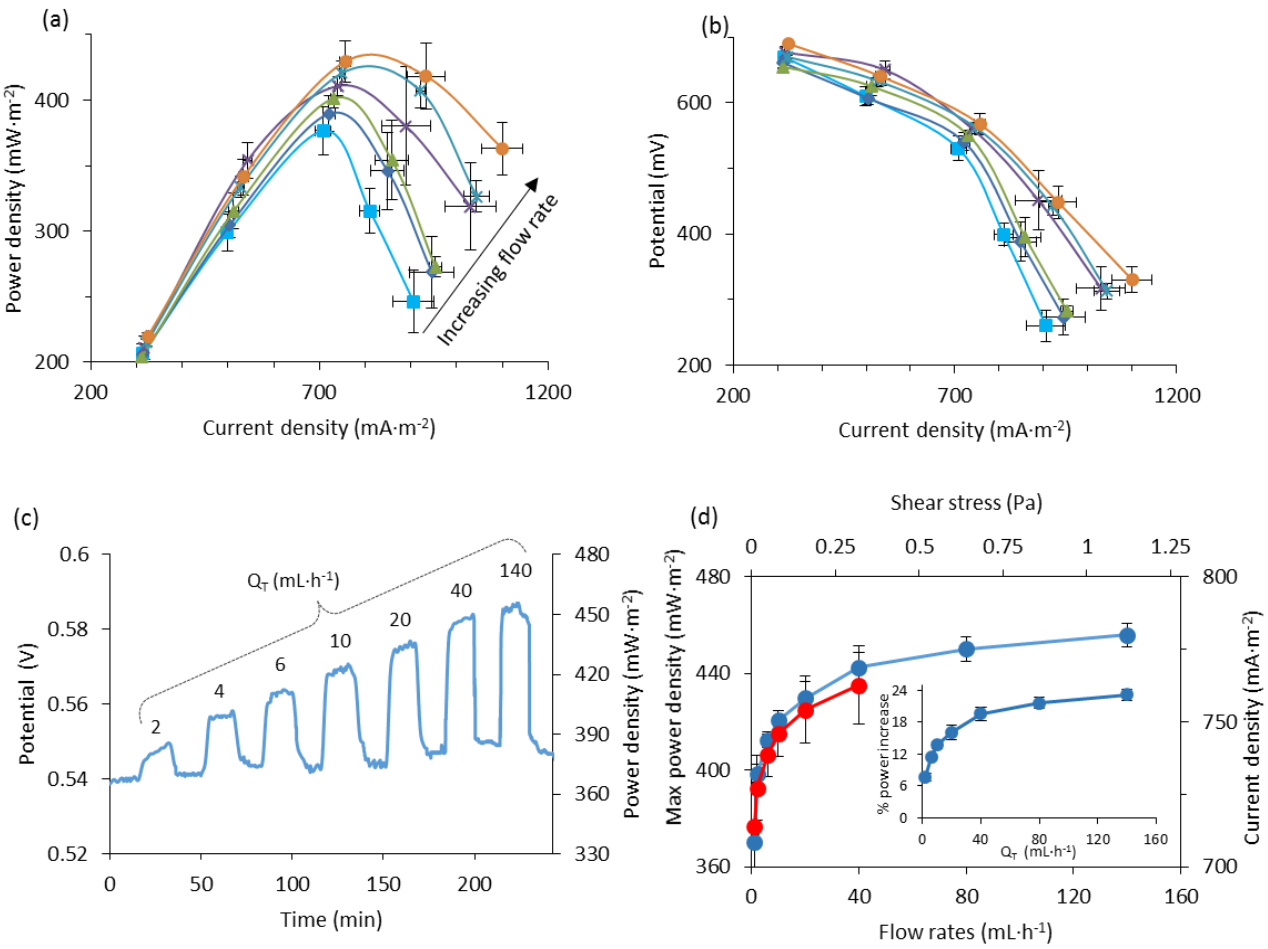

Figure 4.5. Performance of the gas-protected microfluidic MFC with 6 mm electrode spacing. a) Power density curves and b) polarization curves at total flow rates Q_T=1, 2, 6, 10, 20 and 40 mL · h^{-1}. c) Results of pulsing Q_T on the measured potential across a 25 kΩ resistor and the corresponding power density outputs for 7 elevated flow rates separated by exposure to a baseline flow rate (Q_T=1 mL · h^{-1}). d) Maximum power density from data in (a) (red) and power density from (c) (blue). Inset shows percent increase in power ($\triangle p/p_{static} \times 100$ %) with Q_T. In all cases, error bars are the result of 5 separate measurements collected during months 2–6, inclusive.

The growth in current density at 25 kΩ was nearly 8 % in the same range of Q_T values (Figure 4.5 d), but separate measurements with R_{ext} changed to 10 kΩ showed values ranging from 925 to nearly 1100 mA · m^{-2} or approximately 19 % growth. These improvements can be ascribed to enhanced metabolic activity, largely due to enhanced nutrient availability. However, other factors could have contributed. For example, although EAB de-acidification was not observed in previous chronoamperometry studies of the same EAB type exposed to 10 mM acetate concentration,[9] it could have played a role here due to the combination of

higher flow rates, thinner EAB and the lack of an external driving potential, which lowers the relative proton production rate.

4.6. Discussion

Next, we discuss the results presented above with comparisons to the literature. Table 1 summarizes the literature results from other studies using pure cultures of *G. sulfurreducens* EAB in microfluidic MFCs. Included are MFCs with and without membranes to demonstrate that until now, membraneless MFCs have underperformed compared with membrane MFCs, likely due to uncontrolled cross-contamination. In this work, three design features were combined: (i) O_2 elimination without the use of a scavenger, (ii) avoidance of cross-contamination, and (iii) use of graphite electrodes. Implementation of these features together on the same device resulted in the highest power density and the longest operating times to date. The maximum current density obtained in this work was obtained at the relatively high resistance of 10 kΩ, whereas higher currently would likely have been obtained at lower resistances. Table 1 does not include results from mixed-culture or *Geobacter*-enriched EABs, which are generally preferred in the literature due to improved cell potentials related to better tolerance to oxygen. Even among this wider cross-section of the literature, the longest operational times were just over 15 days,[17, 19] although one notable exception is a membraneless microbial electrolysis cell containing pure *G. sulfurreducens* with over 30 days of operation achieved by housing an unprotected PDMS device in a home-built acrylic anaerobic chamber without the use of ferricyanide.[24] Therefore, it appears that the exclusion of ferricyanide might indeed improve gold electrode longevity, whereas the inert graphite electrodes used in this study could still benefit from fast ferricyanide reduction kinetics. We note in passing that L-cysteine is known to form monolayers on gold surfaces,[36] which does not appear to limit the performance of gold electrode MFCs on a short timescale,[19] but it might over longer timescales. In any case, although graphite electrodes should avoid this problem, no O_2 scavenger was used in this work.

Table 4.1: Summarizes the literature results from pure cultures of *G. sulfurreducens* in microfluidic MFCs with and without membranes.

Membrane	µMFC material	Anode material	Cathode material	P_{max} (mW·m^{-2})	I_{max} (mA·m^{-2})	R_{in} Ω	Distance µm	Operation time	Ref
None	PDMS	Gold	Gold	-	18	-	200	-	38
None	PMMA	Gold	Gold	-	65	-	100	7 days	39
Nafion 117	PDMS	Si/CNT	Gold	36	76	25 K	-	-	40
Nafion 212	PMMA	Gold	Gold	120	600	200 K	-	-	41
None	Glass/ PDMS	Graphite	Graphite	456	1100	25 K	6000	6 Months	Our work

Dashes indicate non-reported information

Despite the demonstrated advantages of our system, considerable room for improvement exists considering that the highest performing microfluidic MFCs (0.6, 1.8 and 2.5 $W \cdot m^{-2}$) were also membraneless configurations with graphite electrodes and gas-impermeable plastic materials.[18, 35, 37] These studies benefited from the lowest internal resistances reported in the literature (ca. 1 to 2 kΩ) due to short inter-electrode distances (2 to <1 mm) and thick multispecies EABs (hundreds of microns). Those studies could also benefit from flow, albeit over a small range of flow rates, before reductions in performance were observed, which the authors hypothesized was due to cross-contamination. In contrast, the device presented in this work reached maximum stable power levels without losses at high flow rates. Taken together, it is possible that further optimization can lead to better performance. For example, our goal of limiting acetate contamination at the cathode to 0.05 mM could be relaxed or even maintained with closer electrodes by adjusting $Q_A/Q_C<1$. Other avenues to reducing internal resistance include long-term culture and growth under elevated flow rates to produce compact and conductive EABs.

4.7. Conclusions

The goal of this paper was to implement design enhancements that could produce more consistent performance of membraneless microfluidic MFCs for greater impact among the wider BES community. To this end, we developed an easy-to-fabricate device with optimized

placement of graphite electrodes and O_2 protection. The realization of this device revealed several advantages. Principle among them was the period of continuous operation, which we believe is the most important figure of merit, reflecting overall device stability. The device featured here achieved 6 months of continuous operation before it was sacrificed for SEM, the longest duration yet reported. This is especially significant considering the use of an EAB from pure *G. sulfurreducens* , without an oxygen scavenger. The device stability under flow also appears to have been critical to achieving continuous flow-induced improvements to power outputs without losses at flow rates as high at 200 $mL \cdot h^{-1}$, corresponding to shear forces of more than 1.6 Pa. With assurances that flow-based changes to power output are uncomplicated by device-level instabilities, studies into the critical shear stress required for biofilm erosion can now be undertaken based on the biofilm type or growth history. In addition, other mechanistic studies into molecular transport and conversion kinetics can now be undertaken in a rigorous manner. The next round of technical advancements can target higher performance via optimization of the operating conditions and further design improvements. These improvements can include manipulation of the co-flow interface position to resist the natural tendency of displacement towards the cathode. Closer electrode placement can further reduce internal resistance. Another approach is the introduction of a third inlet for an electrolyte stream with low solution resistance to separate the anolyte and catholyte streams without introducing added internal resistance, as demonstrated previously in a microfluidic chemical fuel cell.[42] Finally, the device should be tested with mixed-species biofilms to expand the range of applicable substrate molecules and to provide better connection with typical macro-MFC studies.

4.8. Experimental Section

4.8.1. Microfabrication Tools and Techniques

Moulds for casting PDMS microchannels were created via photolithography. The microchannel motif was designed using computer aided design software (DraftSightTM, Dassault Systemes, France), and the photomask was printed using a photoplotter (FPS25000, Fortex Engineering Ltd., UK). The photomask was subsequently placed on top of a photoresist layer (SY300 film, Fortex Engineering Ltd., UK) with 160 μm thickness that was previously adhered to a 75×50×1 mm glass slide (12–550 C, Fisher Scientific, Canada) using

a dry film laminator (FL-0304-01, Fortex Engineering Ltd., UK). The photoresist was selectively cross-linked through the mask with a UV exposure system (AY-315, Fortex Engineering Ltd., UK), and excess photoresist was removed using developer and rinse solutions (SY300 Developer/Rinse, Fortex Engineering Ltd., UK). Microfluidic devices were cast against the resulting mould using liquid PDMS and cross-linker (Sylgard184, Dow Corning, Canada) at a 10 to 1 ratio, followed by curing at 70 °C for 4 hours. Inlet and outlet holes were punched through the device, and glass bonding to the PDMS was achieved using air plasma (PCD-001 Harrick Plasma, Ithaca, USA) for 90 seconds at 650 mTorr. Graphite electrodes (GraphiteStore.com Inc., USA) were wrapped in a tight-fitting adhesive barrier to prevent electrode deactivation, which was otherwise observed after contact with liquid PDMS.

4.8.2. *Geobacter sulfurreducens* Preparation and Device Start-Up

All air-sensitive operations were performed in an anaerobic glove box (10 % H_2, 10 % CO_2 and 80 % N_2). *G. sulfurreducens* (wild type, strain PCA, ATCC 51573) were thawed from ceramic beads stored at −80 °C and cultured in a liquid nutrient medium containing fumarate. A maximum of 8 sub-cultures could be generated from one culture. Sub-cultures were used as inoculant solutions that included 40 mM sodium fumarate (as an electron acceptor) to promote growth without the presence of an anode. In addition, the nutrient medium consisted of a sodium acetate carbon source (CH_3COONa (10 mM), NaH_2PHO_4 (3.8 mM), $NaHCO_3$ (30 mM), KCl (1.3 mM), NH_4Cl (28 mM)), a trace mineral supplement (10 $mL \cdot L^{-1}$) (ATCC® MD-TMS™), and a vitamin supplement (10 $mL \cdot L^{-1}$) (ATCC® MD-TMS™). Before use, all nutrient media were sterilized by autoclaving at 110 °C and 20 psi for 20 min. Because sodium fumarate could not be autoclaved, it was added afterwards through a sterilized filter in the glovebox. A second identical solution without fumarate was also prepared as the main nutrient source for use after inoculation to promote growth on the anode. No O_2 scavenger molecules were included in any solutions used in this study.

The MFC anode was inoculated with the sub-culture under a flow rate of 0.5 $mL \cdot h^{-1}$ while a catholyte (30 mM ferricyanide solution in a pH 7.0 sodium phosphate buffer) was co-flowed at 0.5 $mL \cdot h^{-1}$ for 2 h via separate syringe pumps (PhD 2000, Harvard Apparatus, MA). During inoculation, the MFC anode and cathode were connected through an external

resistor R_{ext}=25 kΩ. The inoculum was replaced with a sterilized fumarate-free nutrient medium, and the MFC was allowed to undergo a pre-growth phase for 48 h under the same flow conditions. As a control, all inoculation and pre-growth processes were conducted in a sealed anaerobic enclosure (McIntosh and Filde's, 28029, Sigma-Aldrich) filled with an anaerobic gas (20 % CO_2 and 80 % N_2). All reactors were operated in a temperature-controlled laboratory (23±0.5 °C). Following inoculation, the sub-culture inoculum solution was replaced with the fumarate-free nutrient solution such that only *G. sulfurreducens* that were attached to the anode could complete the Kreb's cycle via anode respiration. Experiments were conducted for 6 months until the device was sacrificed for SEM imaging of the anode-adhered EAB.

4.8.3. Electrochemical measurements

All electrochemical Measurements were collected during a continuous feed of anolyte and catholyte through the microfluidic MFC. A microcontroller data acquisition system (Atmega328pMmicrochip Technologies, Arizona, USA) was used to measure the voltage V at intervals of every 10 min across an external resistor R_{ext} (Ω) connecting the anode and the cathode. The potential drop measurements could be transformed into current measurements using Ohm's law:

$$I=V/R_{ext} \quad \text{(Eqn. 4.1)}$$

The power density was measured via two methods. The first used a commercial potentiostat (VersaSTAT 4, Princeton Applied Research, Oak Ridge, USA) that automatically switched R_{ext} values while measuring the voltage drop to obtain polarisation curves using Eqn. 1 and power density curves using Eqn. 2:

$$P = V^2/R_{ext} \quad \text{(Eqn. 4.2)}$$

The maximum power with this technique is obtained when R_{ext} is equivalent to the internal resistance (R_{int}). Due to the long duration of this experiment, a faster second approach was used in which the potential drop was continuously measured across a single external resistor (with $R_{ext} = R_{int}$) and power was calculated using Eqn. 2. Each week the power curves were acquired via the first method to ensure to verify the R_{int} within measurement accuracy, so

that R_{ext} could be properly set. Measurements of power density ($P_{density}$) were obtained by dividing $P_{density}$ from Eqn. 2 by the exposed electrode area in the channel, A = 30 mm^2:

$$P_{density} = P/A \quad \text{(Eqn. 4.3)}$$

4.8.4. UV/Vis Measurements of O_2 Indicator Resazurin

The presence of O_2 in the microfluidic MFC was measured using a standard 0.15 $mg \cdot L^{-1}$ aqueous solution of the indicator resazurin.[43] Each device was injected with the resazurin solution using two air-tight glass syringes connected to the inlets, and samples were collected using one glass syringe at the outlet. Approximately 2–3 mL of the resazurin solution were collected from the outlet, and absorbance spectra were measured via UV-Vis spectrophotometry (Shimadzu, UV-2450 spectrophotometer, Japan) for analysis of peak position and intensity. An O_2-purged glovebox was used during the transfer to an air-tight UV-Vis cuvette. All experiments and measurements were conducted at 23±0.5 °C.

4.8.5. Imaging

Optical microscopy was used to observe H_2O evaporation through the MFC walls based on the appearance of air bubbles after the flow was stopped. The air volume of the air space in the channel was quantified by image analysis using ImageJ v1.51 (National Institute of Health, USA). Scanning electron microscopy (SEM) analysis was performed at the end of experiment to confirm *Geobacter* attachment to the anode and to visualize and measure the EAB height. The anode-adhered EAB was fixed by washing with 2.5 % glutaraldehyde in a phosphate buffer solution (flow rate of Q=0.5 $mL \cdot h^{-1}$) for 2 h before the electrode was removed from the device. After electrode removal, the EAB was placed in the fixation solution overnight and subsequently transferred to a solution with 1 % osmium tetroxide for 1.5 h before a final washing with pure PBS buffer (pH 7.4). The sample was dehydrated in a series of aqueous ethanol solutions for 15 min each, starting with equal parts ethanol and water and ending with 100 % ethanol. A thin layer of gold metal was applied on dried samples using a sputter coater (Nanotech, SEM PREP 2) prior to SEM imaging (JEOL JSM-6360 LV).

4.8.6. Flow Simulations

Computational studies of the anolyte and catholyte co-flow properties at a variety of flow rates were accomplished using three-dimensional simulations (COMSOL Multiphysics 4.2a, Stockholm, Sweden). A fine mesh was used with physics for laminar flow and transport of dilute species in an incompressible liquid. The molecular diffusion values applied for ferrocyanide and acetate molecules were $D_{Fe}=1.2\times10^{-5}\ cm^2\cdot s^{-1}$ and $D_{Ac}=7\times10^{-6}\ cm^2\cdot s^{-1}$, respectively.

4.9. Acknowledgements

The authors thank Luc Trudel and Laurent Smith (U. Laval) for their help with culture of G. sulfurreducens and Richard Janvier (U. Laval) for technical assistance with SEM. This research was supported by generous funds from the Natural Sciences and Engineering Research Council of Canada, the Canadian Foundation for Innovation and Sentinel North. Greener is the recipient of an early researcher award from the Fonds de Recherche du Quebec – Nature et Technologies. Greener (high risk, high reward) to study microbiological systems using microfluidics. The authors also thank Molly K. Gregas for assistance with technical edits.

4.10. Electronic supplementary information:

Sections:

S1. Resazurin O_2 indicator

S2. Simulations

S3. Long-term voltage measurements

S4. Scanning electron microscopy

4.10.1. Section S1-Resazurin O_2 indicator

Figure 4.S1 shows the colour response of a resazurin O_2 indicator solution in bulk by eye and by spectrophotometry as it passes from purely anaerobic conditions (colourless) to mono- (pink) and di-oxygenated (blue) states during exposure to ambient air conditions. Resazurin has one of the highest Kreft's dichromaticity index,[1] meaning the perceived change in colour hue is high, making it very sensitive to low O_2 concentrations. For example, the onset of pink occurs at pseudoanaerobic conditions. The main paper presents results using the same solution to verify the suitability of the O_2 protection barrier for the anaerobic microfluidic MFC demonstrated in this work.

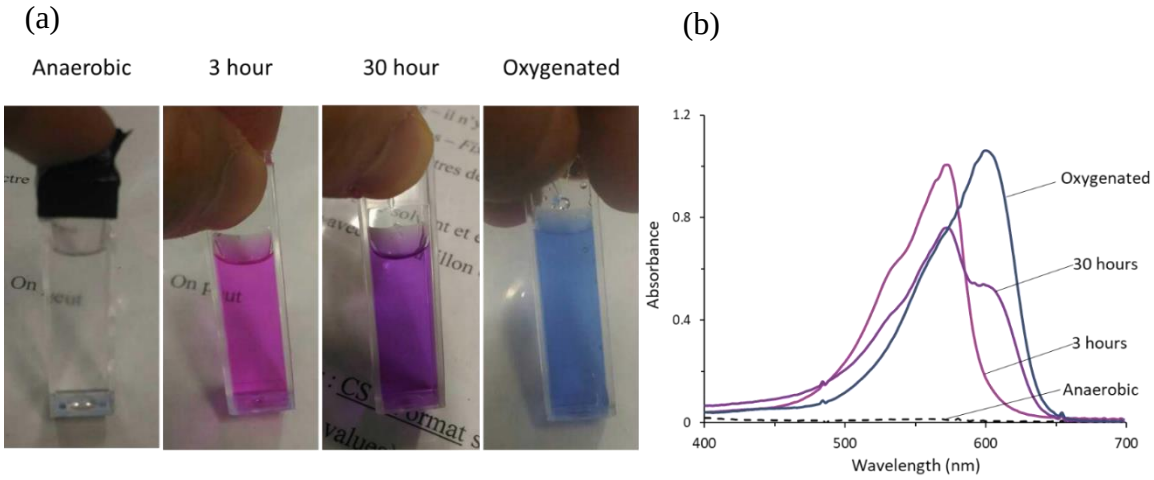

Figure 4. S1. (a) Qualitative changes to resazurin solution under indicated exposure times to ambient (oxygenated) air conditions. (b) Corresponding UV-Vis spectra.

4.10.2. Section S2-Simulations

This section shows a series of hydrodynamic simulations using Comsol Multiphysics with physics for flow of incompressible fluid flow and diffusion mass transport of dilute solutes. Figure 4.S2 shows results from a simulation within the microfluidic MFC used in this study featuring an EAB with height h_B = 80 μm (see schematic of the channel cross-section, Figure 4.S2a) and the resulting displacement of the anolyte toward the cathode chamber (Figure 4. S2b). It is clear from Figure 4.S2c that deflection of flow streamlines are primarily responsible for the co-flow interface position. Figure 4.S2d shows the z-component of flow velocity (v_z), which is mostly zero throughout the channel except near the anode-adhered EAB. This can be due to a combination of Dean vortices and pressure imbalances. While small, approximately 1000 times less than the downstream component of velocity (v_y), this could have an important impact on mixing especially for electrode that are closely spaced.

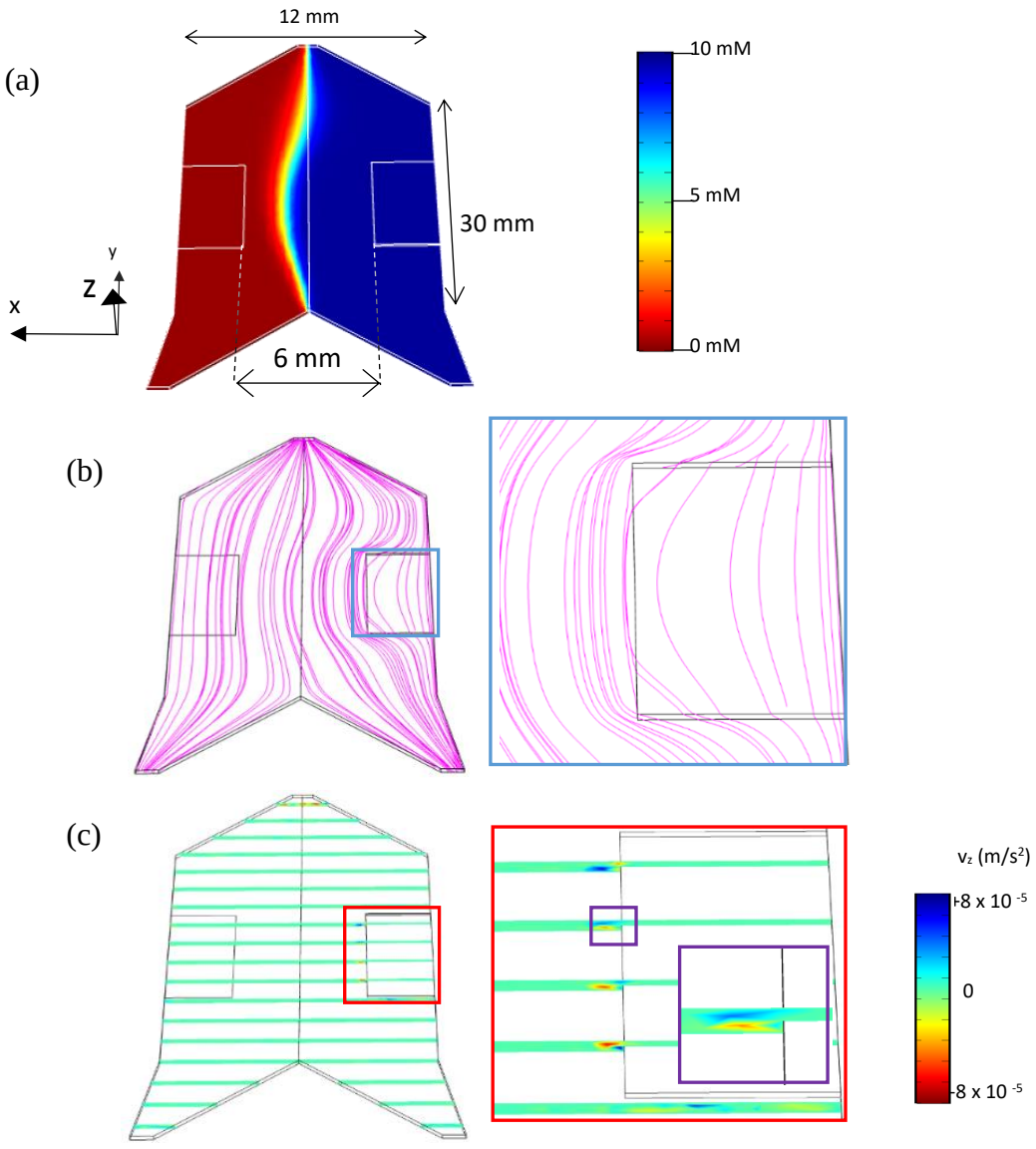

Figure 4.S2. Simulations of chemical and hydrodynamic profiles in a microfluidic MFC with the same design as was used in the experimental work. (a) Schematic showing the device cross-section with embedded electrodes and an anode-adhered electroactive biofilm protruding from the anode surface. (b) Concentration profile of a 10 mM acetate anolyte solution (blue) imposed against a catholyte solution (red) consisting of 0 mM acetate and 30 mM ferricyanide catholyte solution (not shown). (c) Fluid streamlines showing deflection around the electrode adhered EAB, with zoom view in the inset of the blue highlighted area in the main figure. (d) Secondary flow velocity profiles in the zdirection at the edge of the bio-anode, with two inset zoom views from red and purple highlighted zones. Z-component velocities are blue (negative direction) red (positive direction) near the electrode, and zero (green) elsewhere. Simulation conditions in (b)-(d) were the same in all cases, anode-adhered electroactive biofilm thickness, h_B = 80 µm, and flow rate, Q_T=20 mL/h, with Q_A/Q_C = 1. Electrodes were placed at the channel mid-position with a downstream length of 1 cm and anode-cathode separation of 6 mm. Channel dimensions are shown in (b).

Simulations on the position and width of the anolyte/catholyte co-flow interface were conducted under balanced flow conditions ($Q_A/Q_C=1$) with variable h_B. Based on the literature values, we repeated the simulations, anode-adhered EABs ranged from 10 to 80 μm (Figure 4.S3). As expected, increases to h_B tend to push the co-flow position closer to the cathode. It is observed that the mixing region at the interface increased with h_B. This is somewhat counter intuitive because the local fluid velocity should increase with h_B because of local decreases to the channel volume, reducing liquid transit times and diffusion distances. However, as discussed above, mass transport perpendicular to the flow channel, is not strictly diffusion limited, but includes secondary flow profiles in the z and x directions, including the likelihood for vortices near the EAB/liquid interface. Though not completely analogous with the present case where we include the presence of an anode-adhered EAB, this result agrees with previous simulations showing that structured electrodes in a membraneless device.[2] In short, the thickness of the anode-adhered EAB must be accounted for in simulations of the position of both the co-flow interface, and its width.

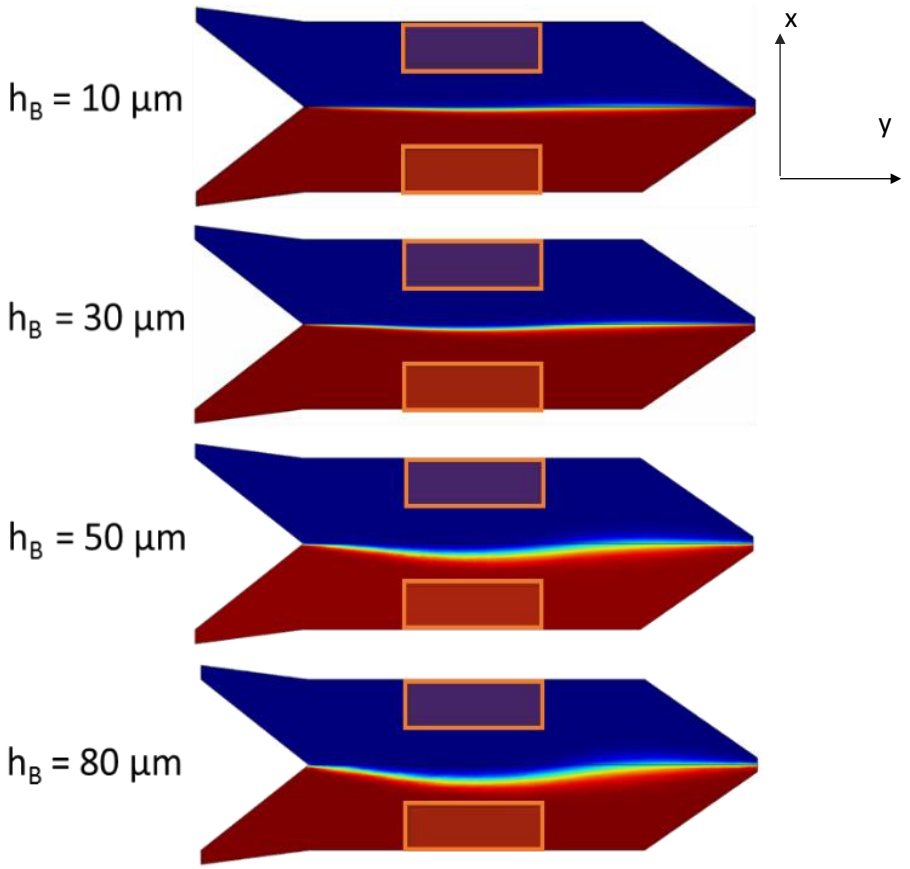

Figure 4.S3. Effect of h_B on concentration gradient and position under balanced flow of the anolyte (blue) and catholyte (red) under balanced flow conditions, Q_A/Q_C=1 and Q_T = 20 mL·h^{-1}.

Figure 4.S4. shows the x-y contours for acetate concentrations of 5 mM and 0.05 mM. These two concentrations represent the mid-point between the two solution streams and the lowest acceptable crossover concentration, respectively. As expected, the displacement of the co-flow interface was less pronounced for h_B = 10 µm (Figure 4.S4a) than for h_B = 80 µm (Figure 4.S4b). The co-flow midpoint could be displaced by up to 1 mm (for h_B = 80 µm), whereas the low-concentration threshold contour could extend an additional 1 to 2.5 mm further (for h_B = 10 and 80 µm, respectively). In addition, each experiment was conducted at two extreme flow rates of Q_T = 1 and 140 mL·h^{-1}. Lower flow rates resulted in slightly pronounced displacement distances, likely due to longer diffusion times, although subtle effects related to secondary flow could also have played a role.

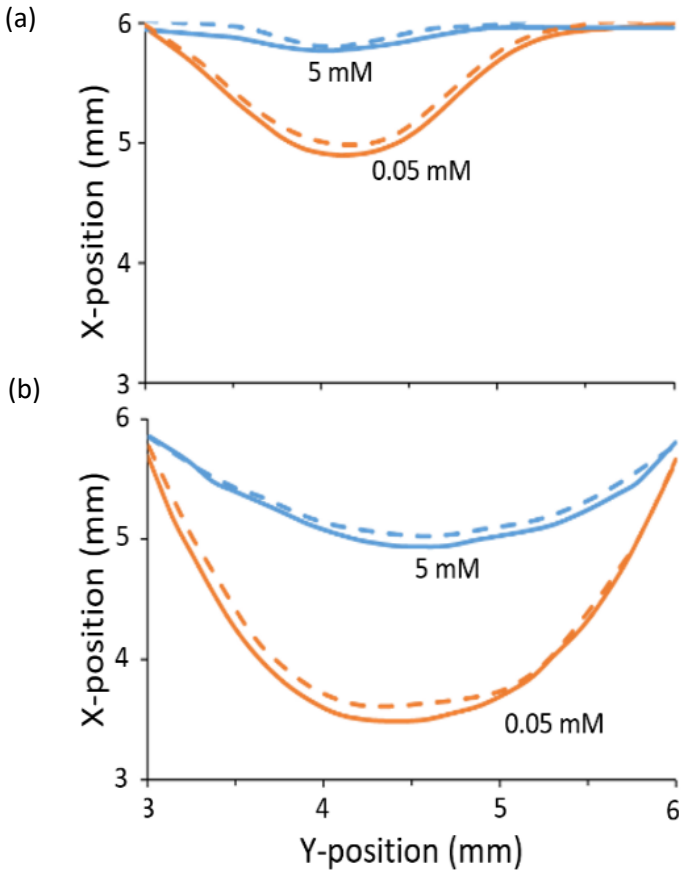

Figure 4.S4. Displacement of the co-flow interface for membraneless MFCs around an electrode-adhered EAB (edge at 6 mm) with EAB height h_B = 10 µm (a) and h_B = 80 µm (b). Acetate concentration contours are shown for 5 mM (blue) and 0.05 mM (orange) at total flow rates of 1 and 140 mL·h^{-1}, with both inlet flow rates held equal. The xand y-coordinates on the plot axes correspond to the directions perpendicular and co-linear to the channel length, as shown in Fig S3a.

In Figure 4.5a we consider the effect of unbalanced flow ($Q_A/Q_C \neq 1$) to determine the acceptable range of flow rate ratios Q_A/Q_C or Q_C/Q_A, for which the positioning of certain threshold contours was directly adjacent to (but not touching) the cathode (Figure 4.S5b) or bio-anode (Figure 4.S5c), respectively, as h_B increased from 10 to 80 µm. For example, for Q_A = 20 mL·h^{-1} and Q_C = 10 mL·h^{-1} (flow rate ratio of Q_A/Q_C = 2) placed the the 0.05 mM acetate (0.5% of the inlet concentration) the position in Figure 4.S5b for h_B = 10 µm. This position remained unchanged independent of total flow rates as long as flow rate ratio and h_B were constant. As h_B increased, so too did the propensity for flow deflection around the anode-adhered EAB, requiring progressively lower values of Q_A/Q_C to maintain the 0.05 mM

acetate concentration contour in the same position. Other 0.05 mM contour lines, could be positioned in the same place as shown in Figure 4.5b for any any h_B value by adjusting the flow rate ratio as shown in Figure 4.S5a (open blue symbols). Higher concentrations of contaminating anolyte at the cathode occurred for larger flow imbalances (larger values of Q_A/Q_C) but followed the same trend. For example, Figure 4.5a (open green symbols) shows Q_A/Q_C values required to position the 5 mM acetate concentration contour (50% of the inlet concentration) at the cathode. Contamination of the anode by the catholyte became more difficult as h_B values increased due to the natural tendency to deflect the flow streamlines away from that side of the device (Figure 4.5a, solid symbols). Unlike the acetate concentration contours adjacent to the cathode, those adjacent to the anode were strongly dependent on h_B, showing a tendency to "surround" the anode for large h_B values due to the tendency of the anolyte stream to cause local deflections of streamlines away from the channel wall (Figure 4.5c). This effect was not observed for low h_B, similar to concentration profile in Figure 4.S5b, because of the lack of EAB is present. The shaded parts of the curves in Figure 4.5a show the range of flow rate ratios that could achieve confinement of the specified acetate and ferricyanide concentration thresholds (expressed as a percentage of inlet concentration) between the cathode and anode.

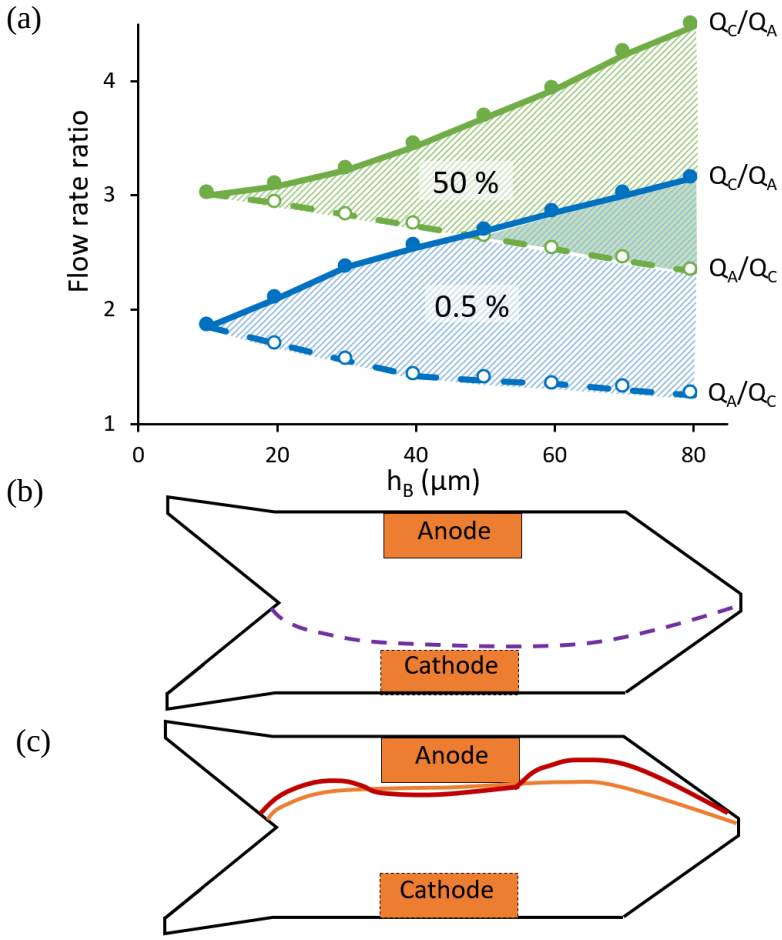

Figure 4.S5. (a) Flow rate ratios required for positioning of 0.05 mM acetate (0.5% of inlet concentration, blue) and 5 mM acetate (50% of inlet concentration, green) contour lines near the cathode (dashed lines, open circles) and the 0.15 mM ferricyanide (0.5% of inlet concentration, blue) and the 15 mM ferricyanide (50% of inlet concentration, green) contour lines adjacent to the anode (solid lines, filled circles). The definition of the flow rate ratio is indicated for cathode- and anode-adjacent concentration profiles. Typical cathode- (b) and anode-adjacent (c) concentration contours. (b) is valid for all h_B values. (c) Anode-adjacent contours for (i) h_B = 10 µm and Q_C/Q_A = 2 (orange) and (ii) h_B = 80 µm and Q_C/Q_A = 3.3 (red).

Finally, computer simulations results show that the average shear stress across the top of the EAB showed linear increases with total flow rate (Q_T) and with h_B, in Figure 4.S6a and S6b, respectively. As this is the first results, to our knowledge, which include the role of h_B on the shear stress values, we include for comparison, results for h_B = 0, the effective conditions modeled where biofilm height is not included in the simulation.[2] In Figure 4.S6b, we see that this trend is also linear with h_B, when keeping Q_T constant.

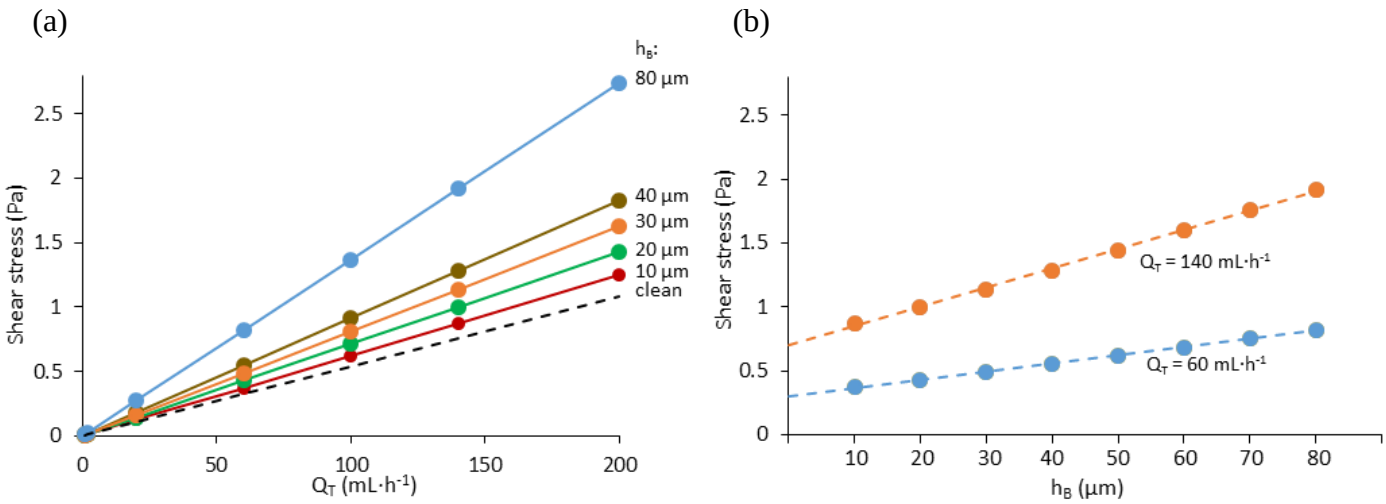

Figure 4.S6. Effect of flow rate and EAB height on shear stress. (a) Changes in shear stress as a function of total flow rate (Q_T) for EAB heights h_B = 10, 20, 30, 40, 80 µm. Dashed line shows results for no EAB (h_B = 0). Linear fits are shown (solid lines) with R^2 = 1 in all cases. (b) Trends in shear stress as a function of h_B for two selected total flow rates Q_T = 60 and 140 mL·h^{-1}. Linear fit is shown (dashed lines) with R^2 = 0.998. Flow rate ratio was Q_A/Q_C = 1 in all cases.

4.10.3. Section S3-Long-term voltage measurements

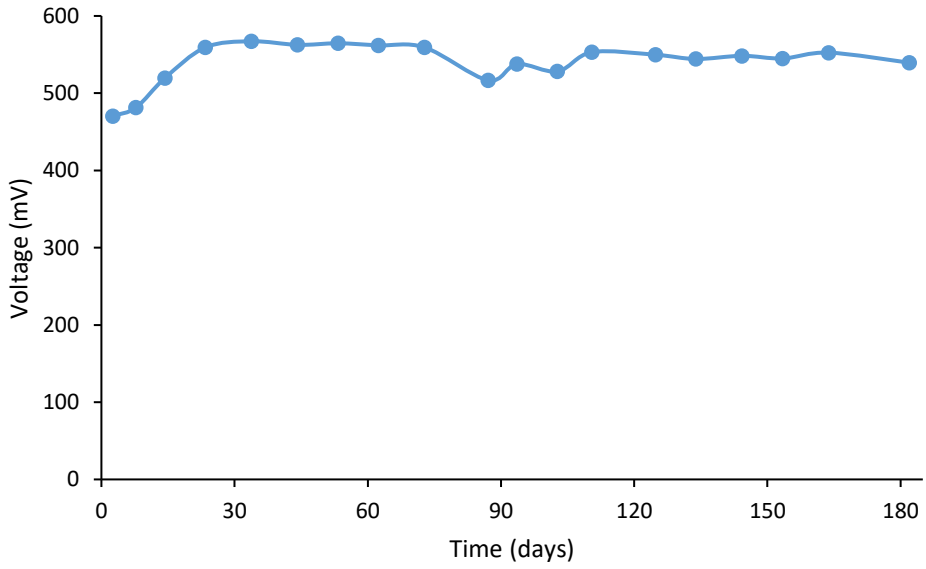

Figure 4.S7. Potential measurements across R_{ext} = 25 kΩ following the end of Figure 4.6a (main paper). Here, t = 0 represents 40 h after exposing the MFC to ambient conditions.

4.10.4. Section S4-Scanning electron microscopy

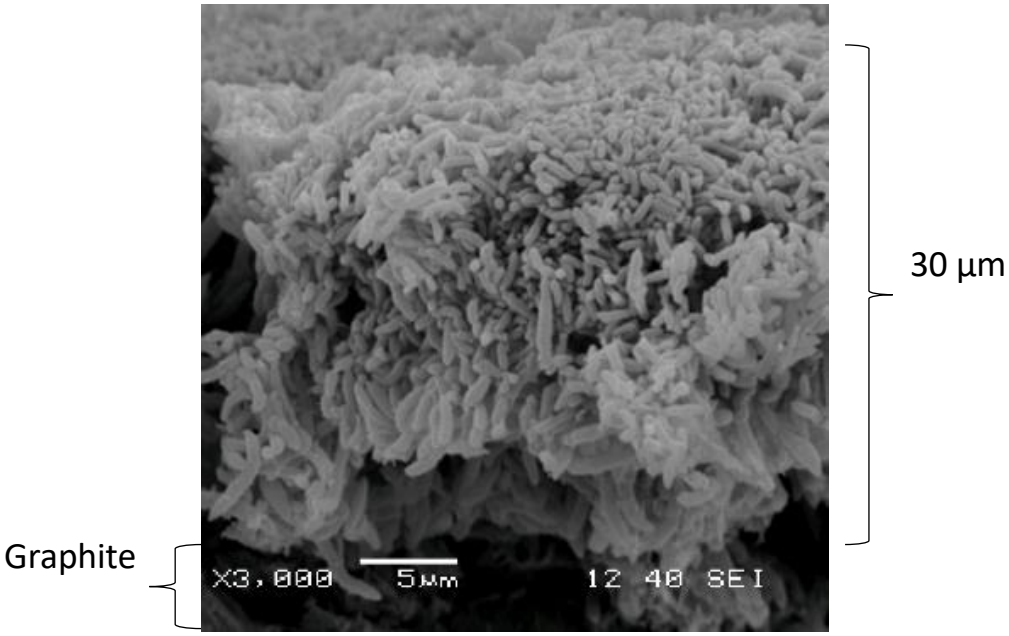

Figure 4.S8. SEM of an anode-adhered EAB.

4.11. Appendix (the Front Cover):

shows a real microfluidic microbial fuel cell (MFC) used in this study. Three graphical elements are superimposed to highlight critical design enhancements over previous literature examples. These include an oxygen protection barrier, embedded graphite electrodes for robust operation and faster redox kinetics, as well as computer simulations to reduce anolyte/catholyte cross-over to the opposite electrode. Bringing these improvements together into the same platform offers new opportunities to bridge the gap between the micro- and macro-MFC studies:

ChemElectroChem

Chemistry Europe

European Chemical Societies Publishing

Front Cover:
M. A. Amirdehi et al.
A High-Performance Membraneless Microfluidic Microbial Fuel Cell for Stable, Long-Term Benchtop Operation under Strong Flow

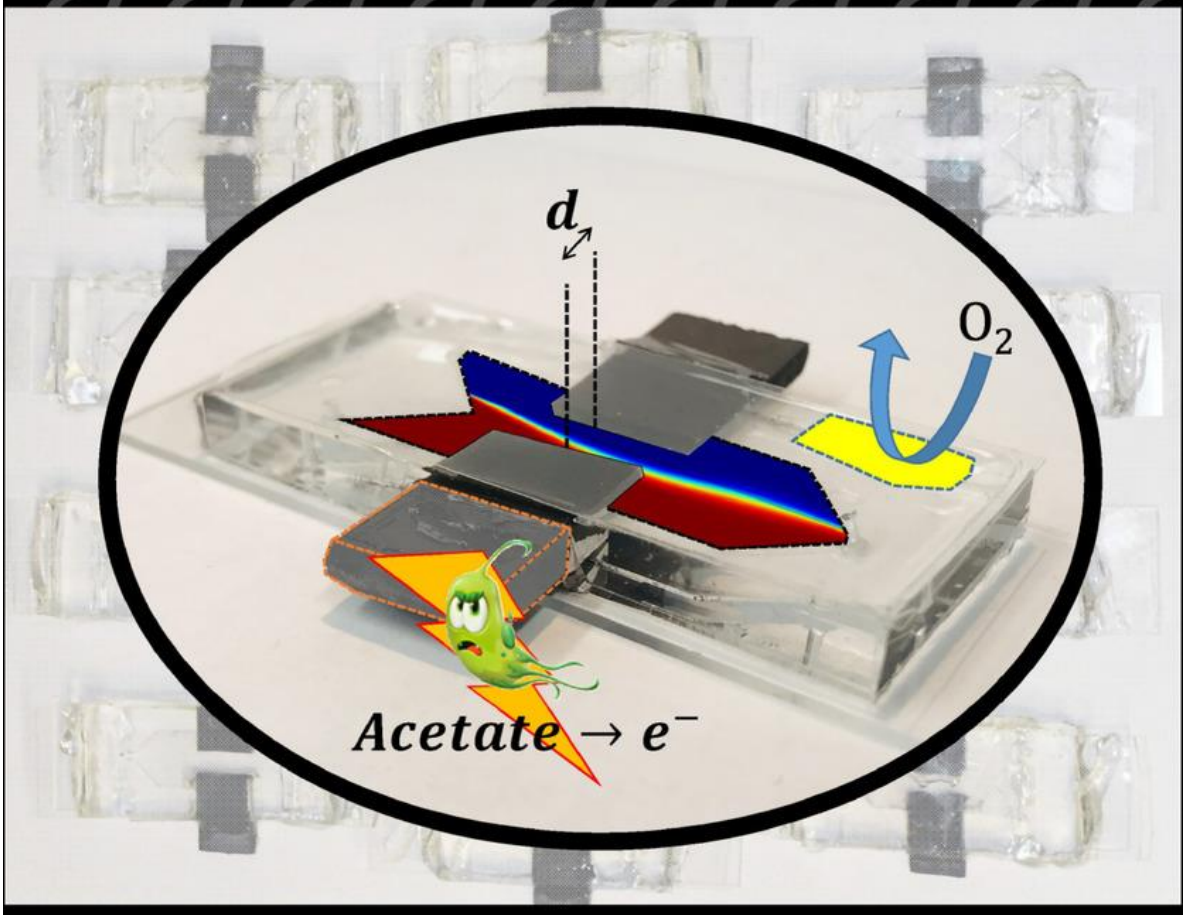

10/2020

WILEY-VCH

4.12. Bibliography

1. Weibel, D. B.; DiLuzio, W. R.; Whitesides, G. M., Microfabrication meets microbiology. *Nature Reviews Microbiology* **2007,** *5* (3), 209.

2. Andersson, H.; Van den Berg, A., Microfluidic devices for cellomics: a review. *Sensors and actuators B: Chemical* **2003,** *92* (3), 315-325.

3. Beebe, D. J.; Mensing, G. A.; Walker, G. M., Physics and applications of microfluidics in biology. *Annual review of biomedical engineering* **2002,** *4* (1), 261-286.

4. Pousti, M.; Zarabadi, M. P.; Amirdehi, M. A.; Paquet-Mercier, F.; Greener, J., Microfluidic bioanalytical flow cells for biofilm studies: a review. *Analyst* **2019,** *144* (1), 68-86.

5. Krieg, T.; Sydow, A.; Schröder, U.; Schrader, J.; Holtmann, D., Reactor concepts for bioelectrochemical syntheses and energy conversion. *Trends in biotechnology* **2014,** *32* (12), 645-655.

6. Rabaey, K.; Angenent, L.; Schroder, U.; Keller, J., *Bioelectrochemical systems*. IWA publishing: 2009.

7. Lovley, D. R., Live wires: direct extracellular electron exchange for bioenergy and the bioremediation of energy-related contamination. *Energy & Environmental Science* **2011,** *4* (12), 4896-4906.

8. Zarabadi, M. P.; Couture, M.; Charette, S. J.; Greener, J., A Generalized Kinetic Framework Applied to Whole-Cell Bioelectrocatalysis in Bioflow Reactors Clarifies Performance Enhancements for Geobacter Sulfurreducens Biofilms. *ChemElectroChem* **2019,** *6* (10), 2715-2718.

9. Zarabadi, M. P.; Charette, S. J.; Greener, J., Flow-Based Deacidification of Geobacter sulfurreducens Biofilms Depends on Nutrient Conditions: a Microfluidic Bioelectrochemical Study. *ChemElectroChem* **2018,** *5* (23), 3645-3653.

10. Zarabadi, M. P.; Charette, S. J.; Greener, J., Toggling Geobacter sulfurreducens metabolic state reveals hidden behaviour and expanded applicability to sustainable energy applications. *Sustainable Energy & Fuels* **2019**.

11. Mardanpour, M. M.; Yaghmaei, S.; Kalantar, M., Modeling of microfluidic microbial fuel cells using quantitative bacterial transport parameters. *Journal of Power Sources* **2017,** *342*, 1017-1031.

12. Mardanpour, M. M.; Yaghmaei, S., Dynamical analysis of microfluidic microbial electrolysis cell via integrated experimental investigation and mathematical modeling. *Electrochimica Acta* **2017,** *227*, 317-329.

13. Logan, B. E.; Rabaey, K., Conversion of wastes into bioelectricity and chemicals by using microbial electrochemical technologies. *Science* **2012,** *337* (6095), 686-690.

14. Lovley, D. R., Bug juice: harvesting electricity with microorganisms. *Nature Reviews Microbiology* **2006,** *4* (7), 497.

15. Ren, H.; Torres, C. I.; Parameswaran, P.; Rittmann, B. E.; Chae, J., Improved current and power density with a micro-scale microbial fuel cell due to a small characteristic length. *Biosensors and Bioelectronics* **2014,** *61*, 587-592.

16. Vigolo, D.; Al-Housseiny, T. T.; Shen, Y.; Akinlawon, F. O.; Al-Housseiny, S. T.; Hobson, R. K.; Sahu, A.; Bedkowski, K. I.; DiChristina, T. J.; Stone, H. A., Flow dependent performance of microfluidic microbial fuel cells. *Physical Chemistry Chemical Physics* **2014,** *16* (24), 12535-12543.

17. Yoon, J. Y.; Ahn, Y.; Schröder, U., Parylene C-coated PDMS-based microfluidic microbial fuel cells with low oxygen permeability. *Journal of Power Sources* **2018,** *398*, 209-214.

18. Ye, D.; Yang, Y.; Li, J.; Zhu, X.; Liao, Q.; Deng, B.; Chen, R., Performance of a microfluidic microbial fuel cell based on graphite electrodes. *international journal of hydrogen energy* **2013,** *38* (35), 15710-15715.

[19] Choi, S.; Lee, H.-S.; Yang, Y.; Parameswaran, P.; Torres, C. I.; Rittmann, B. E.; Chae, J., A μL-scale micromachined microbial fuel cell having high power density. *Lab on a Chip* **2011,** *11* (6), 1110-1117.

[20] Shaegh, S. A. M.; Nguyen, N.-T.; Chan, S. H., A review on membraneless laminar flow-based fuel cells. *International Journal of Hydrogen Energy* **2011,** *36* (9), 5675-5694.

[21] (a) ElMekawy, A.; Hegab, H. M.; Dominguez-Benetton, X.; Pant, D., Internal resistance of microfluidic microbial fuel cell: challenges and potential opportunities. *Bioresource technology* **2013,** *142*, 672-682. (b) Goel, S. From waste to watts in micro-devices: Review on development of Membraned and Membraneless Microfluidic Microbial Fuel Cell. *Applied Materials Today* **2018**, *11*, 270-279.

[22] Biffinger, J.; Ribbens, M.; Ringeisen, B.; Pietron, J.; Finkel, S.; Nealson, K., Characterization of electrochemically active bacteria utilizing a high-throughput voltage-based screening assay. *Biotechnology and bioengineering* **2009,** *102* (2), 436-444.

[23] Moß, C., Patil, S. A., & Schröder, U. Scratching the Surface—How Decisive Are Microscopic Surface Structures on Growth and Performance of Electrochemically Active Bacteria?. *Frontiers in Energy Research* **2019**, 7, 18.

[24] Li, Z.; Venkataraman, A.; Rosenbaum, M. A.; Angenent, L. T., A Laminar-Flow Microfluidic Device for Quantitative Analysis of Microbial Electrochemical Activity. *ChemSusChem* **2012,** *5* (6), 1119-1123.

[25] Mardanpour, M. M.; Yaghmaei, S., Characterization of a microfluidic microbial fuel cell as a power generator based on a nickel electrode. *Biosensors and Bioelectronics* **2016,** *79*, 327-333.

[26] Yang, Y.; Ye, D.; Li, J.; Zhu, X.; Liao, Q.; Zhang, B., Microfluidic microbial fuel cells: from membrane to membrane free. *Journal of Power Sources* **2016,** *324*, 113-125.

27. Ren, H.; Lee, H.-S.; Chae, J., Miniaturizing microbial fuel cells for potential portable power sources: promises and challenges. *Microfluidics and Nanofluidics* **2012,** *13* (3), 353-381.

28. Abbaszadeh Amirdehi, M.; Saem, S.; Zarabadi, M. P.; Moran-Mirabal, J. M.; Greener, J., Microstructured Anodes by Surface Wrinkling for Studies of Direct Electron Transfer Biofilms in Microbial Fuel Cells. *Advanced Materials Interfaces* **2018,** *5* (13), 1800290.

29. Logan, B. E., *Microbial fuel cells*. John Wiley & Sons: 2008.

30. Richter, H.; Nevin, K. P.; Jia, H.; Lowy, D. A.; Lovley, D. R.; Tender, L. M., Cyclic voltammetry of biofilms of wild type and mutant Geobacter sulfurreducens on fuel cell anodes indicates possible roles of OmcB, OmcZ, type IV pili, and protons in extracellular electron transfer. *Energy & Environmental Science* **2009,** *2* (5), 506-516.

31. Choi, S., Microscale microbial fuel cells: Advances and challenges. *Biosensors and Bioelectronics* **2015,** *69*, 8-25.

32. Zarabadi, M. P.; Paquet-Mercier, F. o.; Charette, S. J.; Greener, J., Hydrodynamic Effects on Biofilms at the Biointerface Using a Microfluidic Electrochemical Cell: Case Study of Pseudomonas sp. *Langmuir* **2017,** *33* (8), 2041-2049.

33. Merkel, T.; Bondar, V.; Nagai, K.; Freeman, B. D.; Pinnau, I., Gas sorption, diffusion, and permeation in poly (dimethylsiloxane). *Journal of Polymer Science Part B: Polymer Physics* **2000,** *38* (3), 415-434.

34. Yang, Y.; Ye, D.; Liao, Q.; Zhang, P.; Zhu, X.; Li, J.; Fu, Q., Enhanced biofilm distribution and cell performance of microfluidic microbial fuel cells with multiple anolyte inlets. *Biosensors and Bioelectronics* **2016,** *79*, 406-410.

35. Chen, J. L.; Steele, T. W.; Stuckey, D. C., Modeling and application of a rapid fluorescence-based assay for biotoxicity in anaerobic digestion. *Environmental science & technology* **2015,** *49* (22), 13463-13471.

36. Arrigan, D. M., A study of L-cysteine adsorption on gold via electrochemical desorption and copper (II) ion complexation. *Analyst* **1999,** *124* (11), 1645-1649.

37. Yang, Y.; Ye, D.; Li, J.; Zhu, X.; Liao, Q.; Zhang, B., Biofilm distribution and performance of microfluidic microbial fuel cells with different microchannel geometries. *International Journal of Hydrogen Energy* **2015,** *40* (35), 11983-11988.

38. Li, Z.; Zhang, Y.; LeDuc, P. R.; Gregory, K. B., Microbial electricity generation via microfluidic flow control. *Biotechnology and bioengineering* **2011,** *108* (9), 2061-2069.

39. Fraiwan, A.; Call, D. F.; Choi, S., Bacterial growth and respiration in laminar flow microbial fuel cells. *Journal of Renewable and Sustainable Energy* **2014,** *6* (2), 023125.

40. Inoue, S.; Parra, E. A.; Higa, A.; Jiang, Y.; Wang, P.; Buie, C. R.; Coates, J. D.; Lin, L., Structural optimization of contact electrodes in microbial fuel cells for current density enhancements. *Sensors and Actuators A: Physical* **2012,** *177*, 30-36.

41. Parra, E.; Lin, L. In *Microbial fuel cell based on electrode-exoelectrogenic bacteria interface,* 2009 IEEE 22nd International Conference on Micro Electro Mechanical Systems, IEEE: 2009; pp 31-34.

42. Sun, M.; Casquillas, G. V.; Guo, S.; Shi, J.; Ji, H.; Ouyang, Q.; Chen, Y., Characterization of microfluidic fuel cell based on multiple laminar flow. *Microelectronic Engineering* **2007,** *84* (5-8), 1182-1185.

43. Morris, J. M.; Fallgren, P. H.; Jin, S., Enhanced denitrification through microbial and steel fuel-cell generated electron transport. *Chemical Engineering Journal* **2009,** *153* (1-3), 37-42.

Chapter 5: Microfluidics to studies power overshoot in a microbial fuel cells: symptoms to solutions

5.1. Résumé

Nous présentons la première observation rapportée de dépassement de puissance dans une pile à combustible microbienne (MFC) de *G. sulfurreducens* en culture pure. Les observations ont été recueillies dans une plate-forme microfluidique MFC sans membrane fonctionnant dans des conditions idéales, ce qui a permis de multiples enquêtes sur la source du dépassement et les interventions qui ont conduit à son atténuation. Pour sonder précisément l'effet de ces interventions, nous avons quantifié le degré de dépassement à l'aide de mesures de la densité de courant «double retour» lors d'un balayage de polarisation. Dans le premier ensemble d'expériences, nous avons tiré parti de la capacité supérieure de contrôler les conditions hydrodynamiques dans l'application de l'érosion par cisaillement aux couches externes du biofilm et de la modulation du transport de masse par advection vers le biofilm. Dans les deux cas, le degré de dépassement a été considérablement réduit mais pas éliminé. De plus, nous avons vérifié que l'acclimatation sous de faibles résistances externes pouvait presque éliminer le dépassement. Enfin, une approche d'acclimatation in situ a été démontrée. En tirant parti du flux continu de nutriments frais, les courbes de récupération de tension ont été examinées lors de l'application de différentes résistances externes dans des balayages de polarisation à longue tenue. En utilisant ces données, les courbes de polarisation et de densité de puissance ont été reconstruites en fonction de différents degrés de récupération de tension. En plus de fournir une perspective unique sur le rôle de l'acclimatation sous différents débits, les courbes de densité de puissance reconstruites offrent une voie vers l'optimisation du protocole de mesure qui pourrait éliminer le dépassement et améliorer les performances de mesure. Dans ce travail, les améliorations spécifiques de la puissance maximale et du courant par rapport à une étape d'acclimatation de pré-mesure MFC standard étaient de 20% et 45%, respectivement.

5.2. Abstract

We present the first reported observation of power overshoot in a pure culture *G. sulfurreducens* microbial fuel cell (MFC). The observations were collected in a membraneless microfluidic MFC platform operating under ideal conditions, which enabled multiple investigations into the source of the overshoot and interventions that led to its alleviation. To accurately probe the effect of these interventions, we quantified the degree of overshoot using measurements of the current density "double back" during a polarization scan. In the first set of experiments, we leveraged the superior ability to control the hydrodynamic conditions in application of shear erosion to the biofilm outer layers and modulation of advective mass transport to the biofilm. In both cases, the degree of overshoot was significantly reduced but not eliminated. Additionally, we verified that acclimation under low external resistances could nearly eliminate overshoot. Finally, an approach to *in situ* acclimation was demonstrated. By taking advantage of the continuous flow of fresh nutrient, the voltage recovery curves were examined during application of different external resistances in long-hold polarization scans. Using this data, the polarization and power density curves were reconstructed based on different degrees of voltage recovery. In addition to providing a unique perspective on the role of acclimation under different flow rates, the reconstructed power density curves offer a route to measurement protocol optimization that could eliminate overshoot and improve measurement performance. In this work, the specific improvements in maximum power and current over a standard MFC pre-measurement acclimation step were 20% and 45%, respectively.

5.3. Introduction

Microbial fuel cells (MFCs) are a high-priority sustainable technology due to their ability to simultaneously clean waste water and produce usable power.[1,2] Next generation systems require reliable performance assessment, which is not as straightforward as in other electrochemical systems because this technology relies on living electrode-adhered biofilms (EABs).[3,2] A typical problem for MFCs is the onset of so-called "overshoot" behaviour[4] in which tandem reductions in power and current occur at low external resistance (or high applied potentials) in linear sweep voltammetry.[5] Generally, overshoot leads to underestimation of the maximum power density and maximum current density (although in certain instances, the opposite can occur if data acquisition is too fast).[6] Other than more frequent (but not exclusive) occurrence in immature and underperforming [6] MFCs, the exact reason for the transition to overshoot behaviour is not known. Overshoot in healthy mature EABs can be triggered by low nutrient concentrations, low ionic strengths, weak buffers or low pH,[6,7] but once overshoot is established in mature MFCs under standard conditions, adjustment of these parameters cannot solve the problem. Although the role of flow is generally not considered important because overshoot can persist under stirring, stronger evidence is merited.[4,7] Indeed, no proven methods are available to reverse the tendency to display overshoot after it has been established, but many reliable methods exist to avoid related measurement artifacts. With the exception of multi-MFC coupling strategies,[5] most strategies to ameliorate and overcome overshoot are via pre-measurement acclimation to a high current conditions using a single low R_{ext}[8] or high anode potential.[9] Acclimation can also be accomplished via repeated polarization scans at each individual external resistance, but this is a time-consuming effort in bulk MFCs because it requires a full batch-fed cycle for each R_{ext}.[10] Therefore, most groups routinely subject MFCs to a pre-measurement acclimation step before polarization scans, regardless of the tendency to demonstrate overshoot or not.

The origins of overshoot behaviour still remain mysterious, indicating the need for deeper fundamental studies into MFC technology. To this end, one strategy is to study the effect on pure-culture biofilms. Pure-culture EABs can more rapidly reach steady state following perturbations associated with changes in conditions resulting from a polarization scan

because no changes to microbial population dynamics occur.[6] Pure-culture *Geobacter sulfurreducens* EABs are well suited to this strategy because their electron transfer mechanism is exclusively based on direct physical transport, thereby further simplifying interpretation.[1, 11, 12] However, to the best of our knowledge, until now, no reports of overshoot exist in the literature for pure-culture *Geobacter sulfurreducens* EABs. In addition, new approaches are needed to control the operational parameters and quantitatively study their effect on overshoot. Microfluidic MFCs are a useful tool for studying overshoot without batch-fed nutrient cycling, and other major benefits include control of hydrodynamic conditions of fresh nutrient medium imposed against the EAB.

Recently, we developed a new microfluidic MFC architecture that addressed the major drawbacks that have limited transferability of knowledge to the wider macroscopic MFC research area. The membraneless MFC displayed the longest reported operational time (6 months), demonstrated stable performance at high flow rates, and featured oxygen protection that negated the need for scavengers such as L-cysteine.[16] In this study, using the same device design, we investigate the power overshoot phenomenon for pure-culture *G. sulfurreducens* EABs. A mature reactor that displayed overshoot after two months was selected for experimentation. A series of interventions were applied, and the degree to which they alleviated the measured overshoot was quantitatively characterized.

5.4. Experimental

5.4.1. Microfabrication tools and techniques

Moulds with the geometries of the microchannels used in this study were created via photolithography for PDMS casting. A photomask was designed using computer-aided design software (DraftSightTM, Dassault Systems, France) and was printed using a photoplotter (FPS25000, Fortex Engineering Ltd., UK). The photomask was placed on top of a photoresist layer (SY300 film, Fortex Engineering Ltd., UK) with 160 µm thickness adhered to a 75 x 50 x 1 mm glass slide (12-550C, Fisher Scientific, Canada) using a dry film laminator (FL-0304-01, Fortex Engineering Ltd., UK). Portions of the negative photoresist were cross-linked through the transparent components of the mask using a UV exposure system (AY-315, Fortex Engineering Ltd., UK). Uncross-linked photoresist was removed

using developer and rinse solutions (SY300 Developer/Rinse, Fortex Engineering Ltd., UK). Graphite electrodes (GraphiteStore.com Inc., USA) were wrapped in a plastic film barrier and placed side-by-side on top of the channel feature protruding from the photoresist mould. PDMS devices were cast against the mould using liquid PDMS mixed with a cross-linker solution (Sylgard184, Dow Corning, Canada) at a 10:1 ratio, followed by curing at 70^{o}C for 4 hours. Inlet and outlet holes were punched through the device, and the PDMS device was sealed to a glass cover slip using air plasma (PCD-001 Harrick Plasma, Ithaca, USA) for 90 seconds at 650 mTorr. Other details of the device design and fabrication are explained elsewhere.[13] The final device featured an embedded graphite anode and a cathode with an oxygen protection barrier.

5.4.2. Device architecture

The membraneless device used in this work positioned both electrodes side-by-side on the top PDMS wall. The electrode spacing was optimized to prevent anolyte/catholyte crossover to the opposite chamber.[13] The MFC main chamber (excluding upstream inlets) had dimensions of 160 µm height, 12 mm width, and 30 mm length. Graphite plates with 3 mm thickness were cut to 10 mm widths and protruded 3 mm into the channel from each side. In typical operation, each syringe pump delivered liquids at 0.5 $mL \cdot h^{-1}$ for a total flow rate of $Q_T = 1\ mL \cdot h^{-1}$. A schematic is shown in Figure 5.1.

5.4.3. *Geobacter sulfurreducens* preparation and device start-up

Geobacter sulfurreducens (wild type, strain PCA, ATCC 51573) were stored in a -80 °C biological freezer (Thermo Scientific Revco EXF). *G. sulfurreducens* was sub-cultured in a nutrient medium and 40 mM sodium fumarate (as an electron acceptor) in DI water (30 °C). The nutrient medium consisted of a sodium acetate carbon source CH_3COONa (10 mM), NaH_2PHO_4 (3.8 mM), $NaHCO_3$ (30 mM), KCl (1.3 mM), NH_4Cl (28 mM), a trace mineral supplement (10 mL/L) (ATCC® MD-TMS™), and a vitamin supplement (10 mL/L) (ATCC® MD-TMS™). Nutrient media was sterilized by autoclave at 110°C and 20 psi for 20 min before use. Sodium fumarate, which could not be autoclaved, was delivered through a sterilized filter in the glovebox. The same solution composition except for sodium fumarate, was used in the anodic chamber to promote electrode growth after inoculation. Sub-culturing

(up to the 8th subculture sample) was performed within a glove box to maintain anaerobic conditions (10% H_2, 10% CO_2 and 80% N_2). All operations were conducted inside an anaerobic glovebox.

Using two separate syringe pumps (PhD 2000, Harvard Apparatus, MA), the MFC anode was inoculated with the sub-culture under a flow rate of 0.5 $mL \cdot h^{-1}$ with addition of 30 mM $K_3Fe(CN)_6$ (ferricyanide) in a sodium phosphate buffer with pH 7.0 flowing at 0.5 $mL \cdot h^{-1}$. The ferricyanide catholyte was used to ensure that cathode kinetics were not a limiting factor. This process continued for two 2 h via separate syringe pumps. During inoculation, the MFC anode and cathode were connected through an external resistor with value R_{ext} = 25 kΩ. All reactors were operated in a temperature-controlled laboratory (23 ± 0.5°C).

5.4.4. Electrochemical measurements

Electrochemical measurements were collected during continuous flow of anolyte and catholyte streams through the microfluidic MFC. The voltage drop across R_{ext} was acquired using a microcontroller data acquisition system (Atmega328pMmicrochip Technologies, Arizona, USA) at various intervals from days to seconds. Using Ohm's law (Eqn. 5.1), the corresponding current density, $\bar{I}$ ($A \cdot m^2$) and power density were obtained via:

$$\bar{I} = \frac{I}{a} = \frac{V}{a \cdot R_{ext}} \qquad \text{(Eqn. 5.1)}$$

$$\bar{P} = \bar{I} \cdot V = \frac{V^2}{a \cdot R_{ext}} \qquad \text{(Eqn. 5.2)}$$

where I is the raw current (A), a is the exposed electrode area (m^2), V is the potential (V), a is the area of the graphite electrode (m^2) exposed to the anolyte, and R_{ext} is the external resistance (Ω) placed between the anode and cathode.

Polarization curves were measured via a potentiostat (VersaSTAT 4, Princeton Applied Research, Oak Ridge, USA) that automatically switched between different R_{ext} values while recording the voltage drop. Between each polarization, the system was returned to open circuit voltage (OCV) to limit EAB acclimation to the preceding R_{ext} values during the measurement. The voltage versus current density (using Eqn. 5.1) and power density versus current density curves (using Eqn. 5.2) were subsequently created.

Current overshoot was quantified via two measurements. Absolute overshoot, $\Delta\bar{I}_O$ (A/m^2), which is the decrease in current density from its max value immediately before doubling back ($\bar{I}_{Max}$) to its min values after the full extent of the current double back, occurs ($\bar{I}_{DB}$) at the low resistance side of the power density (or polarization) curve:

$$\Delta\bar{I}_O = \bar{I}_{Max} - \bar{I}_{DB} \quad \text{(Eqn. 5.3)}$$

A second measurement is the relative overshoot, which is obtained by normalizing $\Delta\bar{I}_O$ to $\bar{I}_{Max}$. This calculation yields the overshoot factor θ_O, which ranges from 0 (no overshoot) to 1 (no current after double back):

$$\theta_O = \Delta\bar{I}_O/\bar{I}_{Max} = 1-\bar{I}_{DB}/\bar{I}_{Max} \quad \text{(Eqn. 5.4)}$$

Two overall measurements of the overshoot that are often used in this work are (1) the absolute current difference between the current density at maximum power $\bar{I}_{MaxP}$ and the current density at the lowest resistor used $\bar{I}_{Min\Omega}$, given by

$$\Delta\bar{I}_{O_T} = \bar{I}_{MaxP} - \bar{I}_{Min\Omega} \quad \text{(Eqn. 5.5)}$$

and (2) the total overshoot factor

$$\theta_{O_T} = \Delta\bar{I}_{O_T}/\bar{I}_{MaxP} = 1- \bar{I}_{Min\Omega}/\bar{I}_{MaxP} \quad \text{(Eqn. 5.6)}$$

In certain cases, the so-called recovered current density ($\bar{I}_R$, where $\bar{I}_R > \bar{I}_{DB}$) is measured when the current once again begins to increase as the R_{ext} is decreased. The absolute recovered overshoot ($\Delta\bar{I}_R$) and the recovered overshoot factor (θ_R), which should range between 0 and θ_{DB}, are given in Eqns. 5.5 and 5.6 as analogs to Eqns. 5.3 and 5.4:

$$\Delta I_R = \bar{I}_R - \bar{I}_{DB} \quad \text{(Eqn. 5.7)}$$

$$\theta_R = \Delta\bar{I}_{DB}/\bar{I}_R = 1-\bar{I}_{DB}/\bar{I}_R \quad \text{(Eqn. 5.8)}$$

5.5. Results and discussion

Figure 5.1 shows the schematic of the system used in this study, consisting of a membraneless microfluidic device with two inlets connected to syringe pumps (supplying anolyte and catholyte solutions) and an outlet that drains to a waste container. Graphite electrodes are connected to the potentiostat with automatic control over external resistance.

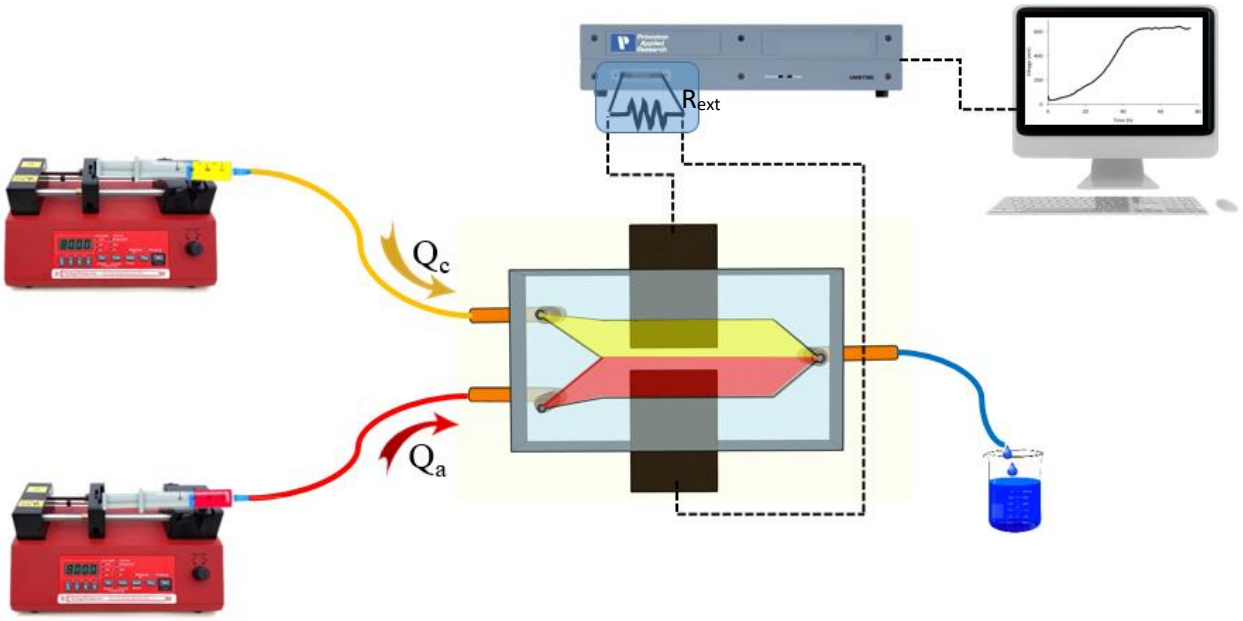

Figure 5.1. Microfluidic MFC setup featuring syringe pumps supplying ferricyanide catholyte solution (yellow) and an acetate anolyte solution (red) at flow rates Q_c and Q_a, respectively, to a two-electrode microfluidic device with two inlets and one outlet (blue). Cathode and anodes are connected to a potentiostat with computer control over R_{ext}.

After inoculation, in the MFC anode compartment, an acetate nutrient (10 mM) anolyte solution and a ferricyanide catholyte solution (30 mM) were co-flowed against the anode and cathode compartments, respectively, while the external resistance was held at R_{ext} = 25 kΩ. Immediate biofilm growth was observed based on the increase in voltage measured across the external resistor (Figure 5.2a). A semi-log plot of the increase in voltage confirms that exponential growth began a few hours later and continued until t = 40 h (Figure 5.2a, inset). After three days, the voltage was constant at 610 mV. The MFC remained under flow conditions (Q = 0.5 mL·h^{-1}) for 5 days to ensure that steady state was reached, corresponding to t = 0 in Figure 5.2b. The potential across the 25 kΩ external resistor was recorded every 4-8 days (Figure 5.2b), and the power density and polarization curves were acquired every week. Based on the power density curves obtained within the first month following inoculation, a MFC maximum power density of 350 mW·m^{-2} was obtained for R_{ext} = 25 kΩ, and no overshoot was detected at low R_{ext} (e.g., Supporting Information, Figure 5.S1). Therefore, we believe that the internal resistance at this time was also 25 kΩ.

After approximately one month, the voltage across the external resistor began to decrease for unknown reasons, reaching 50% of its original value nearly two weeks later (Figure 5.2b). It is unlikely that these reductions were shear-induced or were the result of ferricyanide contamination on the anode-adhered EAB because the same microfluidic MFC design was previously optimized and tested to avoid these problems.[13] The likely causes were biological contamination or O_2 poisoning, the latter arising from slow leaks through breaches in the device's gas-protection layer or fluid connects. We compared the power density curves acquired at different times during the drop in voltage. Initially, the power density curves (t = 37 days) did not show any overshoot behaviour, and the maximum power obtained at R_{ext} = 25 kΩ was slightly higher than 350 $mW \cdot m^{-2}$, similar to measurements during the first month (Figure 5.S1). The next power density measurement at t = 40 days, or approximately 2 weeks after the onset of voltage reduction, showed a transformation to overshoot behaviour. At this time, the overshoot was characterized by a developing decrease in power density at R_{ext} = 25 kΩ and a doubling back of the current density at external resistor values below R_{ext} = 10 kΩ. A slight recovery in current density was observed for the lowest R_{ext} (3.5 kΩ). The power density curve at t = 43 days displayed a more pronounced current density double back after R_{ext}=10 kΩ and no longer recovered at lower R_{ext} values. For the polarization curves corresponding to the power density curves shown in the inset of Figure 5.2b, please see the Supporting information and Figure 5.S2.

A more detailed observation of the voltage versus time profiles during acquisition of the polarization curves indicates that a rapid (exponential) approach to the baseline values occurred for data acquired at 37 days, whereas the reduction in potential was much more gradual and qualitatively differed for data at 43 days. For example, the voltage reduction in response to switching between OCV and different external resistances before (t=37 d) and after (t=43 d) the onset of overshoot is shown in Figures 5.2c and 2d, with highlighting of R_{ext} = 25 kΩ shown as an inset. This view reveals that that the approach to equilibrium during polarization scans was slowing at the same time as the overshoot phenomenon was becoming more pronounced. Therefore, the local decrease in power density at R_{ext} = 25 kΩ was likely an artifact related to insufficient hold times during the polarization scans. This is related to one observed artifact related to overshoot wherein power density curves can both over-represent maximum power densities,[8] as well as produce local depressions in power density,[13]

the latter being similar to what we observed here. The slower approach to equilibrium could have been due to higher internal resistance or an increase in electrode capacitance. A second and more commonly reported overshoot effect manifested as a doubling back of current at the low resistance side of the power density curve. This phenomenon corresponds to the concentration-limited portion of the power density curve (Supporting Information, Figure 5.S2). Because these two effects can be observed independently, so too should their analysis. Because the literature lacks examples of overshoot characterization, we developed a quantitative measure of the overshoot in terms of the degree of current density double back $\Delta\bar{I}_O$ (Eqn. 5.3) and the normalized overshoot factor θ_O (Eqn. 5.4), the latter of which ranges between 0 (no overshoot) and 1 (complete loss of current density). We applied these measurements to the power density curves in Figure 5.2b (inset) after overshoot was observed at t = 40 and t = 43 days. The maximum current density ($\bar{I}_{Max}$) was observed for R_{ext} = 10 kΩ at both time points. At t = 40 days, the overshoot factor was obtained using the double back current density $\bar{I}_{DB}$ at R_{ext} = 8 kΩ ($\bar{I}_{DB} = \bar{I}_{8k\Omega}$), yielding an absolute overshoot of $\Delta\bar{I}_O$ = -54 $mA \cdot m^{-2}$ and an overshoot factor of θ_O = 0.092. The recovered current density $\bar{I}_R$ (Eqn. 5.7) was observed at R_{ext} = 3.5 kΩ ($\bar{I}_R = \bar{I}_{3.5k\Omega}$), resulting in a recovered overshoot (Eqn. 5.8) of θ_R = 0.058. Three days later (t = 43 days), the overshoot was more severe at ΔI_O = -173 $mA \cdot m^{-2}$ and θ_O = 0.188, with no demonstrated recovery after the initial onset of overshoot. See the Supporting Information (Figure 5.S2) for additional details on the absolute overshoot measurements.

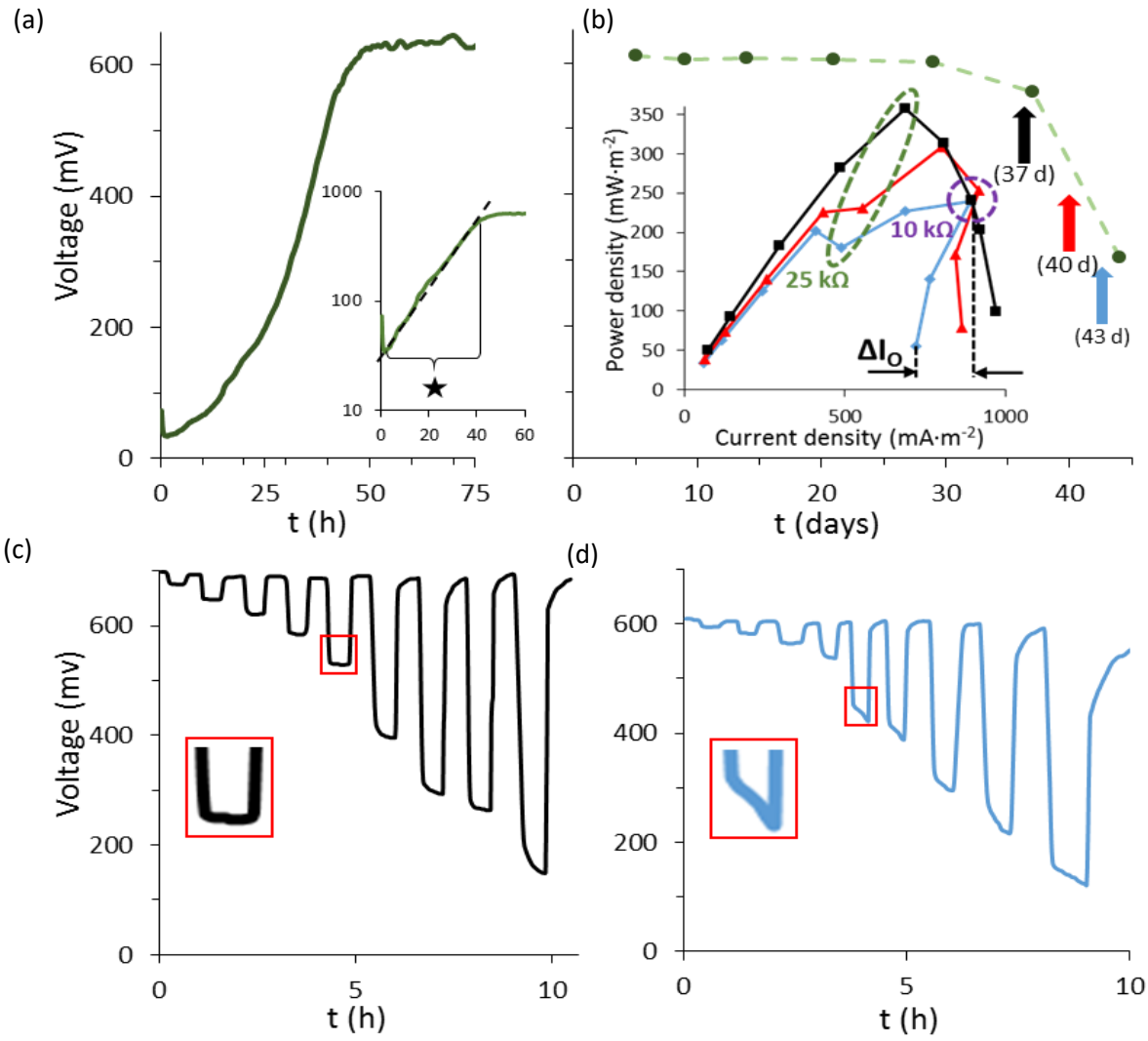

Figure 5.2. (a) Growth profile immediately following inoculation. Inset shows semi-log plot of (a) with a highlighted section from 2 to 40 hours (star) indicating the exponential growth period. (b) Voltage across R_{ext} from intermittent voltage measurements between 5 and 45 days showing the onset of a reduction in voltage after approximately one month. Colour-coded arrows indicate the time at which the polarization and power density curves were obtained with times marked below three arrows. In both (a) and (b), the voltage was measured across R_{ext} = 25 kΩ, time (t) was measured after inoculation and the total flow rate was generated in equal portions of anolyte and catholyte flow, with their total of Q = 1 mL·h^{-1}. Inset to (b) shows power density curves acquired at times matching the colour-coded arrows in the main figure. Highlighted power densities with dashed ellipses indicate corresponding R_{ext} values where the curves deviated from the healthy curve at t=37 h (25 kΩ for green and 10 kΩ for purple). Absolute overshoot ($\Delta\bar{I}_O$) is shown for t=43 d. Potential versus time during polarisation curve acquisition at 37 h (c) and at 43 d (d) with insets showing a close-up of the voltage response for a single transition from OCV to one resistor.

Although debate remains in the literature with respect to the activity state of the outer and inner EAB strata, it has been shown that mature electrode-adhered biofilms (EABs) from *G. sulferreducens* have inactive outer layers formed from older cells that are pushed outward from the electrode attachment surface.[14] This process has the effect of forming a solid diffusion barrier and creating inefficient electron conduction pathways, which could reduce the overall biofilm efficiency. Therefore, we hypothesized that the observed overshoot in this study could be related to problems associated with a poorly performing outer layer. To investigate, we applied a high shear stress to the EAB using 3 second-long pulses of both anolyte and catholyte at 2.5 $mL \cdot s^{-1}$, equivalent to application of 60 Pa, which is approximately 20 times higher than the highest reported shear stresses that cause EAB erosion.[15] These pulses were consecutively applied three times followed by continuous flow with both anolyte and catholyte syringes pumped at 8 $mL \cdot min^{-1}$ (equivalent to 6 Pa) for three minutes (assuming a biofilm thickness of 30 μm, as shown previously in a similar setup[16]). Following the application of high shear, the voltage dropped to 80 mV while remaining connected to the same external resistor (R_{ext} = 25 kΩ), and the system was allowed to settle under a flow of 0.5 $mL \cdot h^{-1}$ for both anolyte and catholyte solutions. The remaining signal was expected to originate from the remaining seed layer to which biofilms can remain attached within the protected regions in the rough surface of the graphite carbon electrodes, even after application of extreme shear stresses.[17] As observed in Figure 5.3a, the potential initially recovered to 375 mV after approximately one day (marked phase i), and subsequently recovered more slowly over the next 20 days (phase ii) until a steady-state potential of 450 mV was attained (phase iii). We hypothesize that the short time-scale of the initial current recovery was due to re-establishment of the initial flow conditions and full washout of cross-over solutions to the opposite electrode compartment. The longer duration for the secondary current recovery suggests a mechanism related to biofilm regrowth. During acquisition of polarization data during phase ii in Figure 5.3a (t=77 d) and after arriving at the new steady state during phase iii (t=109 and 130 d), variations in potential versus time after switching from OCV again returned to exponential decay behaviour (Figure 5.3b). Evaluation of the resulting power density curves in Figure 5.3c showed continuous increases to power and current density with recovery time, likely due to regrowth in the EAB following shear erosion. We note that the polarization curve did not show a significant difference in

slope in the ohmic region, indicating that the internal resistance was stable (Supporting information, Figure 5.S3). Interestingly, the local decrease in power at 25 kΩ that was observed previously in Figure 5.2b disappeared after shear erosion and did not reappear in the ~40 days that followed. We assume that this behaviour occurred because the polarization scans were conducted at steady state due to improved biofilm responsiveness after shear treatment. This observation confirms that the previously observed decrease in power density was indeed a measurement-related artifact. However, overshoot behaviour was still observed at R_{ext} values less than 20 kΩ. The immediate reduction in current density averaged -23 $mA \cdot m^{-2}$ in all 3 cases (77, 109 and 130 d), which can be viewed as an initial overshoot with absolute value $\Delta\bar{I}_{O_1}$ (with $\bar{I}_{Max} = \bar{I}_{20k\Omega}$ and $\bar{I}_{DB} = \bar{I}_{15k\Omega}$ in Eqn. 5.3) and a corresponding overshoot factor of $\theta_O = 0.036$. Recovery at R_{ext} = 8 kΩ led to an average current recovery of $\Delta\bar{I}_R$ = 68 kΩ (with $\bar{I}_{DB} = \bar{I}_{15k\Omega}$ and $\bar{I}_R = \bar{I}_{8k\Omega}$). Finally, a current double back occurred at the lowest resistor value of 3.5 kΩ h, with an average overshoot of $\Delta\bar{I}_{O_2}$ = -89 $mA \cdot m^{-2}$. Taking the current density from the initial double back as $\bar{I}_{Max}$ (= $\bar{I}_{20k\Omega}$) and the last measured current density as $\bar{I}_{DB}$ (= $\bar{I}_{3.5k\Omega}$), we calculated a total absolute overshoot of $\Delta\bar{I}_{O_T}$ = -44 $mA \cdot m^{-2}$ averaged for the three polarization scans on days 77, 109 and 103. These absolute overshoot and recovery values are shown individually for each polarization scan measurement in Figure 5.3d. We note that the re-growth process slightly lessened the overshoot characteristic of the MFC, with the total absolute overshoot reaching -20 $mA \cdot m^{-2}$ in the last polarization scan (130 days). The average total overshoot factor for the three polarization scan measurements was θ_{O_T} = 0.064, a value that was significantly reduced compared with the overshoot factor before high shear treatment at t = 43 d (θ_{O_T} = 0.188). The remaining overshoot was situated in the concentration-limited regime of the polarization curve, and therefore, we hypothesized that increases to mass transfer via increased flow might further alleviate this behaviour. Previous attempts by other researchers to investigate this effect were inconsistent,[4,7] but the superior control over hydrodynamic conditions obtained in our microfluidic MFC offers a better opportunity for accurate studies. As expected, increasing the flow rate from 0.5 $mL \cdot h^{-1}$ to 20 $mL \cdot h^{-1}$ resulted in increases in the maximum power density due to increased nutrient availability and possible de-acidification in the biofilm interior (Figure 5.3c).[18] Of specific interest to this work, the higher flow rate also lessened the overshoot effect. By the strictest

definition of overshoot in this work, a small double back was observed, but it was notably small and was delayed until the lowest resistance value (R_{ext} = 3.5 kΩ). In addition, the total absolute overshoot (taking $\bar{I}_{Max} = \bar{I}_{20k\Omega}$ and $\bar{I}_{DB} = \bar{I}_{3.5k\Omega}$) was positive at $\Delta\bar{I}_{O_T}$ = 30 mA·m^{-2} (Figure 5.3d), indicating that no net overshoot occurred relative to the peak power position in the power density curve.

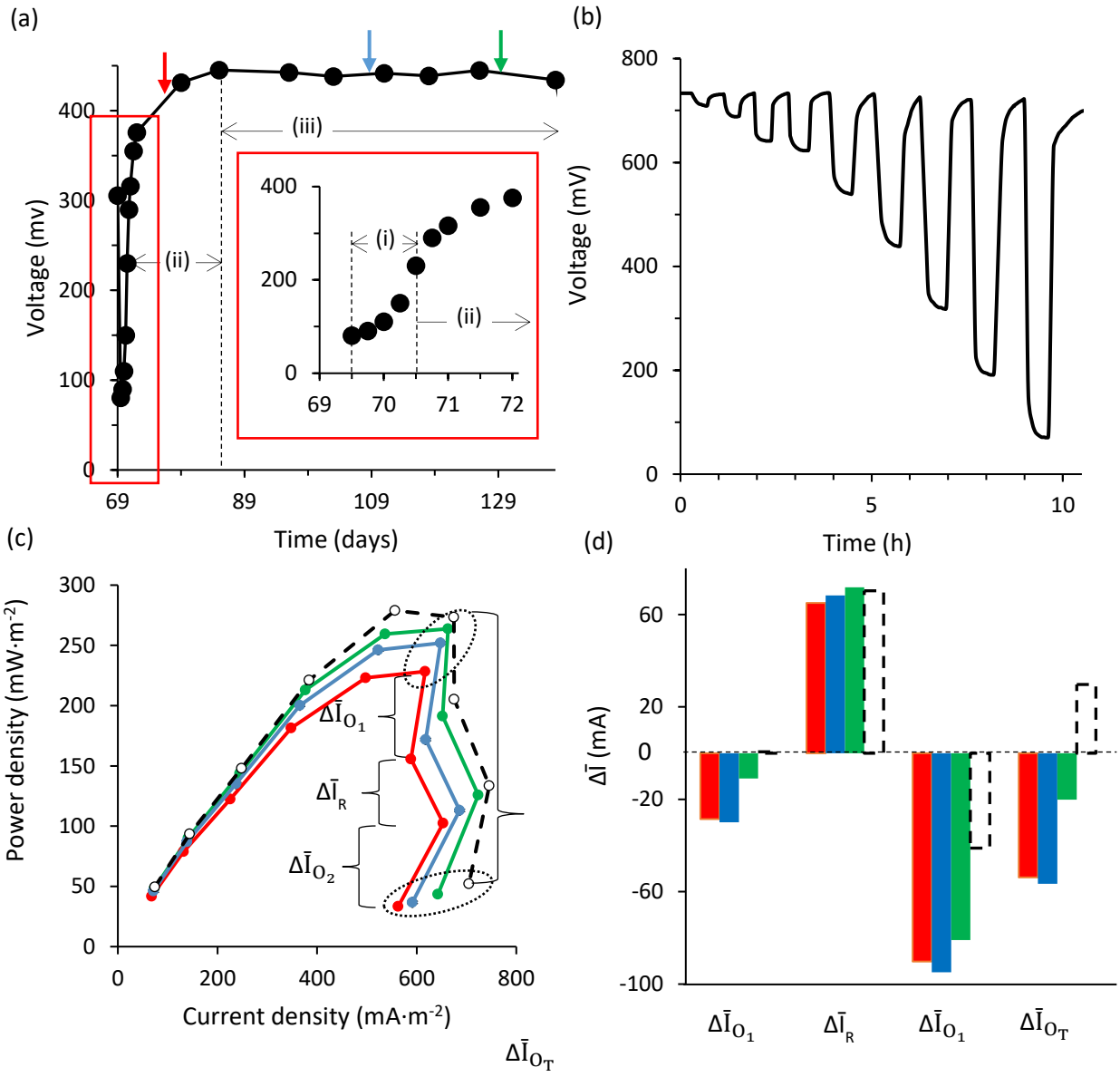

Figure 5.3. (a) Voltage recovery starting 2 days after application of high shear force under external resistor R_{ext} = 25 kΩ. (b) Example of voltage response to changing external resistances during the polarization scan starting at t=62 days (15 days following application of high shear). (c) Power density curves obtained at times 77, 109, 130 d, as indicated with the corresponding colour arrows in (a). All polarization scans were obtained at flow rate, Q=0.5 mL·h^{-1}, except for the dashed curve, which was obtained at 20 mL·h^{-1} at 130 d. Measurement pairs

displaying absolute overshoot ($\Delta\bar{I}_{O_1}$ and $\Delta\bar{I}_{O_2}$), recovery ($\Delta\bar{I}_R$) and total overshoot ($\Delta\bar{I}_{O_T}$) are indicated by the dotted ellipses. For (b, c), the external resistor values were R_{ext} = 300 kΩ, 150 kΩ, 80 kΩ, 50 kΩ, 30 kΩ, 20 kΩ, 15 kΩ, 8 kΩ, and 3.5 kΩ. (d) Plot of the absolute overshoot and recovery values for each measurement pair shown in (c). Total represents overall absolute overshoot $\Delta\bar{I}_{O_T}$ as defined in the main text.

In summary, following the high shear treatment of the MFC, the decrease in power output at 15 kΩ appeared to be related to insufficient settling time during the polarization scan due to the electrically and/or diffusively resistant outer EAB layers. After shear removal of these outer layers, some overshoot behaviour remained, but it was mild based on the MFC's ability to slightly recover after the onset of the first overshoot and because $\Delta\bar{I}_{O_T}$ and θ_{O_T} were significantly reduced. The remaining overshoot remained generally stable over time while subjected to low flow rates, but the overshoot could be nearly eliminated by increasing the flow rates by a factor of 40.

5.5.1. Acclimation to a lower fixed R_{ext}

Next, we investigated acclimation under flow conditions as a method for correcting the remaining overshoot. During acclimation, microbes are allowed time to adjust to the imposed electrical conditions resulting from the choice of external resistance. Because overshoot occurs at low external resistor values, acclimation at low R_{ext} values can acclimatize the bacteria to high currents, whereas acclimation at high R_{ext} should enhance overshoot problems at low resistors.[19,20] Over a period of four days, we acclimated the MFC to 3 external resistances of R_{ext} = 150, 20, and 3.5 kΩ.[8,9] The experiments were conducted three times in random order to prevent any potential hysteresis effects. Figure 5.4a shows that the maximum power was achieved at lower applied external resistance (20 kΩ) after acclimation to the lower resistances (3.5 and 20 kΩ) compared with the applied external resistance required to obtain maximum power (30 kΩ) following acclimation at 150 kΩ. As well, the maximum power increased as the acclimation resistance was decreased, reaching nearly 370 $mV \cdot m^{-2}$ after acclimation to R_{ext} = 3.5 kΩ. We also note that together with increasing power, an easing of the total absolute overshoot occurred, i.e., $\Delta\bar{I}_{O_T}$ = -96, -44 and +28 $mA \cdot m^{-2}$. The reduced overshoot resulted in a corresponding increase in the maximum current density, reaching 810 $mA \cdot m^{-2}$ for acclimation at 3.5 kΩ, a value 35 % higher than those acclimated

to a 20 kΩ (599 mA·m^{-2}) and more than double than those acclimated to 150 kΩ (400 mA·m^{-2}). Measurements of the slope of the polarization curve in the ohmic region reveal that the internal cell resistance decreased with reductions to the acclimation resistance (Figure 5.4b).

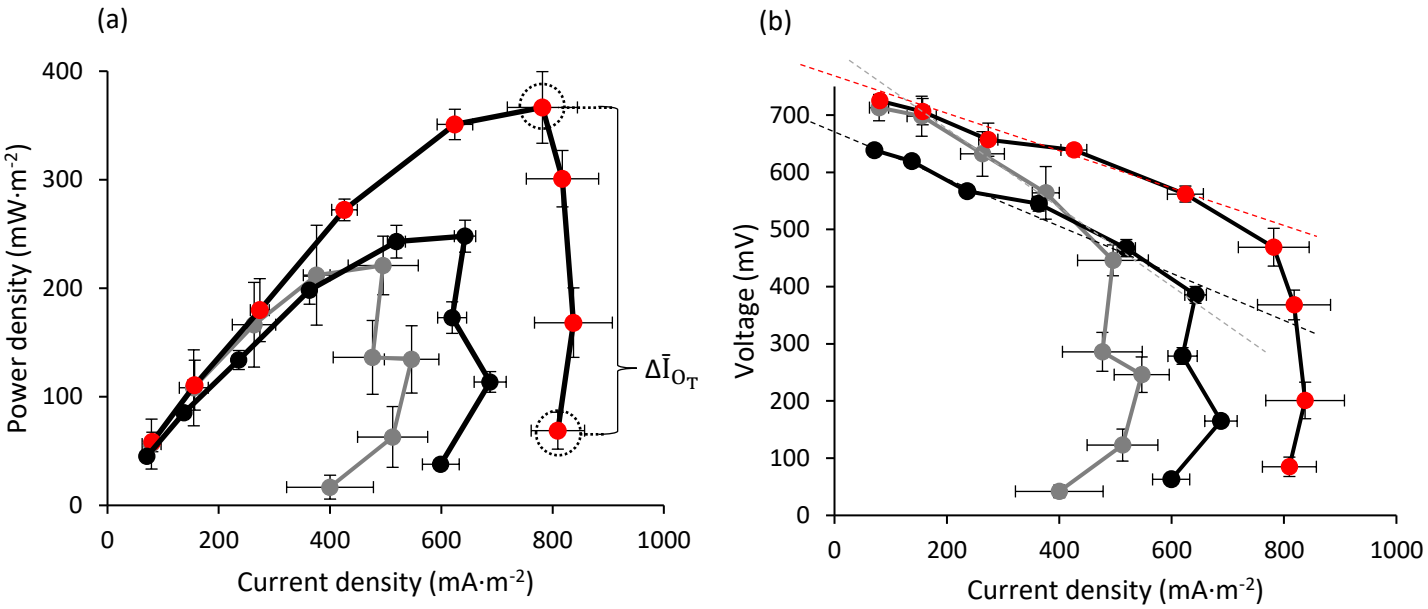

Figure 5.4. Power density (a) and polarization (b) curves after four days of acclimation to 150 (grey), 20 (black), and 3.5 kΩ (red). Acclimation resistances were applied in random order. Error bars are the result of three separate measurements. Total absolute overshoot ($\Delta\bar{I}_{O_T}$) was measured between current densities produced at peak power and the lowest tested resistance, as exemplified for one of the curves in (a). All flow rates were 0.5 m L·h^{-1}. The time interval for application of each resistance was 30 to 45 min. External resistance values used to generate the polarization curves were R_{ext} = 300, 150, 80, 50, 30, 20, 15, 8, and 3.5 kΩ.

5.5.2. *In situ* acclimation

The beneficial effects of acclimation to a single low external resistance might be partially reversed as the EAB readapts to higher loads during a polarization scan. As such, it might be possible to further correct the residual overshoot observed in Figure 5.4 by optimizing the acclimation process. Another approach is an *in-situ* acclimation process in which the acquisition time for the polarization curves is increased so the system can adapt to each resistor value tested individually. In batch systems, continuous nutrient depletion results in differences in concentrations during prolonged polarization curve acquisition time, and these differences could be conflated with electrochemical properties during the polarization scan. This hurdle was overcome by measuring the voltage across each individual external resistance for multiple fill/depletion cycles. The results show excellent elimination of

artifacts related to overshoot but at the expense of notably slow acquisition (up to 1-2 days for each external resistance used in the polarization scan).[21]

In our case, under microflow conditions, the concentrations remained constant in time throughout the polarization scan. Therefore, hold times can be customized based on the voltage dynamics associated with each external resistance, which has the potential to significantly reduce the polarization scan time and to observe the effect of flow. To evaluate the method of *in situ* acclimation in the microfluidic MFC, we acquired polarization curves with dwell times for each applied R_{ext} of up to 15 hours, and each measurement was repeated 3 times at two different flow rates of 0.5 and 5 $mL \cdot h^{-1}$. Following the application of an external resistor after a period at OCV, two critical time parameters emerged in the dynamic voltage vs. time recovery curves. The first-time parameter is the time required to reach the end of the rapid reduction in voltage to its lowest value (t_{low}) after switching from OCV to R_{ext}. The second time parameter is the time required for voltage recovery to higher values (t_{recov}) following successful acclimation. No recovery was observed for resistors greater than 50 kΩ, and thus we considered $t_{low} = t_{recov}$. Generally, the effect of increased flow was to reduce the time for t_{low} and t_{recov} at external resistors less than 50 kΩ. As an example, Figures 5a-c below show three voltage vs. time plots following the switch from OCV to external resistances R_{ext} = 3.5, 30 and 300 kΩ, respectively. The same figures show that the time to reach t_{low} was reduced for all curves under elevated flow rates. For those curves with voltage recovery, corresponding to $R_{ext} \leq 50$ kΩ, the time to reach t_{recov} was also reduced under elevated flow rates. A plot of the measured t_{recov} as a function of R_{ext} under low and high flow rates (Figure 5.5d) confirms certain trends. The voltage recovery occurs 4-7 hours after switching from OCV at flow rates of 5 $mL \cdot h^{-1}$ but this time is significantly longer, between 6 and 11 hours, at 0.5 $mL \cdot h^{-1}$. Compared with *in situ* acclimation over three fill/deplete cycles per external resistance in a bulk MFC,[22] we estimate a 4.5- to 18-times reduction in experimental time.

For each flow rate, we reconstructed the power curves based on the voltages obtained after t_{low} (red symbols in Figure 5.5) and t_{recov} (blue symbols in Figure 5.5) at various flow rates between 0.5 $mL \cdot h^{-1}$ and 5 $mL \cdot h^{-1}$. In all cases, the maximum power density was obtained at R_{ext} = 20 kΩ. Power measurements after t_{low} increased from 346 to 383 $mW \cdot m^{-2}$ when the

flow rate was increased from 0.5 $mL \cdot h^{-1}$ to 5 $mL \cdot h^{-1}$. However, although the increased flow rate slightly reduced the severity of the overshoot, it did not fully eliminate it, and the total absolute overshoot measurements were $\Delta \bar{I}_{O_T}$ = -170 and -70 $mA \cdot m^{-2}$ at 0.5 $mL \cdot h^{-1}$ to 5 $mL \cdot h^{-1}$, respectively. In contrast, the overshoot was fully eliminated in the power density curves reconstructed from voltages acquired at t_{recov}. In addition, the maximum power densities (and current densities) were significantly increased, reaching 405 $mW \cdot m^{-2}$ (and 1038 $mA \cdot m^{-2}$) and 436 $mW \cdot m^{-2}$ (and 1215 $mA \cdot m^{-2}$) at 0.5 and 5 $mL \cdot h^{-1}$, respectively.

We pause to compare the measured performance after *in situ* acclimation to measurements obtained previously in a MFC with the same design as used in this work, which did not show any signs of overshoot.(ref) In the previous work, polarization scans were conducted using a standard procedure with 30-minute hold times without any acclimation. The power densities (and current densities) obtained in the previous work at comparable flow rates were 370 $mW \cdot m^{-2}$ (and 800 $mA \cdot m^{-2}$) at 1 $mL \cdot h^{-1}$ and 400 $mW \cdot m^{-2}$ (and 850 $mA \cdot m^{-2}$) at 6 $mL \cdot h^{-1}$. Even at the highest flow rates attempted (200 $mL \cdot h^{-1}$), the power density (and current density) that we obtained in a healthy MFC without acclimation was only 456 (and 1100 $mA \cdot m^{-2}$). Therefore, even for the MFC displaying overshoot behaviour in this study, *in situ* acclimation significantly improves the figures of merit, and the MFC in this study easily outperformed the maximum power density and current density at comparable flow rates, even setting a new current density record for this microfluidic MFC platform. Therefore, we are confident that applying *in situ* acclimation to a healthy MFC that does not display overshoot behaviour could lead to further benchmark improvements in power and current density.

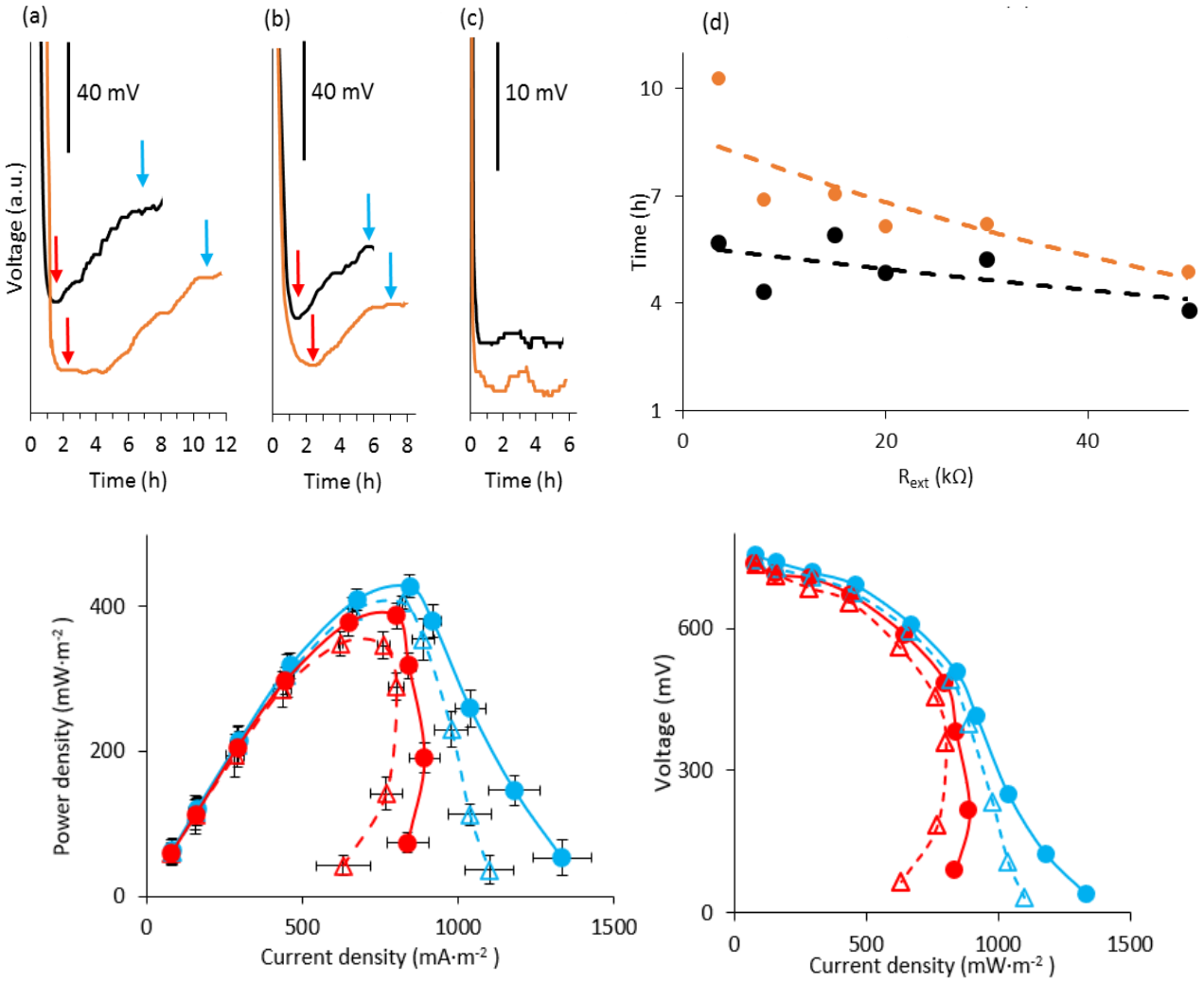

Figure 5.5. MFC voltage after switching from OCV to external resistance of (a) 3.5 kΩ, (b) 30 kΩ, and (c) 300 kΩ. Each figure includes results under flow rates of 0.5 mL·h^{-1} (orange) and 5 mL·h^{-1} (black). Arrows in (a) and (b) show the time after reaching the lowest voltage (red) and after acclimation time sufficient to observe full voltage recovery (blue). Vertical black scale bars indicate the vertical range corresponding to the marked voltage (mV). (d) Acclimation time required to reach the recovered voltage vs. R_{ext} from 30 kΩ to 3.5 kΩ for flow rates of 0.5 mL·h^{-1} (orange) and 5 mL·h^{-1} (black). Dashed lines indicate exponential fits for eye guidance. (e) Power density and (f) polarization for two flow rates 0.5 mL·h^{-1} (Δ) and 5 mL·h^{-1} (●). Each flow rate reports two power outputs; the first (red line) was recorded at time t = t_{low}, and the second (blue line) was recorded at t= t_{recov} for external resistors 300, 150, 80, 50, 30, 20, 15, 8, and 3.5 kΩ.

5.6. Conclusion

A pure culture *Geobacter sulfurreducens* microfluidic MFC with membraneless configuration was used to study overshoot while flow was controlled. The icrofluidic flow conditions of pH[6] and nutrient availability[22] (two important parameters that cause over shoot) were generally well controlled. Power overshoot was observed in the power density curves obtained by applying different external resistors (from high to low) with intervals of 30 to 45 min. It was reported that this drop is most likely related to a slow response from the microbes during adjustment to the new resistance.[23] We investigated the role of MFC acclimation to different external resistors (150, 20, 1 kΩ) to give sufficient time to the biofilm to adjust to the resistances. Our results show that acclimation of EABs to a single external resistor of 1 kΩ produced 102% higher maximum current density (809 $mA \cdot m^{-2}$) compared with those acclimated to 150 kΩ (400 $mA \cdot m^{-2}$). Another approach that fully eliminates the overshoot effect was "*in situ acclimation*" during acquisition of the polarization curves. This approach holds much promise for constant flow reactors, especielaly microfluidic ones which do not consume much nutrient solution over long operational times. Here the performance of an underperforming MFC was restored. Combined with a slight increase in flow rate, the maximum power and current densities that were increased by nearly 30 and 115%. The maximum current density observed here marks a new record performance for this device design.

5.7. Supporting information:

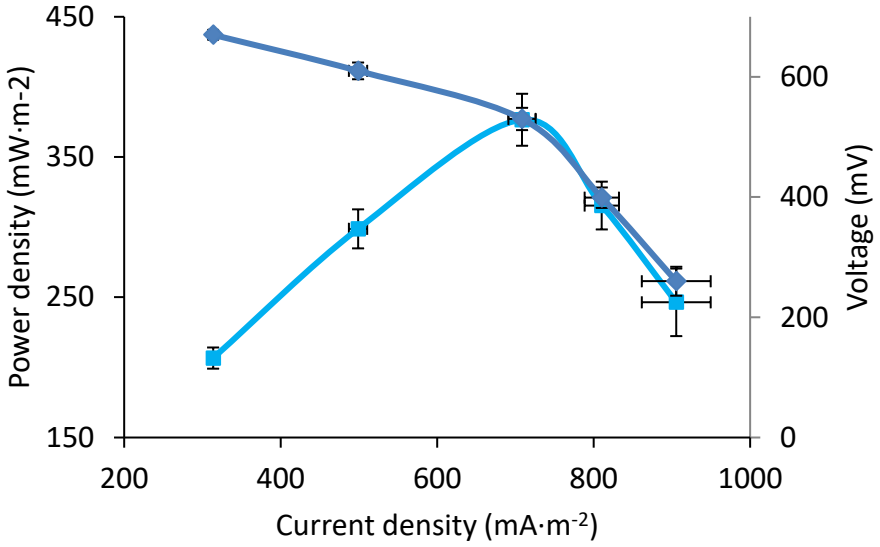

Figure 5.S1. Power density and polarization curves acquired 1 week after reaching steady state with R_{ext} = 25 kΩ. The resistors used were 70, 40, 25, 16 and 10 kΩ. Error bars were generated using the standard deviation from 4 separate measurements.

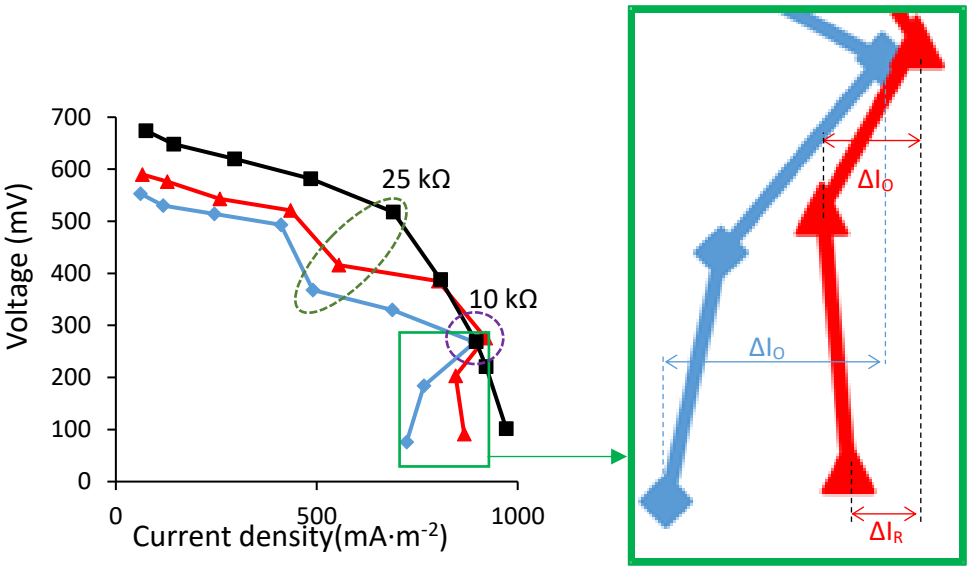

Figure 5.S2. Polarization curves corresponding to those in the main paper, figure2b (inset), acquired at 37 (black), 40 (red) and 43 (blue) days after inoculation. Highlighted power densities with dashed ellipses indicate the corresponding R_{ext} value where curves deviated from the healthy curve at t=37 h (25 kΩ, green and 10 kΩ purple). Absolute overshoot ($\Delta\bar{I}_O$) is shown for t=43 d and 1 week after reaching steady state with R_{ext} = 25 kΩ. The resistors used were 70, 40, 25, 16 and 10 kΩ.

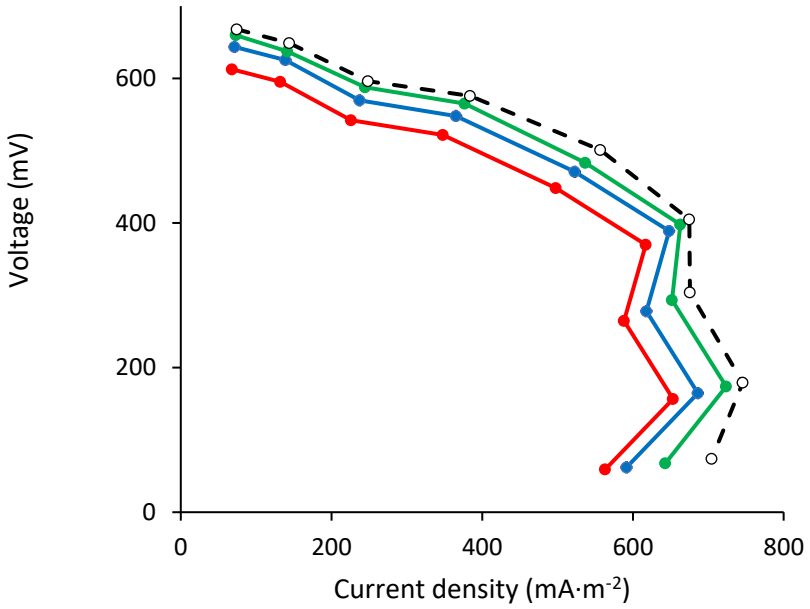

Figure 5.S3. Polarization curve corresponding to the power density curve in the main paper Figure 5.3c. Curves correspond to polarization scans obtained at a low flow rate (0.5 mL·h^{-1}) at different times of t=77 d (red), 109 d (blue), 130 d (green) and at a fast flow rate (20 mL·h^{-1}) at 130 d (dashed line).

5.8. Bibliography

[1] Bond, D. R.; Holmes, D. E.; Tender, L. M.; Lovley, D. R., Electrode-reducing microorganisms that harvest energy from marine sediments. *Science* **2002,** *295* (5554), 483-485.

[2] Logan, B. E., *Microbial fuel cells*. John Wiley & Sons: 2008.

[3] Logan, B. E.; Hamelers, B.; Rozendal, R.; Schröder, U.; Keller, J.; Freguia, S.; Aelterman, P.; Verstraete, W.; Rabaey, K., Microbial fuel cells: methodology and technology. *Environmental science & technology* **2006,** *40* (17), 5181-5192.

[4] Nien, P.-C.; Lee, C.-Y.; Ho, K.-C.; Adav, S. S.; Liu, L.; Wang, A.; Ren, N.; Lee, D.-J., Power overshoot in two-chambered microbial fuel cell (MFC). *Bioresource technology* **2011,** *102* (7), 4742-4746.

[5] Kim, B.; An, J.; Chang, I. S., Elimination of power overshoot at bioanode through assistance current in microbial fuel cells. *ChemSusChem* **2017,** *10* (3), 612-617.

[6] Winfield, J.; Ieropoulos, I.; Greenman, J.; Dennis, J., The overshoot phenomenon as a function of internal resistance in microbial fuel cells. *Bioelectrochemistry* **2011,** *81* (1), 22-27.

[7] Min, B.; Román, Ó. B.; Angelidaki, I., Importance of temperature and anodic medium composition on microbial fuel cell (MFC) performance. *Biotechnology letters* **2008,** *30* (7), 1213-1218.

[8] Hong, Y.; Call, D. F.; Werner, C. M.; Logan, B. E., Adaptation to high current using low external resistances eliminates power overshoot in microbial fuel cells. *Biosensors and Bioelectronics* **2011,** *28* (1), 71-76.

[9] Zhu, X.; Tokash, J. C.; Hong, Y.; Logan, B. E., Controlling the occurrence of power overshoot by adapting microbial fuel cells to high anode potentials. *Bioelectrochemistry* **2013,** *90*, 30-35.

[10] Watson, V. J.; Logan, B. E., Analysis of polarization methods for elimination of power overshoot in microbial fuel cells. *Electrochemistry Communications* **2011,** *13* (1), 54-56.

[11] Tender, L. M.; Reimers, C. E.; Stecher, H. A.; Holmes, D. E.; Bond, D. R.; Lowy, D. A.; Pilobello, K.; Fertig, S. J.; Lovley, D. R., Harnessing microbially generated power on the seafloor. *Nature biotechnology* **2002,** *20* (8), 821-825.

[12] Holmes, D.; Bond, D.; O'neil, R.; Reimers, C.; Tender, L.; Lovley, D., Microbial communities associated with electrodes harvesting electricity from a variety of aquatic sediments. *Microbial ecology* **2004,** *48* (2), 178-190.

[13] Winfield, J.; Ieropoulos, I.; Greenman, J.; Dennis, J., The overshoot phenomenon as a function of internal resistance in microbial fuel cells. *Bioelectrochemistry* **2011,** *81* (1), 22-27.

[14] Chadwick, G. L.; Otero, F. J.; Gralnick, J. A.; Bond, D. R.; Orphan, V. J., NanoSIMS imaging reveals metabolic stratification within current-producing biofilms. *Proceedings of the National Academy of Sciences* **2019,** *116* (41), 20716-20724.

[15] Vigolo, D.; Al-Housseiny, T. T.; Shen, Y.; Akinlawon, F. O.; Al-Housseiny, S. T.; Hobson, R. K.; Sahu, A.; Bedkowski, K. I.; DiChristina, T. J.; Stone, H. A., Flow dependent performance of microfluidic microbial fuel cells. *Physical Chemistry Chemical Physics* **2014,** *16* (24), 12535-12543.

[16] Amirdehi, M. A.; Khodaparastasgarabad, N.; Landari, H.; Zarabadi, M. P.; Miled, A.; Greener, J., A High-Performance Membraneless Microfluidic Microbial Fuel Cell for Stable, Long-Term Benchtop Operation Under Strong Flow. *ChemElectroChem* **2020**.

[17] Zarabadi, M. P.; Paquet-Mercier, F. o.; Charette, S. J.; Greener, J., Hydrodynamic Effects on Biofilms at the Biointerface Using a Microfluidic Electrochemical Cell: Case Study of Pseudomonas sp. *Langmuir* **2017,** *33* (8), 2041-2049.

[18] Zarabadi, M. P.; Charette, S. J.; Greener, J., Flow-Based Deacidification of Geobacter sulfurreducens Biofilms Depends on Nutrient Conditions: a Microfluidic Bioelectrochemical Study. *ChemElectroChem* **2018,** *5* (23), 3645-3653.

[19] Rismani-Yazdi, H.; Christy, A. D.; Carver, S. M.; Yu, Z.; Dehority, B. A.; Tuovinen, O. H., Effect of external resistance on bacterial diversity and metabolism in cellulose-fed microbial fuel cells. *Bioresource technology* **2011,** *102* (1), 278-283.

[20] Lyon, D. Y.; Buret, F.; Vogel, T. M.; Monier, J.-M., Is resistance futile? Changing external resistance does not improve microbial fuel cell performance. *Bioelectrochemistry* **2010,** *78* (1), 2-7.

[21] Nam, J.-Y.; Kim, H.-W.; Lim, K.-H.; Shin, H.-S.; Logan, B. E., Variation of power generation at different buffer types and conductivities in single chamber microbial fuel cells. *Biosensors and Bioelectronics* **2010,** *25* (5), 1155-1159.

[22] Martin, E.; Savadogo, O.; Guiot, S.; Tartakovsky, B., The influence of operational conditions on the performance of a microbial fuel cell seeded with mesophilic anaerobic sludge. *Biochemical engineering journal* **2010,** *51* (3), 132-139.

[23] Ieropoulos, I.; Winfield, J.; Greenman, J., Effects of flow-rate, inoculum and time on the internal resistance of microbial fuel cells. *Bioresource technology* **2010,** *101* (10), 3520-3525.

Chapter 6: Perspectives and future work

6.1. Real-time visualization of microbial activities on a graphite electrode associated with GFP *G. sulfurreducens*

MFCs show promise as an alternative energy source, and most studies on MFCs have focused on improving performance in terms of architectures, membranes and electrode materials, but far fewer studies have focused on the microorganism itself. The cell voltage (or current) is directly related to the quantity of bacteria on the surface of the electrode at the time and the electron transfer rates.[1] Therefore, it is critical to quantify the number of bacteria cells as well as the depth and architecture of the biofilms on the anode electrode. This knowledge is difficult to obtain, especially in the conventional type of MFCs, because often microscopy imaging can only take place at the end of the experiment, which does not provide a direct link between the bacterial colonization or biofilm and the produced current. Furthermore, sampling methods for quantification analysis must be applied very carefully and delicately to the biomass to avoid any physical disruption.[2] Destructive sampling limited to investigate the analysis like total protein,[3] qualitative imaging for morphology and structure of biofilms during the time.[4] A lack of methods for visualizing the electrode has resulted in limited information on the biofilm communities.

In situ imaging of biofilms using fluorescent microscopy is a standard alternative technique in biofilm research.[5] However, this microscopy method usually requires commercial optically transparent electrodes (such as ITO, a popular transparent electrode material) to allow use of the *in situ* CLSM technique. A number of studies have used optically transparent and continuous flow cells with ITO to investigate real-time bacterial (*Pseudomonas aeruginosa* PAO1) adhesion and the role of electrical currents in the detachment and inactivation of bacteria on a fluorescent microscope.[6] This real-time microscopic imaging of the development of the anode biofilm has enabled observation of mature/thick biofilms and monolayers of cells/single attached cells.[7] With this approach, the author were able to accurately monitor microbial activity within the anode at low and high flow rates (such as attachment/detachment), with different concentrations of nutrient and use of different external resistances.

In future, we can design a light-compatible microfluidic MFC device (Figure 6.1) to advance the long-term *in situ* monitoring of *G. sulfurreducens* biofilm growth on the surface of the

anode electrode in a microchannel and use confocal scanning laser microscopy as an improved analytical tool with the precision to allow better understanding and optimization of microbe-anode interactions.

Figure 6.1. Microfluidic MFC device with two graphite electrodes for non-destructive real-time imaging. A channel 160 µm deep and 12 mm wide covered by a glass cover slip allows imaging with confocal scanning laser microscopy.

CSLM is well suited for *in situ* study of microbial biofilms on the surface of the anode electrode, and because it enables non-destructive analysis of living cells, fully hydrated biofilms can be examined without chemical fixation or embedding.

In this case, the bacterial strain used is *G. sulfurreducens* tagged with a chromosomally integrated green fluorescent protein (GFP), known as *Geobacter sp.*, strain CT07. The properties of GFP make it ideal for measuring gene expression or protein localization in real time and at the single cell level with the use of microscopy. GFP can also aid in visualizing the distribution of growth in a biofilm with time.

6.2. *In situ* electrochemical behavior analysis (CV and EIS) with the three-electrode model MFC

Another powerful tool for understanding the real-time bacteria behavior and EET is the three-electrode electrochemical system, which can be coupled with microscopic visualization. This non-destructive voltammetry technique can be used in characterization of viable biofilms. As shown in figure 6.2, a planar gold pseudo-reference electrode can be built via electroless deposition of gold on a planar polystyrene substrate and placed inside the channel (in miniaturized microfluidic electrochemical cells, it is not possible to use a standard reference electrode).

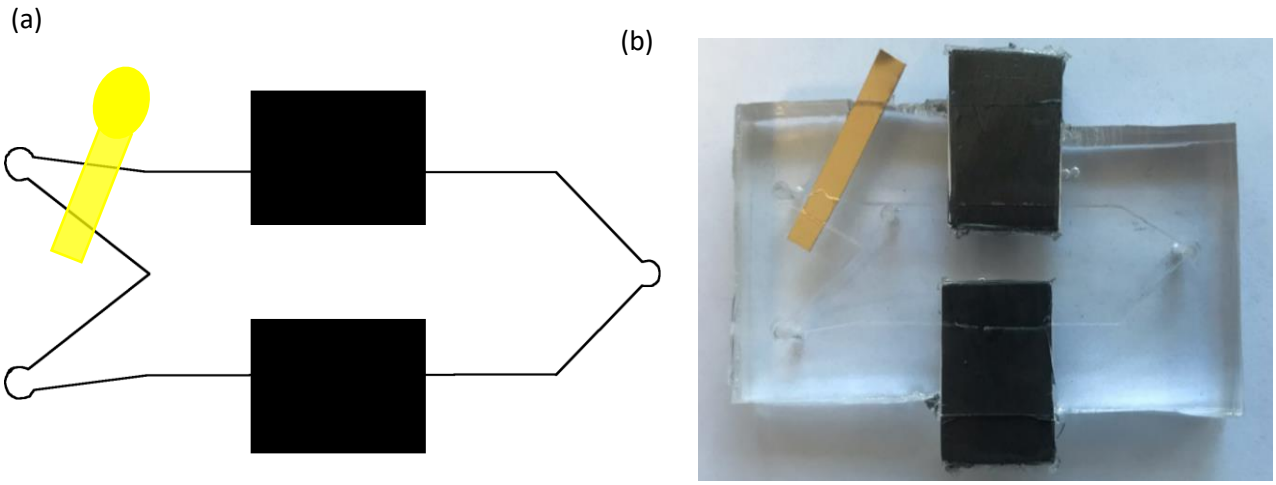

Figure 6.2. Schematic (a) and real image (b) of a proposed three-electrode microfluidic flow cell with dimensions of 1.2 mm width, 150 µm height and 30 mm length. The system consists of graphite working (WE) and counter-electrodes (CE) and a gold pseudo-reference electrode (RE).

The goal in three-electrode real-time measurement coupled with microscopy imaging is collection of valuable information for better understanding of the redox proteins involved in EET of EABs, including cyclic voltammetry and EIS.

With the three-electrode MFC, we can simultaneously find the individual potentials of the cathode and anode with gold as a pseudo-reference electrode. For example, in the power overshoot study, this configuration can aid in delivering a better understanding of the doubling back behaviour from the anode individual potential.

Cyclic voltammetry can provide a variety of information such as catalytic electron transfer between the cells and the electrode, mass transfer at the biofilm/electrode interface, identification of the active sites in turnover conditions and analysis of electron-transfer kinetics.[8]

EIS is another important electrochemical technique used in bio-electrochemical systems (changes in the properties of the bio-interface). *In situ* EIS measurements of the bio-capacitance and bioresistance of the electrode-bound layer of *G. sulfurreducens* biofilms were collected during growth under different shear flow conditions to monitor the capacitance and resistance values of biofilms, which are highly important when the flow rates are changed in microfluidic channels.[9]

6.3. *In situ* formation of chitosan membrane for microfluidic MFC

Other future work based on this thesis includes construction of an *in-situ* chitosan membrane to reduce the internal resistance in microfluidic MFC.

It was previously demonstrated that closer electrode placement leads to reduced internal resistance. With all of the advantages existing in the membraneless MFC, the fuel cross-over problem cannot be completely avoided, as described in chapter 4. This problem becomes more serious when two fuel and oxidants are incompatible (e.g., acidic/basic solution or ferrocyanide) or when the lateral diffusion of one solution is significantly higher than other and can result in a substantial drop in current output. Therefore, a very thin and semi-permeable membrane is necessary, one that can be sandwiched between an anode and a cathode to separate the fuels and oxidants. At the same time, the membrane also allows the passage of protons to complete the electric circuit.[10] However, in a microfluidic MFC, it is difficult to install a piece of pre-synthesized membrane (such as Nafion) inside a microchannel. Because of the abovementioned problems, chitosan is a good choice of membrane material (as our group has experienced in forming a cross-linked in situ chitosan membrane in a microchannel). The proposed schematic diagram of an *in-situ* chitosan membrane for a microfluidic MFC is presented in Figure 6.3, and in this design, two parallel channels (side-by-side arrangement) were used to study the performance of the MFC.

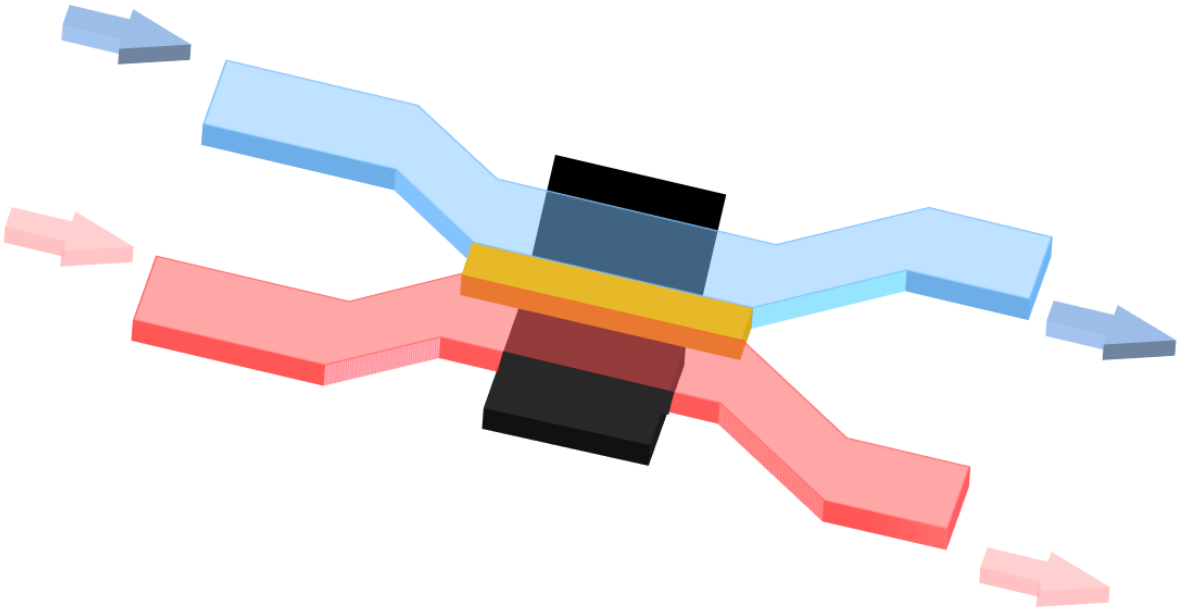

Figure 6.3. Schematic diagram of a microfluidic microbial fuel cell with a chitosan membrane separating fuel and oxidant.

6.4. Comprehensive investigation of flow rate, nutrient concentration and external resistance in a *G. sulfurreducens* biofilm

During this research on pure *G. sulfurreducens* biofilms in a microfluidic MFC system, we observed several new behaviours with respect to biofilm activity under precise nutrient medium concentrations (acetate), flow rates and different (high to low external) resistances, which require further investigations. In most studies using an MFC, the typical nutrient medium contains a high concentration of COD, glucose or acetate, in excess of 2 mM, and a few studies have focused on low concentrations (especially for *G. sulfurreducens*). [11] [12]

Previous investigations have shown that hydrodynamic conditions and molecular transport into the active biofilm have significant roles, particularly under conditions of very low concentrations of nutrient medium.[13,14] A recent study from our group introduced a new generalized kinetic framework applied to whole-cell bioelectrocatalysis by *G. Sulfurreducens* biofilms in bioflow reactors.[15] This system was used in real-time monitoring

of respiration of a *G. sulfurreducens* biofilm and used precise solution conditions changes to maintain the bacteria in active, pseudo-active and inactive conditions.[16]

In this work, we used a microfluidic MFC flow cell with *G. sulfurreducens* inoculated into the microchannel to measure the power of MFC while a range of acetate concentrations from high to low were applied. In future investigation, we can identify the threshold conditions at very low concentrations of acetate (<2 mM) in the active, pseudo-active and inactive metabolic states of *G. sulfurreducens* used as EABs in the MFC. Moreover, these threshold values for concentration should be dependent on flow rates and the external resistors selected.

Our overall goal is a comprehensive study of the relationships among flow rate, nutrient concentration and the external resistances on the electroactive biofilm, an effort undertaken for the first time in MFCs. This study can be coupled with other visualization techniques such as microscopy, which can aid in understanding the distribution of the biofilm along the microchannel in long-term experiments in MFCs under different conditions.

As a preliminary overview, a series of nutrient concentration changes were applied on a mature *G. sulfurreducens* biofilm at different external resistances using a microfluidic MFC flow cell. In Figure 6.4a, acetate concentrations of 10, 5, 2, 1, 0.5 and 0.25 mM were plotted vs. current output of the MFC. Each concentration was applied at four different external resistances (150, 50, 25, 8 kΩ), as shown in Figure 6.4b. The Michaelis-Menten constant K_M, as a kinetic parameter, defines the substrate concentration that results in half-maximal activity. The Lineweaver-Burk plot (in Figure 6.4b) of the reciprocal current output vs. the reciprocal acetate concentration demonstrates the expected linear profile for systems applicable to Michaelis-Menten kinetics. Table 6.1. summarises of K_M and I_{Max} values under different applied resistances

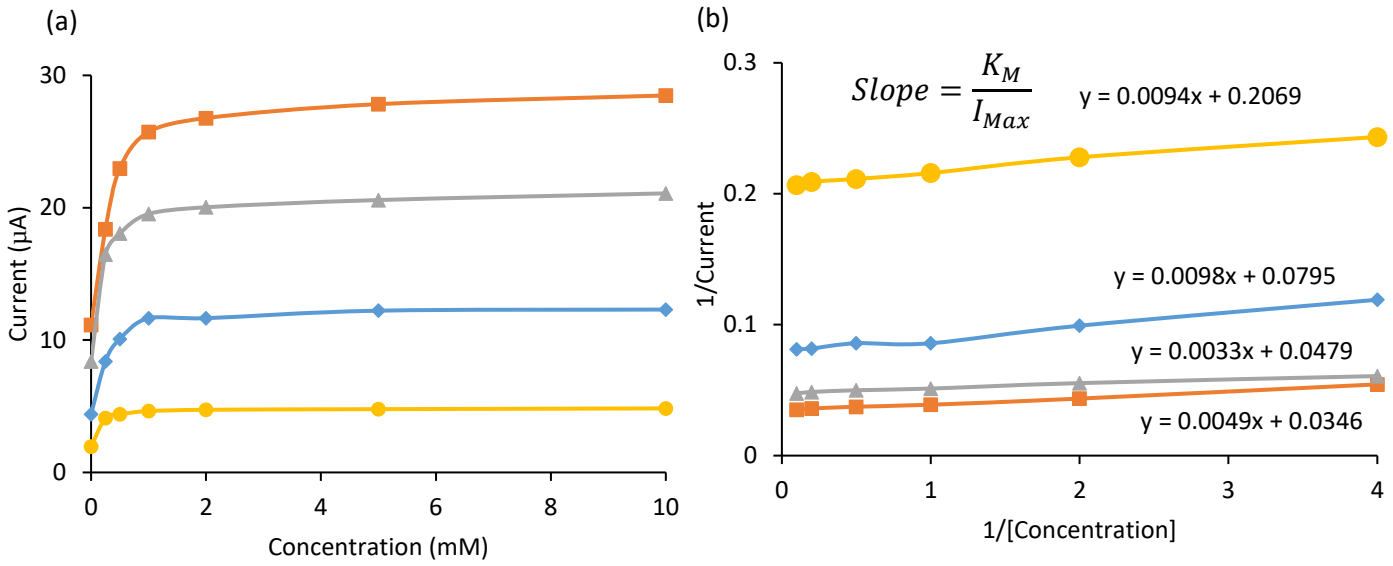

Figure 6.4. (a) Produced current versus concentration for a mature *G. sulfurreducens* biofilm via switching from [Ac]= 10, 5, 2, 1, 0.5 and 0.25 mM acetate as a nutrient medium under different external resistances of 8 (■), 25 (▲), 50 (◆), and 150 kΩ (●). (b) Reciprocal current output vs. the reciprocal acetate concentration shows linear trend and Michaelis-Menten kinetics can be calculated with the line slope.

Table 6.1. Summary of K_M and I_{Max} values under different applied resistances.

R_{ext} (kΩ)	I_{Max} (μA)	K_M (mM)
150	4.83	0.045
50	12.57	0.12
20	20.87	0.06
8	28.90	0.14

6.5. Biocathode MFC with sulfur reducing acidic bacteria

One relatively new area in MFC development is the concept of using microorganisms as catalysts in the cathode compartment. Microorganisms that accept electrons from the cathode electrode are referred as electrotrophs, which have the ability to transfer electrons from the cathode surface to the electron acceptor. As explained in chapter one, biocathodes are

categorized into two types, aerobic and anaerobic biocathodes: (i) In aerobic biocathodes, oxygen acts as a terminal electron acceptor, and electrotrophic microorganisms perform oxidation of transition metals such as Fe^{2+} and manganese (II) for electron delivery to the terminal electron acceptor, oxygen in this case;[17] (ii) In anaerobic biocathodes, where oxygen is not present, compounds such as manganese, sulfate, nitrate, iron and carbon dioxide are used as electron acceptors.

The performance of a biocathode MFC is dependent on the microorganism and its electron transfer. Numerous investigations have examined the electron transfer mechanisms in bioanode MFCs. However, little information is available on the electron transfer mechanisms in biocathode MFCs, and many researchers believe that microorganisms play important roles in both direct and mediated transfer of electrons. [18,19]

Acidithiobacillus ferrooxidans is an autotrophic bacterium that uses CO_2 as a carbon source to obtain energy from the oxidation of ferrous iron, elemental sulphur or reduced sulphur compounds at low pH using O_2 as the final electron acceptor.[20] A previous study showed that in the presence of Fe^{2+}, this bacterium is able to catalyse oxygen reduction in the cathodic compartment of an MFC with a low pH [21] (which is separated from anode compartment by a bipolar membrane). Although it was reported in recent study, the contribution of a direct electron transfer between the cathode and the bacteria cannot be totally ruled out, CV strongly suggest mediated electron transfer (by Fe^{2+}) as the main mechanism for these bacteria.[22]

However, in 2010, Carbajosa et al. reported that *Acidithiobacillus ferrooxidans,* with electrochemical growth in a three-electrode system, could directly accept electrons from the electrode without the need to add iron to the solution, and they referred to this process as direct electrocatalytic reduction of oxygen. [19]

We studied the performance of an *Acidithiobacillus ferrooxidans* biocathode MFC without the use of redox mediators. The goal is to grow this microorganism on the cathode electrode to construct a biocathode MFC that can accept the electrons from the electrode directly. *G. sulfurreducens* and *Acidithiobacillus ferrooxidans* are used at the anode and cathode compartments of a dual-chamber MFC, which are separated with a bipolar membrane. The preliminary result is shown in Figure 6.5. The MFC was first inoculated with *G.*

sulfurreducens at the anode and PBS buffer at the cathode. The bacteria were allowed to mature at the anode surface, and the bioanode biofilm resulted in a stable maximum voltage of 287 mV (with a 10 kΩ external resistance). After development of the bioanodes, the cathode solution replaced with only the nutrient of *Acidithiobacillus ferrooxidans* at pH=2 with the same external resistance. A bipolar membrane is needed to maintain the low catholyte pH, whereas the regular used membrane failed to keep the pH difference between the anolyte and the catholyte when the pH velue are very low (<2.5). A bipolar membrane consists of a cation and an anion exchange layers as described in chapter 1. The changing in pH of catholyte solution shows a significant improvement (86.5 mv) of MFC performance and voltage reached to 373.5 mV after 30 hours (Figure 6.5). This increase is a result from increases of H^+ availability in the acidic solution for oxygen reduction reaction.

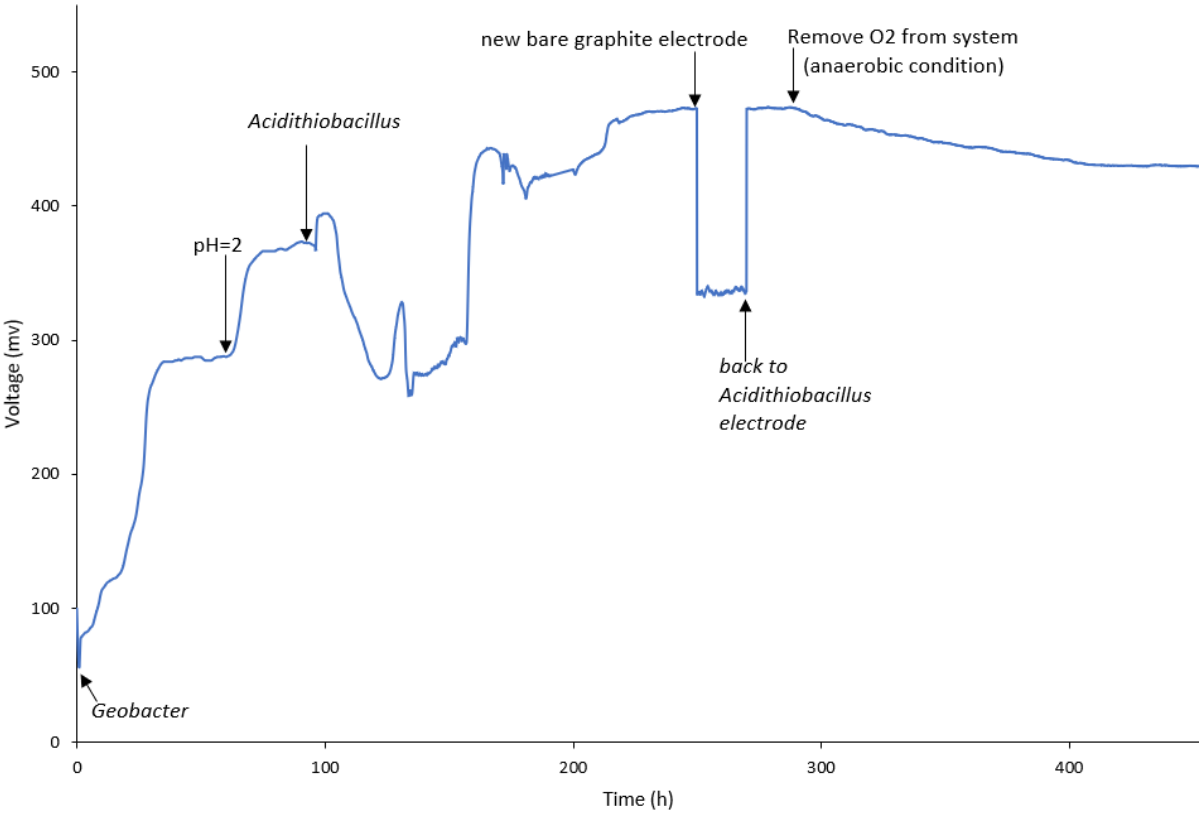

Figure 6.5. Growth of a biocathode MFC with sulfur reducing acidic bacteria (*Acidithiobacillus ferrooxidans*). First Geobacter was inoculated into anode chamber and PBS buffer at the cathode, after reaching to steady state in voltage, biocathode nutrient with pH=2 was added into cathode chamber. Then *Acidithiobacillus ferrooxidans* inoculated into the cathode to growth. By removing the ORR, it is obvious MFC is working based on bacteria included in cathode.

Then at the time of 96 h (when the voltage is stable) the biocathode bacteria were added into cathode chamber. As observed in Figure 6.5, right after the bacteria were added, the voltage of MFC first dropped and subsequently recover to its maximum value at 440 mV after 70 hours which is related to the growth of the *Acidithiobacillus ferrooxidans*.

Then we have changed the cathode grown bacteria's electrode with a bare graphite electrode to show the amount of voltage comes from ORR or biocathode. Result showing the return to pre-bacteria voltage after we added a new bare electrode. Therefore we conclude that ≈30 % of the output voltage is the result of the presence of the bio-cathode. The second portion of the experiment involved removal of O_2 from the system by placing the MFC in an anaerobic location for three days, and voltage is reducing slowly in the MFC from 470mV to 430 mV and continuing to become reduced (data not shown). This losses in voltage is a result of less O_2 available for catalysed ORR on the surface of cathode electrode.

This study needs more investigation and for further study we need to examine the contribution of direct electron transfer between the cathode and the bacteria as the main mechanism using other electrochemical measurements. In the second phase of future work in this study, when MFCs are operated in batch mode, we need to use a costly bipolar membrane; otherwise, the performance cannot be sustained due to the drop in pH in the anodic compartment and the increase in pH in the cathodic compartment. However, in a microfluidic system, we can eliminate this need for a membrane.

6.6. Bibliography

[1] Torres, C. I.; Marcus, A. K.; Parameswaran, P.; Rittmann, B. E., Kinetic experiments for evaluating the Nernst− Monod model for anode-respiring bacteria (ARB) in a biofilm anode. *Environmental science & technology* **2008,** *42* (17), 6593-6597.

[2] Thormann, K. M.; Saville, R. M.; Shukla, S.; Spormann, A. M., Induction of rapid detachment in Shewanella oneidensis MR-1 biofilms. *Journal of bacteriology* **2005,** *187* (3), 1014-1021.

[3] Ishii, S. i.; Watanabe, K.; Yabuki, S.; Logan, B. E.; Sekiguchi, Y., Comparison of electrode reduction activities of Geobacter sulfurreducens and an enriched consortium in an air-cathode microbial fuel cell. *Appl. Environ. Microbiol.* **2008,** *74* (23), 7348-7355.

[4] McLean, J. S.; Wanger, G.; Gorby, Y. A.; Wainstein, M.; McQuaid, J.; Ishii, S. i.; Bretschger, O.; Beyenal, H.; Nealson, K. H., Quantification of electron transfer rates to a solid phase electron acceptor through the stages of biofilm formation from single cells to multicellular communities. *Environmental science & technology* **2010,** *44* (7), 2721-2727.

[5] Ataka, K.; Kottke, T.; Heberle, J., Thinner, smaller, faster: IR techniques to probe the functionality of biological and biomimetic systems. *Angewandte Chemie International Edition* **2010,** *49* (32), 5416-5424.

[6] Hong, S. H.; Jeong, J.; Shim, S.; Kang, H.; Kwon, S.; Ahn, K. H.; Yoon, J., Effect of electric currents on bacterial detachment and inactivation. *Biotechnology and bioengineering* **2008,** *100* (2), 379-386.

[7] McLean, J. S.; Wanger, G.; Gorby, Y. A.; Wainstein, M.; McQuaid, J.; Ishii, S. i.; Bretschger, O.; Beyenal, H.; Nealson, K. H., Quantification of electron transfer rates to a solid phase electron acceptor through the stages of biofilm formation from single cells to multicellular communities. *Environmental science & technology* **2010,** *44* (7), 2721-2727.

[8] Harnisch, F.; Freguia, S., A basic tutorial on cyclic voltammetry for the investigation of electroactive microbial biofilms. *Chemistry–An Asian Journal* **2012,** *7* (3), 466-475.

[9] Zarabadi, M. P.; Paquet-Mercier, F. o.; Charette, S. J.; Greener, J., Hydrodynamic Effects on Biofilms at the Biointerface Using a Microfluidic Electrochemical Cell: Case Study of Pseudomonas sp. *Langmuir* **2017,** *33* (8), 2041-2049.

[10] Haubold, H.-G.; Vad, T.; Jungbluth, H.; Hiller, P., Nano structure of NAFION: a SAXS study. *Electrochimica Acta* **2001,** *46* (10-11), 1559-1563.

[11] Crevecoeur, S.; Vincent, W. F.; Comte, J.; Lovejoy, C., Bacterial community structure across environmental gradients in permafrost thaw ponds: methanotroph-rich ecosystems. *Frontiers in microbiology* **2015,** *6*, 192.

[12] Bottos, E. M.; Vincent, W. F.; Greer, C. W.; Whyte, L. G., Prokaryotic diversity of arctic ice shelf microbial mats. *Environmental microbiology* **2008,** *10* (4), 950-966.

[13] Liu, Y.; Kim, H.; Franklin, R.; Bond, D. R., Gold line array electrodes increase substrate affinity and current density of electricity-producing G. sulfurreducens biofilms. *Energy & Environmental Science* **2010,** *3* (11), 1782-1788.

[14] Ren, H.; Tian, H.; Gardner, C. L.; Ren, T.-L.; Chae, J., A miniaturized microbial fuel cell with three-dimensional graphene macroporous scaffold anode demonstrating a record power density of over 10000 W m− 3. *Nanoscale* **2016,** *8* (6), 3539-3547.

[15] Zarabadi, M. P.; Couture, M.; Charette, S. J.; Greener, J., A generalized kinetic framework for whole-cell bioelectrocatalysis in flow reactors clarifies performance enhancements for Geobacter Sulfurreducins Biofilms. *ChemElectroChem*, **2019,** 6(10), 2715-2718.

[16] Zarabadi, M. P.; Charette, S. J.; Greener, J., Toggling Geobacter sulfurreducens metabolic state reveals hidden behaviour and expanded applicability to sustainable energy applications. *Sustainable Energy & Fuels* **2019**.

[17] Park, D. H.; Zeikus, J. G., Improved fuel cell and electrode designs for producing electricity from microbial degradation. *Biotechnology and bioengineering* **2003,** *81* (3), 348-355.

[18] Rusli, S. F. N.; Bakar, M. H. A.; Loh, K. S.; Mastar, M. S., Review of high-performance biocathode using stainless steel and carbon-based materials in Microbial Fuel Cell for electricity and water treatment. *International Journal of Hydrogen Energy* **2018**.

[19] Lovley, D. R., The microbe electric: conversion of organic matter to electricity. *Current opinion in biotechnology* **2008,** *19* (6), 564-571.

[20] Carbajosa, S.; Malki, M.; Caillard, R.; Lopez, M. F.; Palomares, F. J.; Martín-Gago, J. A.; Rodríguez, N.; Amils, R.; Fernández, V. M.; De Lacey, A. L., Electrochemical growth of Acidithiobacillus ferrooxidans on a graphite electrode for obtaining a biocathode for direct electrocatalytic reduction of oxygen. *Biosensors and Bioelectronics* **2010,** *26* (2), 877-880.

[21] Ter Heijne, A.; Hamelers, H. V.; De Wilde, V.; Rozendal, R. A.; Buisman, C. J., A bipolar membrane combined with ferric iron reduction as an efficient cathode system in microbial fuel cells. *Environmental science & technology* **2006,** *40* (17), 5200-5205.

[22] Izadi, P., Fontmorin, J. M., Fernández, L. F. L., Cheng, S., Head, I., & Yu, E. H. High Performing Gas Diffusion Biocathode for Microbial Fuel Cells Using Acidophilic Iron Oxidizing Bacteria. *Frontiers in Energy Research* **2019** 7, 93.

Conclusion

Due to a large limitation in the source of energy and depletion of fossil fuels, researchers have been focused to look for an alternative source of energy productions.[1,2] MFCs have a great future, as it already described in chapter 1, a bio-reactor that use living microbes as a catalysis to convert organic fuels into electricity.

In present thesis, the details on the fabrication and use of a new membraneless MFC with integrated graphite electrodes and an oxygen protection barrier for energy application of electroactive bacteria has provided. In Chapter 1, exhaustive discussed about previously reported on the possible sources of renewable energies. Then some basic information on microbial fuel cell technologies and its different types was provided for readers. Then it followed with electroactive bacteria and biofilms, bacterial biofilms, The metabolic transportation of electrons from EABs to electrodes, biological fuel cell and MFC concepts as well as power generation characterization of MFCs and MFC components/configuration.

In chapter 3, a method for producing hierarchical wrinkled gold surfaces is used to continuously change characteristic microstructure dimensions of a bioanode in a microbial fuel cell.[3] Using this approach, the effect of anode topography on power outputs from direct electron transfer from *Geobacter sulfurreducens* biofilms can be isolated and studied without the competing effects associated with additive manufacturing. In this study we proposed a guideline for optimization of MFCs (other bioelectrochemical systems) by focusing on their physical access to the anode surface, which can increase electroactive surface area relative to the electrode geometrical footprint.

The goal of chapter 4 was to develop and design rules that can achieve more consistent performance of membraneless microfluidic MFCs, thereby enhancing their impact among the wider BES. A new method for easy-to-fabricate a membraneless MFC with integrated graphite electrodes and an oxygen protection barrier were provided. Guided by computational fluid dynamics simulations, the device architecture was also optimised to

prevent cross-contamination between the anode and cathode compartments under a wide range of flow rates.[4]

Chapter 5 focused on how to eliminate power overshoot behaviour in a constant flow microfluidic microbial fuel cell for a pure culture *G. sulfurreducens* biofilm and enable application of high shear to eliminate nutrient concentration cycling. Two method were used to fully investigate the overshoot, role of MFC acclimation to different external resistors and "*in situ acclimation*" which followed by changing flow rates to accelerated the process.

Chapter 6 provided interesting discussions on future of MFCs and present some of our preliminary results for future study. A Real-time visualization of microbial activities on a graphite electrode associated with GFP *G. sulfurreducens, In situ* electrochemical analysis with the three-electrode model MFC, chitosan membrane for microfluidic MFCto reduce the distance between electrodes, Comprehensive investigation of flow rate, nutrient concentration and external resistance and biocathode MFC with sulfur reducing acidic bacteria are some of these future works.

Bibliography

1. Logan, B. E., *Environmental transport processes*. John Wiley & Sons: 2012.

2. Lewis, N. S.; Nocera, D. G., Powering the planet: Chemical challenges in solar energy utilization. *Proceedings of the National Academy of Sciences* **2006,** *103* (43), 15729-15735.

3. Abbaszadeh Amirdehi, M.; Saem, S.; Zarabadi, M. P.; Moran-Mirabal, J. M.; Greener,J., Microstructured Anodes by Surface Wrinkling for Studies of Direct Electron Transfer Biofilms in Microbial Fuel Cells. *Advanced Materials Interfaces* **2018,** *5* (13), 1800290.

4. Amirdehi, M. A.; Khodaparastasgarabad, N.; Landari, H.; Zarabadi, M. P.; Miled, A.; Greener, J., A High-Performance Membraneless Microfluidic Microbial Fuel Cell for Stable, Long-Term Benchtop Operation Under Strong Flow. *ChemElectroChem* **2020**.